The effects of radiation and convection on stellar oscillations

Motee William Phorah

Supervisor:

Dr Rodney Thebe Medupe[1]

Co-supervisors:

Prof Jøergen Christensen-Dalsgaard[2]

Dr Günter Houdek[3]

Prof Michael John Thompson[4]

Thesis Presented for the Degree of

DOCTOR OF PHILOSOPHY

in the Department of Astronomy

University of Cape Town

November 2007

[1]Department of Astronomy, University of Cape Town, South Africa
[2]Department of Astronomy and Physics, University of Aarhus, Denmark
[3]Institute of Astronomy, University of Cambridge, United Kingdom
[4]Department of Applied Mathematics, University of Sheffield, United Kingdom

I dedicate this thesis to:

My late father **Peter Mosimaneotsile Phorah** and my late mother **Euginia Nkagisang Phorah**, for being everything to me. I put you before the Lord. Ke lebogetse kgodiso e senang bolekanyetso e lo nnetseng yona. Thank you very much!

My brothers **Bootaba**, **Thebolo**, **Gawagakwa** and **Kokisa**; my sisters **Kesetsenao** and **Mosetsanagape**; setlogolo sa rona se se tonna **Botho** and the families of my brothers for support you showed whenever hard times of life needed to be encountered.

Boora Dince, Boora Kwena, Boora Mahole, Boora Mogashoa and my entire relatives. Ke lo lebogela go tlhola batsadi ba me!

Setlagole, my home village, which will always hold a special place in my heart because of the warmth and acknowledgement bestowed upon me by the community.

Thank You

"If I have seen further than others, it is by standing upon the shoulders of giants"

Sir Isaac Newton

I wish to thank the following:

- **Thebe Medupe**, my supervisor for the great supervision, encouragement and for directing me to Theoretical Astrophysics as well as this project. I remember discouraging me when I was considering doing another Masters degree in Astrophysics. I was thinking that my background in pure mathematics will be my major obstacle. Thanks for teaching me computer programming as well as preparing myself for this project. I am also indebted to him for the helps with various non-scientific matters, to which he has never been indifferent. I thank you for help and advice in using your code. Many thanks for the assistance and guidance in preparation of this thesis. I am looking forward to many years of working with you. Ka Serolong ra re kamoso le kamoso!

- **Jøergen Christensen-Dalsgaard**, my co-supervisor for the great supervision, scientific and technical advice, for the invitations to University of Aarhus and many fruitful discussions. In that note thanks for your kind hospitality in Aarhus. Many thanks for the assistance and guidance in the preparation of this thesis. I am looking forward to many years of working with you. Special thanks to let me know about the Danish Rectors conference fellowship. I also thank you for fully supporting my second trip to Aarhus.

- **Michael Thompson**, my co-supervisor for the great supervision and support. Many thanks for the assistance and guidance in the preparation of this thesis. Thanks for numerous discussions on both scientific and non-scientific matters. For the invitation to Sheffield and your kind hospitality during my visit. Many thanks for fully supporting my stay in Sheffield. I am looking forward to many years of working with you.

- **Güenter Houdek**, my co-supervisor for his constant support, great supervision and for guidance in preparation of this thesis . Many thanks for his invaluable help in both scientific and technical matters. Thanks for your invitation to Cambridge and your kind hospitality during my visit. I am

looking forward to many years of working with you. Many thanks for help in using your code and to construct equilibrium models for me. I am looking forward to many years of working with you. Many thanks for partially supporting my stay in Cambridge.

- **Douglas Gough**, Director of Institute of Astronomy in Cambridge, for showing great interest in my work, for supporting my visit to Cambridge and many fruitful discussion we had during his recent visit to South Africa.

- **Patrick Woudt**, for being my supervisor before Thebe Medupe joins University of Cape Town permanently. Many thanks for your support and kindness.

- **Renee Kraan-Kortweg**, Astronomy Head of Department, for your full support and kindness. Many thanks for allowing me the opportunity to join this unniversity.

- **UCT Astronomy Department staff** for the support and encouragement. Special thanks to **Maguerite Armstrong** for the help in dealing with many practicalities here in Cape Town. My deepest thanks to my office mates, **Bonita de Swardt, Michelle Cluver** and **Ihab Riad** for creating conducive learning environment. May the good Lord bless and keep you!

- **South African Astronomical Observatory Staff** for the support you have given to me, in particular **Enrico Olivier** for his contribution to my understanding of stellar convection, **Loui Balona** for giving me a brief introduction to stellar pulsation, **Gareth Dugmore** for helping with all the practicalities related to computers, and **Ramatholo Sefako & Petri Vaisanen** for many helpful conversations.

- Many thanks to **Søren Frandsen** for many helpful conversations. Special thanks to all my colleagues and friends at the Institute of Astronomy and Physics at Aarhus. I also like to thank **Anette Skovgaard** for her support in dealing with many practicalities during my stay in Aarhus.

- At Sheffield I would like to thank all my colleagues and friends in particular **Lynda Harrison** for her support and kindness, and at Cambridge I thank **Paul Aslin** for his support.

- **Mrs Lillyman**, my landlady in Sheffield for your kind hospitality.

- My special thanks to **Kate** and **Robin** for your kind hospitality in Sheffield.
- **Charlimagne Pooe**, my former Mathematics lecturer, for approaching me to register for this PhD degree. Many thanks for the trust and faith you have shown on me.
- **Mahomed Karodia**, former Superitendent General of North West Education department for approving my study leave.
- **Mutle Mefane and family** (my pastor), as well as the congregation of Mokoto Memorial AME church for prayers and supports.
- **Motseothata Tsogang**, my former student and now my friend, for your support and motivation. Ke lebogile go menagane Bra Feles!
- **Letlhogonolo Selaledi**, my former student and now my friend, for your support and motivation. Many thanks to **Nokuzola Shosha** for her support. I enjoyed my stay in Cape Town because of you. Montsamaisa bosigo ke mo leboga bosele!
- **Edward Jurua**, my friend, for your support, kindness and encouragement. Many thanks Ladit! I am very greatful to **Zolile Mguda** for your encouragement and support. Siyabulela Buti!
- **Leslie Moji, Moalusi Makwea, Mooketsi Sebe, Reuben Maffeo, Moses Lesolle and Tuelo Botlhoko**, my friends, for your support, encouragement and kindness.
- My friends, **Ntaoleng Khathatso, Windy Lechuti, Masego Morakile, Lerato Mmutle, Ntswaki Shiya , Ntshadi Kgabi and Portia Metswamere**. This work could not have been completed in such a peaceful way without your encouragements.
- Special thanks to **Lucky Maleka, Kenneth Seleka, Gontse Pai, Simon Letlojane and Montlafatsi Moiloa** to have supported one another in a way.
- My former students **Tshepiso Lepholletsa, Cassius Mphatse, James Poeng, Terrance Mahlatsi, Peace Mosimanyana, Fikile Serame, Innocent Matlhare, Hensley Rotrick, Tshepo Mosiane & William Rammaledi** for your support.

- These young Boys from my village, **Mogapi Mashomemg, Lebogang Seane, Peloentle Motoko, Tlhalefo Motoko, Steve Seane and Eddie Seabelo**. Ke lebogile basimane baetsho. Special thanks to my many friends at home, the likes of **Tatenki Maopong**.
- I acknowledge financial support from the **National Research Foundation of South Africa**, **University of Cape Town**, **Timbaktu Project** and **Danish Rectors Conference**. Special thanks to **Envor Moeng** and **Danile Busakwe** for the manner in which they handled my scholarship. Ke lebogile go menagane.

Abstract

We consider the effects of radiation and convection on atmospheric oscillations of A, F and G stars. The linear non-adiabatic radial pulsation equations are solved. Convection is modelled with a time-dependent, non-local mixing length theory, and a consistent treatment of radiative transfer in a grey atmosphere is adopted. Previous investigations, by Houdek and Medupe, have each solved only part of the problem: Medupe used a consistent treatment of radiation but neglected the effects of convection, whereas Houdek used non-local mixing-length theory to model convection but adopted the Eddington approximation to radiative transfer. The present approach takes radiative transfer elements form Medupe's code and incorporates them into Houdek's code which includes the non-local time-dependent mixing-length formulation. The new code is applied to a study of zero-age main-sequence stars with masses ranging from $1.0M_{\odot}$ to $2.1M_{\odot}$.

In these stars the superadiabatic gradient near the surface may exhibit a "dip". We have found that this produces a corresponding dip in the hydrogen ionization zone in the temperature eigenfunction of the modes. Furthermore, we have shown that the main effect that determines whether the dip is present or not is the opacity fluctuations. We have shown that the effect on the eigenfrequencies of including the proper treatment of radiation can be under one per cent. The significance of this seemingly small difference can be obtained by comparing this with the observational accuracy, as well as with other possible systematic errors in the frequencies. These days, the observed pulsational frequencies can be measured with an accuracy better than one per cent, thus the effect of including a consistent treatment of radiation is significant if we exclude the effects of uncertainties in other parameters such as the mass and radius. There may still be other effects that would dominate the effect of including consistent treatment of radiation on the eigenfrequency.

A comparison of the results obtained using the new code with those using Houdek's code shows that using the Eddington approximation or consistent radiative transfer makes only a small difference to the computed frequencies of δ Scuti oscillations. However, within the roAp stars frequency region of $1 < \nu < 3$ mHz, the differences can be large. Therefore for accurate determination of frequencies it is important to use a consistent treatment of radiative transfer when studying the roAp stars. It is also shown that except for the radial mode $n = 1$ there is significant difference in the shape of the temperature eigenfunctions introduced by improved treatment of radiation for models with $M < 1.6M_{\odot}$.

Except for the $1.5M_{\odot}$ and $1.6M_{\odot}$ models, all the modes are damped. The unstable modes for the $1.5M_{\odot}$ and $1.6M_{\odot}$ models are near 2.5 mHz and 2 mHz respectively. Comparison of the surface luminosity perturbations computed using the new code with those computed using Houdek's

code shows the largest difference in the $1.0M_{\odot}$ model and the smallest difference in the $2.1M_{\odot}$ model.

A comparison of convective models with radiative models for $1.8M_{\odot}$ and $2.1M_{\odot}$ stars shows that when convection is neglected on both the equilibrium and pulsation model one does not introduce an error at frequencies below 1 mHz, but within the roAp stars frequency region $1 < \nu < 3$ mHz the error is significant. When convection is neglected in roAp stars the growth rates are underestimated. We have also shown that when convection is neglected one over-estimates the dip in the temperature eigenfunctions. Preliminary results, for comparing the new code with Medupe's code, have shown that by neglecting the perturbed convective flux one over-estimates the growth rates at high-frequency modes in A stars.

Contents

1 Introduction **1**

1.1 Stellar oscillations . . . 3

1.1.1 The description of the oscillations . . . 5

1.1.2 Mode identification . . . 7

1.1.3 δ Scuti and roAp stars . . . 14

1.1.4 The basic equations of hydrodynamics . . . 17

1.2 The radiative transfer . . . 19

1.2.1 In the atmosphere . . . 20

1.2.2 In the envelope . . . 21

1.3 Convective Transfer . . . 22

1.3.1 The mixing length theory . . . 26

1.3.2 Gough's local mixing length theory . . . 27

1.3.3 Non-local mixing-length theory . . . 34

2 Pulsation Equations **41**

2.1 Radial pulsation equations . . . 41

2.1.1 Continuity equation . . . 41

2.1.2 Equation of motion . . . 43

2.1.3 Radiative transfer equation . . . 44

2.1.4 The energy equation . . . 45

2.1.5 Convection equations . . . 46

2.1.6 The Temperature eigenfunction . . . 49

2.1.7 The scheme used to solve the pulsation equations . . . 50

2.1.8 Boundary conditions for pulsation equations . . . 51

2.1.9 Eigenfrequencies . . . 58

2.2 Work Integral . . . 59

2.3 Description of the code . . . 61

3 Results for Pulsation Equations **63**

3.1 Equilibrium models . . . 63

3.2 The Equilibrium Eddington factors . . . 66

3.3 Tests on the code 66
3.4 The eigenfunctions 73
3.4.1 The Temperature eigenfunctions 73
3.4.2 Displacement eigenfunctions 85
3.5 Growth rates 93
3.6 Work Integral 95

4 Comparison of radiative transfer and Eddington approximation 103
4.1 Comparison of Houdek's results with my results 103
4.1.1 The effect on the eigenfrequencies 103
4.1.2 The effect on the eigenfunctions 106
4.1.3 The effect on theoretical growth rates 123
4.1.4 Work Integral 124
4.1.5 The effect on the surface luminosity perturbations 128
4.2 Comparison of equilibrium models with convection and those with inefficient convection 131
4.2.1 The effect on the eigenfrequencies 134
4.2.2 The effect on the temperature eigenfunctions 135
4.2.3 The displacement eigenfunctions 139
4.2.4 The effects on the growth rates 141
4.2.5 The effects on the work integrals 142
4.2.6 The effect on the surface luminosity perturbations 143
4.3 Comparisons of the new code with Medupe's code 143
4.3.1 The effect on the eigenfunctions 144
4.3.2 The effect on the growth rates 144

5 Conclusions 157
5.1 Limitations of the work 159
5.2 Suggested Future Research 159

References 161

A The Equilibrium model 165
A.1 The differential equations 165
A.2 Boundary conditions 166

B The Pulsation model 167
B.1 Linear adiabatic pulsation equations 167

B.2 Linear non-adiabatic pulsation equations local mixing-length theory of convection 168
B.3 Linear non-adiabatic pulsations equations using non-local mixing-length theory of convection 169

C The Feautrier method **171**
C.1 The unperturbed transfer equation 171
C.1.1 The atmosphere 171
C.1.2 The envelope 172
C.1.3 Moments of the transfer equation 172
C.1.4 Boundary conditions 173
C.2 The perturbed transfer equation 173
C.2.1 Moments of the perturbed transfer equation 174
C.2.2 Boundary conditions for the perturbed transfer equation 174

D Houdek's calculations **177**

E Medupe's calculations **179**
E.1 The atmosphere 179
E.2 The envelope 180
E.3 Boundary condition 180

F Coefficients of Gough's time-dependent mixing-length equations **181**

List of Figures

1.1 Hertzsprung-Russell diagram showing the location of several classes of pulsating stars. The dashed line shows the zero-age main-sequence (ZAMS). This diagram is taken from Christensen-Dalsgaard (2003). 4

1.2 The propagation of p-modes is shown in **A** and g-modes in **B**. Higher degree p-mode has $n = 8$, $\ell = 100$, whereas the lower degree p-mode has $n = 8$, $\ell = 2$. The g-mode has $n = 10$, $\ell = 5$. The p-modes can travel throughout the Sun, whereas the g-modes are confined beneath the convection zone of the Sun. This sketch is taken from Gough, Leibacher & Toomre (1996). 6

1.3 A plot of (A_{B-V}/A_V) versus $(\phi_{B-V} - \phi_V)$, in radians, for δ Scuti star. The theoretical areas for the $(R,\ \Psi)$ loci were calculated with $0.25 \leq R_{ad} \leq 1$ and $90^\circ \leq \Psi_T \leq 140^\circ$. The modes $\ell = 0,\ 1,\ 2$ are written next to the areas in which observed points of those modes should lie. Taken from Watson (1988). 10

1.4 Example of pulsational line profile variations for δ Scuti star τ Peg with $\ell = 10$, $m = -10$ and $\nu \sin i = 80 km/s$. Taken from Kennelly et al. (1998). 12

1.5 The temperature gradient ∇ as a function of logarithmic pressure for a 1.3 $M_\odot$ ZAMS equilibrium model envelope. The left panel shows the upper part of the convection zone, and right panels show the lower part. The non-local mixing-length theory solution for using the parameters $\alpha_c = 2.0$, $a^2 = b^2 = 300$ is shown by the solid line. The dotted line is the results of local theory, (see Houdek 1996). 37

1.6 Temperature gradient ∇ for the same model as in figure 1.5, but using $\alpha_c = 1.8$, $a^2 = 900$ and $b^2 = 2000$ for the non-local solution. The non-local solution is shown by solid line, and the local solution with the dashed line. (see Houdek 1996) 37

1.7 The radius of the base of the convection zone, r_b, as a function of the parameters of the mixing-length theory. Panel (a) shows $r_b/R_\odot$ as a function of a^2, for $b^2 = 100$. Seven curves are shown, each corresponds to a different value for α_c. The horizontal dashed line indicates lines computed according to local theory. Panel (b) shows $r_b/R_\odot$ as a function of b^2 with $a^2 = 300$. These figures were taken from Balmforth (1992). 38

3.1 Each panel shows ∇_{ad} and $\nabla - \nabla_{ad}$ for the ZAMS model listed in Table 3.1 plotted against the depth coordinate $\log p$, the logarithm of pressure. 65
3.2 The quantity $(f_{eq}B)/K$ as a function of depth for $1.8M_{\odot}$ model. 67
3.3 The plots of equilibrium and perturbed Eddington factors as a function of depth. The solid line displays the real part of f_{osc} at a frequency 0.252 mHz and dashed line represent f_{eq}. 68
3.4 The plots show $4\,\delta T/T$ and $\delta J/J$ compared as a function of depth for the modes with frequencies 0.252 mHz and 2.169 mHz. As expected there is a departure from radiative equilibrium in the atmosphere since $4\,\delta T/T$ deviates from $\delta J/J$. The left panels show the real parts of $\delta J/J$ and $\delta T/T$, and right panels show the imaginary parts of those eigenfunctions 69
3.5 The real and imaginary parts of $\delta T/T - \nabla_{ad}\delta p/p$ as a function of depth for the modes with frequencies 0.252 mHz and 2.169 mHz are shown in . In the atmosphere there is a departure from zero which verifies that the oscillations is non-adiabatic. 70
3.6 A plot of $\rho^{1/2}c^{1/2}r\delta r$ calculated from our code compared with equation (3.3) for modes with frequencies 1.893 mHz and 2.815 mHz at the growth rates $-3.6 \times 10^{-9}s^{-1}$ and $-3.9 \times 10^{-5}s^{-1}$ respectively. Values of the amplitude A and phase constant α are shown. This is for $1.8M_{\odot}$ model. 71
3.7 The growth rates calculated from using the mechanical boundary condition (2.130) that takes into consideration the fact that modes with $\omega > \omega_{ac}$ are not reflected but dissipate out through the atmosphere. The dashed line shows the results from the work integral calculations, and the solid line is from the code. The arrow indicates the acoustic cut-off frequency. 72
3.8 The real and imaginary parts of $\delta T/T$ for the $1.0M_{\odot}$ model plotted as a function of depth at various frequencies. The optical depth $\tau = 2/3$ is indicated on the first panel by the arrow. 74
3.9 The real and imaginary parts of $\delta T/T$ for the $1.2M_{\odot}$ model plotted as a function of depth at various frequencies. 75
3.10 The real and imaginary parts of $\delta T/T$ for the $1.3M_{\odot}$ model plotted as a function of depth. 76
3.11 The real and imaginary parts of $\delta T/T$ for the $1.5M_{\odot}$ model plotted as a function of depth at various frequencies. 77
3.12 The real and imaginary parts of $\delta T/T$ for the $1.6M_{\odot}$ model plotted as a function of depth at various frequencies. 78
3.13 The real and imaginary parts of $\delta T/T$ for the $1.8M_{\odot}$ model plotted as a function of depth at various frequencies. 79

3.14 The real and imaginary parts of $\delta T/T$ for the $2.0M_{\odot}$ model plotted as a function of depth at various frequencies. 80
3.15 The real and imaginary parts of $\delta T/T$ for the $2.1M_{\odot}$ model plotted as a function of depth at various frequencies. 81
3.16 Comparison of $\delta T/T$ obtained using ZAMS models listed in Table 3.1 at various frequencies. The left and right panels show the real and imaginary parts of $\delta T/T$ respectively. 82
3.17 The real and imaginary parts of $\delta T/T$ for the ZAMS models listed in Table 3.1 plotted as a function of depth at various frequencies. 83
3.18 The real and imaginary parts of $\delta T/T$ for the ZAMS models listed in Table 3.1 plotted as a function of depth at various frequencies. 84
3.19 The real and imaginary parts of $\delta r/r$ for the $1.0M_{\odot}$ model plotted as a function of depth at various frequencies. 85
3.20 The real and imaginary parts of $\delta r/r$ for the $1.2M_{\odot}$ model plotted as a function of depth at various frequencies. 86
3.21 The real and imaginary parts of $\delta r/r$ for the $1.3M_{\odot}$ model plotted as a function of depth at various frequencies. 87
3.22 The real and imaginary parts of $\delta r/r$ for the $1.5M_{\odot}$ model plotted as a function of depth at various frequencies. 88
3.23 The real and imaginary parts of $\delta r/r$ for the $1.6M_{\odot}$ model plotted as a function of depth at various frequencies. 89
3.24 The real and imaginary parts of $\delta r/r$ for the $1.8M_{\odot}$ model plotted as a function of depth at various frequencies. 90
3.25 The real and imaginary parts of $\delta r/r$ for the $2.0M_{\odot}$ model plotted as a function of depth at various frequencies. 91
3.26 The real and imaginary parts of $\delta T/T$ for the $2.1M_{\odot}$ model plotted as a function of depth at various frequencies. 92
3.27 The growth rates as function of the cyclic frequency ν for ZAMS models. They are obtained from using the upper boundary condition (2.130) that takes into consideration the fact that modes with $\omega > \omega_{ac}$ are not reflected but propagate through the atmosphere. The arrow indicates the acoustic cut-off frequency. . . 94
3.28 Growth rates as a function of frequency for ZAMS models listed in Table 3.1. . 96
3.29 The quantities η, η_g and η_t plotted as functions of frequency for $1.5M_{\odot}$ model. . 98
3.30 The quantities η, η_g and η_t plotted as functions of frequency for $1.6M_{\odot}$ model. 98
3.31 The accumulated work integrals (W_{tot}) (in units $10^{30}erg$) for the $1.0M_{\odot}$ model at various frequencies. The curve labelled W_g shows the work integral for the same mode when the contribution from the turbulent pressure is neglected. . . . 99

3.32 The accumulated work integrals (W_{tot}) (in units $10^{30}erg$) for the $1.2M_{\odot}$ model at various frequencies. The curve labelled W_g shows the work integral for the same mode when the contribution from the turbulent pressure is neglected. . . 99
3.33 The accumulated work integrals (W_{tot}) (in units $10^{30}erg$) for the $1.3M_{\odot}$ model at various frequencies. The curve labelled W_g shows the work integral for the same mode when the contribution from the turbulent pressure is neglected. . . . 100
3.34 The accumulated work integrals (W_{tot}) (in units $10^{30}erg$) for the $1.5M_{\odot}$ model at various frequencies. The curve labelled W_g shows the work integral for the same mode when the contribution from the turbulent pressure is neglected. . . 100
3.35 The accumulated work integrals (W_{tot}) (in units $10^{30}erg$) for the $1.6M_{\odot}$ model at various frequencies. The curve labelled W_g shows the work integral for the same mode when the contribution from the turbulent pressure is neglected. . . . 101
3.36 The accumulated work integrals (W_{tot}) (in units $10^{30}erg$) for the $1.8M_{\odot}$ model at various frequencies. The curve labelled W_g shows the work integral for the same mode when the contribution from the turbulent pressure is neglected. . . 101
3.37 The accumulated work integrals (W_{tot}) (in units $10^{30}erg$) for the $2.0M_{\odot}$ model at various frequencies. The curve labelled W_g shows the work integral for the same mode when the contribution from the turbulent pressure is neglected. . . . 102
3.38 The accumulated work integrals (W_{tot}) (in units $10^{30}erg$) for the $2.1M_{\odot}$ model at various frequencies. The curve labelled W_g shows the work integral when the contribution from the turbulent pressure is neglected. 102

4.1 The difference between the eigenfrequencies obtained using the new code and the eigenfrequencies computed using Houdek's code for the ZAMS models. The upper panel shows the real part, and the lower shows the imaginary part. . . . 105
4.2 A comparison of real and imaginary parts $\delta T/T$ obtained from the the new code (MP) and those using Houdek's code (GH) for the $1.0M_{\odot}$ model at various frequencies. Each panel is divided into real and imaginary parts of temperature eigenfunctions. The position of optical depth $\tau = 2/3$ is indicated on the first panel by an arrow. The largest relative difference between using proper treatment of radiation and Eddington approximation is up to about 25%. 107
4.3 A comparison of real and imaginary parts $\delta T/T$ obtained from the new code (MP) and those using Houdek's code (GH) for the $1.2M_{\odot}$ model at various frequencies. Each panel is divided into real and imaginary parts of temperature eigenfunctions. The position of optical depth $\tau = 2/3$ is indicated on the first panel by an arrow. The largest relative difference between using proper treatment of radiation and Eddington approximation is up to about 30%. 108

4.4 A comparison of real and imaginary parts $\delta T/T$ obtained from the new code (MP) and those using Houdek's code (GH) for the $1.3M_{\odot}$ model at various frequencies. Each panel is divided into real and imaginary parts of temperature eigenfunctions. The position of optical depth $\tau = 2/3$ is indicated on the first panel by an arrow. The largest difference between using proper treatment of radiation and Eddington approximation is up to about 72%. 109

4.5 A comparison of real and imaginary parts $\delta T/T$ obtained from the new code (MP) and those using Houdek's code (GH) for the $1.5M_{\odot}$ model at various frequencies. Each panel is divided into real and imaginary parts of temperature eigenfunctions. The position of optical depth $\tau = 2/3$ is indicated on the first panel by an arrow. The largest relative difference between using proper treatment of radiation and Eddington approximation is up to about 33%. 110

4.6 A comparison of real and imaginary parts $\delta T/T$ obtained from the new code (MP) and those using Houdek's code (GH) for the $1.6M_{\odot}$ model at various frequencies. Each panel is divided into real and imaginary parts of temperature eigenfunctions. The position of optical depth $\tau = 2/3$ is indicated on the first panel by an arrow. The largest relative difference between using proper treatment of radiation and Eddington approximation is up to about 70%. 111

4.7 A comparison of real and imaginary parts $\delta T/T$ obtained from the new code (MP) and those using Houdek's code (GH) for the $1.8M_{\odot}$ model at various frequencies. Each panel is divided into real and imaginary parts of temperature eigenfunctions. The position of optical depth $\tau = 2/3$ is indicated on the first panel by an arrow. The largest relative difference between using proper treatment of radiation and Eddington approximation is up to about 33%. 112

4.8 A comparison of real and imaginary parts $\delta T/T$ obtained from the new code (MP) and those using Houdek's code (GH) for the $2.0M_{\odot}$ model at various frequencies. Each panel is divided into real and imaginary parts of temperature eigenfunctions. The position of optical depth $\tau = 2/3$ is indicated on the first panel by an arrow. The largest relative difference between using proper treatment of radiation and Eddington approximation is up to about 33%. 113

4.9 A comparison of real and imaginary parts $\delta T/T$ obtained from the new code (MP) and those using Houdek's code (GH) for the $2.1M_{\odot}$ model at various frequencies. Each panel is divided into real and imaginary parts of temperature eigenfunctions. The position of optical depth $\tau = 2/3$ is indicated on the first panel by an arrow. The largest relative difference between using proper treatment of radiation and Eddington approximation is up to about 39%. 114

4.10 A comparison of real and imaginary parts of $\delta r/r$ obtained from the new code (MP) and those using Houdek's code (GH) for the $1.0M_{\odot}$ model at various frequencies. The left and right panels show real and imaginary parts of $\delta r/r$ respectively. The largest relative difference between using proper treatment of radiation and Eddington approximation for the imaginary part of $\delta r/r$ is up to about 21.5%. 115

4.11 A comparison of real and imaginary parts $\delta r/r$ obtained from the new code (MP) and those using Houdek's code (GH) for the $1.2M_{\odot}$ model at various frequencies. The left and right panels show real and imaginary parts of $\delta r/r$ respectively. The largest relative difference between using proper treatment of radiation and Eddington approximation for the imaginary part of $\delta r/r$ is up to about 30%. 116

4.12 A comparison of real and imaginary parts $\delta r/r$ obtained from the new code (MP) and those using Houdek's code (GH) for the $1.3M_{\odot}$ model at various frequencies. The left and right panels show real and imaginary parts of $\delta r/r$ respectively. The largest relative difference between using proper treatment of radiation and Eddington approximation for the imaginary part of $\delta r/r$ is up to about 22.6%. 117

4.13 A comparison of real and imaginary parts $\delta r/r$ obtained from the new code (MP) and those using Houdek's code (GH) for the $1.5M_{\odot}$ model at various frequencies. The left and right panels show real and imaginary parts of $\delta r/r$ respectively. The largest relative difference between using proper treatment of radiation and Eddington approximation for the imaginary part of $\delta r/r$ is up to about 23.7%. 118

4.14 A comparison of real and imaginary parts $\delta r/r$ obtained from the new code (MP) and those using Houdek's code (GH) for the $1.6M_{\odot}$ model at various frequencies. The left and right panels show real and imaginary parts of $\delta r/r$ respectively. The largest relative difference between using proper treatment of radiation and Eddington approximation for the imaginary part of $\delta r/r$ is up to about 6.5%. 119

4.15 A comparison of real and imaginary parts $\delta r/r$ obtained from the new code (MP) and those using Houdek's code (GH) for the $1.8M_{\odot}$ model at various frequencies. The left and right panels show real and imaginary parts of $\delta r/r$ respectively. The largest relative difference between using proper treatment of radiation and Eddington approximation for the imaginary part of $\delta r/r$ is up to about 17%. 120

4.16 A comparison of real and imaginary parts $\delta r/r$ obtained from the new code (MP) and those using Houdek's code (GH) for the $2.0M_{\odot}$ model at various frequencies. The left and right panels show real and imaginary parts of $\delta r/r$ respectively. The largest relative difference between using proper treatment of radiation and Eddington approximation for the imaginary part of $\delta r/r$ is up to about 33%. 121

4.17 A comparison of real and imaginary parts $\delta r/r$ obtained from the new code (MP) and those using Houdek's code (GH) for the $2.1M_{\odot}$ model at various frequencies. The left and right panels show real and imaginary parts of $\delta r/r$ respectively. The largest relative difference between using proper treatment of radiation and Eddington approximation for the imaginary part of $\delta r/r$ is up to about 19%. 122

4.18 The growth rates as function of the cyclic frequency ν for ZAMS models. The curve labelled "MP" was obtained from the new code, whereas for the curve "GH" we used Houdek's code. The arrow indicates the acoustic cut-off frequency. 123

4.19 A comparison of the accumulated work integrals (in units $10^{30}erg$) computed using the new code (MP) with those using Houdek's code (GH) for the $1.0M_{\odot}$ model at various frequencies. Here the largest relative difference is up to about 9% 124

4.20 A comparison of the accumulated work integrals (in units $10^{30}erg$) computed using the new code (MP) with those using Houdek's code (GH) for the $1.2M_{\odot}$ model at various frequencies. Here the largest relative difference is up to about 35% 125

4.21 A comparison of the accumulated work integrals (in units $10^{30}erg$) computed using the new code (MP) with those using Houdek's code (GH) for the $1.3M_{\odot}$ model at various frequencies. Here the largest relative difference is up to about 4% 125

4.22 A comparison of the accumulated work integrals (in units $10^{30}erg$) computed using the new code (MP) with those using Houdek's code (GH) for the $1.5M_{\odot}$ model at various frequencies. Here the largest relative difference is up to about 19% 126

4.23 A comparison of the accumulated work integrals (in units $10^{30}erg$) computed using the new code (MP) with those using Houdek's code (GH) for the $1.6M_{\odot}$ model at various frequencies. Here the largest relative difference is up to about 60%. 126

4.24 A comparison of the accumulated work integrals (in units $10^{30}erg$) computed using the new code (MP) with those using Houdek's code (GH) for the $1.8M_{\odot}$ model at various frequencies. Here the largest relative difference is up to about 29% 127

4.25 A comparison of the accumulated work integrals (in units $10^{30}erg$) computed using the new code (MP) with those using Houdek's code (GH) for the $2.0M_{\odot}$ model at various frequencies. Here the largest relative difference is up to about 7% 127

4.26 A comparison of the accumulated work integrals (in units $10^{30}erg$) computed using the new code (MP) with those using Houdek's code for the $2.1M_{\odot}$ model at various frequencies. Here the largest relative difference is up to about 3.2% . 128

4.27 The real part of $\delta L/L$ at the surface as a function of frequency for ZAMS equilibrium models listed in table. The curve labelled "MP" was obtained using the new code, whereas for the curve "GH" we used Houdek's code. 129

4.28 The imaginary part of $\delta L/L$ at the surface as a function of frequency for ZAMS equilibrium models listed in table. The curve labelled "MP" was obtained using the new code, whereas for the curve "GH" we used Houdek's code. 130

4.29 The differences between the convective models (Con) and radiative models (Rad) for $1.8M_{\odot}$ and $2.1M_{\odot}$ in (a) and (b) superadiabatic gradient $\nabla - \nabla_{ad}$, (c) and (d) dimensionless sound speed, (e) and (f) ratio of convective flux to the total heat flux F_c/F, and (g) and (h) the turbulent pressure fraction p_t/p compared as a function of $\log p$. 132

4.30 The differences between the convective models (Con) and radiative models (Rad) for $1.8M_{\odot}$ and $2.1M_{\odot}$ in (i) and (j) temperature T, (k) and (l) density, (m) and (n) ∇_{ad}, and (o) and (p) compared as a function of $\log p$. 133

4.31 The difference between the eigenfrequencies obtained using the convective models and the eigenfrequencies obtained using radiative models. 134

4.32 A comparison of real and imaginary parts of the temperature eigenfunctions computed using radiative model (Rad) with those using convective model (Con) for the $1.8M_{\odot}$ at various frequencies. The left and right panels show real and imaginary parts of temperature eigenfunctions. 135

4.33 A comparison of real and imaginary parts of $\delta T/T$ computed using radiative model (Rad)with those using convective models (Con) for the $1.8M_{\odot}$ model at various frequencies. The left and right panels show real and imaginary parts of temperature eigenfunctions. 136

4.34 A comparison of real and imaginary parts of $\delta T/T$ computed using radiative model (Rad) with those using convective model (Con) at various frequencies. The left and right panels show real and imaginary parts of temperature eigenfunctions for $2.1M_{\odot}$ model. 137

4.35 A comparison of real and imaginary parts of the temperature eigenfunctions computed using radiative model (Rad) with those using convective model (Con) at various frequencies. The left and right panels show real and imaginary parts of temperature eigenfunctions for $2.1M_{\odot}$ model. 138

4.36 A comparison of $\delta r/r$ obtained using radiative model (Rad) with those using convective model (Con) at various frequencies. The real (Re) and imaginary (Im) parts of $\delta r/r$ are shown for $1.8M_{\odot}$ model. 139

4.37 A comparison of $\delta r/r$ obtained using radiative model (Rad) with those using convective model (Con) at various frequencies. The real (Re) and imaginary (Im) parts of $\delta r/r$ are shown for $2.1M_{\odot}$ model. 140

4.38 The growth rates as function of the cyclic frequency for $1.8M_{\odot}$ and $2.1M_{\odot}$ models. The curve labelled 'Con' was obtained using convective models, whereas for the curve labelled 'Rad' we used radiative models. 141

4.39 A comparison of the accumulated work integrals (in units $10^{30}erg$) computed using radiative model (Rad) with those obtained using convective model (Con) for the $1.8M_{\odot}$ model at various frequencies. 142

4.40 A comparison of the accumulated work integrals (in units $10^{30}erg$) computed using radiative model (Rad) with those obtained using convective model (Con) for the $2.1M_{\odot}$ model at various frequencies. 142

4.41 The $\delta L/L$ at the surface plotted as function of frequency for $1.8M_{\odot}$ and $2.1M_{\odot}$ equilibrium models. The curve labelled 'Rad' was obtained using radiative model, whereas for the curve labelled 'Con' we used the convective models. . 143

4.42 A comparison between the equilibrium models used in the new code (MP) with those used in Medupe's code (TM). The quantities ρ, κ, ∇_{ad} and T for $1.6M_{\odot}$ model are compared. 145

4.43 A comparison between the equilibrium models used in the new code (MP) with those used in Medupe's code (TM). The quantities ρ, κ, ∇_{ad} and T for $1.8M_{\odot}$ model are compared. 145

4.44 The differences between the equilibrium models used in the new code (MP) with those used in Medupe's code (TM). The quantities ρ, κ, ∇_{ad} and T for $2.0M_{\odot}$ model are compared as a function $\log p$. 146

4.45 The differences between the equilibrium models used in the new code (MP) with those used in Medupe's code (TM). The quantities ρ, κ, ∇_{ad} and T for $2.1M_{\odot}$ model are compared as a function of $\log p$. 146
4.46 A comparison of real and imaginary parts of $\delta T/T$ obtained using the new code (MP) and those using Medupe's code (TM) for the $1.6M_{\odot}$ model at various frequencies. 147
4.47 A comparison of real and imaginary parts of $\delta T/T$ obtained using the new code (MP) and those using Medupe's code (TM) for the $1.8M_{\odot}$ model at various frequencies. 148
4.48 A comparison of real and imaginary parts of $\delta T/T$ obtained using the new code (MP) and those using Medupe's code (TM) for the $2.0M_{\odot}$ model at various frequencies. 149
4.49 A comparison of real and imaginary parts of $\delta T/T$ obtained using the new code (MP) and those using Medupe's code (TM) for the $2.1M_{\odot}$ model at various frequencies. 150
4.50 A comparison of real and imaginary parts of $\delta r/r$ obtained using the new code (MP) and those using Medupe's code (TM) for the $1.6M_{\odot}$ model at various frequencies. 151
4.51 A comparison of real and imaginary parts of $\delta r/r$ obtained using the new code (MP) and those using Medupe's code (TM) for the $1.8M_{\odot}$ model at various frequencies. 152
4.52 A comparison of real and imaginary parts of $\delta r/r$ obtained using the new code (MP) and those using Medupe's code (TM) for the $2.0M_{\odot}$ model at various frequencies. 153
4.53 A comparison of real and imaginary parts of $\delta r/r$ obtained using the new code (MP) and those using Medupe's code (TM) for the $2.1M_{\odot}$ model at various frequencies. 154
4.54 The growth rates as function of the cyclic frequency for ZAMS models. The curve labelled "MP" was obtained from the new code, whereas for the curve "TM" we used Medupe's code. 155

List of Tables

3.1 Parameters of theoretical models. The first column denotes the model sequence number. The second column shows the mass and the third effective temperature. The forth column gives the luminosity. 64

3.2 First column denotes the mass of the equilibrium models, second column denotes the positions of convective regions and third column is the acoustic cut-off frequency ν_{ac}. 66

4.1 The maximum differences between the eigenfrequencies obtained using the new code and the eigenfrequencies obtained using Houdek's code. The first column denotes the mass of the equilibrium models, the second column denote the changes $|\Delta\nu_r|$ relative to cyclic frequency ν_r (in mHz), and the third column denotes the changes $|\Delta\nu_i|$ relative to ν_r (in mHz). 106

4.2 The maximum errors introduced by the Eddington approximation in the surface luminosity perturbations. The first column denotes the mass of the equilibrium models, the second column denotes $|\Delta L_{s,r}|$ relative to $Re(L_{f_{osc}})$, and the third column denotes $|\Delta L_{s,i}|$ relative to $Im(L_{f_{osc}})$. 131

4.3 The maximum differences between the eigenfrequencies obtained using convective models and the eigenfrequencies obtained using radiative models. The first column denotes the mass of the equilibrium models, the second column denote the changes $|\Delta\nu_r|$ relative to cyclic frequency ν_r (in mHz), and the third column denotes the changes $|\Delta\nu_i|$ relative to ν_r (in mHz). 134

Chapter 1

Introduction

Understanding the properties of stars forms the backbone of modern astrophysics since stars provide vital information about the history and the structure of the Universe. To study stellar oscillations allows us to probe inside the stars because different modes penetrate to different depths. This means that the more modes are observed the more information we can acquire about that star. Much has been done in the study of stellar oscillations both from the observational and theoretical points of view. Observations provide us with information that can be used to understand the physical processes in the interiors of stars.

This project studies the effects of radiation and convection on atmospheric oscillations in A, F and G stars. This is done by solving the non-adiabatic radial pulsation equations with a consistent treatment of radiation and a non-local mixing-length theory of convection. This research improves our current understanding of how turbulent convection modifies the properties of the observed oscillations in stars with convectively unstable surface layers. Furthermore, the project will provide further insight into the details of the interior structure of stars. High quality data is already available from various space projects, such as from the Canadian project MOST[1] and will be available from the French project COROT[2]. The availability of such high quality data demands detailed and accurate models such as the ones we have developed.

The interest of studying the non-adiabatic oscillations is that it allows one to compute the eigenfunctions that can be related to multicolor photometric observables, since the oscillations are always non-adiabatic in the atmosphere of the star. It also allows us to study the mechanisms responsible for the damping and excitation of pulsating stars. In all the methods for mode identification developed so far, whether on multicolor photometry or spectroscopic observations, the non-adiabatic character of the oscillations were neglected. Codes that perform calculations of non-adiabatic stellar oscillations have been developed by different scientists (e.g., Dziembowski 1977, Saio & Cox 1980, Pesnell 1989, Townsend 2002) but their methods adopted diffusion approximation to radiative transfer in the stellar atmosphere.

[1] Microvariability and Oscillations of STars

[2] COnvection, ROtation and planetary Transits

The effects of radiation and convection on stellar oscillations have been studied in the past. Baker & Gough (1979) studied models of RR Lyrae stars using linear non-adiabatic theory, including the local mixing length theory to model convection and diffusion approximation to model radiative transfer. It was shown by Balmforth & Gough (1988) that the diffusion approximation seems to underestimate atmospheric radiative damping. Balmforth (1992a) improved their theory by using the non-local mixing theory of convection and the standard Eddington approximation (Unno and Spiegel 1966) to radiative transfer to model the sun. The Eddington approximation used by Balmforth was later improved by Houdek (1996) by introducing the Eddington-factor technique (see Auer and Mihalas 1970) to correct for the thermal stratification of the optically thin layers. Therefore, up to this point we have non-adiabatic theory with non-local mixing length theory of convection and Eddington approximation to radiative transfer.

Christensen-Dalsgaard & Frandsen (1983) developed a non-adiabatic theory with consistent treatment of radiation. They also found that the Eddington approximation introduces a difference of about 0.05% in the calculations of solar eigenfrequencies compared to when the full radiative transfer equation is used. Another contribution to the uncertainties in their eigenfrequencies was the effect of convection. Thus we want to estimate the uncertainties in the calculation of eigenfrequencies if radiative transfer and non-local mixing length theory of convection is used. The formalism used by Christensen-Dalsgaard & Frandsen (1983) was later used by Medupe (2002) to study roAp stars.

Using an approach similar to ours, Balmforth et al (2001) showed that convection inhibits oscillations, and that the absence of convection in polar regions of the rapidly oscillating Ap (roAp) stars can lead to the excitation of high overtone pulsations in their hydrogen ionization zone. They used the pulsation code developed by Houdek (1996). Although their equilibrium models involved more elaborate physics of roAp stars, their calculations included radiation energy transfer in the Eddington approximation and they made use of non-local mixing length theory in their treatment of convection.

We are aware of the limitation of our approach since our equilibrium models are not as elaborate as those of Balmforth et al (2001). They used a composite equilibrium model, consisting of polar regions with strong magnetic fields that suppress convection and an equatorial region that allow convection.

Our treatment of convection is similar to those of Balmforth et al (2001) and our treatment of radiation is based on Christensen-Dalsgaard & Frandsen (1983) and Medupe (2002). We took elements of Medupe's code and implemented them in Houdek's code (see Houdek 1996).

It should be noted that the modes observed in roAp stars and δ Scuti stars are generally non-radial. The new code can still be applied to the roAp stars because they are high overtone pulsators and therefore non-radial components are negligible according to the equation

$$\frac{\xi_h(R)}{\xi_r(R)} = \frac{1}{\sigma_d^2}. \tag{1.1}$$

The high order modes are trapped in shallow acoustic cavities just below the surface. Here ξ_r and ξ_h are radial and horizontal components of the displacement δr, and σ_d is a dimensionless frequency defined by

$$\sigma_d^2 = \frac{R^3}{GM}\omega^2, \tag{1.2}$$

where ω is the pulsation frequency, R is the stellar radius, M the stellar mass and G the gravitational constant. In case of δ Scuti stars the code can only be applied to the one pulsating in radial modes. In general the new code is more applicable to the roAp stars than δ Scuti stars.

The outline of this thesis is presented as follows. In this chapter I give a brief introduction to stellar oscillations, followed by a brief description of the properties of roAp and δ Scuti stars. I pay particular attention to these stars since they are good candidates to apply our calculations to. In addition, a background to the theory of radiation and convection as applicable to the roAp and δ Scuti stars is presented. In chapter 2, I present derivations of the pulsation equations that we want to solve. The solutions to the pulsation equations presented in chapter 2 resulting from combining Medupe and Houdek codes are presented in chapter 3. In chapter 4, I compare the new code with Houdek's code. We end with the conclusions in chapter 5.

1.1 Stellar oscillations

One of the benefits of studying stellar oscillations is that it can be used to obtain information about the interior of the stars in the same way that seismic studies of the earth has revealed information about the structure of the earth. Pulsating stars are stars whose luminosity varies periodically due to intrinsic properties of the stars themselves. This variation could be understood in terms of radial and non-radial pulsations. Radial pulsation is where the star expands and contracts while maintaining a spherical symmetry. The non-radial pulsation is where some parts of the star surface move inwards while other parts move outwards. Pulsating stars are found throughout the Hertzsprung-Russell (HR) diagram shown in Figure 1.1. According to Christensen-Dalsgaard (2003) the Cepheid instability strip is an important region in the diagram. Stars like Cepheids (' δ Cep ') and RR Lyrae (' RR Lyr '), δ Scuti (' δ Sct ') and rapidly oscillating Ap (' roAp') are located in that region. This diagram shows that pulsations in a star are connected to its mass and evolutionary status.

Pulsating stars show periodic variations in luminosity, radial velocities and sometimes even in their line profiles. Luminosity variations have been known for centuries, for example, Mira has been known to change brightness since 1596 (see Carroll & Ostlie 1996). Many pulsating stars have low effective temperatures, placing them on the right-hand side of the HR diagram. The pulsational frequencies depend on the properties of stellar matter, and they can be measured to very high precision compared to other observable quantities like temperature and gravity (see Arentoft 2001). The stellar pulsations can be used to obtain information about the interior structure

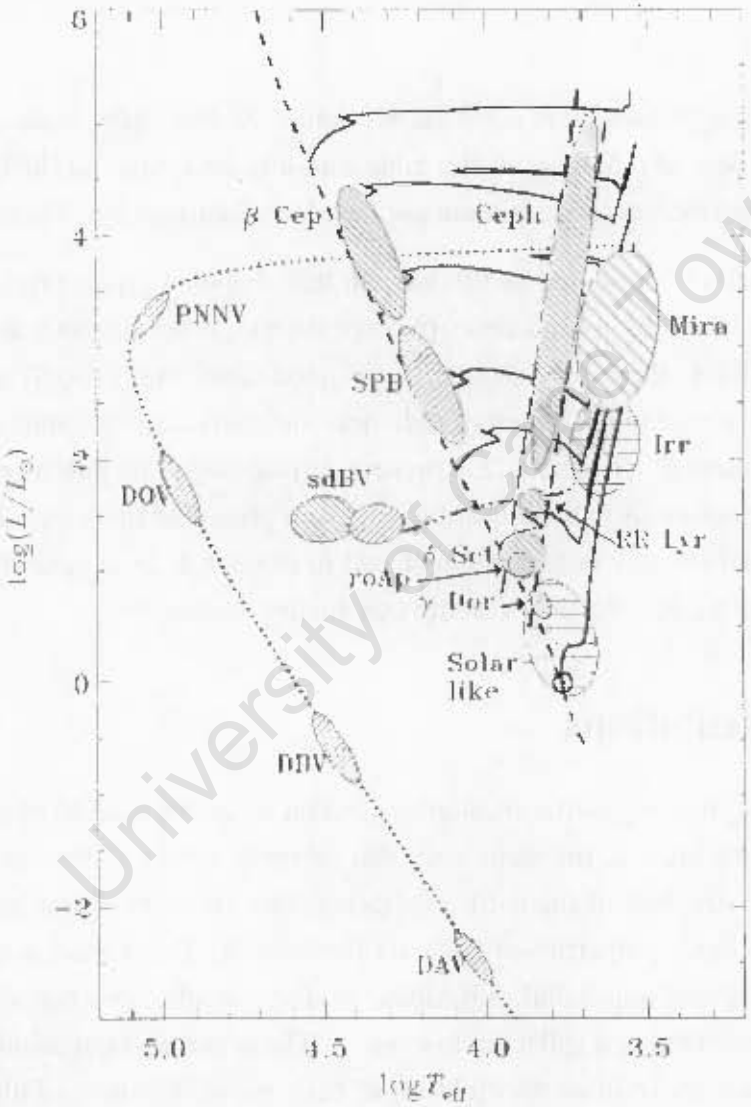

Figure 1.1: Hertzsprung-Russell diagram showing the location of several classes of pulsating stars. The dashed line shows the zero-age main-sequence (ZAMS). This diagram is taken from Christensen-Dalsgaard (2003).

of the stars in the same way that seismic studies of the earth has revealed information about the structure of the earth. The techniques of seismology were first developed to study the modes of oscillation in the Sun, which gave rise to helioseismology. The accurate determination of sound speed and rotation rate as a function of depth and latitude in the sun are some of the important results of helioseismology. The more detailed discussion of the theory of stellar pulsations can be found in Cox (1980), Unno et al. (1989) and Christensen-Dalsgaard (2000, 2003).

1.1.1 The description of the oscillations

1.1.1.1 The pulsation mode

Stars are three dimensional bodies, therefore their individual pulsation modes can be characterised by the quantum numbers n, ℓ and m. These are defined in detail below:

- The radial quantum number n gives the total number of nodes in the radial direction. A mode with $n = 0$ is called the lowest-order mode, $n = 1$ the first overtone, $n = 2$ the second overtone, etc.
- The spherical degree ℓ is the total number nodal lines on the surface of the star. For $\ell = 0$, there are no nodal lines on the surface and the star pulsates radially.
- The azimuthal order m is the number of surface nodal lines parallel to lines of longitude.

Furthermore, $\ell - |m|$ is the number of surface nodes that are lines of latitude. Also the values of m range from $-\ell$ to $+\ell$.
The pulsation equation solutions are of the form:

$$y(r, \theta, \phi, t) \quad A_n(r) Y_\ell^m(\theta, \phi) \exp(i\omega t). \tag{1.3}$$

where y is any perturbed quantity. Here A_n gives the radial dependence of the eigenfunctions and is typically obtained from the numerical solutions of pulsation equations. The function Y_ℓ^m is a spherical harmonic with, θ the co-latitude, ϕ the azimuth angle in spherical coordinates and time t.

1.1.1.2 Seismic waves

The different types of seismic waves which probe different regions of a star are described below:

- For the p-modes, the principal restoring force for oscillations is pressure. They reach maximum amplitude near the stellar surface. As the frequencies of the p-modes increases the number of radial nodes increases.

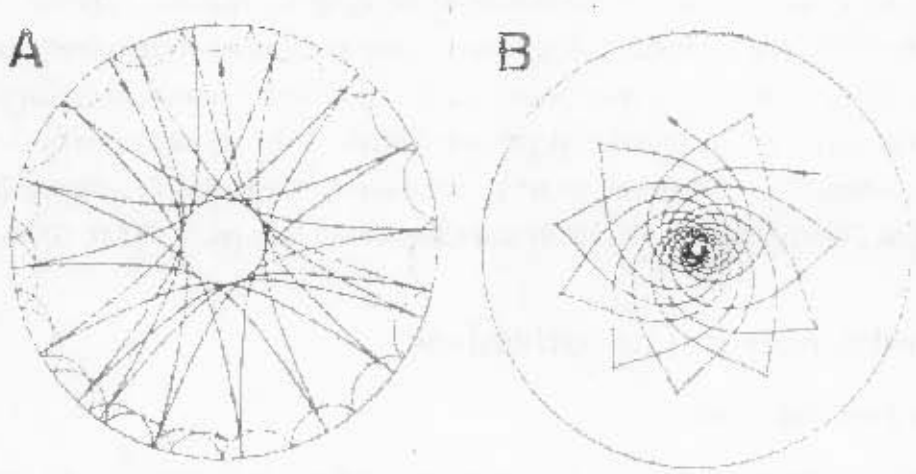

Figure 1.2: The propagation of p-modes is shown in **A** and g-modes in **B**. Higher degree p-mode has $n = 8$, $\ell = 100$, whereas the lower degree p-mode has $n = 8$, $\ell = 2$. The g-mode has $n = 10$, $\ell = 5$. The p-modes can travel throughout the Sun, whereas the g-modes are confined beneath the convection zone of the Sun. This sketch is taken from Gough, Leibacher & Toomre (1996).

- For the g-modes, the gravity (or negative buoyancy) is the restoring force. They reach their maximum amplitude near the stellar core. The number of radial nodes increases as the frequencies of the g-modes decrease. The region where g-modes reach their maximum amplitude is different for degenerate stars (e.g. white dwarfs) than for non-degenerate stars modelled in this thesis.

- f-modes are horizontal surface waves, very similar to the ocean waves.

Figure 1.2 (**A**) shows how acoustic cavities are set up in the Sun and other stars. Let us consider a p-mode starting from the surface at some angle, as it propagates inward, it penetrates regions of increasing temperature. Its speed increases as $c_s \propto \sqrt{T/\mu}$, where T is the temperature, μ is the mean molecular weight and c_s is the sound speed. Therefore such a wave is refracted back towards the surface. As it approaches the surface, it experiences a drastic drop in density and is reflected back towards the interior again. The two p-modes are shown, one inclined far from the vertical resulting in a shallow acoustic cavity. Another one with relatively smaller inclination to the vertical penetrates deeper into the star. The radial mode (ℓ 0) can go right through the center. Therefore large ℓ-value modes have shallower acoustic cavities, while small ℓ values create deeper cavities. It means valuable information about the core of a star can be obtained from the modes that reach the center of the star. However for a medium to influence

the properties of sound wave, the wave needs to spend some time in that medium. Unfortunately the sound waves spend little time in the core due to the high sound speed there.

In figure 1.2 (**B**) the g-modes are mostly confined to the regions below the convection zone. This means the boundaries of the convection zone are the reflection points for the g-modes.

1.1.2 Mode identification

Mode identification is the process of determining n, ℓ and m quantum numbers that describe a mode from the data of a pulsating star. The pulsation modes are identified from the accurate multi-color photometry, single-color frequency spectra, spectroscopic techniques and the techniques that combine photometric and spectroscopic data. I discuss the multi-color photometry and line profile variation techniques in the next subsections. The single color frequency spectrum has been critical in determining the ℓ-value in the roAp stars. In fact, it is the only method that currently works for roAp stars.

1.1.2.1 Multi-color photometry Technique

An expression to describe the variation of non-radial pulsation amplitude with surface brightness and area was first derived by Dziembowski (1977). However his formula was bolometric therefore it could not be easily compared with data. The formula is presented as follows:

$$\Delta m_\lambda = -1.086 \left(\frac{\Delta S_\lambda}{S_\lambda} + \frac{\Delta A}{A_0} \right), \tag{1.4}$$

where ΔS_λ is the surface brightness variation due to pulsations and $\Delta A/A_0$ is the geometric variation. The linear relation between perturbed surface brightness ΔS_λ and some color index $\Delta(m_{\lambda_1} - m_{\lambda_2})$ was assumed in order to make Dziembowski's formula comparable with data by Balona & Stobie (1979). Therefore, ΔS_λ is obtained and the degree ℓ could be determined from photometric and radial velocity data and the knowledge of the radius of the star under consideration. It was shown by Stamford & Watson (1981) that for $\ell > 1$ the assumption of a single-value relation between surface brightness changes and color variations does not apply. The improvement made by Stamford & Watson (1981) to the formalism of Dziembowski (1977) are as follows:

1. The stellar flux is defined in terms of effective temperature (T_{eff}) and surface gravity ($\log g$). This means that in their formula, perturbations in T_{eff} and $\log g$ are included in ΔS_λ.

2. The flux derivatives in ΔS_λ and limb–darkening were calculated from model atmospheres.

These two effects are included in the formula by Watson (1988). The formula by Watson which describes the dependence of the magnitude of a pulsating star on wavelength and pulsational parameters is:

$$\Delta m(\lambda, t) = -1.086\epsilon P_\ell^m(\mu_0)[(T_1 + T_2)\cos(\omega t + \psi_T) + (T_3 + T_4 + T_5)\cos(\omega t)], \quad (1.5)$$

where $\epsilon \ll 1$ is an amplitude parameter and μ_0 is the cosine of the inclination of the stellar pulsation axis to the observer. The function P_ℓ^m is the Legendre polynomial of degree ℓ and m. The terms T_1 to T_5 are explained below:

$$T_1 = b_{\ell\lambda}\frac{\partial \log F_\lambda}{\partial \log T_{eff}}B^*, \quad T_2 = \frac{\partial b_{\ell\lambda}}{\partial \log T_{eff}}\frac{B^*}{2.3026}, \quad T_3 = b_{\ell\lambda}(2 + \ell)(1 - \ell),$$

$$T_4 = -b_{\ell\lambda}p^*C\frac{\partial \log F_\lambda}{\partial \log g} \qquad T_5 = -\frac{p^*C}{2.3026}\frac{\partial b_{\ell\lambda}}{\partial \log g}. \quad (1.6)$$

The terms T_1 and T_2 account for the local temperature changes on stellar surface and limb-darkening variations due to surface temperature variations. The terms T_3 and T_4 account, respectively, for the variations in the actual geometry of the star and the local surface pressure changes. Here term T_5 accounts for the limb-darkening variations due to surface gravity variations. The quantity p^* appearing in terms T_4 and T_5 is a measure of the variation of surface gas pressure as surface gravity varies and is given as

$$p^* = \left(\frac{\partial \log g}{\partial \log p_g}\right)_{\tau=1}. \quad (1.7)$$

The $b_{\ell\lambda}$ is the weighted limb-darkening integral:

$$b_{\ell\lambda} = \int_0^1 h_\lambda \mu P_\ell dx. \quad (1.8)$$

where h_λ is the limb-darkening function. Here quantity C is a measure of whether the radial or the horizontal component of the oscillations dominates and is defined as

$$C = (1 + \alpha_H^{-1}) - \ell(\ell + 1)\alpha_H, \quad (1.9)$$

which is the inverse of σ_a^2. The quantity α_H is the ratio of horizontal to radial velocity amplitudes and is related to ω by:

$$\alpha_H = \frac{GM/R^3}{\omega^2}. \quad (1.10)$$

For pure radial oscillations C is negative, meaning that pressure variations always act in opposition to radius variations, and for the non-radial case C may be either positive where horizontal motions dominate, zero or negative where the radial motions dominate the horizontal ones. The

parameter B^* appearing in T_1 and T_2 is the ratio of relative temperature to radius perturbations and can be written as:

$$B^* = \frac{\delta T/T}{\delta r(R)/R} \tag{1.11}$$

For the adiabatic case the energy equation is

$$\frac{\delta T}{T} = \nabla_{ad}\frac{\delta p}{p}, \tag{1.12}$$

where

$$\nabla_{ad} \equiv \left(\frac{\partial \ln T}{\partial \ln p}\right)_{ad}, \tag{1.13}$$

is the adiabatic temperature gradient.
According to Dziembowski (1977), in non-radial oscillators, the pressure perturbation can have the same sign of radius perturbation at the stellar surface whenever horizontal motions dominate in the oscillation. The relation is as follows:

$$\frac{\delta p}{p} = \left[(1+\alpha_H^{-1}) - \ell(\ell-1)\alpha_H\right]\frac{\delta r}{r} + \left[\ell(\ell+1)\alpha_H - \ell - 1\right]\frac{\tilde{\Phi}_1}{gr} \qquad \text{at the surface.} \tag{1.14}$$

where $\tilde{\Phi}_1$ is the Eulerian perturbation of gravitational potential. Using Cowling approximation $\tilde{\Phi}_1$ can be neglected, since $\tilde{\Phi}_1/gR$ is sufficiently small to be ignored at the stellar surface. Hence equation (1.14) can be written as

$$\frac{\delta p}{p} = C\frac{\delta r}{r} \qquad \text{at the surface.} \tag{1.15}$$

This means $\delta T/T$ and $\delta r(R)/R$ near the surface for adiabatic oscillations can be related as:

$$\frac{\delta T}{T} = \nabla_{ad} C\frac{\delta r(R)}{R}, \tag{1.16}$$

hence $B^* = \nabla_{ad} C$. For the non-adiabatic oscillations those two quantities are typically related as

$$\frac{\delta T}{T} = R_{ad}\nabla_{ad}\exp(i\Psi_T)C\frac{\delta r(R)}{R}, \tag{1.17}$$

where R_{ad} is the amplitude parameter and Ψ_T the phase difference between the temperature and radius perturbations. In case of adiabatic oscillations $R_{ad} = 1$ and for non-adiabatic oscillations R_{ad} approaches zero.

Watson (1988) used equation (1.5) to show that different modes occupy different regions of the amplitude ratio versus phase difference diagram over a broad range of parameters. Watson has showed that different ℓ modes occupy different areas on such diagram where the size and

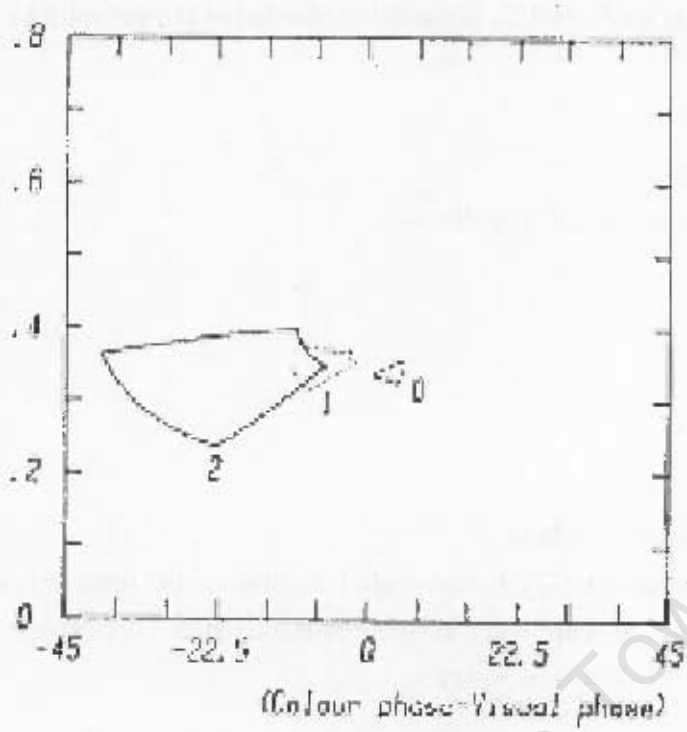

Figure 1.3: A plot of (A_{B-V}/A_V) versus $(\phi_{B-V}-\phi_V)$, in radians, for δ Scuti star. The theoretical areas for the (R, Ψ) loci were calculated with $0.25 \leq R_{ad} \leq 1$ and $90^\circ \leq \Psi_T \leq 140^\circ$. The modes $\ell = 0, 1, 2$ are written next to the areas in which observed points of those modes should lie. Taken from Watson (1988).

location of the area is determined by the values of R_{ad} and Ψ_T. An example of this diagram as applied by Watson (1988) to a δ Scuti star is given in Fig. 1.3 in the ranges $0 \leq R_{ad} \leq 1$ and $90^\circ \leq \Psi_T \leq 140^\circ$. The ℓ mode for the observed star can then be determined from the area in which the observed point lies in this figure. Watson attempted to do this for other pulsating star classes and succeeded in most but not with the roAp stars.

CDP94 improved on the method for the evaluation of monochromatic flux variation described by Watson (1988) by using linear non-adiabatic eigenfunctions. They calculated values for f and ψ using a linear non-adiabatic code used by Dziembowski & Pamyatnykh (1993), which uses the diffusion approximation for the radiative transfer and neglects effects of convection. They used amplitude ratio f and phase difference ψ instead of B^* and Ψ_T respectively as was done by Watson. The quantities f and ψ are defined as $f = (\delta L/L)/(\delta r/r)$ and $\psi = arg(f)$ where $\delta L/L$ is the perturbed luminosity. They have shown that it is possible to determine the radial order of the observed modes as well as the mean stellar parameters from the comparison

of the non-adiabatic observables with data of β Cephei stars. Our new code is an improvement on CDP94's code therefore it will be worth attempting to apply CDP94's technique using our code on the data of δ Scuti stars.

Fountaine et al (1996) developed a method which does not require these plots, and their method was applied on pulsating white dwarfs where only the calculated amplitudes of pulsation were compared with the observed ones. They quantified the comparison by calculating quantity χ^2 defined by:

$$\chi^2(\ell) = \sum_{i=1}^{b} \left(\frac{q a_{\ell i} - b_i}{\sigma_i} \right). \tag{1.18}$$

where the summation is taken over the wavebands i. Here b_i is the observed amplitude in waveband i with corresponding uncertainty σ_i and $a_{\ell i}$ is the computed amplitude for degree ℓ. The factor q is the normalisation constant. They calculated $\chi^2(\ell)$ for $\ell = 1$ and 2 at each point on three 91×91 grids in $(T_{eff}, \log g)$-plane where each grid allowed a different treatment of convection (see section for convection). At each point the value q that minimized χ^2 is chosen. The place on each grid where $\chi^2(\ell)$ is the lowest gives the point at which the observed and predicted amplitudes are in best agreement. For all the three grids, values of $\chi^2(1)$ were lower than $\chi^2(2)$ then the $\ell = 1$ solutions are favoured. The advantage of this method is that it does not rely on the arbitrary choice of a specific waveband for normalisation. These results are sensitive to the treatment of convection.

The method by Fountaine et al (1996) was later generalised by Balona & Evers (1999) to include the case where both amplitude and phase are used in determining the mode. Mode identification in δ Scuti stars is made difficult by the presence of the g-modes, modes of mixed character and by stellar rotation. This is because rotation introduces a fine structure in the modes and also modifies the frequency expected in a non-rotating star (see Balona & Evers 1999). The identified modes can be used to determine the stellar parameters (eg. effective temperature and luminosity) from the pulsation frequencies.

In case of the roAp stars the Watson's formula fails because of its limitations. The Watson formula is based on the atmosphere that is treated as a single layer with the assumption that the eigenfunctions are constant there. It was shown by Medupe, Kurtz & Christensen-Dalsgaard (2000) and Medupe, Christensen-Dalsgaard & Kurtz (2002) that the eigenfunctions are not constant in the atmosphere of the roAp stars.

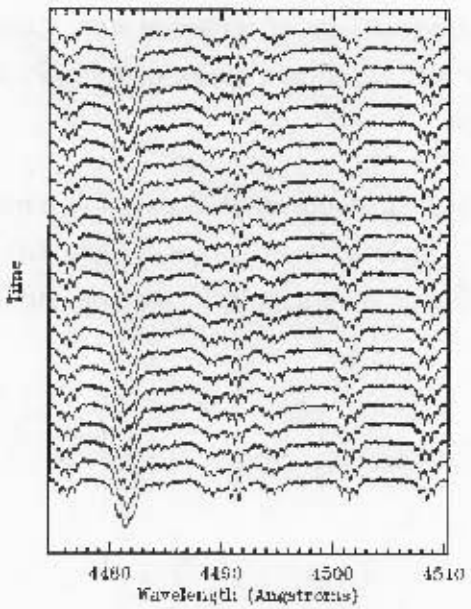

Figure 1.4: Example of pulsational line profile variations for δ Scuti star τ Peg with $\ell = 10$, $m = -10$ and $v \sin i = 80 km/s$. Taken from Kennelly et al. (1998).

1.1.2.2 Line profile variations

The determination of the azimuthal order m can be possible by means of an analysis of spectral line profile changes. The non-radial oscillations can produce line-profile variations (abbreviated hereafter as LPVs) by the following means:

1. the Doppler shift of the spectral lines due to surface velocities,

2. and the local surface brightness variation.

The line profiles of a star depend on the surface velocity and the temperature of the line-forming region, which means the shape of the line is affected by the velocity and temperature perturbations due to pulsation. There are two types LPV's; moving bumbs across a rotationally broadened absorption line of a rapidly rotator such as ζ Oph stars (Walker et al. 1979, Vogt & Penrod 1983), and variations in the whole shape of an absorption line of a slow rotator such as 53 Per variables (Smith 1977,1978) and most of the β Cep stars. The LPVs take the form of travelling bumps that move across the line from the blue to the red part. The LPVs may be confused with the travelling bumps due to spots on the surface of a rotating star. However, the fact that one expects to derive an estimate of the rotational velocity from the starspot-induced LPVs makes the travelling bumps to be differentiated. Figure 1.4 shows line profiles for δ Scuti star τ Peg at inclination $i = 70°$ for a mode with $\ell = 10$ and $m = -10$. If the pulsational model is applied to

the bumps and one finds that the number and the spacing of the bumps on the line depend on ℓ and m then those travelling bumps are the results of pulsation.

To understand how pulsational LPVs can be used for mode identification we discuss how LPVs are modelled. For detailed description see Kambe & Osaki (1988), Lee & Saio (1986, 1990) and Pesnell (1989). To model LPVs, you need to specify:

- the parameters that describe the pulsational mode (ℓ and m) and its amplitude,
- and orientations of rotation and pulsation axes with respect to the observer which come in the form of three angles, namely the inclination of the rotation axis to the observer i, the magnetic obliquity β_{mo} and the azimuth of pulsational pole α_p.

An expression for the pulsational velocity field for p- or g-modes is given as

$$\nu_{osc} = \hat{A} Re \left[\left(1,\ \alpha_H \frac{\partial}{\partial \theta},\ \alpha_H \frac{1}{\sin\theta} \frac{\partial}{\partial \phi} \right) Y_\ell^m(\theta,\ \phi) \exp(i\omega t) \right] \tag{1.19}$$

where ν_{osc} is the velocity caused by oscillation, $\hat{A}$ is the velocity amplitude, Re indicates that we are interested in the real parts of the expressions inside the bracket. For a p-mode in which the radial velocity component dominates the horizontal component A^* is the radial velocity amplitude, and for the g-mode in which horizontal component dominates $\hat{A}$ represents horizontal velocity amplitude. Thereafter the LPVs are modelled by dividing the visible surface of a star into a number small surface elements, then Doppler shifting an intrinsic line profile assuming a velocity field as given in equation (1.19) at each surface element.

In order to compare the LPVs model with data, the above mentioned parameters are chosen by trial and error and adjusted until a best fit is made with data. According to Balona (1986a) this method works fine for single mode stars but becomes more difficult when more than one mode of comparable amplitudes are present. To cover the multimode stars Balona (1986a, 1986b) proposed a method in which the line profile variations is characterised by the series of moments. Thereafter series of moments are Fourier transformed to yield frequency spectra. The ℓ and m can be determined from relationship that exist between relative amplitudes and phases of moments. This method of Balona allows one to deduce the following pulsational parameters in addition to ℓ and m:

- the angle of inclination to the line of sight i,
- the projected rotational velocity $v \sin i$,
- and the pulsational velocity v_p.

1.1.3 δ Scuti and roAp stars

Since I pay more attention to A stars I will give a brief introduction to examples of A stars namely δ Scuti and roAp stars. The results of linear non-adiabatic equations to be presented in the next chapter can be used to calculate the non-adiabatic observables such as amplitude ratios and phase differences for roAp stars and δ Scuti stars separately. This is the work we intend to do in future. The non-adiabatic observables are useful for the mode identification which is the essential step in asteroseismology (see Watson 1988 and Cugier, Dziembowski & Pamyatnykh 1994, hereafter CDP94).

1.1.3.1 δ Scuti stars

For a detailed review on δ Scuti stars see Breger (1995; 2000). The δ Scuti stars have spectral types of A and F and are located in the classical instability strip in the HR diagram in Figure 1.1. They have effective temperatures of between $7000K$ and $9000K$ and masses around $2-2.5M_{\odot}$. They pulsate in radial and non-radial p (and possibly g) modes with periods between 20 minutes and 8 hours with low radial order n. According to Breger (2000) the non-radial pulsation of δ Scuti found photometrically are low degree ($\ell \leq 3$) and low order ($n = 0$ to 7) p-modes, while spectroscopic investigations can detect modes of higher ℓ. In addition, the mixed modes with p-mode character towards the surface and g-mode character in the deep interior may be observed, and are reported to have been found in FG Vir star (see Viskum et al 1998, Breger et al 1999). These mixed modes are due to changes in the core as hydrogen is converted to helium which affects the frequencies of the g-modes. The p- and g-modes frequency regions are well separated in the unevolved stars, but as the stars evolve the frequencies of the g-modes increase and finally mix with the p-modes. This is known as the avoided crossings between interacting p- and g- modes (see Christensen-Dalsgaard 2000), and this allows studies of the deep interior of these stars to be possible.

According to Chevalier (1971) pulsation in the δ Scuti stars is driven by the κ-mechanism in the second partial helium ionization zone. For the κ-mechanism to work opacity must increase with compression. In most regions of the star, using Kramers law, the opacity decreases as temperature increases upon compression. However in the partial ionization zone (eg. hydrogen and helium ionization zones) upon compression opacity increases due to small temperature increase. This increase in opacity blocks radiation from inside of the star, and the ionization zone gains energy which causes the star to expand. During expansion, the opacity decreases and this causes energy to be released. It must be noted that the partial zone is responsible for pulsation in a sense that, it can absorb heat during compression, move towards the surface to release heat during expansion, and move backwards again to start another cycle. See Baker & Kippenhahn (1962) and

Cox (1980).

The δ Scuti stars can be divided into two subgroups namely the high-amplitude δ Scuti stars (HADS) and the low amplitude δ Scuti stars (LADS). The HADS show an amplitude of the order of $0.3\,mag$ in their light curves, whereas the LADS show amplitude of the order $0.03\,mag$. Many HADS appear to pulsate radially, while both radial and non-radial pulsations are observed among the LADS. Many of the δ Scuti stars are fast rotators with rotational speeds of up to $250\,km/s$. The LADS can be both fast and slow rotators and the HADS are only found among slowly rotating stars with a velocity below $30\,km/s$.

1.1.3.2 The roAp stars

In this section I give a short description of roAp stars. For detail reviews see Kurtz (1990) and Martinez & Kurtz (1995). The roAp stars are found in the instability strip on the HR diagram located on the the main sequence (see North et al. 1997). They have an effective temperature in the range of about 6600 to $10000\,K$ and pulsate in high overtone p-modes with a period between 6 and 21 minutes. These stars are chemically peculiar, slow rotators and have strong global magnetic fields with field strengths varying from hundreds G to a few kG. They are peculiar because their spectra show enhanced lines of iron-peak and rare earth elements.

The pulsation properties of roAp stars have been explained by the oblique-pulsator model (Kurtz 1982). According to this model the pulsation axis is aligned with the magnetic axis and both are inclined to the rotation axis. This model has been improved upon and put on firm theoretical basis by Dziembowski & Goode (1985), Shibahashi & Takata (1993) and Takata & Shibahashi (1993). In this version of the oblique pulsator model, the effects of the Coriolis force and those of the centrifugal force are neglected. One of the effects of centrifugal force is to distort the shape of a star. For other effects of rotation in general see Tassoul (1978) and Wolff (1983). In addition, the effects of magnetism on pulsation were treated as a small perturbation.

In trying to apply this approximation to the roAp stars, Dziembowski & Goode (1996) showed that the large surface magnetic fields found in most roAp stars create magnetic pressures comparable to gas pressures in the atmosphere of these stars. Dziembowski & Goode (1996) argued that magnetic effects cannot be treated as a small perturbation and as a result they suggested an improvement to the oblique pulsator model that treats the effects of surface magnetic field non-perturbatively. The non-perturbative treatment of the effects of magnetic field in roAp stars are presented by Bigot et al (2000), Dziembowski & Goode (1996) and Cunha & Gough (2000). They show that the strong magnetic field distorts axi-symmetric pulsation modes so that their angular dependence is described by a linear combination of spherical harmonics of different ℓ with the same m value. They also find that the treatment of the effects of Coriolis force cannot

be ignored over those of the centrifugal force. Bigot & Dziembowski (2002) have succeeded in reproducing the model where the pulsation axis is inclined to both the magnetic field and the rotation axis.

The roAp stars have luminosities and masses similar to those of the δ Scuti stars. Because of this it was suggested that oscillations observed in roAp stars might also be driven by the κ mechanism operating in the region of the second ionization of helium. Balmforth et al (2001) have showed that the strong magnetic field near the magnetic poles of roAp stars is enough to suppress convection, whereas convection is unsuppressed near the equator. The detail of Balmforth et al (2001) equilibrium stellar model is given in section 1.1. They showed that the high frequency pulsations are excited by the κ mechanism in the hydrogen ionization zone of the polar regions. Balmforth et al (2001) also showed that the presence of turbulent pressure in the equatorial regions stabilizes the high overtone modes. Cunha (2002) used the models used by Balmforth et al. (2001) to predict theoretical instability strip (TIS) for roAp stars and compare them with observations. They however found the red edge of the TIS appears hotter than according to the observations. They also found that all high radial order modes of models around $1.6\,M_{\odot}$ to be unstable. Recent work by Cunha and Sousa (2006) has shown that helium settling is responsible for the stabilization of low-order modes in roAp stars.

Here I give a summary of the recent observation results of roAp stars obtained using high-resolution spectroscopy. In particular the results on the monotonic blue-to-red motion in the line profile variation found in lines of third ionization states of the rare-earth elements (hereafter REE), Neodymium (Nd) and Praeseodymium (Pr), in roAp stars. It was found by Kochukhov & Ryabchikova (2001) in roAp star, γ Equ, that the features in the line profiles of Nd III and Pr III are seen to move only from blue to red, and not in a sinusoidal form as typically expected. According to the interpretation of Kochukhov & Ryabchikova (2001) the blue-to-red LPV of γ Equ is caused by pulsation modes of degree $\ell = 2$ or 3 and azimuthal order $m = -\ell$ or $m = -\ell + 1$.

This blue-to-red movement has previously been observed in rapidly rotating B stars (Vogt & Penrod 1983; Balona et al. 2002). Thus it is surprising to find this behaviour in a slow rotating star like γ Equ which does not have rotationally broadened lines. In fast rotating stars, lines are rotationally broadened and the blue-to-red LPV phenomenon is regarded as a manifestation of prograde sectoral modes that produces LPV's on a rotationally broadened line.

In trying to interpret this problem Shibahashi et al. (2004, 2008) proposed the following hypothesis: In the atmosphere of roAp stars the radial velocity increases with an increasing height above the photosphere. At a certain level the radial velocity exceeds the sound speed and a shock wave is generated. As the shock wave propagates through the layer under consideration, the shock wave pushes up that layer and the layer falls back again after reaching the maximum

height. This process repeats itself and the resultant variation in the Doppler shift is in agreement with the LPV observed in Nd line similar to the one observed in rapidly rotating B stars. If the postulation is correct the following were expected: (a) The spectral lines formed deep in the atmosphere where the motion is subsonic the LPV will be sinusoidal; (b) The chemical elements not concentrated in magnetic polar regions should show sinusoidal LPV because their pulsation velocities remain subsonic; (c) The lines formed in the upper part of the atmosphere near the magnetic polar regions the LPV should show monotonic blue-to-red motion only. Unfortunately the simulation based on this hypothesis did not reproduce radial velocity curve obtained by Kochukov and Ryabchikova (2004) from the moment method.
Given the new observational information of γ Equ, Shibahashi et al. (2008) estimated the height of shock wave formation and found that given the limitation on the model atmospheres, they think it is plausible for shocks to occur in the REE layers.
The equilibrium models that we will use are more appropriate for modelling δ Scuti stars rather than the composite models required for the roAp stars.

1.1.4 The basic equations of hydrodynamics

A star is composed of gas (or a fluid), therefore it can be described by equations of hydrodynamics, i.e., continuity equation, equation of motion and energy equation. We shall assume the equilibrium star to be static, hence the time derivatives of the equilibrium quantities will be ignored, as a result, there are no equilibrium velocities for example. These equations are described below.

1.1.4.1 The continuity equation

The mass conservation in a fluid is described by the continuity equation

$$\frac{d\rho}{dt} + \mathrm{div}(\rho \mathbf{u}) = 0, \tag{1.20}$$

where ρ is density and $\mathbf{u}$ is the fluid velocity. These quantities are functions of position $\mathbf{r}$ and time t. This equation balances the rate of change of mass inside a volume with the total mass into and out of the volume. For the incompressible fluid the equation (1.20) reduces to

$$\nabla \cdot \mathbf{u} = 0. \tag{1.21}$$

1.1.4.2 The equation of motion

The equation of motion states that a small volume element moving with the fluid is accelerated because of the forces acting upon it. Therefore, it is the fluid dynamic expression of Newton's

second law. The equation of motion can be written as:

$$\rho\frac{d\mathbf{u}}{dt} = -\nabla p + \mu^*\nabla^2\mathbf{u} + \boldsymbol{f}^*, \tag{1.22}$$

where μ^* is the coefficient of viscosity, $p = p(\mathbf{r}, t)$ is pressure and d/dt is the material or Lagrangian time derivative, i.e., the time derivative corresponding to what is seen by an observer who follows the motion of the fluid. The term on the left hand side of equation (1.22) is of the type $mass \times acceleration$. On the right hand side, the first term is due to the gas pressure and second term is the viscosity (internal friction in the gas). The forces on the volume of gas consist of surface forces and body forces. The former are the forces that act only at the surface for example surface gas pressure forces, and the latter are the forces that act throughout the whole fluid such as gravity and magnetic forces. The third term $\boldsymbol{f}^*$ represents the body forces. The equation of motion (1.22) for the incompressible fluid may be re-written as

$$\frac{\partial u_i}{\partial t} + u_j\frac{\partial u_i}{\partial x_j} = -\frac{1}{\rho}\frac{\partial p}{\partial x_i} + \nu\frac{\partial^2 u_i}{\partial x_j^2} + g_i, \tag{1.23}$$

where p is the gas pressure, $\nu = \mu^*/\rho$ is the property of the fluid called kinematic viscosity and $g_i = (0, 0, -g)$ is the gravitational acceleration.

Large scale magnetic fields are normally too weak to have an impact on the condition of hydrostatic equilibrium. In small regions such as sunspots the magnetic force may be comparable to gas pressures, and in the case of the roAp stars Cunha & Sousa (2006) shows that near the surface of these stars, magnetic pressures become comparable to gas pressures, even dominating gas pressure closer to the surface. In this case a proper description of the physics of these atmospheric layers must include magnetic terms in the equation of motion. Other forces like the Centrifugal and Coriolis due to rotation can also be represented by $\boldsymbol{f}^*$. The centrifugal force is of the form $-\vec{\Omega} \times (\vec{\Omega} \times \vec{r})$, and Coriolis force is of the form $-2\vec{\Omega} \times v_r$, where $\vec{\Omega}$ is the angular velocity vector, $\vec{r}$ is the position vector of the body and v_r is the velocity of the body relative to the rotating frame.

If we only include gas pressure and exclude both turbulence and viscosity the equation of motion for radial motion looks like

$$\frac{d^2r}{dt^2} = -4\pi r^2\frac{dp}{dm} - \frac{Gm}{r^2}, \tag{1.24}$$

where m is the mass contained in the sphere of radius r. The inclusion of turbulent pressure will be discussed in section 1.4.

1.1.4.3 Energy Equation

To derive the energy equation for stars, we use the first law of thermodynamics given by:

$$\frac{dq}{dt} = \frac{dE}{dt} + p\frac{dV}{dt}, \tag{1.25}$$

where E is the internal energy of the matter, V is the volume of the fluid, dq/dt is the heat gain or loss which goes partly into changing the internal energy and partly into expanding or compressing the gas according to equation (1.25).

Using the thermodynamic identities, equation (1.25) can be expressed as (see Christensen-Dalsgaard 2003)

$$\frac{dq}{dt} = \frac{1}{\rho(\Gamma_3 - 1)}\left(\frac{dp}{dt} - \frac{\Gamma_1 p}{\rho}\frac{d\rho}{dt}\right), \tag{1.26}$$

$$= c_p\left(\frac{dT}{dt} - \frac{\Gamma_2 - 1}{\Gamma_2}\frac{T}{p}\frac{dp}{dt}\right), \tag{1.27}$$

$$= c_V\left(\frac{dT}{dt} - (\Gamma_3 - 1)\frac{T}{\rho}\frac{d\rho}{dt}\right), \tag{1.28}$$

where c_p and c_V are the specific heat capacity per unit mass at constant pressure and volume respectively. The adiabatic exponents are defined by

$$\Gamma_1 = \left(\frac{\partial \ln p}{\partial \ln \rho}\right)_{ad}, \quad \frac{\Gamma_2 - 1}{\Gamma_2} = \left(\frac{\partial \ln T}{\partial \ln p}\right)_{ad}, \quad \text{and} \quad \Gamma_3 - 1 = \left(\frac{\partial \ln T}{\partial \ln \rho}\right)_{ad}. \tag{1.29}$$

The heat gain per unit volume can also be written as

$$\rho\frac{dq}{dt} = \rho\epsilon - \operatorname{div}\mathbf{F}. \tag{1.30}$$

where ϵ is the rate of energy generation per unit mass, and $\mathbf{F}$ is the flux of energy. In stars contributions to ϵ come from nuclear reactions in their cores. It is thus equal to zero in the stellar atmospheres and envelopes. The last term in equation (1.30) is the net flux out. In this project radiation and convection are only the contributors to the energy flux.

Equations (1.27) and (1.30) are combined to obtain

$$\rho c_p\left(\frac{dT}{dt} - \nabla_{ad}\frac{T}{p}\frac{dp}{dt}\right) = \rho\epsilon - \operatorname{div}\mathbf{F}. \tag{1.31}$$

1.2 The radiative transfer

In this section we present the way in which we included radiative transfer in our code. We divide the star into two regions, the atmosphere and the envelope. In the atmosphere the full radiative transfer equation is used, and in the envelope the diffusion approximation is imposed. The two regions are then matched.

The transport of energy by radiation is thoroughly treated in Mihalas (1978). We will present a short description of radiative transfer equation and introduce some radiation quantities. Radiation energy is carried by light quanta (photons). The motion of the photons through the gas is

described in terms of the mean free path between interactions of photons and gas particles. As one approaches the surface of a star, the density decreases and consequently the mean free path of the photon increases, hence diffusion approximation breaks down. Therefore, in this case one has to solve the full radiative transfer equation.

1.2.1 In the atmosphere

The radiative transfer equation describes how the electromagnetic radiation interacts with the material as it is absorbed, emitted and scattered. The full radiative transfer equation for the grey static plane parallel atmosphere (see Mihalas 1978) is given by

$$\mu \frac{dI(r,\mu)}{dr} = \rho\kappa_s J + \rho\kappa_a B - \rho(\kappa_s + \kappa_a)I, \tag{1.32}$$

where μ here is the direction cosine of the incident beam with respect to the radius vector, $I(r,\mu)$ is the specific intensity, κ_s and κ_a are the scattering and absorption coefficient per unit mass respectively. This is for the case where the atmosphere is very thin compared to the stellar radius. The mean intensity J (also called zeroth-order moment) is given by the equation

$$J = \frac{1}{4\pi}\int I d\Omega, \tag{1.33}$$

where the integration of specific intensity is over solid angle Ω.
Here B is the Planck function given as

$$B = \frac{a_r c}{4\pi} T^4, \tag{1.34}$$

where c is the speed of light and a_r is the radiation constant. Furthermore equation (1.32) is integro-differential equation, since the source function includes $J = 1/2\int_{-1}^{1} I d\mu$ which is the integral of I, hence it is difficult to solve.

To obtain the radiative transfer equation with no scattering, we set all κ_s in equation (1.32) to zero to obtain

$$\mu \frac{dI}{dr} = \rho\kappa(B - I), \tag{1.35}$$

where the opacity κ includes absorption only. The first and second moments are given as

$$H = \frac{1}{4\pi}\int \mu I d\Omega, \tag{1.36}$$

and

$$K = \frac{1}{4\pi}\int \mu^2 I d\Omega, \tag{1.37}$$

respectively, where $\mu = \cos\theta$. The Eddington flux H is related to radiative flux F_r by

$$H = \frac{F_r}{4\pi}, \tag{1.38}$$

and K is related to radiation pressure by $P_{rad} = (4\pi/c)K$. The radiation pressure P_{rad} is pressure of the photon gas, hence is analogous to gas pressure.
The amount of energy transported by radiation through a sphere of radius r is

$$L_r = 4\pi r^2 F_r, \tag{1.39}$$

where L_r is the radiative luminosity.
Equation (1.35) is then integrated over $\mu \epsilon [-1 : 1]$ to obtain the following expression of H:

$$\frac{dH}{dm} = \frac{\kappa}{4\pi r^2}(B - J). \tag{1.40}$$

Substituting equations (1.38) and (1.39) into (1.40) we obtain

$$\frac{dL_r}{dm} = 4\pi\kappa(B - J). \tag{1.41}$$

Similarly multiplying equation (1.35) by μ and integrating over $\mu \epsilon [-1, 1]$ we obtain:

$$\frac{dK}{dm} = -\frac{\kappa L_r}{64\pi^3 r^4}. \tag{1.42}$$

1.2.2 In the envelope

In the envelope the mean free path of photons is very small as compared to the stellar radius. In this case the transport of radiative energy is modelled with diffusion approximation. This type of approximation involves flow of energy as a result of temperature gradient. The diffusion approximation is more simplified as compared to the modelling of radiation in the atmosphere (see §1.2.1). According to Mihalas (1978), under the diffusion approximation, the specific intensity is given as

$$I(\tau, \mu) = B(\tau) + \mu\frac{dB}{d\tau}. \tag{1.43}$$

The equation (1.43) was obtained from the solution of transfer equation

$$I(\tau, \mu, t) = \int_{\tau}^{\infty} S(t)e^{-(t-\tau)/\mu}dt/\mu, \qquad 0 \leq \mu \leq 1, \tag{1.44}$$

and source function S represented by a power series:

$$S(t) = B(\tau) + (t - \tau)\frac{dB}{d\tau}. \tag{1.45}$$

By substituting equation (1.43) into the equations (1.33), (1.36) and (1.37) we obtain respectively

$$J(\tau) = B(\tau), \tag{1.46}$$

$$H(\tau) = \frac{1}{3}\frac{dB}{d\tau}, \tag{1.47}$$

and

$$K(\tau) = \frac{1}{3}B(\tau), \tag{1.48}$$

where τ is the optical depth.

1.3 Convective Transfer

In this section we describe the mixing-length theory in some detail. More detailed description of stellar mixing-length theory can be found, for example, in Gough (1976, 1977) and Houdek (1996). Convection is the transport of energy by mass motion in a fluid. To find whether a region in a fluid is stable against convection the well known Schwarzschild criterion is used (see Kippenhahn and Weigert 1990). This criterion is often written as:

$$\nabla > \nabla_{ad}, \tag{1.49}$$

where

$$\nabla = \frac{d\ln T}{d\ln p}, \tag{1.50}$$

is the temperature gradient.

If $\nabla > \nabla_{ad}$ the temperature gradient is said to be superadiabatic, if $\nabla < \nabla_{ad}$ it is subadiabatic. Convective instability requires only a very small superadibatic gradient (see Thompson 2006).

Should this criterion be satisfied, a small fluid element perturbed from its initial position in the fluid, will accelerate away from its original position, due to buoyancy forces. This convective instability in a fluid can lead to turbulence. According to Tritton (1977), turbulence is a type of flow characterised by series of rapid irregular fluctuations of velocity and pressure in space and time.

The concept of turbulent pressure comes into the equation of motion (1.23) from breaking the velocity u_i (as well as pressure p) into large-scale component and small-scale fluctuating component, for example

$$u_i = \overline{u_i} + u_i', \tag{1.51}$$

where $\overline{u_i}$ is the large-scale component and u_i' is the fluctuating component. According to the Reynold's rules of averages if $a = \overline{a} + a'$ and $b = \overline{b} + b'$ represent fluctuating quantities then

$$\overline{a+b} = \overline{a} + \overline{b}, \quad \overline{ab} = \overline{a}\,\overline{b} + \overline{a'b'}, \quad \overline{\frac{\partial a}{\partial x}} = \frac{\partial \overline{a}}{\partial x}, \quad \overline{a'} = \overline{b'} = 0. \tag{1.52}$$

Before applying these rules to the equation of motion (1.23) we first apply them to the incompressible continuity equation (1.21) to obtain

$$\frac{\partial}{\partial x_i}(\overline{u_i} + u_i') = 0. \tag{1.53}$$

Taking an ensemble average of the continuity equation (1.53) we get the mean continuity equation:

$$\frac{\partial \overline{u_i}}{\partial x_i} = 0. \tag{1.54}$$

We subtract equation (1.54) from equation (1.53) to obtain the continuity equation of fluctuating flow:

$$\frac{\partial u_i'}{\partial x_i} = 0. \tag{1.55}$$

The equation of motion (1.23), after decomposition into mean and fluctuating components is

$$\frac{\partial(\overline{u_i} + u_i')}{\partial t} + (\overline{u_j} + u_j')\frac{\partial(\overline{u_i} + u_i')}{\partial x_j} = -\frac{1}{\rho}\frac{\partial(\overline{p} + p')}{\partial x_i} + \nu\frac{\partial^2(\overline{u_i} + u_i')}{\partial x_j^2} + g_i. \tag{1.56}$$

Taking an ensemble average of the equation (1.56) we get

$$\frac{\partial \overline{u_i}}{\partial t} + \overline{u_j}\frac{\partial \overline{u_i}}{\partial x_j} + \overline{u_j'\frac{\partial u_i'}{\partial x_j}} = -\frac{1}{\rho}\frac{\partial \overline{p}}{\partial x_i} + \nu\frac{\partial^2 \overline{u_i}}{\partial x_j^2} + g_i. \tag{1.57}$$

With the help of equation (1.55), it can be shown that the third term on the left hand side of equation (1.57) can be expressed as

$$\overline{u_j'\frac{\partial u_i'}{\partial x_j}} = \frac{\partial}{\partial x_j}(\overline{u_i'u_j'}). \tag{1.58}$$

Therefore, the mean equation of motion is

$$\overline{\rho}\frac{\partial \overline{u_i}}{\partial t} + \overline{\rho u_j}\frac{\partial \overline{u_i}}{\partial x_j} = -\frac{\partial \overline{p}}{\partial x_i} - \frac{\partial}{\partial x_j}(\overline{\rho u_i'u_j'}) + \mu\frac{\partial^2 \overline{u_i}}{\partial x_j^2} + g_i, \tag{1.59}$$

where the first and second terms on the left hand side represent the rate of change of the large-scale momentum and the flux of the large-scale momentum respectively. The first, third and fourth terms on the right hand side represent the large-scale forces per unit mass from pressure, viscosity and gravity respectively.

The equation (1.59), neglecting viscosity, can be rewritten as

$$\overline{\rho}\frac{d\overline{u_i}}{dt} = -\frac{\partial \overline{p}}{\partial x_i} - \frac{\partial}{\partial x_j}(\overline{\rho u_i' u_j'}) + g_i, \tag{1.60}$$

where

$$\frac{d}{dt} = \frac{\partial}{\partial t} + \overline{u_j}\frac{\partial}{\partial x_j}. \tag{1.61}$$

The second term on the right hand side of equation (1.60), hereafter ST^*, looks like minus the gradient pressure:

$$ST^* = -\frac{\partial(p_t^* \delta_{ij})}{\partial x_i}, \tag{1.62}$$

where p_t^* is defined as

$$p_t^* \delta_{ij} = \overline{\rho u_i u_j}, \tag{1.63}$$

and δ_{ij} is a Kronecker delta. Contracting over i and j equation (1.63) can be written as

$$p_t^* \delta_{ii} = \rho(u^2 + \nu^2 + w^2). \tag{1.64}$$

By convention, following Gough (1977), turbulent pressure is defined as

$$p_t = \rho w^2. \tag{1.65}$$

We are assuming here averages, but not writing those explicitly. Hence we can write equation (1.64) as

$$3p_t^* = \Phi p_t, \tag{1.66}$$

where Φ is a measure of the anisotropy of the turbulence. The function Φ is defined by

$$\Phi = \frac{u^2 + v^2 + w^2}{w^2}, \qquad \text{or} \qquad \Phi = 1 + \frac{k_v^2}{k_h^2}, \tag{1.67}$$

where k_v and k_h are the vertical and horizontal wavenumbers. When $\Phi = 1$, the cell is long and thin and if $\Phi = 2$ then the horizontal and vertical dimensions of the cell are equal. The vertical wavenumber is related to mixing length ℓ of an eddy by $k_v = \pi/\ell$. Equation (1.119) can be rewritten as

$$ST^* = -\frac{\partial}{\partial x_j}\left(\frac{\Phi p_t \delta_{ij}}{3}\right), \tag{1.68}$$

$$= -\frac{\partial}{\partial x_i}\left(\frac{\Phi p_t}{3}\right). \tag{1.69}$$

The equation that we want to derive is the radial component of the momentum equation. The radial component of this term is

$$ST^* = -\frac{\partial}{\partial r}\left(\frac{\Phi p_t}{3}\right), \tag{1.70}$$

which can be rewritten as

$$ST^* = -\frac{\partial p_t}{\partial r} + \frac{\partial}{\partial r}\left[\left(\frac{3-\Phi}{3}\right)p_t\right]. \tag{1.71}$$

The first term on the right hand side of equation (1.71) gets absorbed into the pressure gradient term (first term on the right hand side of Eq. 1.60). Replacing the gradient $\partial/\partial r$ by $3/r$, following Gough (1977), the second term on the right hand side of equation (1.71) gets rewritten as $-(3-\Phi)p_t/r$.
Thus the radial component of the mean equation of motion (Eq. 1.60), can be expressed as

$$\rho r\frac{d^2r}{dt^2} = -4\pi\rho r^3\frac{dp}{dm} - (3-\Phi)p_t - \rho\frac{Gm}{r}. \tag{1.72}$$

Hence the hydrostatic equilibrium equation can be expressed as

$$\frac{dp}{dm} = -\frac{g}{4\pi r^2}\tilde{\mu}, \tag{1.73}$$

where $\tilde{\mu}$ is defined as

$$\tilde{\mu} = 1 + (3-\Phi)p_t/\rho g r. \tag{1.74}$$

The factor $\tilde{\mu}$ describes the dynamical correction to the total pressure gradient due to the anisotropy of Reynolds stresses . Additional effects such as magnetic field may also complicate the stability analysis (see Gough & Tayler 1966). Convection in stellar modelling is approached using the mixing–length theory.

The Boussinesque approximation is often used for the analysis of convection. In this approximation, the density variations are neglected except in the buoyancy term and the fluid is treated as incompressible. The presence of sound waves brings numerical difficulties because they require much short time steps than those needed to resolve convective motions. In order to solve this problem Gough (1969) developed the anelastic approximation. In this approximation the sound waves are suppressed, resulting in a set of equations that are suitable for the treatment of convection.

1.3.1 The mixing length theory

It was introduced independently by Taylor (1915) and Prandtl (1925) to understand the transport of heat and momentum in a turbulent fluid. The idea behind the theory, at least as described by Prandtl is to imagine that the stellar fluid is composed of elements, and that the perturbed fluid element moves from region of high heat content to regions of lower heat content (and vice versa) of the fluid under the influence of buoyancy forces over a certain characteristic length ℓ called the mixing length. It is defined as

$$\ell = \alpha_c H_p, \tag{1.75}$$

where H_p is the pressure scale height and α_c is a constant (see Gough & Weiss 1976). After travelling the length ℓ, the elements are dissolved. The mixing length ℓ is proportional to the local pressure scale height. The element may release heat to its surrounding as it rises. Also, cool elements at a higher level may sink a distance ℓ and break up. The mixing length may be compared with the mean free path in the kinetic theory of gases. Based on this description the mean heat flux can be estimated. There are two physical pictures of turbulent convection used to derive mixing-length models. The two pictures are as follows:

- The first picture interprets the turbulent flow by direct analogy with kinetic theory. In this case, turbulent elements accelerate from rest and break up having travelled over approximately one mixing length. The evolution of the fluid elements is approximated by the linear growth rate which is based on the original idea of Taylor (1915) and Prandtl (1925). The time-dependent mixing-length theory by Gough (1969) is based on this picture.

- In the second picture convection is interpreted as a complex of transient cells. The vertical structure of these cells is approximately the mixing length ℓ. Having evolved out of some chaotic state, the convective cells break up after overturning approximately once. Also the cells may continue to be in steady state due to buoyancy forces balancing the effects of radiation heat loss and turbulent dissipation. Hence acceleration is neglected. This treatment is based on the idea of Prandtl (1932). The time-dependent mixing-length theory by Unno (1967) emerged from this picture.

Our code uses the first picture.

What I have described so far treats convection locally, this means that the nature of the convective flow in a given region of the fluid depends on the local properties only, not on the average properties of the region in which a fluid travels. However at the edges of a convective instability region the local theory does not hold. This is because the theory predicts that convective velocity sharply becomes zero. In real stars the momentum of convective cells carries them into adjacent convectively stable region. This phenomenon is called overshoot.

For non-pulsating stars there are many different prescriptions of local mixing theory, and it was established that each prescription is no different from one another (see Gough & Weiss 1976). However this is not true for the mixing length theory applied to pulsating envelopes. Several authors have investigated time-dependent convection(e.g. Unno 1967; Gough 1977; Xiong 1978; Stellingwerf 1982, Kuhfuss 1986). Each of the methods used by these authors has its own special characteristics, but they are closely related (see Baker 1987).

1.3.2 Gough's local mixing length theory

In this section we summarise the local mixing length theory introduced by Gough (1976) since our treatment of convection in our code is based on this method. Here we present definitions, relevant to our project under this local mixing-length theory. The Gough local mixing length theory is based on the first picture by Taylor (1925).

To obtain the Boussinesq equations of motion and energy governing fluctuations, first the variables are expressed as the sum of mean and fluctuating parts. For example the temperature variable T is expressed as $T = \bar{T} + T'$. Thereafter these variables are substituted into the equations of motion and energy. We then take the average of the sum of the mean plus fluctuations. The mean equation of motion [Eq. (1.72)] is subtracted from the full equations of motion to obtain the fluctuating equation of motion. Similarly the mean energy equation [Eq. (1.31)] is subtracted from the full energy equation to obtain the fluctuating energy equation. The fluctuating equations of motion and energy are as follows (see Gough 1977):

$$\frac{\partial u_i'}{\partial t} + \frac{\partial}{\partial x_i}(u_i'u_j' - \overline{u_i'u_j'}) - \frac{\partial(\ln r^2\bar{\rho})}{\partial t}u_i' = -\frac{1}{\bar{\rho}}\frac{\partial p_g'}{\partial x_i} + g\frac{\bar{\delta}}{\bar{T}}T'\hat{\boldsymbol{r}}. \tag{1.76}$$

and

$$\frac{\partial T'}{\partial t} + \frac{\partial}{\partial x_j}(u_i'T' - \overline{u_i'T'}) + \left[(\bar{c}_{pT} - \bar{\delta})\frac{\partial \ln \bar{T}}{\partial t} - \frac{\bar{\delta}_T \bar{p}_g \bar{\delta}}{\bar{c}_p \bar{\rho}\bar{T}}\frac{\partial \ln \bar{p}_g}{\partial t}\right]T' = \beta w - \frac{1}{\bar{\rho}\bar{c}_p}\frac{\partial F_{r,i}'}{\partial x_i}, \tag{1.77}$$

where g is the gravitational acceleration, p_g the gas pressure, F_r the radiative flux and $\hat{\boldsymbol{r}}$ is the radial direction unit vector. The thermodynamic derivative δ is

$$\delta\,(\rho, T) = -\left(\frac{\partial \ln \rho}{\partial \ln T}\right)_{p_g}, \tag{1.78}$$

c_{pT} and δ_T are the logarithmic derivatives of c_P and δ with respect to temperature at constant pressure. The second term on the right hand side of equation (1.77) describes a radiative leakage from a convective eddy. The non-linear terms appearing in equations (1.76) and (1.77) are

called turbulent drag and turbulent conductivity respectively. The viscosity is neglected in equation (1.76). The second term on the right hand side of equation (1.76) describes the acceleration due to the buoyancy. The superadiabatic temperature gradient β is given by

$$\beta = -\frac{d\bar{T}}{dr} + \frac{\bar{\delta}}{\bar{c}_p\bar{\rho}}\frac{d\bar{p}_g}{dr}. \tag{1.79}$$

The third terms in both the left hand side of equations (1.76) and (1.77) are results of the mean continuity equation.

1.3.2.1 Static Envelope

Here we discuss the case where changes in the overall structure of a star take place over a much longer time scale compared to the time scale for convection. Since we use kinetic theory picture of convection the non-linear terms in equations (1.76) and (1.77) are neglected. In addition, the third terms on the left hand side of both equations (1.76) and (1.77) which are time dependent are neglected. Therefore, equations (1.76) and (1.77) are written as

$$\frac{\partial u_i'}{\partial t} = -\frac{1}{\bar{\rho}}\frac{\partial p_g'}{\partial x_i} - g\frac{\bar{\delta}}{\bar{T}}T'\hat{\boldsymbol{r}}, \tag{1.80}$$

and

$$\frac{\partial T'}{\partial t} - \beta w = -\frac{1}{\bar{c}_p\bar{\rho}}\boldsymbol{\nabla}\cdot\mathbf{F}_r'. \tag{1.81}$$

The pressure fluctuations on the right hand side of equation (1.80) is removed by taking the double curl of that equation to obtain

$$\frac{\partial\boldsymbol{\nabla}^2 w}{\partial t} = \frac{g\bar{\delta}}{\bar{T}}\boldsymbol{\nabla}_h^2 T', \tag{1.82}$$

where

$$\boldsymbol{\nabla}_h^2 = \frac{1}{r^2\sin\theta}\frac{\partial}{\partial\theta}\left(\sin\theta\frac{\partial}{\partial\theta}\right) + \frac{1}{r^2\sin^2\theta}\frac{\partial^2}{\partial\varphi^2}, \tag{1.83}$$

and w is the vertical velocity fluctuation. The pressure fluctuations is removed because in the Boussinesq approximation, it does no work but increases the inertia of the vertical flow (see Gough 1977 and Baker 1987).

We suppose that the solutions w and T' can be written in the form

$$w = W f_1, \tag{1.84}$$

and

$$T' = f_1\Theta, \tag{1.85}$$

where the function W and Θ are sinusoidal in r and depend on time (see Chandrasekhar 1961). The horizontal flow is described by the function $f_1(\theta, \varphi)$ which satisfies

$$\nabla_h^2 f_1 = -k_h^2 f_1, \qquad \text{and} \quad \bar{f}_1^2 = 1. \tag{1.86}$$

The Eddington approximation to the radiative transfer modifies the diffusion approximation for the radiative heat loss from bubbles in the optically thin limit. Thus

$$\nabla \cdot \mathbf{F}'_r = \begin{cases} K_c \hat{k}^2 T', & \text{optically thick} \\ \phi K_c \hat{k}^2 T', & \text{optically thin} \end{cases} \tag{1.87}$$

where

$$\hat{k}^2 = k_h^2 + k_v^2, \tag{1.88}$$

and

$$\phi = \frac{[(\kappa_T - \delta)(B - J)/4B + 1]}{[1 + \Phi \sum /(\Phi - 1)]}, \qquad \sum = \frac{1}{3} \frac{\pi^2}{(\rho \kappa \ell)^2}. \tag{1.89}$$

accounts for partial optical transparency which extends radiative leakage to optically thin case. The radiative conductivity K_c is defined as

$$K_c = \frac{4 a_r c T^3}{3 \rho \kappa}. \tag{1.90}$$

Using equation (1.87) the fluctuating equations (1.81) can be expressed as

$$\frac{\partial \Theta}{\partial t} + \frac{K_c}{\rho c_p} \hat{k}^2 \phi \Theta = \beta W. \tag{1.91}$$

Equation (1.82) becomes:

$$\Phi \frac{\partial W}{\partial t} = \frac{g \delta}{T} \Theta. \tag{1.92}$$

We combine the two differential equations (1.92) and (1.91) into single second-order differential equation:

$$\frac{\partial^2 \Theta}{\partial t^2} + \phi \frac{K_c \hat{k}^2}{\rho c_p} \frac{\partial \Theta}{\partial t} - \beta \frac{g \delta}{\Phi T} \Theta = 0. \tag{1.93}$$

Since all the coefficients in the equation (1.93) are constant, the solution of W and Θ are of the form W or $\Theta' \propto \exp(\hat{\sigma} t)$ where $\hat{\sigma}$ is a complex angular frequency. The real part of $\hat{\sigma}$ describes the growth (or decay) of convection. The characteristic equation of equation (1.93) is given as

$$\hat{\sigma}^2 + \frac{\phi K_c}{\rho c_p} \hat{k}^2 \hat{\sigma} - \frac{g \delta \beta}{\Phi T} = 0. \tag{1.94}$$

From the characteristic equation (1.94) convective growth rate σ is given as

$$\hat{\sigma} = \hat{\eta}^{-1} S^{-1/2} \left(\frac{g\delta\beta}{\Phi T} \right)^{1/2} [(1 + \hat{\eta}^2 S)^{1/2} - 1], \tag{1.95}$$

where η is a geometrical factor of order unity given by

$$\hat{\eta} = 2\pi^{-2}\Phi^{-3/2}(\Phi - 1), \tag{1.96}$$

and

$$S = \frac{g(\delta/T)\beta\ell^4}{(\phi K_c/\rho\, c_p)^2}, \tag{1.97}$$

is the product of Prandtl and Rayleigh numbers. The Prandtl number (Pr) measures the ratio of damping due to viscosity to radiative leakage and is defined as $P_r = \nu/\nu_T$ where ν_T is the thermal diffusivity. It is about 10^{-9} in stars. The Rayleigh number (Ra) measures how the driving of convection compares to the damping process and is given as

$$Ra = \frac{g\chi_T}{H_p\chi_\rho}(\nabla - \nabla_{ad})\frac{\ell^4}{\nu_T\nu}, \tag{1.98}$$

where χ_T and χ_ρ are defined as

$$\chi_T = \left(\frac{\partial \ln p_g}{\partial \ln T} \right)_\rho, \quad \text{and} \quad \chi_\rho = \left(\frac{\partial \ln p_g}{\partial \ln \rho} \right)_T, \tag{1.99}$$

respectively. The Ra number is approximately 10^{20} in stars (see Hansen, Kawaler & Trimble 1994).

Here we estimate the magnitudes of W and Θ in terms of $\hat{\sigma}$. From the definition of velocity

$$W \approx \frac{dz}{dt}, \tag{1.100}$$

and since W vary as $\exp(\hat{\sigma}t)$ then

$$\frac{dW}{dt} = \hat{\sigma}W. \tag{1.101}$$

From equations (1.100) and (1.101) I have

$$W = \hat{\sigma}z. \tag{1.102}$$

If we take $z = \ell/2$, the fluctuating velocity of a convective parcel is

$$W = \frac{1}{2}\hat{\sigma}\ell. \tag{1.103}$$

Similarly

$$\frac{d\Theta}{dt} = \hat{\sigma}\Theta = -\frac{\phi K_c}{\rho c_p}\hat{k}^2\Theta + \beta W. \tag{1.104}$$

After we substitute equation (1.103) into equation (1.104) the estimate of Θ is

$$\Theta = \frac{1}{2}\frac{\hat{\sigma}\ell\beta}{\hat{\sigma} + \phi K_c \hat{k}^2/\rho c_p}. \tag{1.105}$$

Using the characteristic equation (1.94) the equation (1.105) can be written as

$$\Theta = \frac{1}{2}\frac{\hat{\sigma}^2\beta\ell T\Phi}{g\delta\beta}. \tag{1.106}$$

The convective flux is defined as

$$F_c = \rho c_p W\Theta, \tag{1.107}$$

thus after substituting equation (1.106) we get

$$F_c = \frac{1}{4}\frac{\rho c_p \Phi T}{g\delta}\hat{\sigma}^3\ell^2. \tag{1.108}$$

The turbulent pressure is defined as

$$p_t = \rho W^2, \tag{1.109}$$

therefore

$$p_t = \frac{1}{4}\rho\hat{\sigma}^2\ell^2. \tag{1.110}$$

1.3.2.2 Applying local mixing length theory to pulsating stars

Here we show how the local mixing length theory of convection is applied to pulsating stars. This is based on the work by Gough (1977). The equations (1.76) and (1.77) are written as:

$$\frac{\partial W}{\partial t} - \frac{1}{\Phi}\frac{\partial \ln(r^2\rho)}{\partial t}W - \frac{g\delta}{\Phi T}\Theta = 0, \tag{1.111}$$

and

$$\left[\frac{\partial}{\partial t} + (c_{pt} - \delta)\frac{\partial \ln T}{\partial t} - \delta_t \nabla_{ad}\frac{\partial \ln p}{\partial t}\right]\Theta - \beta W + \frac{\phi K_c}{\rho c_p}\hat{k}^2\Theta = 0. \tag{1.112}$$

Note that the second term in equation (1.111), second and third terms in equation (1.112) which were ignored in the static case are now brought back into equations of motion and energy. The time dependent shape factor Φ which describes the effect of pulsating atmosphere on the shape of the eddy is given by

$$\Phi = \Phi_0[1 + \Phi_{10}\exp(-i\omega t_0) + \Phi_{11}\exp(-i\omega t)], \tag{1.113}$$

where Φ_{10} and Φ_{11} are given in Appendix F.

Gough (1976) introduced the function $\mathcal{P}(r,t,t_0)$ as the probability that an eddy created at time t_0 survives until time t. If one wants to find the average of any function that describes an eddy at height r, that function is multiplied with $\mathcal{P}$ and then integrated with respect to the time of creation of that eddy. The shape of this probability function was hinted at by Spiegel (1963) where according to him the probability of destruction of an eddy that is displaced by a distance dx along ℓ is dx/ℓ. Therefore, the probability that an eddy will survive until time t is given as

$$\mathcal{P}(r,t,t_0) = \exp\left[\int_{t_0}^{t} \frac{W(t',t_0)dt'}{\ell}\right]. \tag{1.114}$$

If we assume that the convective fluctuations do not contribute to the final heat flux at the parcel's creation time, W and Θ can be expressed in terms of linear growth rate $\hat{\sigma}$ as

$$W = \hat{W}_0 \exp[\hat{\sigma}(t-t_0)], \quad \Theta = \hat{\Theta}\exp[\hat{\sigma}(t-t_0)], \tag{1.115}$$

where $\hat{W}_0 = W(t=t_0)$ and $\hat{\Theta}_0 = \Theta(t=t_0)$ are the fluctuations of velocity and temperature of the eddy at the time of eddy creation. Therefore, it is reasonable to estimate the probability function as

$$\mathcal{P}(r,t,t_0) = \exp\left\{-\frac{\hat{W}_0 \exp[\hat{\sigma}(t-t_0)]}{\hat{\sigma}\ell}\right\}. \tag{1.116}$$

The convective flux, turbulent pressure and the shape factor for eddies created at rate n with mass m at r are given as follows:

$$F_c = nmc_p \int_{-\infty}^{t} W\Theta\mathcal{P}dt_0, \tag{1.117}$$

$$p_t = nm \int_{-\infty}^{t} W^2\mathcal{P}dt_0, \tag{1.118}$$

and

$$\Phi = p_t^{-1} \int_{-\infty}^{t} nmW^2\mathcal{P}dt_0. \tag{1.119}$$

According to Gough (1976) in a statistically steady state where as many eddies are created as destroyed the total density can be evaluated as

$$\rho = nm \int_{-\infty}^{t} \mathcal{P}dt_0. \tag{1.120}$$

The eddy creation rate is given by

$$nm = \rho\hat{\tau}^{-1}, \tag{1.121}$$

where $\hat{\tau}$ is the mean life time of the eddy.

We combine the equations (1.111) and (1.112) to obtain the second order differential equation:

$$\frac{\partial^2 W}{\partial t^2} = -2\kappa\phi\hat{k}^2[1 + \kappa_{10}\exp(-i\omega t_0) - \kappa_{11}\exp(-i\omega t)]\frac{\partial W}{\partial t} - \\ - \frac{N^2}{\Phi}[1 + 2\mu_{10}\exp(-i\omega t_0) + 2\mu_{11}\exp(-i\omega t)]W, \tag{1.122}$$

where κ_{1i} and μ_{1i} are shown in Appendix F. The quantity N is the Brunt–Väisälä frequency defined as

$$N^2 = -\frac{\delta}{T}g\beta, \tag{1.123}$$

for the convective instability, $N^2 < 0$.
The solution of equation (1.122), as given by Gough (1977), becomes:

$$W \approx W_0[1 + W_{10}\exp(-i\omega t_0) + W_{11}\exp(-i\omega t) + \hat{\sigma}(t - t_0)W_{12}\exp(-\omega t_0)], \tag{1.124}$$

where

$$W_0 \approx \hat{W}_0\exp[\hat{\sigma}(t - t_0)], \tag{1.125}$$

is the evolving convective velocity fluctuation in a static atmosphere and $\hat{W}_0$ is the initial value of W_0. Similarly Θ can be expressed in the same way as W.

We substitute solutions W and Θ of equations (1.111) and (1.112) into equations (1.117), (1.118) and (1.119). They are then perturbed to first order to obtain:

$$\frac{\delta F_c}{F_{c,0}} = \\ \frac{\delta\rho}{\rho_0} + \frac{\delta c_p}{c_{p,0}} + W_{11} + \Theta_{11} + W_{21} + (W_{10} + \Theta_{10})\mathcal{F} + (W_{12} + \Theta_{12})\mathcal{F}\mathcal{G} + \mathcal{H}, \tag{1.126}$$

$$\frac{\delta p_t}{p_{t,0}} = \frac{\delta\rho}{\rho_0} + 2W_{11} + W_{21} + 2(W_{10}\mathcal{F} + W_{12}\mathcal{F}\mathcal{G}) + \mathcal{H}, \tag{1.127}$$

and

$$\frac{\delta\Phi}{\Phi_0} = \Phi_{11} - \Phi_{10}\mathcal{F}, \tag{1.128}$$

where the subscript zero represents the static equilibrium model quantities. The functional expressions $\mathcal{F}$, $\mathcal{G}$ and $\mathcal{H}$ are for a statistical averaging of the convective fluctuations. These expressions $\mathcal{F}$, $\mathcal{G}$ and $\mathcal{H}$ together with the coefficients W_{1i}, Θ_{1i} and W_{21} are given in Appendix F.

1.3.3 Non-local mixing-length theory

The purpose of this theory is to address the following shortcomings of the local mixing-length theory:

1. The mixing-length ℓ is required to be shorter than the scale height of the envelope. However this condition is violated for red giants and solar like stars according to the stellar calibration (see Gough & Weiss 1976).

2. The assumption that superadiabatic lapse rate β is constant over scale height. This is not a good assumption in the upper layers of the convection zone where β varies on a scale much shorter than ℓ.

3. Eddies are not allowed to overshoot into stable regions, since they loose their momentum as soon as they reach the edge of the unstable zone (see Baker 1987).

In the non-local mixing-length theory of convection the finite size of an eddy is taken into account, and the averages of convective fluxes over mixing length are described. The rising and falling elements were described by a distribution function by Spiegel (1963). He derived an equation describing the flux of elements by considering the conservation of the distribution. The detail description of the equation shall be given in the next section.

1.3.3.1 Stationary atmosphere

In the equation by Spiegel (1963), the aggregate of turbulent convective elements is described by a distribution function $\psi(x_i, u_i, t)$ where u_i is the velocity vector at the position x_i, and ψ is the number density of elements in (x_i, u_i)-space. The conservation of eddies is described by this equation

$$\frac{\partial \psi}{\partial t} + \frac{\partial}{\partial x_i}(u_i \psi) + \frac{\partial}{\partial u_i}(\dot{u}_i \psi) = q - \frac{\hat{u}\psi}{\ell}, \tag{1.129}$$

where q is a source term describing the initial creation of convective elements, the dot denotes the derivative with respect to time, $\hat{u}$ is the magnitude of the velocity, and the last term on the right hand side describes the disappearance of eddies at end of their paths. The third term on the left hand side describes how the properties of an eddy changes as it is affected by buoyancy and pressure forces.

If we consider the static plane-parallel case, equation (1.129) can be written as

$$\mu \frac{d(\hat{u}\psi)}{dz} + \frac{\hat{u}\psi}{\ell} = q_1, \tag{1.130}$$

where

$$q_1 = q - \frac{\partial}{\partial u_i}(\dot{u}_i \psi), \tag{1.131}$$

and $\mu = \cos\theta$ with θ being the angle between the vertical co-ordinate z and the direction of line along fluid element trajectories .
The variables Ψ and ξ are introduced as follows

$$\Psi = \hat{u}\psi, \tag{1.132}$$

and

$$d\xi = -\frac{dz}{\ell}. \tag{1.133}$$

Therefore equation (1.130) can be written as

$$\mu \frac{d\Psi}{d\xi} = \Psi - Q, \tag{1.134}$$

where

$$Q = q_1 \ell. \tag{1.135}$$

Equation (1.134) describes the flux of elements and looks similar to the radiative transfer equation given in equation (1.32). Hence it can be solved for Ψ in terms of Q like in radiative transfer theory (see Section 1.2). The convective flux in the local mixing length description, computed by averaging appropriate moments of Ψ over μ is

$$\mathcal{F}_c = \int_{-1}^{1} |h'| \Psi \mu d\mu \tag{1.136}$$

$$= \int_{0}^{\infty} |h'| Q(\xi_0) E_2(\xi_0 - \xi) d\xi_0, \tag{1.137}$$

where h' is a specific enthalpy fluctuation in an element, $h'Q$ is a source function and E_2 is the second exponential integral. For comparison with analytical solutions to radiative transfer, see Mihalas (1978).
The non-local convective flux equation (1.137) can be written as

$$\mathcal{F}_c = 2 \int_{\xi-1/2}^{\xi+1/2} F_c(\xi_0) \cos^2[\pi(\xi_0 - \xi)] d\xi_0. \tag{1.138}$$

where F_c is the source function which is the local convective heat flux given in equation (1.108). Similarly the non-local turbulent pressure can be written as

$$\mathcal{P}_t = 2 \int_{\xi-1/2}^{\xi+1/2} p_t(\xi_0) \cos^2[\pi(\xi_0 - \xi)] d\xi_0. \tag{1.139}$$

where p_t is the source function which is the local turbulent pressure expressed by equation (1.110). In order to account for the case where the trajectories of the elements are larger than the local scale height, Spiegel suggested replacing the superadiabatic lapse rate (β) by the average superadiabatic lapse rate ($\bar{\beta}$)

$$\bar{\beta} = 2\int_{\xi-1/2}^{\xi+1/2} \beta\left(\xi_0\right)\cos^2[\pi(\xi_0-\xi)]d\xi_0. \tag{1.140}$$

We now convert the integral expressions for convective heat flux, turbulent pressure and the average superadiabatic lapse rate to integro differential equations. To obtain the equation for F_c, moment equations are obtained by multiplying equation (1.134) by $h'\ell$ and by $\mu h'\ell$ and integrating with respect to μ. The Eddington approximation is used to close the system of moment of equations at second order (see Gough 1976). We obtain the differential equation:

$$\frac{1}{a^2}\frac{d^2\mathcal{F}_c}{d\xi^2} = \mathcal{F}_c - F_c, \tag{1.141}$$

where a is constant of order unity and F_c is the local convective flux.
The general solution of for the differential equation (1.141) is

$$F_c(\xi) = \int_0^\infty \mathcal{F}(\xi_0)\mathcal{K}_0(\xi,\xi_0)d\xi_0, \tag{1.142}$$

where the kernel $\mathcal{K}_0$ is by

$$\mathcal{K}_0(\xi,\xi_0) = \frac{1}{2}a\exp(a|\xi-\xi_0|). \tag{1.143}$$

In a similar way the integro differential equations for the averaged superadiabatic lapse rate is given as

$$\frac{1}{b^2}\frac{d^2\bar{\beta}}{d\xi^2} = \bar{\beta} - \beta, \tag{1.144}$$

and for the turbulent pressure as

$$\frac{1}{a^2}\frac{d^2\mathcal{P}_t}{d\xi^2} = \mathcal{P}_t - p_t, \tag{1.145}$$

where b is another constant and p_t is the local turbulent pressure. Thus in order to solve for non-local flux, one must calculate flux for local theory. Here we show how the non-local parameters a and b affect convection. In figure 1.5 the temperature gradient ∇ as a function of logarithmic pressure for an equilibrium model of a $1.3M_\odot$ star is shown. The model was constructed using the values $a^2 = b^2 = 300$ for the non local solution (solid line). The dashed line is for the model constructed using the local solution. The temperature gradient for the non-local solution in the upper superadiabatic regions is smaller than the local theory.

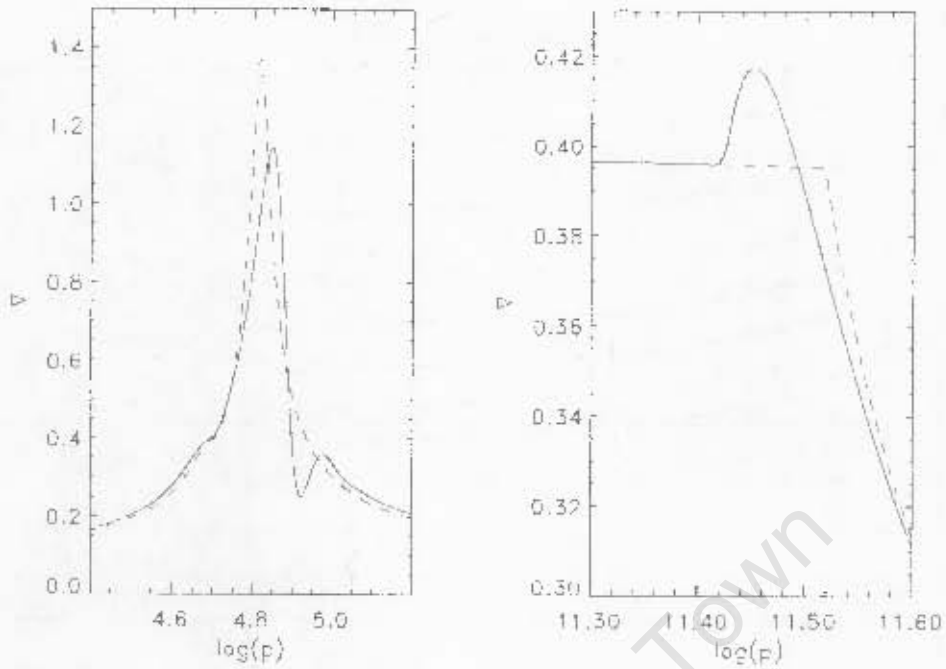

Figure 1.5: The temperature gradient ∇ as a function of logarithmic pressure for a $1.3\,M_{\odot}$ ZAMS equilibrium model envelope. The left panel shows the upper part of the convection zone, and right panels show the lower part. The non-local mixing-length theory solution for using the parameters $\alpha_c = 2.0$, $a^2 = b^2 = 300$ is shown by the solid line. The dotted line is the results of local theory, (see Houdek 1996).

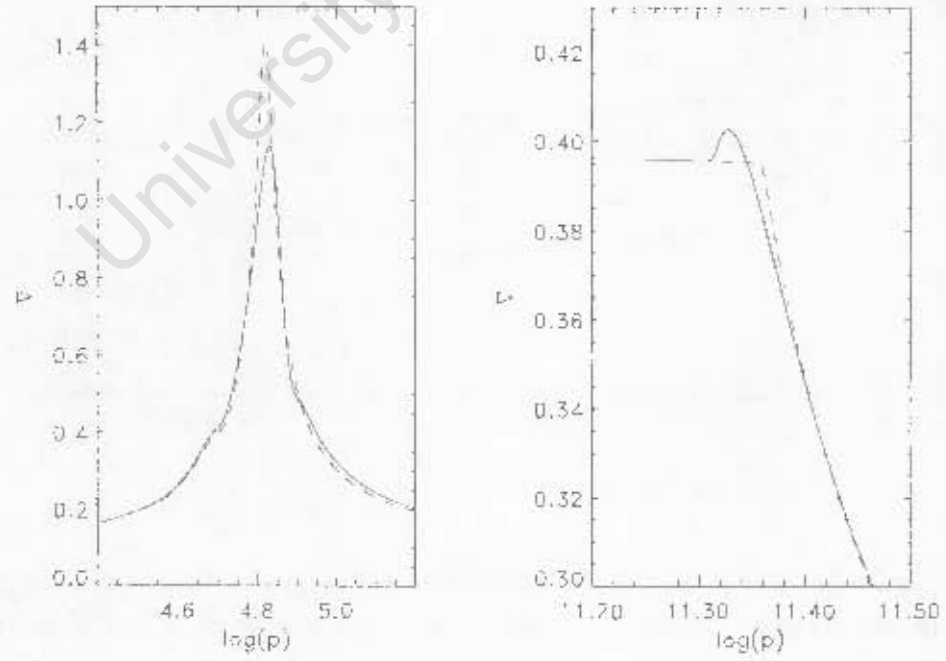

Figure 1.6: Temperature gradient ∇ for the same model as in figure 1.5, but using $\alpha_c = 1.8$, $a^2 = 900$ and $b^2 = 2000$ for the non-local solution. The non-local solution is shown by solid line, and the local solution with the dashed line. (see Houdek 1996)

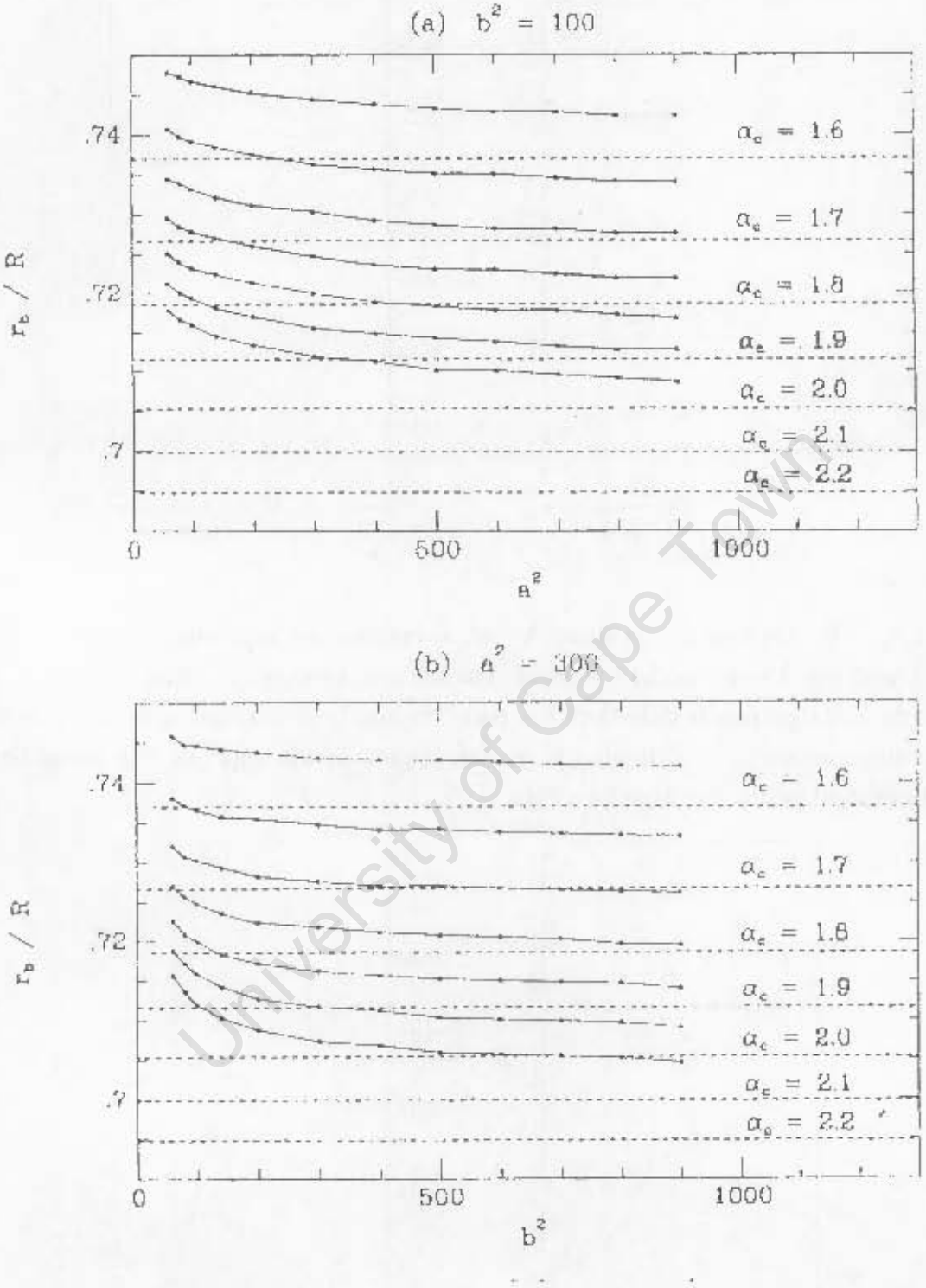

Figure 1.7: The radius of the base of the convection zone, r_b, as a function of the parameters of the mixing-length theory. Panel (a) shows $r_b/R_\odot$ as a function of a^2, for $b^2 = 100$. Seven curves are shown, each corresponds to a different value for α_c. The horizontal dashed line indicates lines computed according to local theory. Panel (b) shows $r_b/R_\odot$ as a function of b^2 with $a^2 = 300$. These figures were taken from Balmforth (1992).

This is because the small value of a increases the contribution from eddies located at different layers to the turbulent heat flux, hence reducing temperature gradient. The dip at $\log p = 4.93$ in the non-local temperature gradient is the results of the decoupling of the turbulent fluxes from the local stratification controlled by the non-local parameter b. Decreasing the value b, means the changes in the local structure like the ionization zone are no longer made to be small by the response of turbulent heat flux (see Houdek 1996).

The temperature gradients for a non-local model envelope computed for the parameters $a^2 = 900, b^2 = 2000$ and the corresponding local model are shown in figure 1.6. For larger values of a and b the non-local temperature gradient becomes closer to the local solution. The constants a and b are treated as parameters that determine the degree of non-locality of the turbulence. Low values of a and b imply highly non-local solution and high values reduces the system of equations to the local theory.

In figure 1.7 we show how the radius of the base of the convective zone r_b is determined by the mixing-length parameter α_c. This shows that an increase of the non-local parameters a and b reduces the extent of the convective zone. If we decrease the mixing-length parameter α_c (see Balmforth 1992a) the extent of the convection zone is reduced.

Chapter 2

Pulsation Equations

In this chapter I present radial pulsation equations that include convection and radiation. The perturbed convection equations are as presented by Houdek (1996). We modified elements of these equations to include consistent treatment of radiative transfer in the atmosphere. Houdek's energy equation includes radiation by means of the Eddington approximation. The non-adiabatic pulsation equations consist of the perturbed equation of motion and the perturbed continuity and energy equations. Here the energy equation includes contributions from radiation and convection transport mechanism.

We modify Houdek's equation to include radiative transfer equation as presented in Christensen-Dalsgaard & Frandsen (1983) and Medupe (2002). As for convection, we use a time-dependent, non-local mixing-length theory which introduces six equations. In total we need to solve ten pulsation equations by iteration since radiative transfer equation introduces one extra dependent variable. The whole system of equation is closed by means of variable Eddington factors (see Christensen-Dalsgaard & Frandsen 1983, Medupe 2002).

Thus the perturbed continuity equation and the perturbed equation of motion are as presented in Houdek (1996). It is the energy equations that I modify to include plane parallel radiative transfer in the atmosphere.

2.1 Radial pulsation equations

2.1.1 Continuity equation

The unperturbed continuity equation is given by:

$$\frac{dr}{dm} = \frac{1}{4\pi r^2 \rho}. \tag{2.1}$$

We perturb equation (2.1) by expressing radius and density as

$$r = r_0 + \delta r, \qquad \rho = \rho_0 + \delta\rho, \tag{2.2}$$

where subscript zero on radius (r_0) and density (ρ_0) denotes the equilibrium model quantities. Here δr and $\delta\rho$ are the Lagrangian radius and density perturbations respectively.
Replacing the radius and density in equation (2.1) by the perturbed values of (2.2) gives

$$(r_0+\delta r)^2(\rho_0+\delta\rho)\frac{d(r_0+\delta r)}{dm}=\frac{1}{4\pi}. \tag{2.3}$$

The equation (2.3) is linearised by keeping those terms that are of first order in δr and $\delta\rho$, and using the relation $r_0^2\rho_0 dr_0/dm = 1/4\pi$ yield

$$\frac{d\delta r}{dm}=-\frac{\delta\rho}{\rho_0}\frac{dr_0}{dm}-2\frac{\delta r}{r_0}\frac{dr_0}{dm}. \tag{2.4}$$

Applying the following relation to equation (2.4) we get:

$$\frac{d}{dm}\left(\frac{\delta r}{r_0}\right)=\frac{1}{r_0}\frac{d\delta r}{dm}-\frac{\delta r}{r_0^2}\frac{dr_0}{dm}, \tag{2.5}$$

and replacing dr_0/dm by $1/4\pi r_0^2\rho_0$ finally gives

$$\frac{d}{dm}\left(\frac{\delta r}{r_0}\right)=-\frac{1}{4\pi\rho_0 r_0^3}\left(\frac{\delta\rho}{\rho_0}+3\frac{\delta r}{r_0}\right). \tag{2.6}$$

Arising from the dependence of opacity and density on temperature and pressure the perturbed density can be defined as

$$\frac{\delta\rho}{\rho_0}=\alpha_0\frac{\delta p_g}{p_{g0}}-\delta_0\frac{\delta T}{T_0}, \tag{2.7}$$

where the derivatives α_0 is

$$\alpha_0=\left(\frac{\partial\ln\rho_0}{\partial\ln p_{g0}}\right)_{T_0}, \tag{2.8}$$

and the derivative δ_0 is the same as δ defined in equation (1.78).
The perturbed opacity is given by

$$\frac{\delta\kappa}{\kappa_0}=\kappa_T\frac{\delta T}{T_0}+\kappa_p\frac{\delta p_g}{p_{g0}}, \tag{2.9}$$

where the perturbed gas pressure is related to perturbed turbulent pressure as

$$\frac{\delta p_g}{p_{g0}}=\frac{1}{1-\nu_1}\left(\frac{\delta p}{p_0}-\frac{\delta p_t}{p_0}\right). \tag{2.10}$$

The ratio $\nu_1 = p_t/p_0$ gives a contribution of turbulent pressure to the total pressure, and the opacity derivatives κ_T and κ_p are given as

$$\kappa_T=\left(\frac{\partial\ln\kappa_0}{\partial\ln T_0}\right)_{p_{g0}}, \quad \text{and} \quad \kappa_p=\left(\frac{\partial\ln\kappa_0}{\partial\ln p_{g0}}\right)_{T_0}. \tag{2.11}$$

Inserting an expression for the perturbed density $\delta\rho/\rho_0$ into equation (2.6) results in

$$\frac{d}{dm}\left(\frac{\delta r}{r_0}\right) = -\frac{1}{4\pi\rho_0 r_0^3}\left[3\frac{\delta r}{r_0} + \frac{\alpha_0}{1-\nu_1}\left(\frac{\delta p}{p_0} - \frac{\delta p_t}{p_0}\right) - \delta_0\frac{\delta T}{T_0}\right]. \tag{2.12}$$

To make logarithm of pressure $\ln p_0$ the independent variable instead of radial mass m in equation (2.12), we use the pressure scale height H_p including turbulence

$$H_p = -\frac{dr_0}{d\ln p_0} = -\frac{p_0}{\rho_0 g_0}\tilde{\mu}, \tag{2.13}$$

where $\tilde{\mu}$ is explained in equation (1.74) to obtain:

$$\frac{d}{d\ln p_0}\left(\frac{\delta r}{r_0}\right) = \tilde{\mu}\frac{p_0 r_0}{Gm\rho_0}\left[3\frac{\delta r}{r_0} + \frac{\alpha_0}{1-\nu_1}\left(\frac{\delta p}{p_0} - \frac{\delta p_t}{p_0}\right) - \delta_0\frac{\delta T}{T_0}\right]. \tag{2.14}$$

2.1.2 Equation of motion

We perturb the left and right hand sides of equation (1.72) separately. Perturbing and linearising the left hand side of equation (1.72) we obtain

$$\rho_0 r_0\frac{d^2 r_0}{dt^2} + \rho_0\,\delta r\frac{d^2 r_0}{dt^2} + r_0\,\delta\rho\frac{d^2 r_0}{dt^2} + \rho_0 r_0\frac{d^2\delta r}{dt^2}. \tag{2.15}$$

The perturbed right hand side of the equation (1.72) results in:

$$\begin{aligned}-4\pi r_0^3\rho_0\left[\left(1+\frac{\delta\rho}{\rho_0}+3\frac{\delta r}{r_0}\right)\frac{dp_0}{dm}+\frac{d\delta p}{dm}\right] - (3-\Phi_0)\delta p_t + p_{t0}\delta\Phi \\ + \frac{Gm\rho_0}{r_0}\left(\frac{\delta r}{r_0}-\frac{\delta\rho}{\rho_0}\right) - (3-\Phi_0)p_{t0} - \rho_0\frac{Gm}{r_0}.\end{aligned} \tag{2.16}$$

To obtain the perturbed equation of motion we use the following procedure:

- We set two sides of equations (2.15) and (2.16) equal and assume that for the static equilibrium star all the time derivatives of equilibrium quantities are set to zero.
- Here the time evolution of perturbed quantities is assumed to be $\exp(i\omega t)$ where ω is the complex angular pulsation frequency $\omega = \omega_r + i\omega_i$.
- The following relation is applied

$$\frac{d\delta p}{dm} = p_0\frac{d}{dm}\left(\frac{\delta p}{p_0}\right) + \frac{\delta p}{p_0}\frac{dp_0}{dm}. \tag{2.17}$$

Applying above procedure and using the independent variable $\ln p_0$ to replace m yields:

$$\frac{d}{d\ln p_0}\left(\frac{\delta p}{p_0}\right) = -\frac{\delta p}{p_0} - \left[3+\tilde{\mu}\left(1+\frac{\omega^2}{\Omega^2}\right)\right]\frac{\delta r}{r_0} + \tilde{\mu}\frac{p_0 r_0}{Gm\rho_0}\frac{p_{t\,0}}{p_0}\times\left[(3-\Phi_0)\left(\frac{\delta p_t}{p_{t\,0}}-\frac{\delta\rho}{\rho_0}\right)-\delta\Phi\right]. \tag{2.18}$$

Inserting the perturbed equation of state (2.7) into equation (2.18) we obtain

$$\frac{d}{d\ln p_0}\left(\frac{\delta p}{p_0}\right) = -\frac{\delta p}{p_0} - \left[3+\tilde{\mu}\left(1+\frac{\omega^2}{\Omega^2}\right)\right]\frac{\delta r}{r_0} - \tilde{\mu}\nu_1\frac{p_0 r_0}{Gm\rho_0} \times\left\{(3-\Phi_0)\left[\delta_0\frac{\delta T}{T_0}-\frac{\alpha_0}{1-\nu_1}\left(\frac{\delta p}{p_0}-\frac{\delta p_t}{p_0}\right)+\frac{1}{\nu_1}\frac{\delta p_t}{p_0}\right]+\delta\Phi\right\}, \tag{2.19}$$

where

$$\Omega^2 = \frac{Gm}{r_0^3}. \tag{2.20}$$

2.1.3 Radiative transfer equation

Applying perturbations to equation (1.42) results in

$$\frac{d}{dm}\left(\frac{\delta K}{K_0}\right) = -\frac{\kappa_0 L_{r\,0}}{64\pi^3 r_0^4 K_0}\left(\frac{\delta L_r}{L_{r\,0}}+\frac{\delta\kappa}{\kappa_0}-4\frac{\delta r}{r_0}-\frac{\delta K}{K_0}\right). \tag{2.21}$$

After inserting an expression for the perturbed opacity $\delta\kappa/\kappa_0$ given in equation (2.9) and rearranging equation (2.21) to use independent variable $\ln p_0$ we get

$$\frac{d}{d\ln p_0}\left(\frac{\delta K}{K_0}\right) = \tilde{\mu}\frac{\kappa_0 p_0(1-f)L_0}{16\pi^2 Gm(f_{eq}J_0)}\left[\kappa_T\frac{\delta T}{T_0}+\frac{\kappa_p}{1-\nu_1}\left(\frac{\delta p}{p_0}-\frac{\delta p_t}{p_0}\right)-4\frac{\delta r}{r_0} - \frac{\delta K}{K_0}+\frac{1}{1-f}\left(\frac{\delta L}{L_0}-\frac{\delta L_c}{L_0}\right)\right], \tag{2.22}$$

where $f = L_c/L_0$ is the contribution of convective luminosity to the total luminosity. This is the new equation that I derived.

The equilibrium Eddington factor f_{eq} (Auer & Mihalas 1970) can be defined as

$$f_{eq} = \frac{K_0}{J_0}. \tag{2.23}$$

We perturb equation (1.41) to obtain the following equation

$$\frac{d\delta L_r}{dm} = 4\pi\kappa_0 B_0\left(4\frac{\delta T}{T_0}-\frac{\delta J}{B_0}\right)+4\pi(B_0-J_0)\delta\kappa. \tag{2.24}$$

Also the perturbed radiative transfer equation is

$$\mu\frac{d\delta I}{dm} = \frac{1}{4\pi r^2}\Big[\delta\kappa_{s0}J_0 + \delta\kappa_{a0}B_0 - (\delta\kappa_{s0} + \delta\kappa_{a0})I_0 + \kappa_{s0}\,\delta J + \kappa_{a0}\,\delta B - (\kappa_{s0} + \kappa_{a0})\delta I\Big], \tag{2.25}$$

where

$$\delta B = 4B_0\frac{\delta T}{T_0}, \tag{2.26}$$

is the perturbed Planck function.
Equation (2.22) which I derived will replace the following equation

$$\frac{d}{d\ln p_0}\left(\frac{\delta J}{J_0}\right) = \tilde{\mu}\frac{\kappa_0 p_0(1-f)L_0}{16\pi^2 Gm(f_{eq}J_0)}\left[\kappa_T\frac{\delta T}{T_0} + \frac{\kappa_p}{1-\nu_1}\left(\frac{\delta p}{p_0} - \frac{\delta p_t}{p_0}\right) - 4\frac{\delta r}{r_0} - \frac{\delta J}{J_0} + \frac{1}{1-f}\left(\frac{\delta L}{L_0} - \frac{\delta L_c}{L_0}\right)\right], \tag{2.27}$$

derived by Houdek (1996).
The moments of the perturbed transfer equation with respect to μ become:

$$\delta J = \frac{1}{2}\int_{-1}^{+1}\delta I\,d\mu, \tag{2.28}$$

$$\delta H = \frac{1}{2}\int_{-1}^{+1}\mu\delta I\,d\mu, \tag{2.29}$$

and

$$\delta K = \frac{1}{2}\int_{-1}^{+1}\mu^2\delta I\,d\mu. \tag{2.30}$$

2.1.4 The energy equation

The general energy equation is given by

$$\rho\,c_p\left(\frac{dT}{dt} - \nabla_{ad}\frac{T}{p_g}\frac{dp_g}{dt}\right) = \rho\,\epsilon - \mathrm{div}\,\mathbf{F}, \tag{2.31}$$

where the adiabatic temperature gradient ∇_{ad} defined in equation (1.13) is expressed as (see Kippenhahn & Weigert 1990):

$$\nabla_{ad} = \frac{\delta_0 p_g}{T\rho c_p}. \tag{2.32}$$

Using the fact that the energy generation rate per unit mass ϵ equals to zero in the stellar atmosphere and equation (2.32), we can write equation (2.31) as

$$c_p \frac{dT}{dt} - \frac{\delta}{\rho}\frac{dp_g}{dt} = -4\pi \frac{d}{dm}\left[r^2(F_r + F_c)\right], \tag{2.33}$$

where F_r is the radiative flux and F_c is the convective flux.

For a static envelope the term on the right hand side of equation (2.33) can be expressed in terms of total luminosity L by

$$4\pi r^2(F_r + F_c) = L. \tag{2.34}$$

Therefore inserting equation (2.34) into equation (2.33) the energy equation can be written as

$$c_p\left(\frac{dT}{dt} - \nabla_{ad}\frac{T}{p}\frac{dp_g}{dt}\right) = -\frac{dL}{dm}. \tag{2.35}$$

Note that with the static envelope the divergence of the total energy flux vanishes. Perturbing and linearising equation (2.35) we obtain

$$\frac{d}{dm}\left(\frac{\delta L}{L_0}\right) = -i\omega\frac{c_p T_0}{L_0}\left(\frac{\delta T}{T_0} - \nabla_{ad}\frac{\delta p_g}{p_{g0}}\right). \tag{2.36}$$

Using equations (2.10) and (2.32), and by making $\ln p_0$ the independent variable, equation (2.36) can be written as

$$\frac{d}{d\ln p_0}\left(\frac{\delta L}{L_0}\right) = i\omega\tilde{\mu}\frac{4\pi r_0^4 p_0}{Gm}\frac{p_0\delta_0}{\rho_0 L_0}\left(\frac{1-\nu_1}{\nabla_{ad}}\frac{\delta T}{T_0} - \frac{\delta p}{p_0} + \frac{\delta p_t}{p_0}\right). \tag{2.37}$$

2.1.5 Convection equations

The non-local mixing-length theory of convection yields three second-order, ordinary differential equations which we derived in section 1.4.3.

$$\frac{\alpha_c^2}{a^2}\frac{d^2 L_c}{d\ln p^2} = L_c - L_c^L, \tag{2.38}$$

$$\frac{\alpha_c^2}{a^2}\frac{d^2\bar{\beta}}{d\ln p^2} = \bar{\beta} - \beta, \tag{2.39}$$

$$\frac{\alpha_c^2}{a^2}\frac{d^2 p_t}{d\ln p^2} = p_t - p_t^L, \tag{2.40}$$

where

$$F_c^L = \frac{1}{4}\frac{\rho c_p \Phi T}{g\delta}\hat{\sigma}^3\ell_c^2, \tag{2.41}$$

and

$$p_t^L = \frac{1}{4}\rho\hat{\sigma}^2\ell_c^2, \tag{2.42}$$

are the turbulent heat and momentum flux from the local mixing length theory respectively and α_c is the mixing-length parameter. The superscript L indicate quantities obtained from local theory.

2.1.5.1 Convective luminosity equation

We first convert the second-order differential equation (2.38) into two first-order differential equations, namely

$$\frac{dL_c}{d\ln p} = z_L, \tag{2.43}$$

$$\frac{dz_L}{d\ln p} = \frac{a^2}{\alpha_c^2} L_c(1-\varphi_L), \tag{2.44}$$

where

$$\varphi_L = \frac{L_c^L}{L_c}, \tag{2.45}$$

is the ratio of local to non-local convective luminosity.
After applying perturbation to equation (2.43) we obtain

$$\frac{d\delta L_c}{dm} = \delta z_L \frac{d\ln p_0}{dm} + z_L \frac{d}{dm}\left(\frac{\delta p}{p_0}\right). \tag{2.46}$$

By multiplying each term of equation (2.46) by $dm/d\ln p_0$, and dividing each term by total luminosity L_0 we obtain

$$\frac{d}{d\ln p_0}\left(\frac{\delta L_c}{L_0}\right) = \frac{\delta z_L}{L_0} + \frac{z_L}{L_0}\frac{d}{d\ln p_0}\left(\frac{\delta p}{p_0}\right). \tag{2.47}$$

We apply perturbation to equation (2.44) to obtain

$$\frac{d}{dm}\left(\frac{\delta z_L}{L_0}\right) = \frac{a^2}{\alpha_c^2}\left[\frac{L_{c0}}{L_0}\left(1-\frac{L_{c0}^L}{L_{c0}}\right)\frac{d}{dm}\left(\frac{\delta p}{p_0}\right) + \frac{\delta L_c}{L_0}\frac{d\ln p_0}{dm} - \frac{\delta L_c^L}{L_0}\frac{d\ln p_0}{dm}\right]. \tag{2.48}$$

If we use $\ln p_0$ as the independent variable, replacing m, we obtain the following equation

$$\frac{d}{d\ln p_0}\left(\frac{\delta z_L}{L_0}\right) = \frac{a^2}{\alpha_c^2}\left[f_L(1-\varphi_L)\frac{d}{d\ln p_0}\left(\frac{\delta p}{p_0}\right) + \frac{\delta L_c}{L_0} - f_L\varphi_L\frac{\delta L_c{}^L}{L_{c0}}\right], \tag{2.49}$$

where

$$f_L = \frac{L_{c0}}{L_0}, \tag{2.50}$$

is the contribution of convective luminosity to the total luminosity.

2.1.5.2 Averaged superadiabatic lapse rate equation

We perturb equation (2.39) in a similar manner to equation (2.38) and obtain:

$$\frac{d}{d\ln p_0}\left(\frac{\delta\bar{\beta}}{\bar{\beta}_0^{osc}}\right) = \frac{z_\beta}{\bar{\beta}_0^{osc}}\frac{d}{d\ln p_0}\left(\frac{\delta p}{p_0}\right) + \frac{\delta z_\beta}{\bar{\beta}_0^{osc}}, \tag{2.51}$$

and

$$\frac{d}{d\ln p_0}\left(\frac{\delta z_\beta}{\bar{\beta}_0^{osc}}\right) = \frac{b^2}{\alpha_c^2}\left[f_\beta(1-\varphi_\beta)\frac{\partial}{\partial\ln p_0}\left(\frac{\delta p}{p_0}\right) + \frac{\delta\bar{\beta}}{\bar{\beta}_0^{osc}} - f_\beta\varphi_\beta\left(\frac{\delta\beta}{\beta_0}\right)\right], \tag{2.52}$$

where

$$\varphi_\beta = \frac{\beta_0}{\bar{\beta}_0}, \tag{2.53}$$

$$z_\beta = \frac{d\bar{\beta}_0}{d\ln p_0}, \tag{2.54}$$

and

$$f_\beta = \frac{\bar{\beta}_0}{\bar{\beta}_0^{osc}}. \tag{2.55}$$

The constant value $\bar{\beta}_0^{osc}$ is defined as

$$\bar{\beta}_0^{osc} = \mathrm{Max}[\bar{\beta}_0(p)] - \mathrm{Min}[\bar{\beta}_0(p)], \tag{2.56}$$

which denotes the peak to peak amplitude of the averaged superadiabatic lapse rate.

2.1.5.3 Turbulent Pressure equation

Here the turbulent pressure given by equation (2.40) is perturbed like equations (2.38) and (2.39) to obtain

$$\frac{d}{d\ln p_0}\left(\frac{\delta p_t}{p_0}\right) = \frac{\delta z_t}{p_0} - \frac{\delta p_t}{p_0} + \frac{z_t}{p_0}\frac{d}{d\ln p_0}\left(\frac{\delta p}{p_0}\right), \tag{2.57}$$

and

$$\frac{d}{d\ln p_0}\left(\frac{\delta z_t}{p_0}\right) = \frac{a^2}{\alpha_c^2}\left[\nu_1(1-\varphi_t)\frac{d}{d\ln p_0}\left(\frac{\delta p}{p_0}\right) + \frac{\delta p_t}{p_0} - \nu_1\varphi_t\frac{\delta p_t}{p_{t\,0}}^L\right] - \frac{\delta z_t}{p_0}, \tag{2.58}$$

where

$$z_t = \frac{dp_{t0}}{d\ln p_0}, \tag{2.59}$$

$$\nu_1 = \frac{p_{t0}}{p_0}, \tag{2.60}$$

and

$$\varphi_t = \frac{p_{t0}^L}{p_{t0}}, \tag{2.61}$$

is the ratio of local to non-local turbulent pressure.

2.1.6 The Temperature eigenfunction

To obtain an expression for the temperature eigenfunction $\delta T/T_0$ we use the constraint

$$\frac{\delta L}{L_0} = \frac{\delta L_c}{L_0} + \frac{\delta L_r}{L_0}, \tag{2.62}$$

where L_r and L_c are the radiative luminosity and convective luminosity respectively.
We substitute the energy equation, the radiative and convective luminosity equations (2.24), (2.37) and (2.47) into the following relation

$$\frac{d}{dm}\left(\frac{\delta L}{L_0}\right) = \frac{d}{dm}\left(\frac{\delta L_r}{L_0}\right) + \frac{d}{dm}\left(\frac{\delta L_c}{L_0}\right), \tag{2.63}$$

derived from equation (2.62) to yield

$$\left[4 + i\frac{\omega}{\omega_R}\frac{(1-\nu_1)}{\nabla_{ad}} + \left(1 - \frac{J_0}{B_0}\right)\kappa_T\right]\frac{\delta T}{T_0} = \frac{J_0}{B_0}\frac{\delta J}{J_0} - \frac{\kappa_p}{1-\nu_1}\left(1 - \frac{J_0}{B_0}\right)\left(\frac{\delta p}{p_0} - \frac{\delta p_t}{p_0}\right)$$
$$+ i\frac{\omega}{\omega_R}\left(\frac{\delta p}{p_0} - \frac{\delta p_t}{p_0}\right) + \left(1 - \frac{J_0}{B_0}\right)\left[\frac{\delta z_L}{z_L} - \left(4 + \frac{\omega^2}{\Omega^2}\right)\frac{\delta r}{r_0} - \frac{\delta p}{p_0}\right], \tag{2.64}$$

where

$$\omega_R = \frac{4\pi\kappa_0 B_0}{c_{p0}T_0}\frac{1-\nu_1}{\nabla_{ad}}, \tag{2.65}$$

is the radiative relaxation rate.
If there is no convection and turbulence then equation (2.64) becomes

$$\left[4 + i\frac{\omega}{\omega_R}\frac{1}{\nabla_{ad}} + \left(1 - \frac{J_0}{B_0}\right)\kappa_T\right]\frac{\delta T}{T_0} = \frac{J_0}{B_0}\frac{\delta J}{J_0} + \left[i\frac{\omega}{\omega_R} - \kappa_p\left(1 - \frac{J_0}{B_0}\right)\right]\frac{\delta p}{p_0}. \tag{2.66}$$

The difference between equation (2.66) and equation (2.32) of Christensen-Dalsgaard & Frandsen (1983) as well as equation (4.81) of Medupe (2002) is that there is no ρ_T and ρ_P in our

equation (Eq. 2.66). This is because in deriving equation (2.64) we have used equation of motion (Eq. B.2), which does not contain δ_0 and α_0, instead of Eq. (B.18). Equation (B.18) contains δ_0 and α_0 which can be related to ρ_T and ρ_p respectively. Since ω_R increases with depth, the areas where ω/ω_R is so small as to be ignored (such as in the envelope where $J_0 = B_0$) will have $\delta T/T_0$ and $\delta J/J_0$ related as (see Medupe 2002):

$$\frac{\delta J}{J_0} = 4\frac{\delta T}{T_0}. \tag{2.67}$$

The pulsation equations described in this chapter are listed in Appendix B.

2.1.7 The scheme used to solve the pulsation equations

The transfer equations (1.32) and (2.25) are solved using the Feautrier method (see Medupe 2002). This method is described in Appendix C.

These pulsation equations form a system of ten equations with eleven dependent variables. We can solve this problem only if we can relate one of the variables with another one thereby closing the system of equations. We relate $\delta K/K_0$ and $\delta J/J_0$ by the variable Eddington factor

$$f_{osc} = \frac{\delta K}{\delta J}. \tag{2.68}$$

If the value of f_{osc} was known beforehand the system could be closed. But since this is not the case we determine f_{osc} by iteration, the initial value of f_{osc} being J/K. To solve this system of equation we used the formalism suggested by Christensen-Dalsgaard & Frandsen (1983). The method was later used by Medupe (2002). The formalism is applied as follows:

1. Make initial guess of $f_{osc} = f_{eq}$ where f_{eq} is the equilibrium Eddington factor defined in equation (2.23).

2. These equations are solved by replacing $\delta J/J_0$ in equation (2.64) by

$$\frac{f_{eq}}{f_{osc}}\frac{\delta K}{K_0}, \tag{2.69}$$

   for the first iteration.

3. We obtain $\delta\kappa$ and δB from $\delta T/T_0$ and $\delta P/P_0$ calculated in step 2 using equations (2.9) and (2.26). Then δI is obtained by integrating equation (2.25).

4. Compute δJ and δK using equations (2.28) and (2.30) respectively and then obtain f_{osc}.

5. If f_{osc} has not converged go to item 2.

2.1.8 Boundary conditions for pulsation equations

The above system of equations has been reduced to ten equations with ten dependent variables, therefore ten boundary conditions are needed.

2.1.8.1 The Thermal boundary condition

Houdek (1996) used the following boundary condition at the surface

$$\frac{\delta L}{L_0} = 2\left(1+\frac{\tau_0}{\tau_0+\frac{2}{3}}\right)\frac{\delta r}{r_0}+\left(4-\frac{\tau_0}{\tau_0+\frac{2}{3}}\kappa_T\right)\frac{\delta T}{T_0}-\left(\frac{\tau_0}{\tau_0+\frac{2}{3}}\right)\kappa_p\frac{\delta p}{p_0}. \tag{2.70}$$

He obtained this equation by perturbing the temperature-optical depth relation:

$$T^4=\frac{3}{4}T_{eff}^4[\tau_0+q(\tau)]. \tag{2.71}$$

where T_{eff} is the effective temperature and $q(\tau)$ is the Hopf function (in Eddington approximation $q(\tau)=2/3$). But because we consider the stellar atmosphere in detail, we need to use boundary condition that there is no incoming radiation at the surface (see Christensen-Dalsgaard & Frandsen 1983 and Medupe 2002). In terms of Eddington factors g_{osc} that condition can be expressed as

$$\delta H = g_{osc}\delta J \quad \text{at the surface,} \tag{2.72}$$

where g_{osc} is calculated from the iteration for f_{osc}, with initial estimate of $g_{osc}=g_{eq}=H_0/J_0$. According to equation (1.38), at the surface where there is no convection the Eddington flux H_0 can be related to total luminosity L_0 by

$$H_0=\frac{L_0}{16\pi^2 r_0^2}. \tag{2.73}$$

Applying perturbation to equation (2.73) we obtain

$$\frac{\delta H}{H_0}+2\frac{\delta r}{r_0}=\frac{1}{16\pi^2 r_0^2}\frac{\delta L}{H_0}. \tag{2.74}$$

We use equations (2.72) and (2.74) to get

$$\frac{\delta L}{L_0}=\frac{g_{osc}}{g_{eq}}\frac{\delta J}{J_0}+2\frac{\delta r}{r_0}, \tag{2.75}$$

Unfortunately for now we do not implement this condition in our code because the atmosphere of the equilibrium models we are using at the moment is inconsistent with the radiative transfer (see §3.2). Once this inconsistency is resolved we will implement the boundary condition (Eq. 2.75).

2.1.8.2 The Mechanical Boundary Condition

To obtain the mechanical boundary condition at the surface we imposed the oscillations in the stellar atmosphere to be adiabatic. This is done even though there are indications from the eigenfunctions that the oscillations are far from adiabatic at outermost mesh point in the current models. This is a problem that still need to be fixed, see Medupe et al. (in preparation). In the adiabatic case it is assumed that the mass elements in the star neither gain nor lose heat, i.e., the entropy s remains constant. The eigenfrequency ω is real only if the oscillations are adiabatic everywhere. The equation of state for adiabatic case can be written as

$$\frac{\delta p_g}{p_{g0}} = \Gamma_1 \frac{\delta \rho}{\rho_0}. \tag{2.76}$$

We use the adiabatic pulsation equations to obtain the mechanical boundary condition. Here the atmosphere is assumed to be isothermal near $\tau = 0$, (See Baker & Kippenhahn 1965; Houdek 1996; Christensen-Dalsgaard 2003; Medupe 2002). The linear adiabatic pulsation equations are obtained by perturbing the continuity equation (2.1) and equation of motion (1.24), and by using the equation (2.76). The adiabatic pulsation equations become

$$\frac{d}{dr}\left(\frac{\delta r}{r_0}\right) = -\frac{1}{r_0}\left(3\frac{\delta r}{r_0} + \frac{1}{\Gamma_1}\frac{\delta p}{p_0}\right), \tag{2.77}$$

and

$$\frac{d}{dr}\left(\frac{\delta p}{p_0}\right) = \frac{1}{H_p}\left[\frac{\delta p}{p_0} + \left(4 + \frac{\omega^2}{\Omega^2}\right)\frac{\delta r}{r_0}\right]. \tag{2.78}$$

Substituting equation (2.78) into equation (2.77) we obtain a single second–order differential equation

$$\frac{d^2x}{dr_0^2} + \left(\frac{4}{r_0} - \frac{1}{H_p}\right)\frac{dx}{dr_0} + \frac{1}{r_0 H_p}\left[\frac{1}{\Gamma_1}\left(4 + \frac{\omega^2}{\Omega^2}\right) - 3\right]x = 0, \tag{2.79}$$

where $x = \delta r/r_0$ and H_p is the pressure scale height.
By using the relation between sound speed, pressure and density:

$$c_s^2 = \frac{\Gamma_1 p_0}{\rho_0}, \tag{2.80}$$

and the definition of the acoustic cut-off frequency

$$\omega_{ac} = \frac{c_s}{2H_p}, \tag{2.81}$$

equation (2.79) can be written as

$$\frac{d^2x}{dr_0^2} + \left(\frac{4}{r_0} - \frac{1}{H_p}\right)\frac{dx}{dr_0} + \left[\frac{1}{H_p\Gamma_1}\left(\frac{4}{r_0} - \frac{3\Gamma_1}{r_0}\right) + \frac{1}{4H_p^2}\frac{\omega^2}{\omega_{ac}}\right]x = 0. \tag{2.82}$$

We assume the thickness of the atmosphere to be small as compared to the radius of the star. Therefore the gravitational acceleration g is taken to be constant throughout the atmosphere. Applying the assumption that $r_0 \gg H_p$ everywhere in the atmosphere we neglect the terms in $4/r_0$ and $3\Gamma_1/r_0$ to express equation (2.82) as

$$\frac{dx^2}{dr_0^2} - \frac{1}{H_p}\frac{dx}{dr_0} + \frac{1}{4H_p^2}\frac{\omega^2}{\omega_{ac}^2} = 0. \tag{2.83}$$

The general solution of equation (2.83) is

$$x(r_0) = C_1 \exp\left(\frac{r_0}{H_p}\lambda_+\right) + C_2 \exp\left(\frac{r_0}{H_p}\lambda_-\right), \tag{2.84}$$

where

$$\lambda_\pm = \frac{1}{2} \pm \frac{1}{2}\left(1 - \frac{\omega^2}{\omega_{ac}^2}\right)^{1/2}, \tag{2.85}$$

and C_1 and C_2 are constant coefficients.

We fix one of the constant C_1 and C_2 by considering energy density in the stellar atmosphere. The energy density is expected to approach zero as r_0 tends to infinity. The energy density (or pulsational energy) is proportional to $\rho_0 \delta r^2$, and is given as

$$\rho_0\, \delta r^2 \sim \exp\left[\pm\left(1 - \frac{\omega^2}{\omega_{ac}^2}\right)^{1/2} \frac{r_0}{H_p}\right]. \tag{2.86}$$

Therefore for $\omega < \omega_{ac}$ the solution with λ_- is acceptable as the energy decreases exponentially. Hence we set $C_1 = 0$ and equation (2.84) is written as

$$x(r) = C_2 \exp\left(\frac{r}{H_p}\lambda_-\right). \tag{2.87}$$

Inserting equation (2.87) into equation (2.77) the mechanical boundary condition at the surface becomes

$$\frac{\delta p}{p_0} = -\frac{\Gamma_1 R}{H_p}\lambda_- \frac{\delta r}{r_0}, \tag{2.88}$$

where R is the radius of the star at the temperature minimum.
This condition is like the reflective mechanical boundary

$$\frac{\delta p}{p_0} = -(4 + 3\sigma_d^2)\frac{\delta r}{r_0}, \tag{2.89}$$

derived by Baker & Kippenhahn (1965).
For $\omega > \omega_{ac}$, the solution with λ_+ is the acceptable solution since this requires the waves to propagate through the atmosphere. Therefore the boundary condition can be written as

$$\frac{\delta p}{p_0} = -\frac{\Gamma_1 R}{H_p}\lambda_+ \frac{\delta r}{r_0}, \tag{2.90}$$

where

$$\lambda_+ = \frac{1}{2} + \frac{1}{2}i\left(\frac{\omega^2}{\omega_{ac}^2} - 1\right)^{1/2}. \tag{2.91}$$

The two boundary conditions (equations 2.88 and 2.90) can be expressed as:

$$\frac{\delta p}{p_0} = -\frac{\Gamma_1 R}{H_p}\lambda_{\pm}\frac{\delta r}{r_0}. \tag{2.92}$$

2.1.8.3 Normalisation of displacement

The normalisation condition on the displacement $\delta r/r_0$ set as follows

$$\frac{\delta r}{r_0} = 1. \tag{2.93}$$

is applied at the surface.

2.1.8.4 At the base of the envelope

We require the oscillations to be adiabatic at the base of the envelope. Thus we require

$$\frac{\delta T}{T} - \nabla_{ad}\frac{\delta p}{p} = 0. \tag{2.94}$$

2.1.8.5 Boundary conditions resulting from non-local mixing-length theory

For the bubble to continue rising the temperature difference between the bubble and the surroundings should be positive.

- At the upper part of the convection zone which is beyond the convectively unstable zone the temperature difference will decrease. As a result the velocity of the bubble will decrease to zero. The local convective and turbulent fluxes will be zero there too.

- At the lower part of the convection zone which is below the convective unstable zone the temperature difference is almost zero. Therefore the local convective and turbulent fluxes will be zero.

This means the local source functions F_c^L and p_t^L are set to zero to derive the boundary conditions.

2.1.8.6 Convective flux

In this case the quantity φ_L defined in equation (2.45) is set to be zero. Therefore the equations (2.47) and (2.49) are reduced to

$$\frac{d}{d\ln p_0}\left(\frac{\delta L_c}{L_0}\right) = \frac{\delta z_L}{L_0} + \frac{z_L}{L_0}\frac{d}{d\ln p_0}\left(\frac{\delta p}{p_0}\right), \tag{2.95}$$

and

$$\frac{d}{d\ln p_0}\left(\frac{\delta z_L}{L_0}\right) = \frac{a^2}{\alpha_c^2}\left[f_L\frac{d}{d\ln p_0}\left(\frac{\delta p}{p_0}\right) + \frac{\delta L_c}{L_0}\right]. \tag{2.96}$$

Using the definition of f_L given as

$$f_L = \frac{L_c}{L_0}, \tag{2.97}$$

we obtain

$$\frac{df_L}{d\ln p_0} = \frac{d}{d\ln p_0}\left(\frac{L_c}{L_0}\right) = \frac{z_L}{L_0}. \tag{2.98}$$

If we take the second derivative of f_L with respect to $\ln p_0$ in equation (2.98), and using equation (2.44) then

$$\frac{d^2 f_L}{d\ln p_0^2} = \frac{a^2}{\alpha_c^2} f_L. \tag{2.99}$$

The general solution to second–order differential equation (2.99) is given by

$$f_L = A\,\exp\left(\frac{a}{\alpha_c}\ln p_0\right) + B\,\exp\left(-\frac{a}{\alpha_c}\ln p_0\right). \tag{2.100}$$

Above the convection zone $\ln p$ is decreasing outwards implying

$$f_L \propto \exp\left(\frac{a}{\alpha_c}\ln p_0\right), \tag{2.101}$$

and below it $\ln p$ increases outwards implying that

$$f_L \propto \exp\left(-\frac{a}{\alpha_c}\ln p_0\right). \tag{2.102}$$

We let

$$\lambda = \pm a/\alpha_c, \tag{2.103}$$

and thus

$$\lambda f_L = z_L/L_0, \tag{2.104}$$

where $+a/\alpha_c$ is above the convective zone and $-a/\alpha_c$ below the convective zone.
Hence we substitute equation (2.103) into equations (2.95) and (2.96) respectively to obtain

$$\frac{d}{d\ln p_0}\left(\frac{\delta L_c}{L_0}\right) = \frac{\delta z_L}{L_0} + \lambda f_L \frac{d}{d\ln p_0}\left(\frac{\delta p}{p_0}\right) \tag{2.105}$$

$$= \left(\frac{\delta z_L}{L_0} - \lambda^2 f_L \frac{\delta p}{p_0}\right) + \frac{d}{d\ln p_0}\left(\lambda f_L \frac{\delta p_0}{p_0}\right), \tag{2.106}$$

and

$$\frac{d}{d\ln p_0}\left(\frac{\delta z_L}{L_0}\right) = \lambda^2 f_L \frac{d}{d\ln p_0}\left(\frac{\delta p}{p_0}\right) + \lambda^2 \frac{\delta L_c}{L_0} \tag{2.107}$$

$$= \lambda^2\left(\frac{\delta L_c}{L_0} - \lambda f_L \frac{\delta p}{p_0}\right) + \frac{d}{d\ln p_0}\left(\lambda^2 f_L \frac{\delta p}{p_0}\right). \tag{2.108}$$

Differentiating equation (2.106) with respect to $\ln p$ we get

$$\frac{d^2}{d\ln p^2}\left(\frac{\delta L_c}{L_0} - \lambda f_L \frac{\delta p}{p_0}\right) = \frac{d}{d\ln p_0}\left(\frac{\delta z_L}{L_0} - \lambda^2 f_L \frac{\delta p}{p_0}\right). \tag{2.109}$$

We rearrange equation (2.106) to yield

$$\frac{d^2}{d\ln p_0^2}\left(\frac{\delta L_c}{L_0} - \lambda f_L \frac{\delta p}{p_0}\right) = \lambda^2\left(\frac{\delta L_c}{L_0} - \lambda f_L \frac{\delta p}{p_0}\right). \tag{2.110}$$

Solving second-order differential equation (2.110) we obtain

$$\frac{\delta L_c}{L_0} = A\,\exp(\lambda \ln p_0) + B\,\exp(-\lambda \ln p_0) + \lambda f_L \frac{\delta p}{p_0}. \tag{2.111}$$

Therefore making $\delta z_L/L_0$ the subject of the formula in equation (2.106) yields

$$\frac{\delta z_L}{L_0} = \lambda A\,\exp(\lambda \ln p_0) + \lambda B\,\exp(-\lambda \ln p_0) + \lambda^2 f_L \frac{\delta p}{p_0}. \tag{2.112}$$

Hence relating two solutions (2.111) and (2.114) we have

$$\frac{a}{\alpha_c}\frac{\delta L_c}{L_0} = \pm\frac{d}{d\ln p_0}\left(\frac{\delta L_c}{L_0}\right). \tag{2.113}$$

The boundary condition at the upper part of the convective zone is given as

$$\frac{a}{\alpha_c}\frac{\delta L_c}{L_0} = \frac{d}{d\ln p_0}\left(\frac{\delta L_c}{L_0}\right), \tag{2.114}$$

and at the lower boundary of the convective zone we obtain

$$\frac{a}{\alpha_c}\frac{\delta L_c}{L_0} = -\frac{d}{d\ln p_0}\left(\frac{\delta L_c}{L_0}\right). \tag{2.115}$$

2.1.8.7 Turbulent pressure

Here we set φ_t defined in equation (2.61) to be zero at the boundaries of convection zone. Equations (2.57) and (2.58) can be reduced to

$$\frac{d}{d\ln p_0}\left(\frac{\delta p_t}{p_0}\right) = \frac{\delta z_t}{p_0} - \frac{\delta p_t}{p_0} + \frac{z_t}{p_0}\frac{d}{d\ln p}\left(\frac{\delta p}{p_0}\right). \tag{2.116}$$

and

$$\frac{d}{d\ln p_0}\left(\frac{\delta z_t}{p_0}\right) = \frac{a^2}{\alpha_c^2}\left[\nu_1\frac{d}{d\ln p_0}\left(\frac{\delta p}{p_0}\right) + \frac{\delta p_t}{p_0}\right] - \frac{\delta z_t}{p_0}. \tag{2.117}$$

We multiply both sides of equations (2.116) and (2.117) by the integrating factor $\exp(\ln p_0)$ to obtain

$$\frac{d}{d\ln p_0}\left[\exp(\ln p_0)\frac{\delta p_t}{p_0}\right] = \exp(\ln p_0)\frac{\delta z_t}{p_0} + z_t\frac{d}{d\ln p_0}\left(\frac{\delta p}{p_0}\right). \tag{2.118}$$

and

$$\frac{d}{d\ln p_0}\left[\exp(\ln p_0)\frac{\delta z_t}{p_0}\right] = \frac{a^2}{\alpha_c^2}\left[\exp(\ln p_0)\frac{\delta p_t}{p_0} + p_{t0}\frac{d}{d\ln p_0}\left(\frac{\delta p}{p_0}\right)\right]. \tag{2.119}$$

For the mean state solution we have

$$p_t \propto \exp(\lambda \ln p_0). \tag{2.120}$$

Using the relation (2.120) into equations (2.118) and (2.119) produce

$$\frac{d}{d\ln p_0}\left[\exp(\ln p_0)\frac{\delta p_{t0}}{p_0} - \lambda p_{t0}\frac{\delta p}{p_0}\right] = \exp(\ln p_0)\frac{\delta z_t}{p_0} - \lambda^2 p_{t0}\frac{\delta p}{p_0}, \tag{2.121}$$

and

$$\frac{d}{d\ln p_0}\left[\exp(\ln p_0)\frac{\delta z_t}{p_0} - \lambda^2 p_{t0}\frac{\delta p}{p_0}\right] = \lambda^2\left[\exp(\ln p_0)\frac{\delta p_t}{p_0} - \lambda p_{t0}\frac{\delta p}{p_0}\right]. \tag{2.122}$$

We differentiate equation (2.121) with respect to $\ln p_0$ to obtain

$$\frac{d^2}{d\ln p_0^2}\left[\exp(\ln p_0)\frac{\delta p_t}{p_0} - \lambda p_t\frac{\delta p}{p_0}\right] = \tag{2.123}$$

$$= \frac{d}{d\ln p_0}\left[\exp(\ln p_0)\frac{\delta z_t}{p_0} - \lambda^2 p_t\frac{\delta p}{p_0}\right], \tag{2.124}$$

$$= \lambda^2\left[\exp(\ln p_0)\frac{\delta p_t}{p_0} - \lambda p_t\frac{\delta p}{p_0}\right]. \tag{2.125}$$

The general solution of equation (2.125) can be written as

$$\frac{\delta p_t}{p_0} = [A\exp(\lambda\ln p_0) + B\exp(-\lambda\ln p_0)] + \exp(-\ln p_0) + \lambda\nu_1\frac{\delta p}{p_0}. \tag{2.126}$$

We substitute equation (2.126) into equation (2.118) to yield

$$\frac{\delta z_t}{p_0} = [\frac{a}{\alpha_c} A \exp(\ln p_0) - \lambda B] \exp(-\ln p_0) + \lambda^2 \nu_1 \frac{\delta p}{p_0}. \tag{2.127}$$

Thus again we have the following condition

$$\frac{a}{\alpha_c} \frac{\delta p_t}{p_0} = \pm \frac{d}{d \ln p_0} \left(\frac{\delta p_t}{p_0} \right). \tag{2.128}$$

2.1.8.8 Superadiabatic lapse rate

At the upper and lower boundaries of the convection zone the average superadiabatic temperature gradient will be the same as the local superadiabatic temperature gradient at those boundaries.Therefore the boundary conditions can be obtained from the requirement

$$\delta \bar{\beta} = \delta \beta, \tag{2.129}$$

above and below the convective instability region.

2.1.9 Eigenfrequencies

Any value of the complex eigenfrequency ω can determine the solution of the problem defined in section 2.2. We look for a standing wave solution by forcing the no displacement condition, $\delta r / r_0 = 0$ near the inner boundary of our equilibrium model. This becomes an eigenvalue problem. However our equilibrium model does not extend to the center therefore we impose the additional boundary condition at the bottom of the envelope. We shall take the condition that the displacement vanishes at the base of the envelope, i.e.

$$\frac{\delta r}{r} = 0 \quad \text{at} \quad r = r_b. \tag{2.130}$$

We then search for values of ω that makes the above condition true

An alternative condition that can be imposed at the bottom of the envelope is that part of the star interior to the base point of the model perform no work on the part above that point, i.e.

$$Im(\delta r^* \delta p) = 0 \quad \text{at} \quad r = r_b, \tag{2.131}$$

where a (*) denotes a complex conjugate. In this case we regard the real part ω_r of ω as a continuous variable and iterate just for the imaginary part ω_i of ω that makes condition at equation (2.131) satisfied. For the detailed description see Christensen-Dalsgaard & Frandsen (1983) and Medupe (2002).

A second-order Newton-Raphson-Kantorovich algorithm (Baker, Moore & Spiegel 1971) is used to solve the system of equations with the boundary conditions.

2.2 Work Integral

The work integral, W, is an important tool for investigating the location of excitation or damping in a star. We derive the work integrals by considering the gaseous sphere of volume V. We also use the equation of motion (1.72). This done in the same way as in Baker & Gough (1979). The equations are:

$$\rho r\frac{d^2r}{dt^2} = -4\pi r^3\rho\frac{dp}{dm} - (3-\Phi)p_t - \frac{Gm}{r}\rho, \tag{2.132}$$

and

$$\frac{dV}{dm} = \frac{1}{\rho}, \tag{2.133}$$

where $V = 4\pi r^3/3$ is the volume of the sphere.
Equations (2.132) and (2.133) are linearised to obtain

$$\left[\omega^2 + 4\frac{Gm}{r_0^3} + 3(3-\Phi_0)\frac{p_{t0}}{\rho r_0^2}\right]\delta r = 4\pi r_0^2\rho_0\frac{d\delta p}{dm} + (3-\Phi_0)\frac{\delta p_t}{\rho_0 r_0^2} - \frac{p_{t0}}{\rho_0 r_0}\delta\Phi - (3-\Phi_0)\frac{p_{t0}}{\rho_0^2}\delta\rho, \tag{2.134}$$

and

$$\frac{d\delta V}{dm} = -\frac{\delta\rho}{\rho_0^2}. \tag{2.135}$$

The equation (2.134) is multiplied by δr^* and then the relation $\delta V = 4\pi r_0^2\delta r$ is used. The asterisk, "*" denotes complex conjugate. We substitute equation (2.135) into the right hand side of the resulting equation to obtain

$$\left[\omega^2 + 4\frac{Gm}{r_0^3} + 3(3-\Phi_0)\frac{p_{t0}}{\rho r_0^2}\right]|\delta r|^2 = \frac{d}{dm}(\delta V^*\delta p) + \frac{\delta\rho^*\delta p}{\rho_0^2} + (3-\Phi_0)\frac{\delta p_t}{\rho_0 r_0}\delta r^* - \frac{p_t}{\rho_0 r_0}\delta\Phi\delta r^* - (3-\Phi_0)\frac{p_{t0}}{\rho_0^2 r_0}\delta\rho\delta r^*. \tag{2.136}$$

Taking the imaginary part of this expression and after some rearrangements we obtain

$$4\pi\frac{\omega_i}{\omega_r}\left(\frac{1}{2}\omega_r^2 r_0^2|r_1|^2\right) = -\pi\left\{\frac{d}{dm}\left[4\pi^2 p_0 r_0^3 Im(p_1^* r_1)\right] + \frac{p_0}{\rho_0}\mathrm{Im}(p_1 * \rho_1)\right\} + \pi\frac{p_{t0}}{\rho_0}\left\{(3-\Phi_0)[\mathrm{Im}(p_{t1}r_1^*) - \mathrm{Im}(\rho_1 r_1^*)] - \Phi_0\mathrm{Im}(\Phi_1 r_1^*)\right\}. \tag{2.137}$$

where

$$\delta r = r_0 r_1, \quad \delta p = p_0 p_1, \quad \delta V = V_0 V_1,$$
$$\delta\rho = \rho_0\rho_1, \quad \delta\Phi = \Phi_0\Phi_1, \quad \delta p_t = p_{t0}p_{t1}, \tag{2.138}$$

and ω_r and ω_i are real and imaginary parts of angular frequency ω, respectively. Left hand side of equation (2.137) is the kinetic energy of unit mass. The second term on the right hand side of equation (2.137) can be expanded in terms of gas pressure and turbulent pressure as follows:

$$\frac{p_0}{\rho_0}\mathrm{Im}(p_1^*\rho_1) = \frac{1}{\rho_0^2}\mathrm{Im}(\delta p_g^*\delta\rho) + \frac{1}{\rho_0^2}\mathrm{Im}(\delta p_t^*\delta\rho). \tag{2.139}$$

Integrating equation (2.137) from the bottom of the envelope ($m = m_b$) to the surface ($m = M$) we obtain

$$\frac{4\pi\eta E_k}{\omega_r} = F + [W_g(M) + W_t(M)], \tag{2.140}$$

where

$$W_g(M) = \pi\int_{m_b}^{M}\mathrm{Im}(\delta p_g^*\delta\rho)\frac{dm}{\rho_0^2}, \tag{2.141}$$

$$W_t(M) = \pi\int_{m_b}^{M}\mathrm{Im}(\delta p_t^*\delta\rho)\frac{dm}{\rho_0^2} + \pi\int_{m_b}^{M}\left\{(3-\Phi_0)\left[\mathrm{Im}(\delta r^*\delta p_t) - \frac{p_{t0}}{\rho_0}\mathrm{Im}(\delta r^*\delta\rho)\right] - p_t\mathrm{Im}(\delta r^*\delta\Phi)\right\}\frac{dm}{\rho_0 r_0}, \tag{2.142}$$

and

$$F = \frac{\omega_r[4\pi^2 r_0^2\mathrm{Im}(\delta p^*\delta r)]_{m_b}^{M}}{4\pi E_k}. \tag{2.143}$$

The kinetic energy of the oscillations (E_k) is defined as

$$E_k = \frac{1}{2}\omega_r^2\int_{m_b}^{M}|\delta r|^2 dm. \tag{2.144}$$

The integrals W_g and W_t are the work performed by the gas pressure perturbations and the turbulent pressure variations respectively.

Equation (2.140) may be written as

$$\eta = \eta_s + W_{tot}(M), \tag{2.145}$$

where $\eta = -\omega_i$ and η_s

$$\eta_s = \frac{\omega_r F}{4\pi E_k}, \tag{2.146}$$

gives the surface losses, and

$$W_{tot}(M) = \omega_r\frac{[W_t(M) + W_g(M)]}{4\pi E_k}, \tag{2.147}$$

is the normalized work integral.

2.3 Description of the code

In this section we describe the code that solves the non-adiabatic radial pulsation equations presented in Section 2.2. To solve those pulsation equations the following three steps are performed:

1. the linear adiabatic pulsation equations (see Appendix B) are solved to provide trial solution for the next step,

2. then the linear non-adiabatic pulsation equations using local mixing-length theory of convection (see Appendix B) are solved to provide a trial solution for the next step,

3. the non-adiabatic pulsation equations using non-local mixing-length theory of convection (see Section 2.2) are then solved.

Chapter 3

Results for Pulsation Equations

In this chapter I present the solutions to the non-adiabatic pulsation equations presented in chapter 2. The code used to obtain the solutions presented here includes non-local theory of convection and consistent treatment of radiation (i.e no Eddington approximation used). First I describe how the equilibrium models were constructed followed by tests to show that the code works. I then present eigenfunctions at various pulsation frequencies for different stellar masses. In addition, the iterated variable Eddington factors, growth rates and work integrals are presented.

3.1 Equilibrium models

The equilibrium models used were kindly provided by Guenter Houdek, and are described in detail by Balmforth & Gough (1990a), Balmforth (1992a) and Houdek (1996). All the equilibrium models listed in table 3.1 are characterized by non-local convection parameters $a^2 = b^2 = 300$ except for the Sun which is $a^2 = b^2 = 600$ and mixing-length parameter $\alpha_c = 2.0$. They all have solar chemical composition $X = 0.7$, $Y = 0.28$ and $Z = 0.02$ where X is the hydrogen mass fraction, Y the helium mass fraction and Z the mass fraction of metals. To generate these models, the stellar mass, luminosity and effective temperature were specified. A preliminary integration proceed inwards from an optical depth of $\tau \quad 10^{-4}$ and end at a radius fraction 0.2.

The convective layers are treated with local mixing length theory in this initial integration. Thereafter, the model was then re-integrated using the non-local mixing-length theory and the Eddington approximation to radiative transfer. In the atmosphere an Eddington factor is used to correct the thermal stratification of the optically thin layers. The optical depth dependent Eddington factor derived from model C of Vernazza et al. (1981) is used to correct the temperature gradient. The opacities were obtained from OPAL95 opacity tables by Iglesias & Rogers (1996). The boundary value problem that was solved to construct these equilibrium models is presented in the Appendix A.

The Schwarzchild condition used to determine convection is $\nabla - \nabla_{ad} > 0$. We use this criterion to determine which parts of the equilibrium model is convective by plotting $\nabla - \nabla_{ad}$ as a function

Table 3.1: Parameters of theoretical models. The first column denotes the model sequence number. The second column shows the mass and the third effective temperature. The forth column gives the luminosity.

Model No.	$M/M_{\odot}$	T_{eff}	$L/L_{\odot}$
1	1.00	5778	1.000
2	1.20	6164	1.657
3	1.30	6430	2.438
4	1.50	7072	4.712
5	1.60	7512	6.249
6	1.80	8340	10.279
7	2.00	9088	15.843
8	2.10	9440	19.305

of depth (see Fig. 3.1) for each of the equilibrium models listed in Table 3.1. The dips of ∇_{ad} seen in Fig. 3.1, and indicated by HI, HeI and HeII correspond to hydrogen, first helium and second helium ionization zones respectively. For each model, we show how $\nabla \quad \nabla_{ad}$ and ∇_{ad} behaves. For the models with $M \leq 1.3M_{\odot}$, the broad trough in the region $5 < \log p < 7$ corresponds to a combination of hydrogen and first helium ionization zones. It is noticeable that the dip corresponding to HeI ionization is separated from hydrogen ionization zone for models with $M \geq 1.5M_{\odot}$. The depth of the HeI dip increases with mass.

One can observe that the dip corresponding to second helium ionization zone gets narrower for models with $M \geq 1.8M_{\odot}$. The dip seen in the $\nabla - \nabla_{ad}$ increases with mass up to $1.8M_{\odot}$ model and then decreases with increasing mass. The model is radiative in the regions where $\nabla < \nabla_{ad}$ and convective in the regions where $\nabla > \nabla_{ad}$. In Table 3.2 the extent of convective regions for each model are depicted. It is clear that the size of the convective zone decreases with increasing mass. Stars with $M > 1.6M_{\odot}$ have more than one convective zones which are smaller nonetheless.

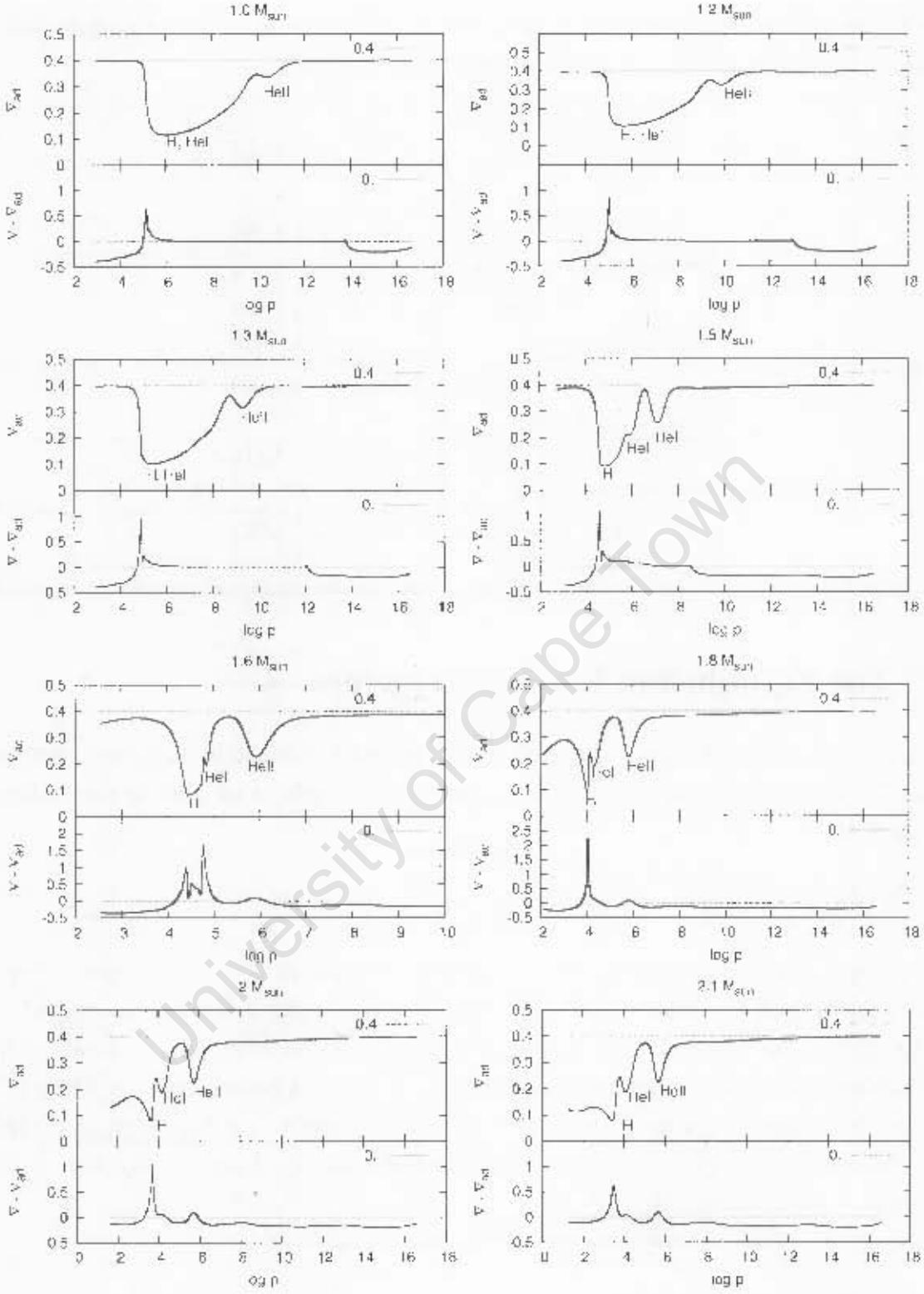

Figure 3.1: Each panel shows ∇_{ad} and $\nabla - \nabla_{ad}$ for the ZAMS model listed in Table 3.1 plotted against the depth coordinate $\log p$, the logarithm of pressure.

Table 3.2: First column denotes the mass of the equilibrium models, second column denotes the positions of convective regions and third column is the acoustic cut-off frequency ν_{ac}.

$M/M_\odot$	Convective zones	ν_{ac} (mHz)
1.0	$5 < \log p < 14$	5.451
1.2	$4.8 < \log p < 13$	4.140
1.3	$4.6 < \log p < 12$	3.486
1.5	$4.3 < \log p < 8.5$	2.734
1.6	$4.1 < \log p < 5.0$ & $5.6 < \log p < 6.1$	2.565
1.8	$3.7 < \log p < 4.5$ & $5.5 < \log p < 6.0$	2.393
2.0	$3.2 < \log p < 4.3$ & $5.4 < \log p < 5.9$	2.215
2.1	$3.0 < \log p < 4.3$ & $5.4 < \log p < 5.8$	2.083

3.2 The Equilibrium Eddington factors

Here we decide on which equilibrium Eddington factors (f_{eq}) to use in the scheme outline in chapter 2 for solving our equations. This is because in Houdek's calculation the Eddington factor used is

$$f_{eq} = \frac{1}{3}\left[2 + \frac{\tau + q(2/3)}{\tau + q(\tau)}\right]. \tag{3.1}$$

This Eddington factor was derived from a model C of Vernazza, Avrett & Loeser (1981). It is clear that we have to decide which f_{eq} to use between the one defined in equation (3.1) or equation (2.23). We have looked at $(f_{eq}B)/K$ for $1.8M_\odot$ model, using the K calculated from the Feautrier method and f_{eq} defined in equation (3.1). This is a measure of consistency of the radiation field. The results are shown in Fig. 3.2. The value we get is as high as 1.3 in the upper parts of the atmosphere. It is clear that we need to use f_{eq} defined in equation (3.1) for consistency in our calculations.

3.3 Tests on the code

In this section we discuss the tests to show that the code gives reasonable results. The tests are based on the equilibrium model with parameters $L/L_\odot = 10.279$, $M/M_\odot = 1.8$ and $T_{eff} =$

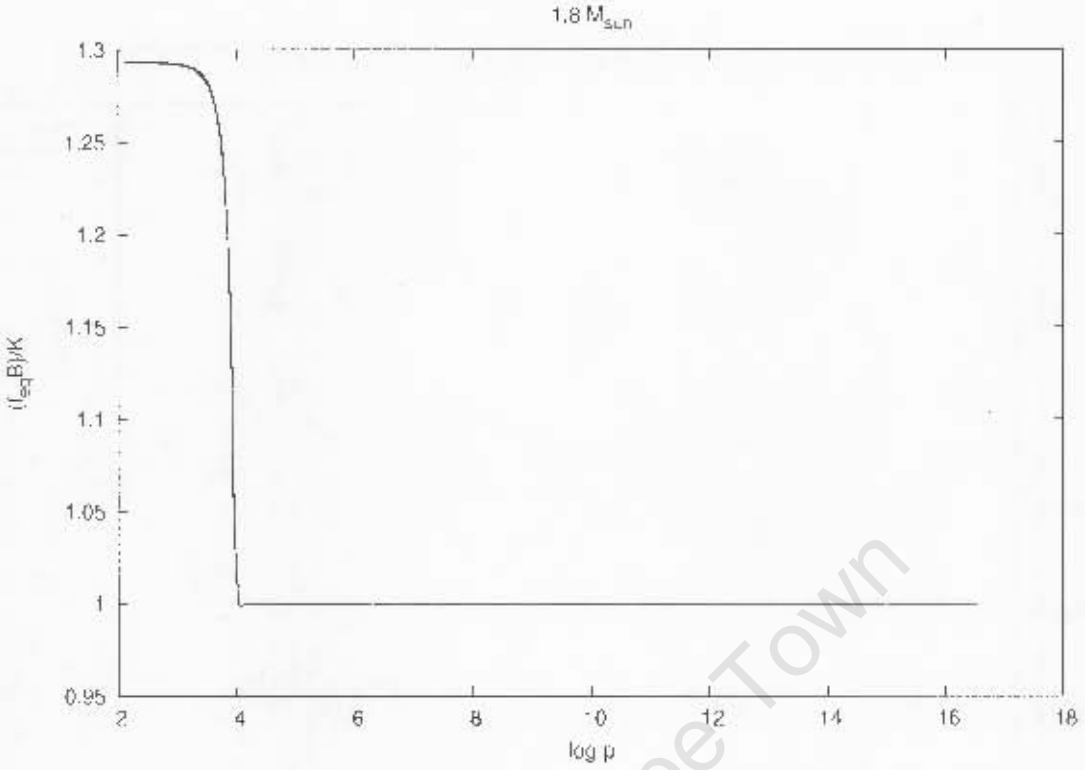

Figure 3.2: The quantity $(f_{eq}B)/K$ as a function of depth for $1.8M_{\odot}$ model.

$8340.2K$. The first test is to verify that the consistently iterated Eddington factor f_{osc} obtained from the code approaches $1/3$ at large optical depths. In Fig. 3.3, f_{osc} (see Eq. 2.68) is plotted as a function of $\log p$ and we find that indeed f_{osc} approaches $1/3$ at large optical depth. There is a significant difference between f_{osc} and f_{eq} near the surface. However they both tend to $1/3$ at large optical depth.

In chapter 2, we showed that ω/ω_R approaches zero as the optical depth increases. Therefore, in the optically thick regions of the star the following relation should hold:

$$\frac{\delta J}{J_0} = 4\frac{\delta T}{T_0}. \tag{3.2}$$

In Figs. 3.4, plots of $4\,\delta T/T$ and $\delta J/J$ as a function of $\log p$ for modes of low and high frequencies are shown. The left panels show the real parts of $\delta J/J$ and $\delta T/T$, and right panels show the imaginary parts of those eigenfunctions. In the atmosphere $4\,\delta T/T$ deviates from $\delta J/J$ for both frequencies. This indicates that in the atmosphere the condition for radiative equilibrium does not hold. Below, in the envelope $4\delta T/T$ and $\delta J/J$ matches completely.

We also determined the parts of the star where oscillations are adiabatic and those that are non-adiabatic by plotting $\delta T/T - \nabla_{ad}\delta p/p$ as a function of depth in Fig. 3.5. The figure shows that

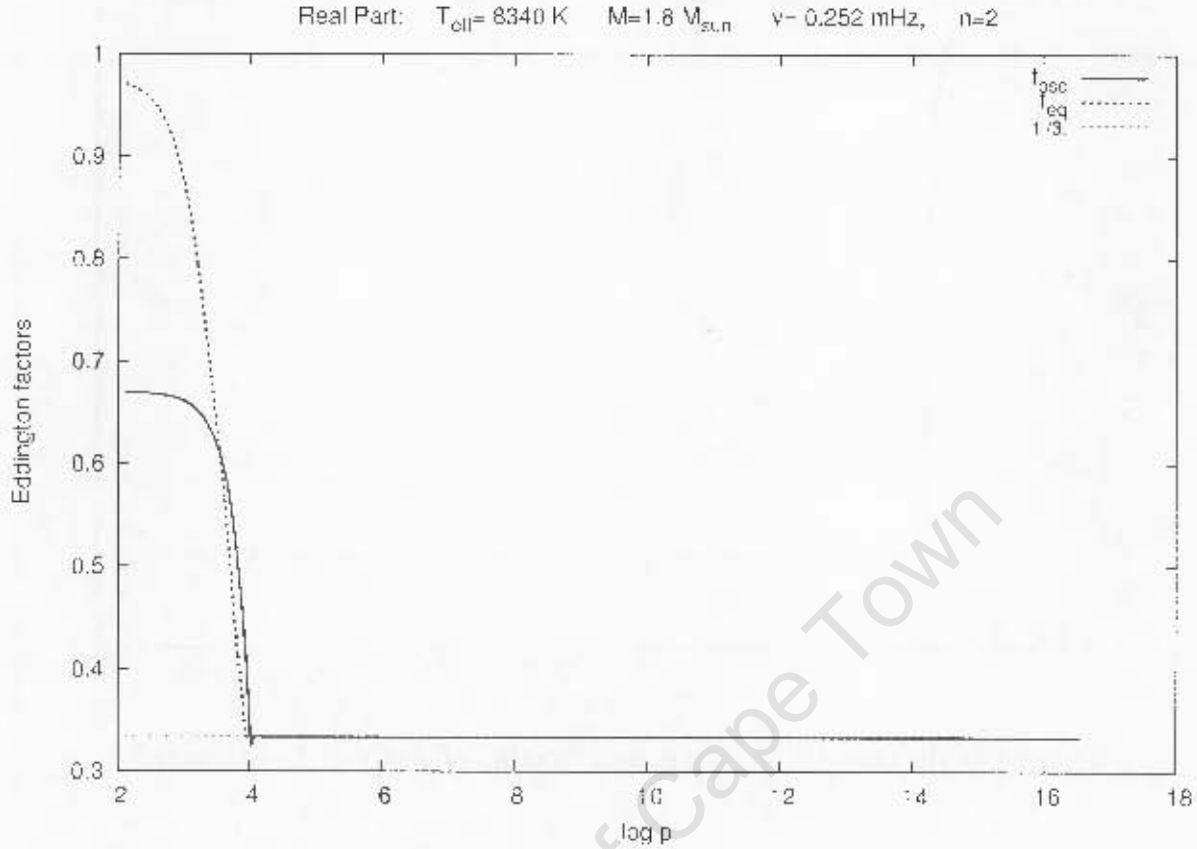

Figure 3.3: The plots of equilibrium and perturbed Eddington factors as a function of depth. The solid line displays the real part of f_{osc} at a frequency 0.252 mHz and dashed line represent f_{eq}.

well below the atmosphere the solution is adiabatic and in the whole atmosphere the solution is non-adiabatic irrespective of frequency. Therefore, one cannot ignore non-adiabaticity in the atmosphere.

We also compare our code with asymptotic relations for high overtone adiabatic pulsations. The asymptotic expression for displacement eigenfunctions is given by Tassoul & Tassoul (1968) and Christensen-Dalsgaard (2003) as:

$$\delta r = A\rho(r)^{-\frac{1}{2}}c(r)^{-\frac{1}{2}}r^{-1}\cos\left(\omega\int_r^R \frac{dr'}{c(r)} - \left(\frac{1}{A}+\alpha\right)\pi\right) \tag{3.3}$$

where A is the amplitude obtainable from the boundary condition far from the turning points, $c(r)$ is the sound speed and α is a phase constant. The equation (3.3) breaks down near the surface and the inner turning points for trapped modes. We have shown that the oscillations are adiabatic in the stellar interior (see Fig. 3.5), therefore we expect that if our code works

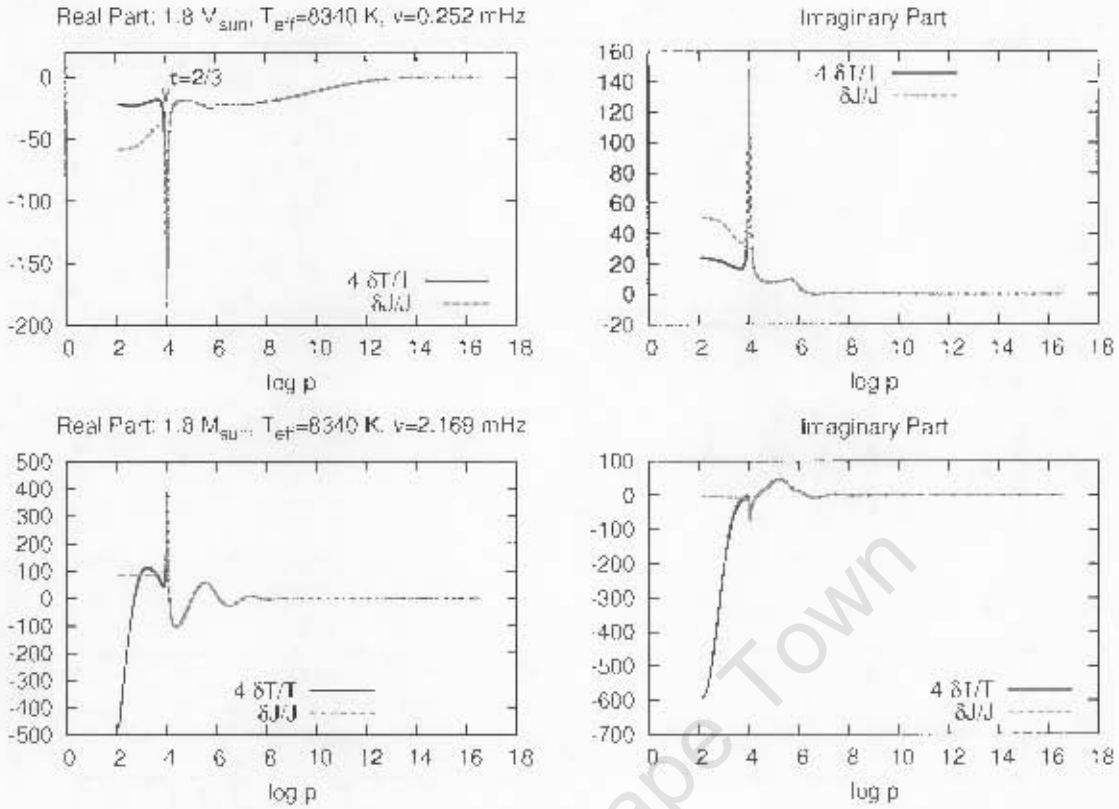

Figure 3.4: The plots show $4\delta T/T$ and $\delta J/J$ compared as a function of depth for the modes with frequencies 0.252 mHz and 2.169 mHz. As expected there is a departure from radiative equilibrium in the atmosphere since $4\delta T/T$ deviates from $\delta J/J$. The left panels show the real parts of $\delta J/J$ and $\delta T/T$, and right panels show the imaginary parts of those eigenfunctions

well the solutions from our code must agree very well with equation (3.3). For adiabatic oscillations (zero damping), it means that $\rho^{1/2}c^{1/2}r\delta r$ should have a constant amplitude with depth. We calculate $\rho^{1/2}c^{1/2}r\delta r$ using our code and compare it with $A\cos(\omega\int_r^R dr'/c(r) - (1/4+\alpha)\pi)$.

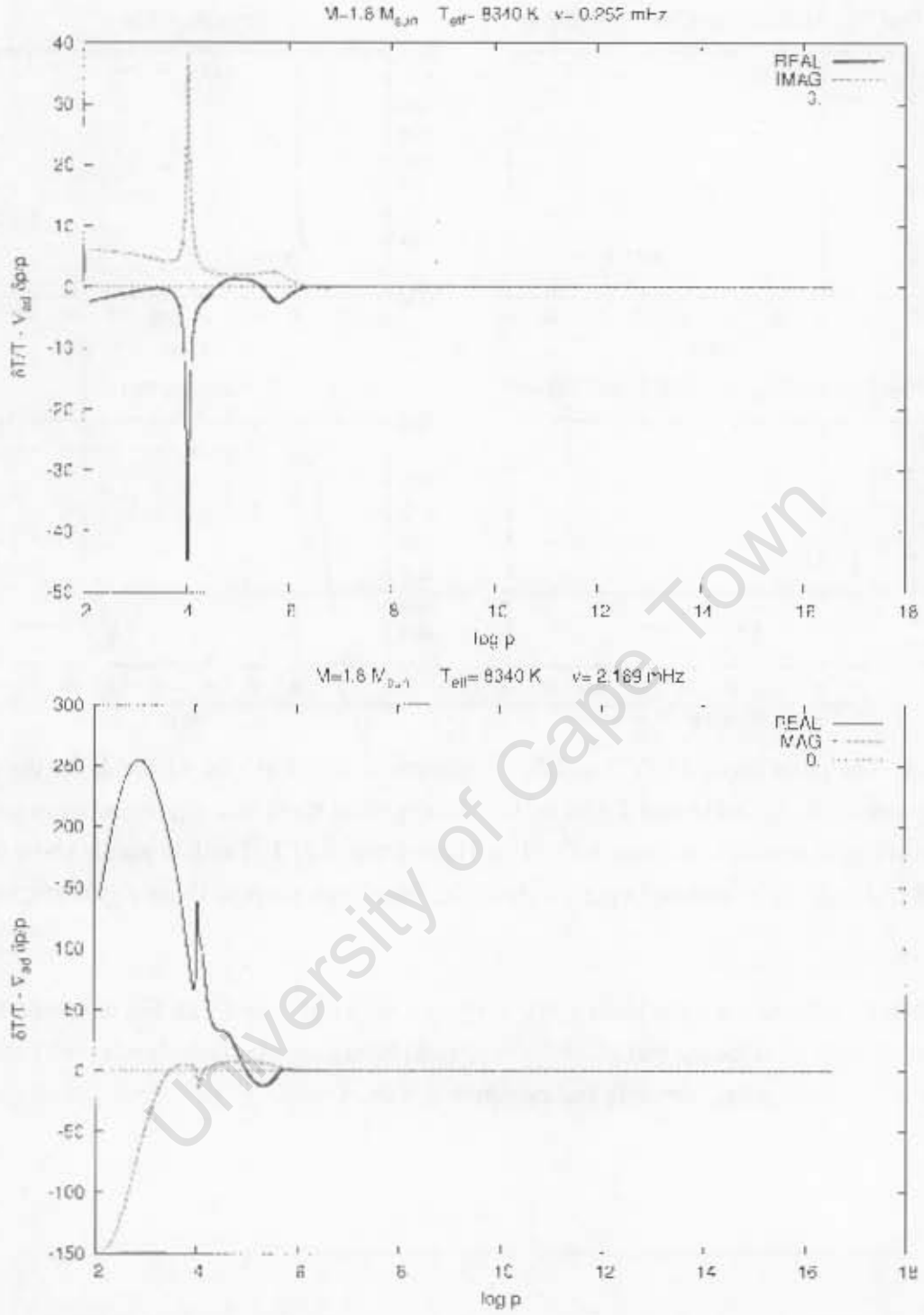

Figure 3.5: The real and imaginary parts of $\delta T/T \quad \nabla_{ad}\delta p/p$ as a function of depth for the modes with frequencies 0.252 mHz and 2.169 mHz are shown in . In the atmosphere there is a departure from zero which verifies that the oscillations is non-adiabatic.

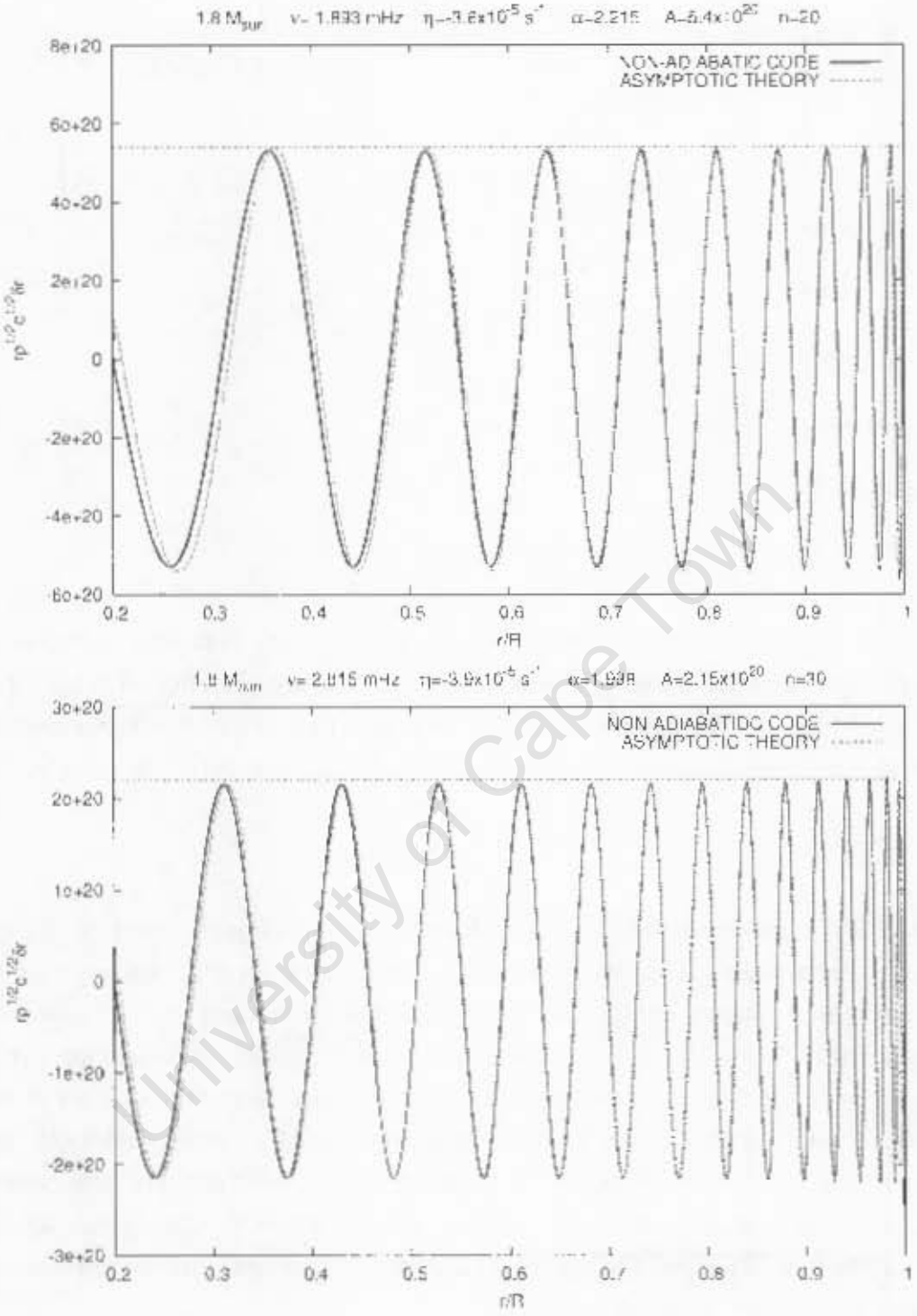

Figure 3.6: A plot of $\rho^{1/2}c^{1/2}r\delta r$ calculated from our code compared with equation (3.3) for modes with frequencies 1.893 mHz and 2.815 mHz at the growth rates $-3.6 \times 10^{-9}s^{-1}$ and $-3.9 \times 10^{-5}s^{-1}$ respectively. Values of the amplitude A and phase constant α are shown. This is for $1.8M_{\odot}$ model.

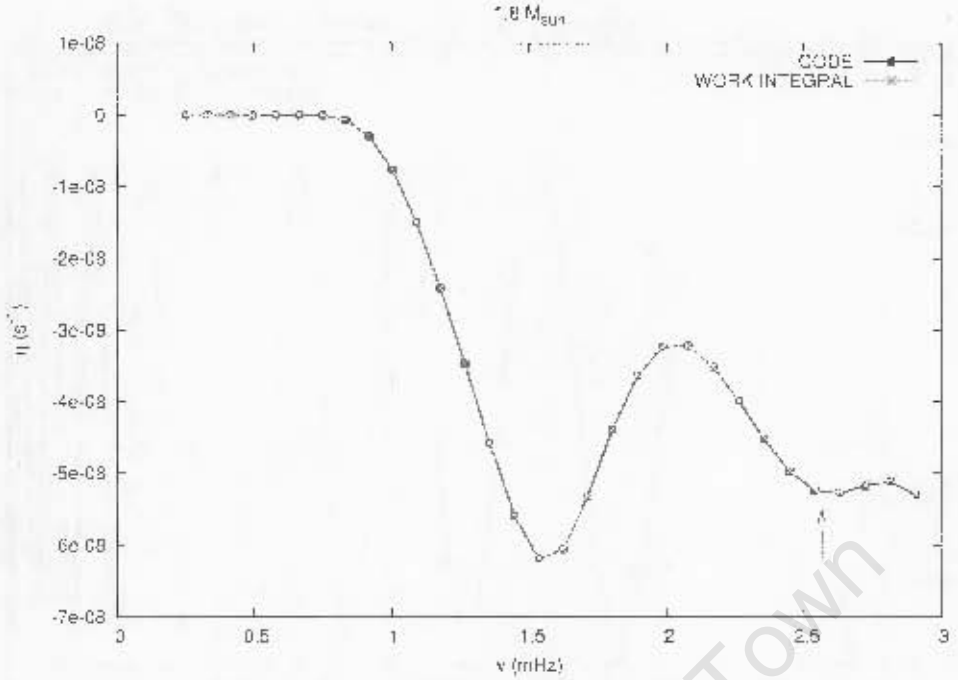

Figure 3.7: The growth rates calculated from using the mechanical boundary condition (2.130) that takes into consideration the fact that modes with $\omega > \omega_{ac}$ are not reflected but dissipate out through the atmosphere. The dashed line shows the results from the work integral calculations, and the solid line is from the code. The arrow indicates the acoustic cut-off frequency.

Amplitude A is made to match the numerical solution at some point in the envelope. We also adjusted α for different frequencies (below and above the acoustic cut-off frequency) and growth rates. The results are shown in Fig. 3.6. We can see that for the frequency of 1.89 mHz and the growth rate of $-3.6 \times 10^{-9} s^{-1}$ the code gives almost a constant amplitude throughout the envelope. There is slight decrease of amplitude from the surface towards the center of the star. In addition, we note that for frequency 1.89 mHz the phase angle α varies with depth. For frequency below the acoustic cut-off frequency, variation of phase with depth is more pronounced as compared to the frequency above the acoustic cut-off frequency. Clearly non-adiabaticity introduces a phase variation [see Medupe et al (in prep.)]. The phase variation can become very small as shown in the bottom panel of Fig. 3.6.

Finally, we compare the growth rates η calculated by imposing an additional boundary condition (no displacement at the base of the envelope) and those calculated using the work integral (see Eq. 2.140). Here $\eta = -\omega_i$ where ω_i is the imaginary part of ω. The results are depicted in Fig. 3.7. As expected the two approaches are in good agreement.

3.4 The eigenfunctions

In this section we present eigenfunctions for the equilibrium models listed in Table 3.1 at various frequencies. We investigate the behaviour of our solution as the function of effective temperature and mass. We also give the summary of the results at the end of the section.

3.4.1 The Temperature eigenfunctions

In Figs. 3.8 to 3.15 the real and imaginary parts of $\delta T/T$ are depicted. There is a dip seen just below the photosphere in the first hydrogen ionization zone. This dip was noticed in the results by Baker & Kippenhahn (1965), Balmforth (1992a) and Medupe (2002). Another noticeable result is that the depth of the dip changes with frequency. Within the main dip there is a smaller dip which is pronounced between radial modes.
It is noticeable that the shape of the dip in superadiabatic gradient $\nabla - \nabla_{ad}$ looks the same as the dip found in temperature eigenfunctions $\delta T/T$ as shown in Fig. 3.1. The dip moves progressively towards the stellar surface as the effective temperature increases. This makes sense because in hot stars hydrogen starts to ionize in atmospheric layers. Therefore the hydrogen ionization zone extends towards the layers above the photosphere. As for the lowest radial mode the $1.8M_{\odot}$ model has the largest dip in all the equilibrium models considered here. A general observation is that, at that frequency the models with $M \leq 1.6M_{\odot}$ have small dip as compared to the models with $M \geq 1.8M_{\odot}$. At the higher frequency as seen for radial mode $n = 30$ the models $M \leq 1.6M_{\odot}$ have large dip as compared to the models $M \geq 1.8M_{\odot}$ (see Fig. 3.16).

The real part of $\delta T/T$ is definitely highly variable in the atmosphere and sub-photospheric layers at higher frequencies. This is contrary to the assumption often made in analytic formula such as the presented in Watson (1988). Thus, the $\delta T/T$ plots show that even at low frequencies the atmosphere cannot be regarded as a single layer with constant eigenfunctions. The highly variable $\delta T/T$ is consistent with Medupe & Kurtz (1998) idea that the steep decreases in photometric amplitudes with wavelength is related to the highly variable $\delta T/T$.

We also notice that there are wiggles for models with $M \leq 1.5M_{\odot}$. The only possible explanation for the wiggles in those models is a result of the time-dependent treatment of convection. In a local time-dependent model these wiggles are rather huge due to an imaginary diffusivity in the equations describing the convective temperature fluctuations. In a non-local treatment of convection the wiggles are reduced but still noticeable. A discussion on these rapidly oscillating eigenfunctions is given by Baker & Gough (1979).

3.4.1.1 $1.0M_{\odot}$ model

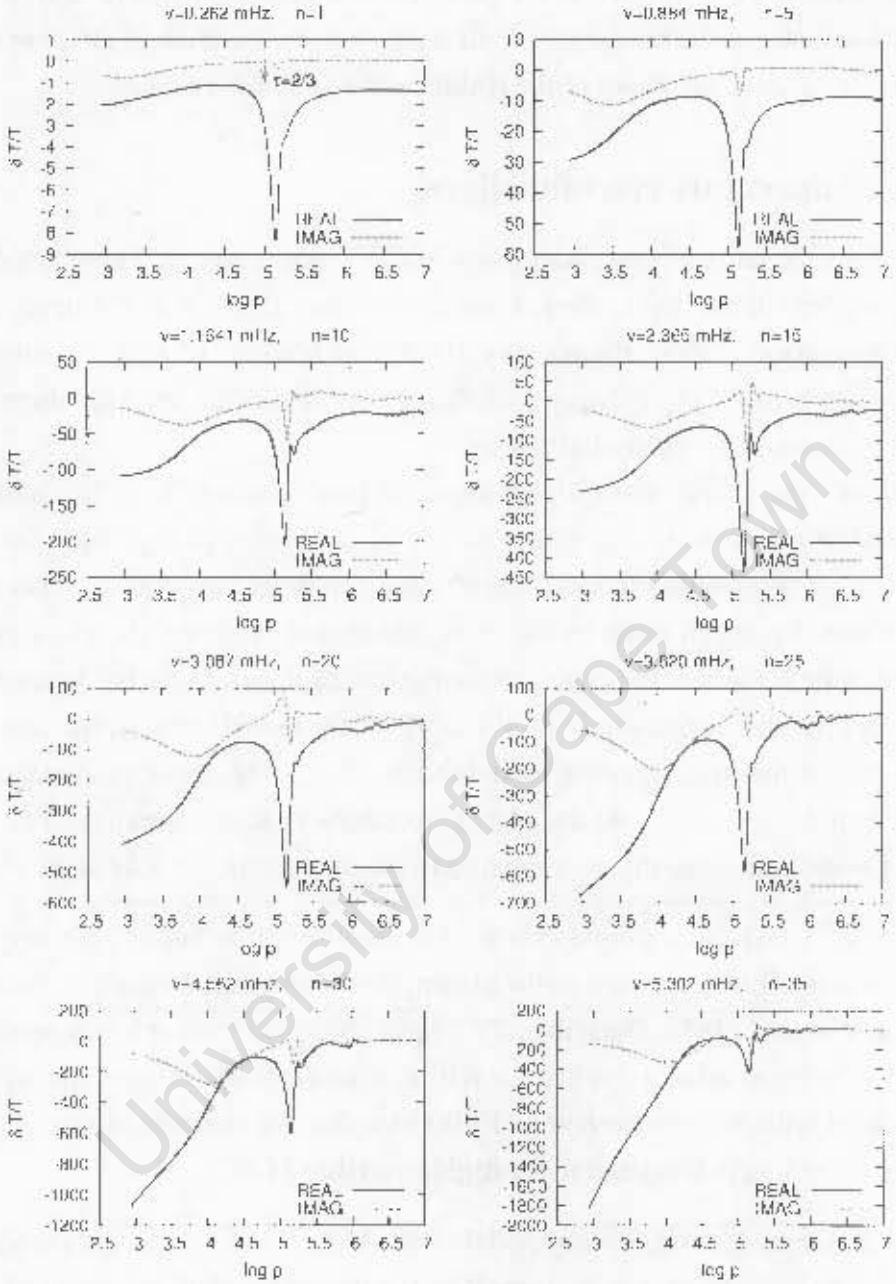

Figure 3.8: The real and imaginary parts of $\delta T/T$ for the $1.0M_{\odot}$ model plotted as a function of depth at various frequencies. The optical depth $\tau = 2/3$ is indicated on the first panel by the arrow.

3.4.1.2 $1.2M_{\odot}$ model

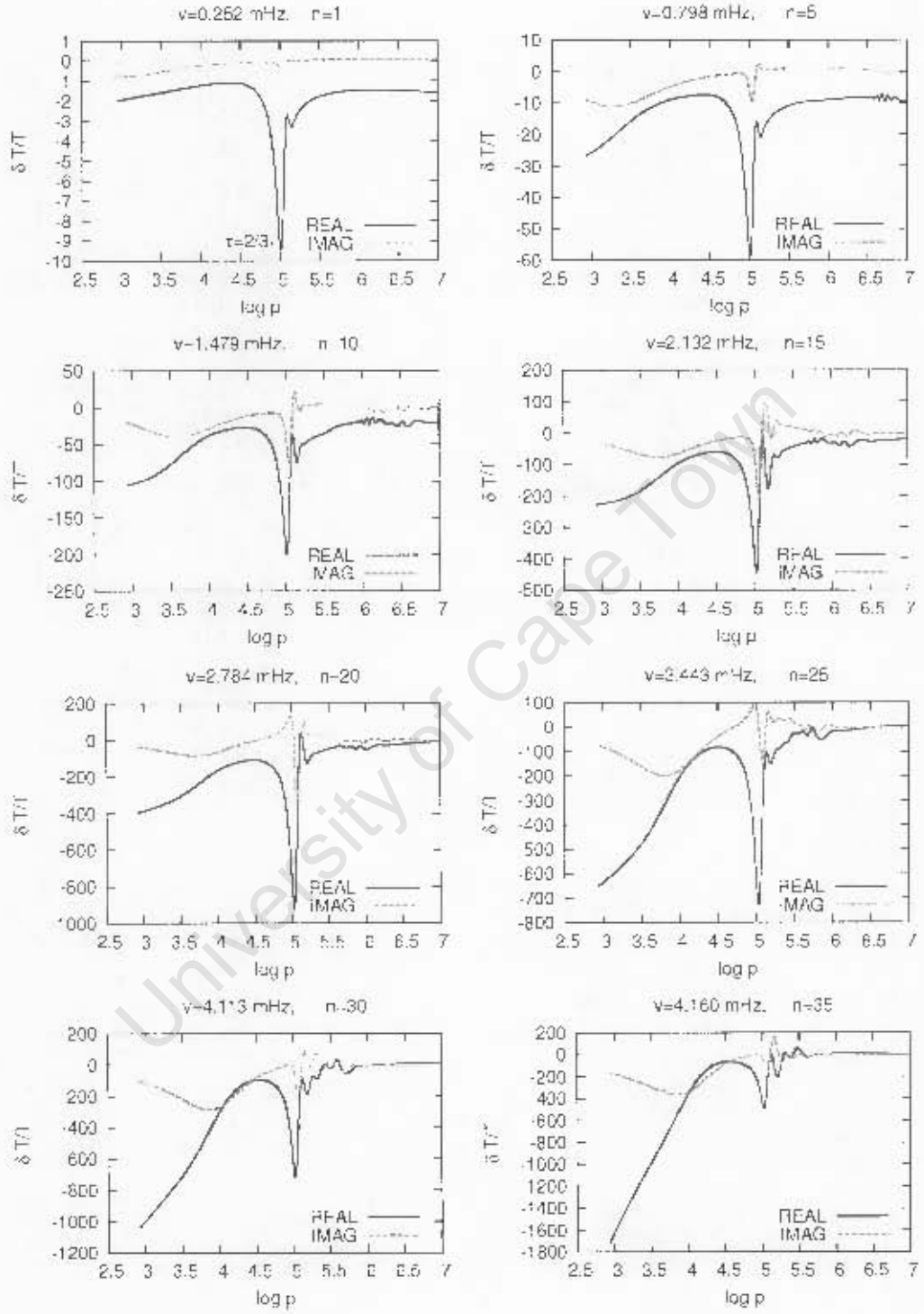

Figure 3.9: The real and imaginary parts of $\delta T/T$ for the $1.2M_{\odot}$ model plotted as a function of depth at various frequencies.

3.4.1.3 $1.3M_{\odot}$ model

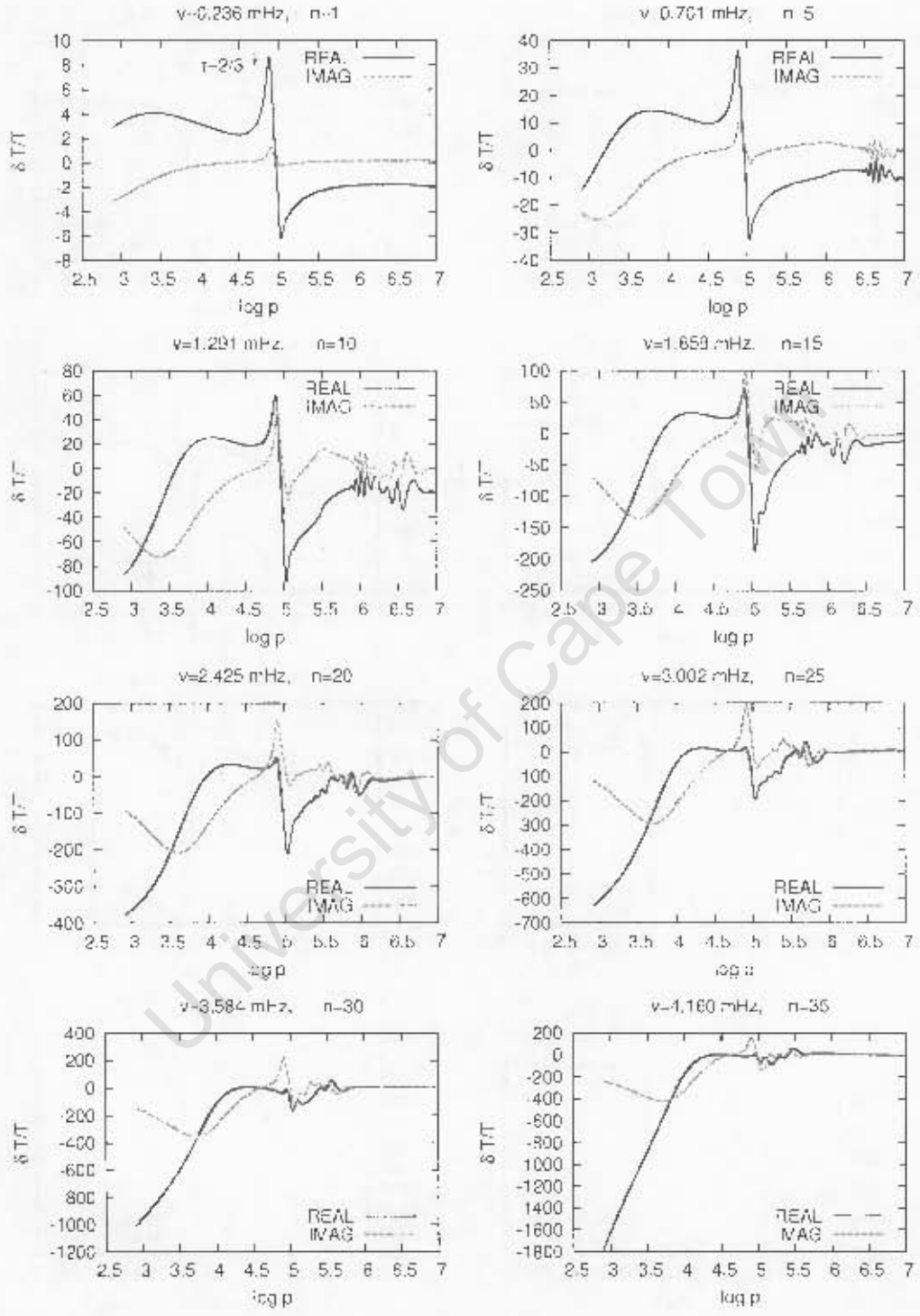

Figure 3.10: The real and imaginary parts of $\delta T/T$ for the $1.3M_{\odot}$ model plotted as a function of depth.

3.4.1.4 $1.5M_{\odot}$ model

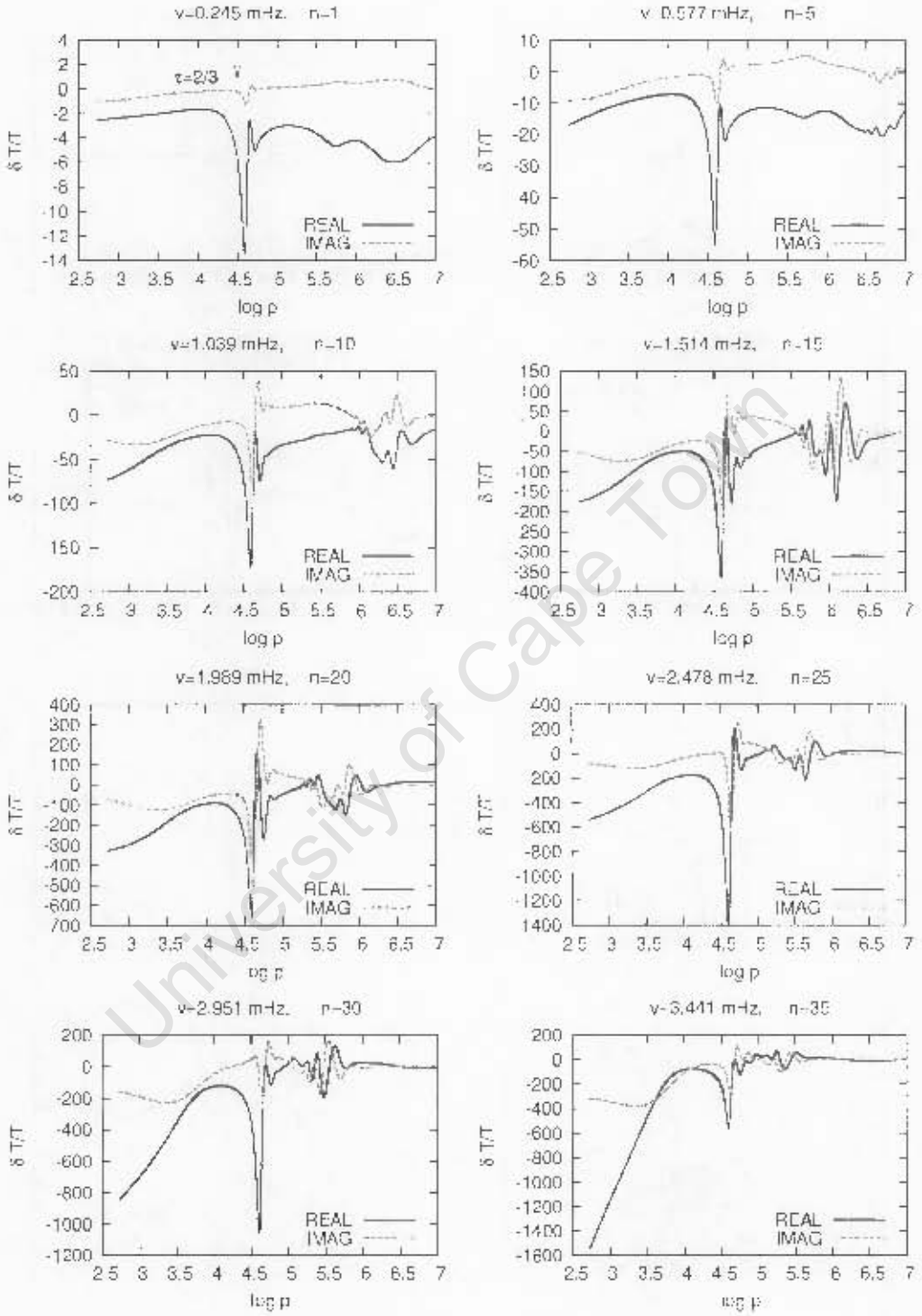

Figure 3.11: The real and imaginary parts of $\delta T/T$ for the $1.5M_{\odot}$ model plotted as a function of depth at various frequencies.

3.4.1.5 $1.6M_{\odot}$ model

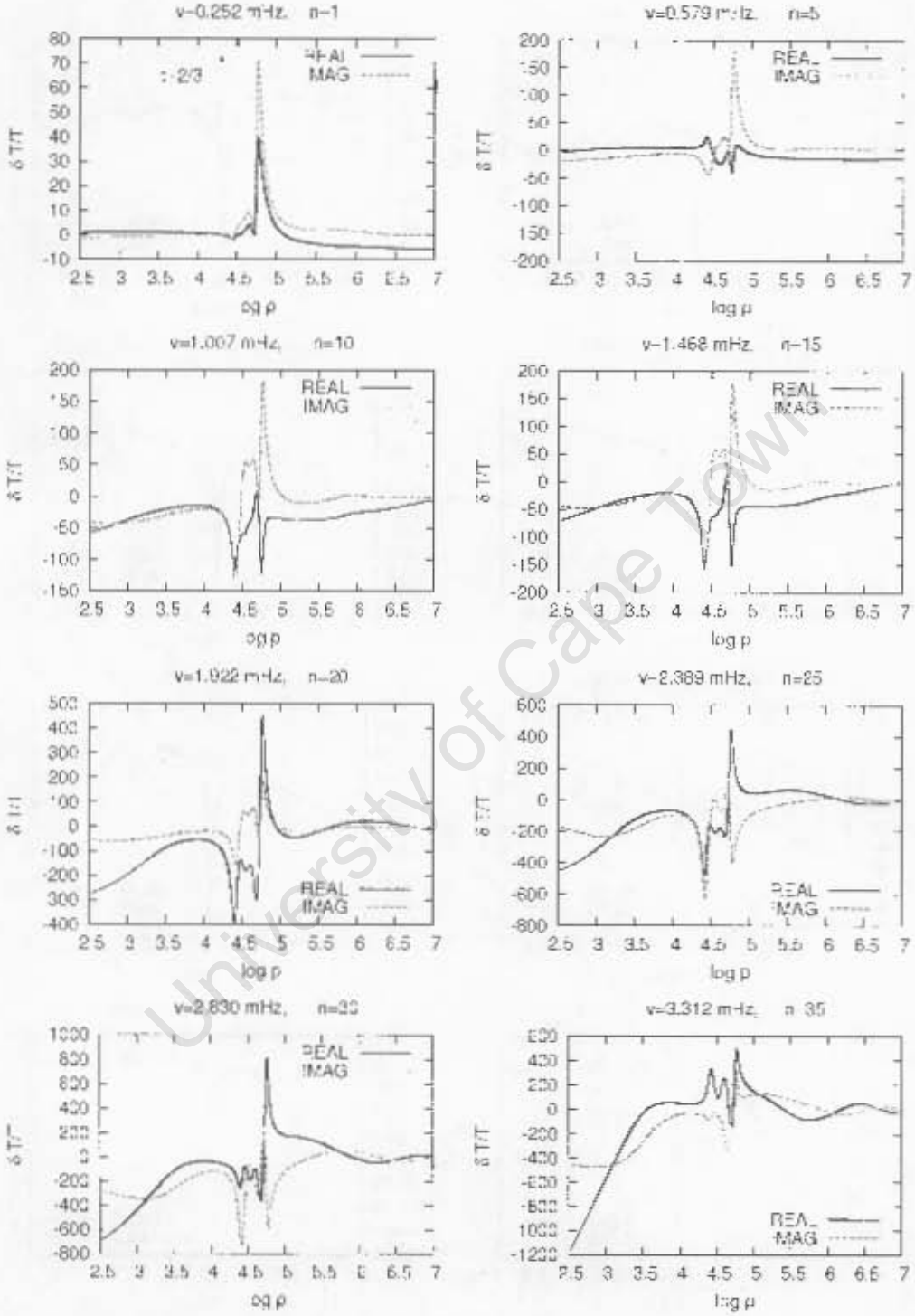

Figure 3.12: The real and imaginary parts of $\delta T/T$ for the $1.6M_{\odot}$ model plotted as a function of depth at various frequencies.

3.4.1.6 $1.8M_{\odot}$ model

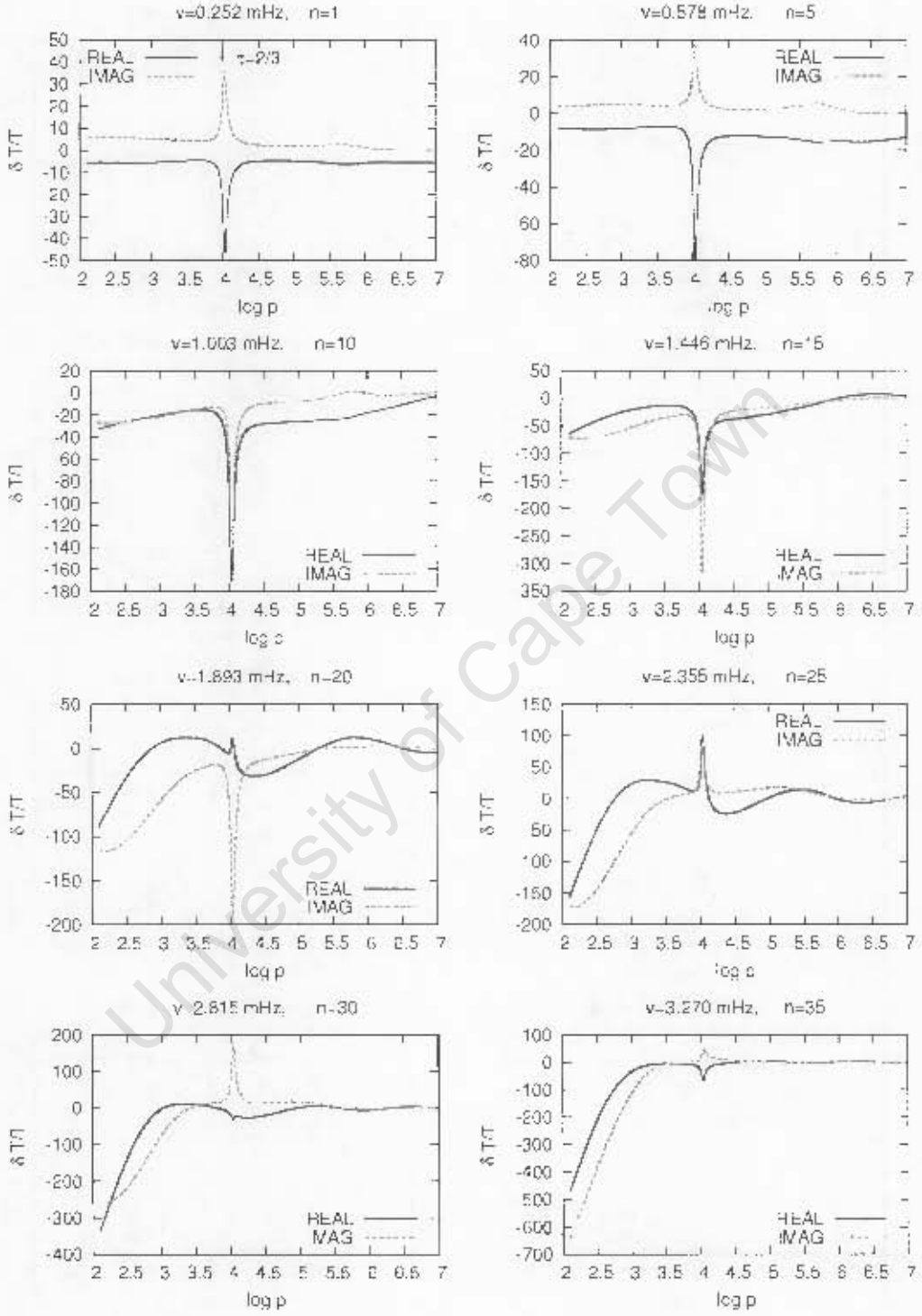

Figure 3.13: The real and imaginary parts of $\delta T/T$ for the $1.8M_{\odot}$ model plotted as a function of depth at various frequencies.

3.4.1.7 $2.0M_{\odot}$ model

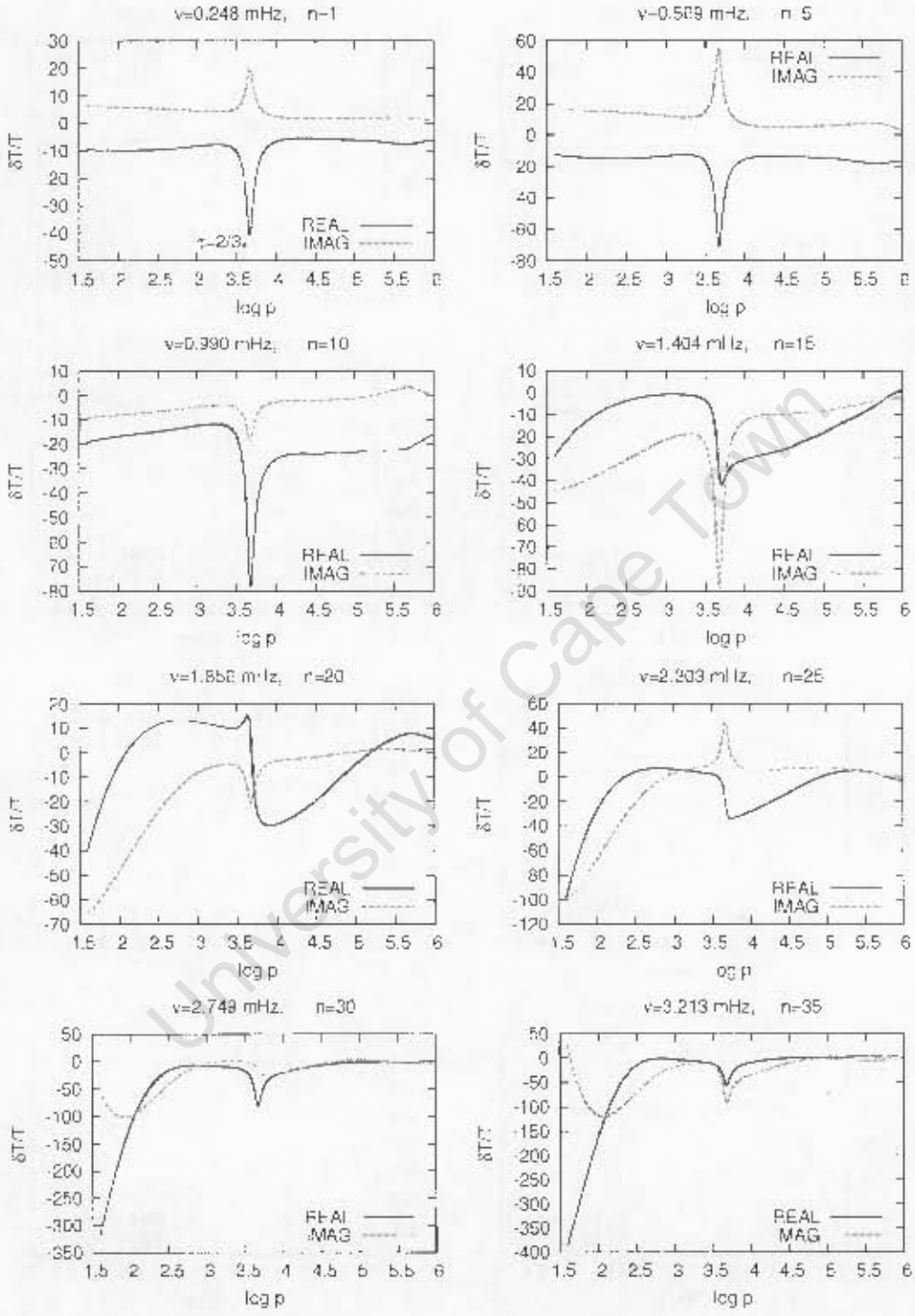

Figure 3.14: The real and imaginary parts of $\delta T/T$ for the $2.0M_{\odot}$ model plotted as a function of depth at various frequencies.

3.4.1.8 $2.1M_{\odot}$ model

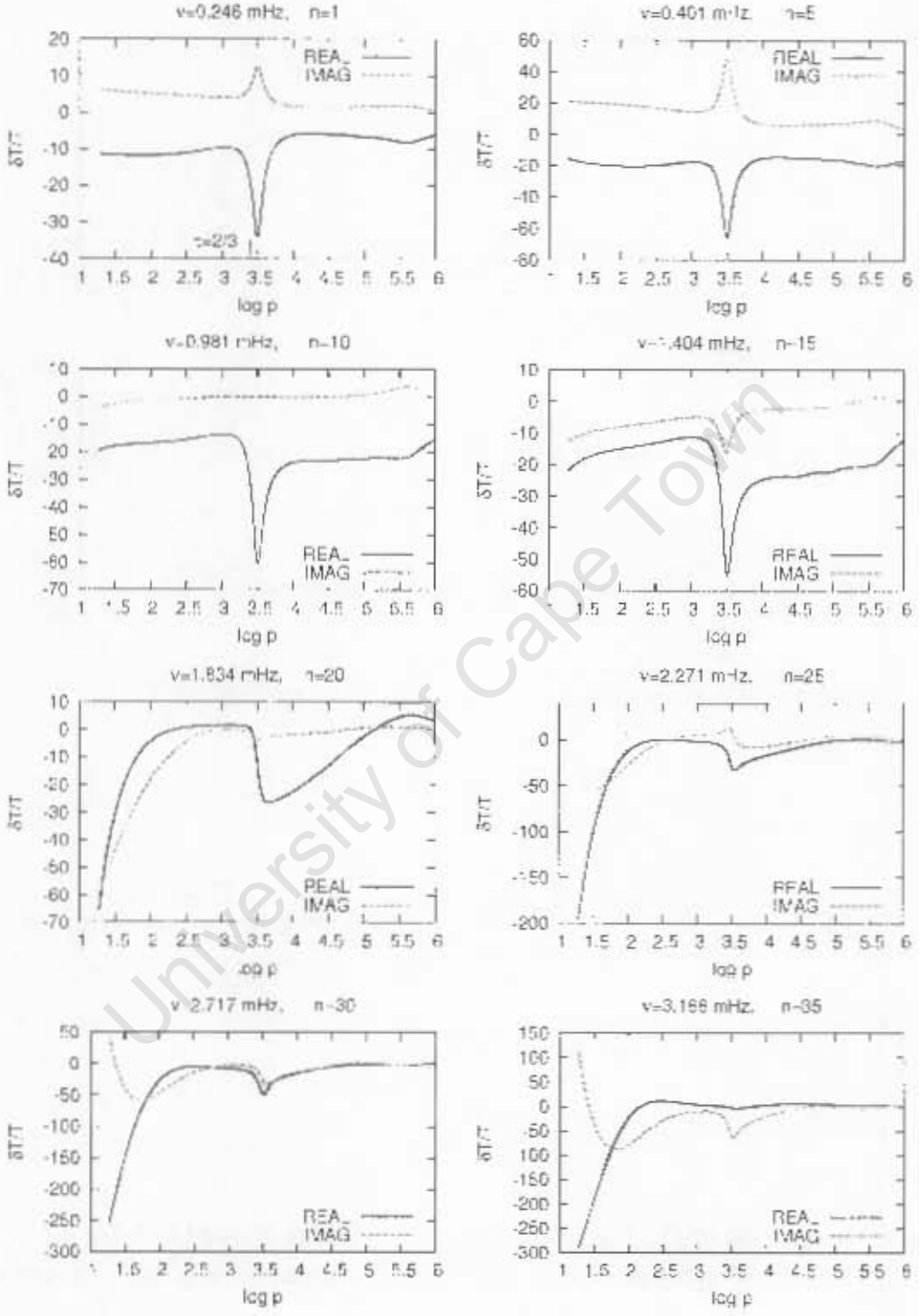

Figure 3.15: The real and imaginary parts of $\delta T/T$ for the $2.1M_{\odot}$ model plotted as a function of depth at various frequencies.

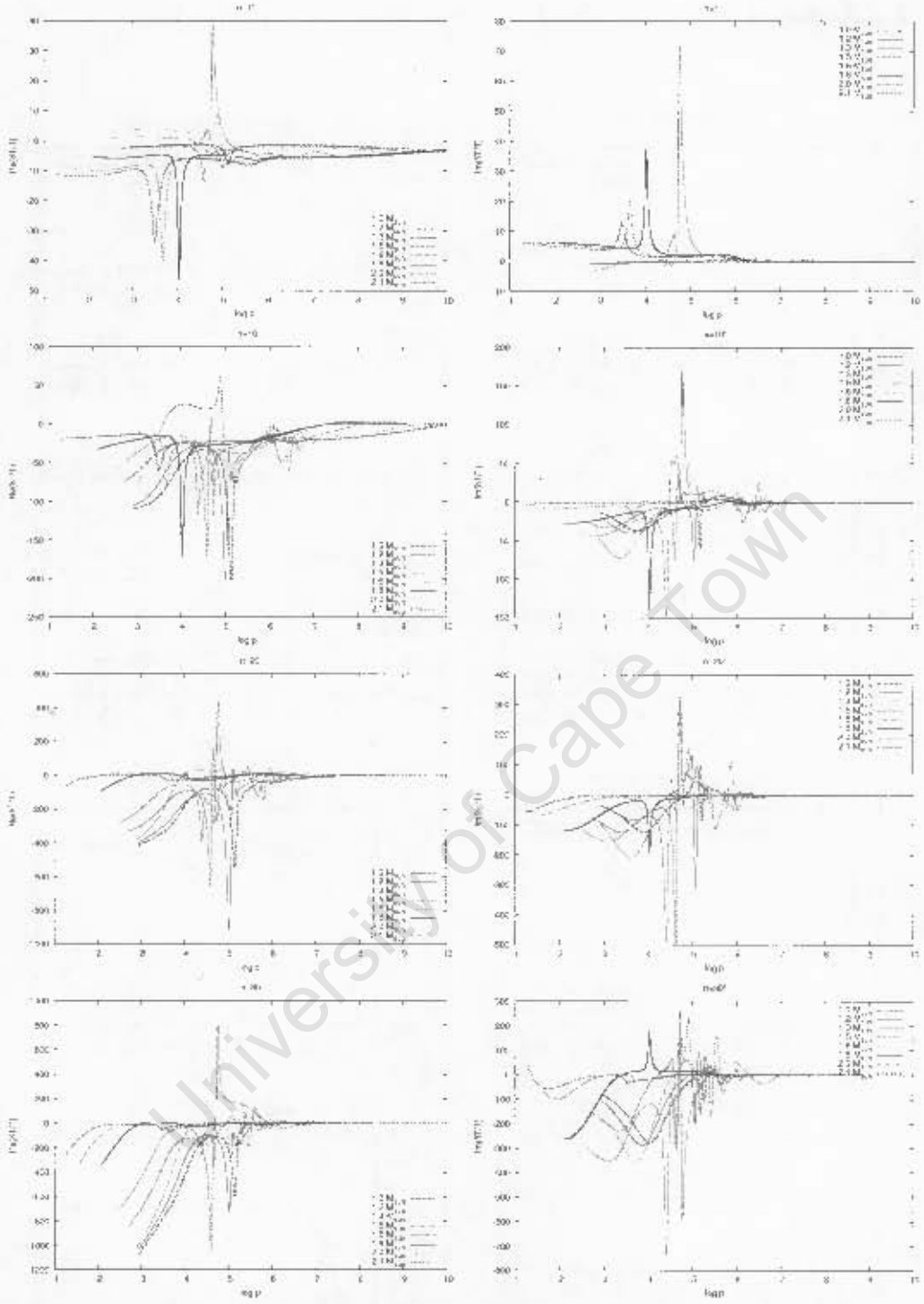

Figure 3.16: Comparison of $\delta T/T$ obtained using ZAMS models listed in Table 3.1 at various frequencies. The left and right panels show the real and imaginary parts of $\delta T/T$ respectively.

3.4.1.9 The "dip" in temperature eigenfunctions

Here we discuss the dip in $\delta T/T$. In Figs. 3.17 to 3.18 we compare $\delta T/T$ for ZAMS models at radial mode $n = 5$ obtained by setting $\kappa_p = 0$ and $\kappa_T = 0$ with the one for $\kappa_p \neq 0$ and $\kappa_T \neq 0$ [see Eq. (2.64)]. It is clear that when there is no opacity fluctuations the dip disappears for masses larger than $1.8M_\odot$. For masses less than this, the dip is there but much smaller than when opacity perturbations are present. We also notice that opacity fluctuations partially contributes towards the wiggles found in $\delta T/T$ for models with $M < 1.6M_\odot$. The main point about our discussion is that while the shape of the dip is determined by the shape of the superadiabatic lapse rate, the main effect that determines whether the dip is there or not is the opacity fluctuation. For detailed analysis, see Medupe et al (in preparation).

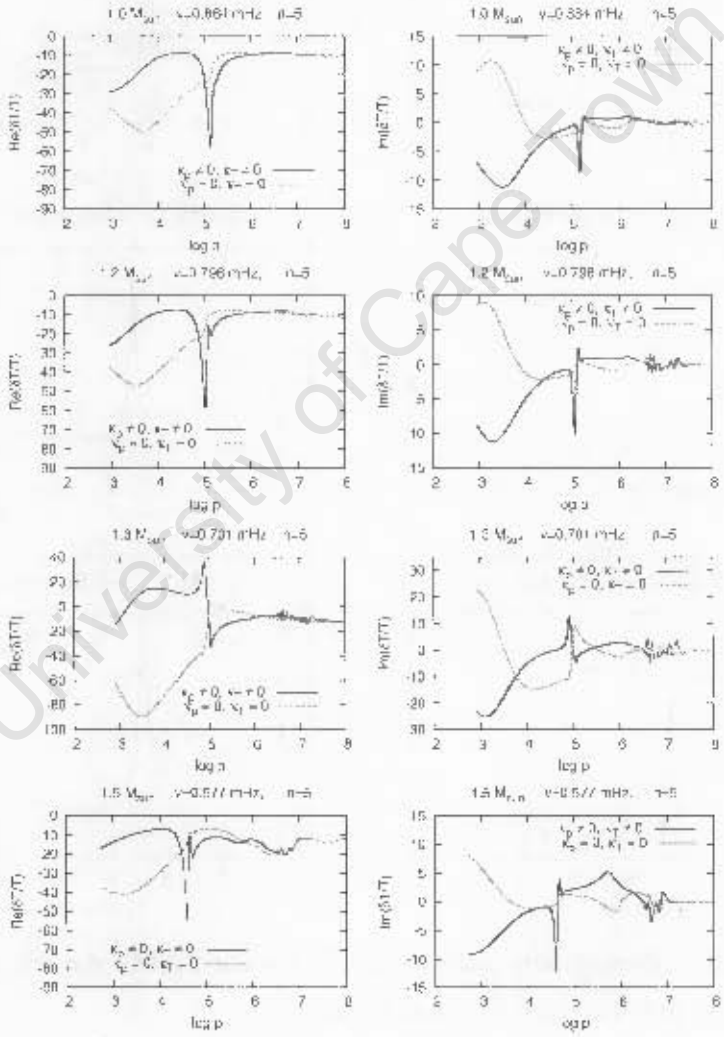

Figure 3.17: The real and imaginary parts of $\delta T/T$ for the ZAMS models listed in Table 3.1 plotted as a function of depth at various frequencies.

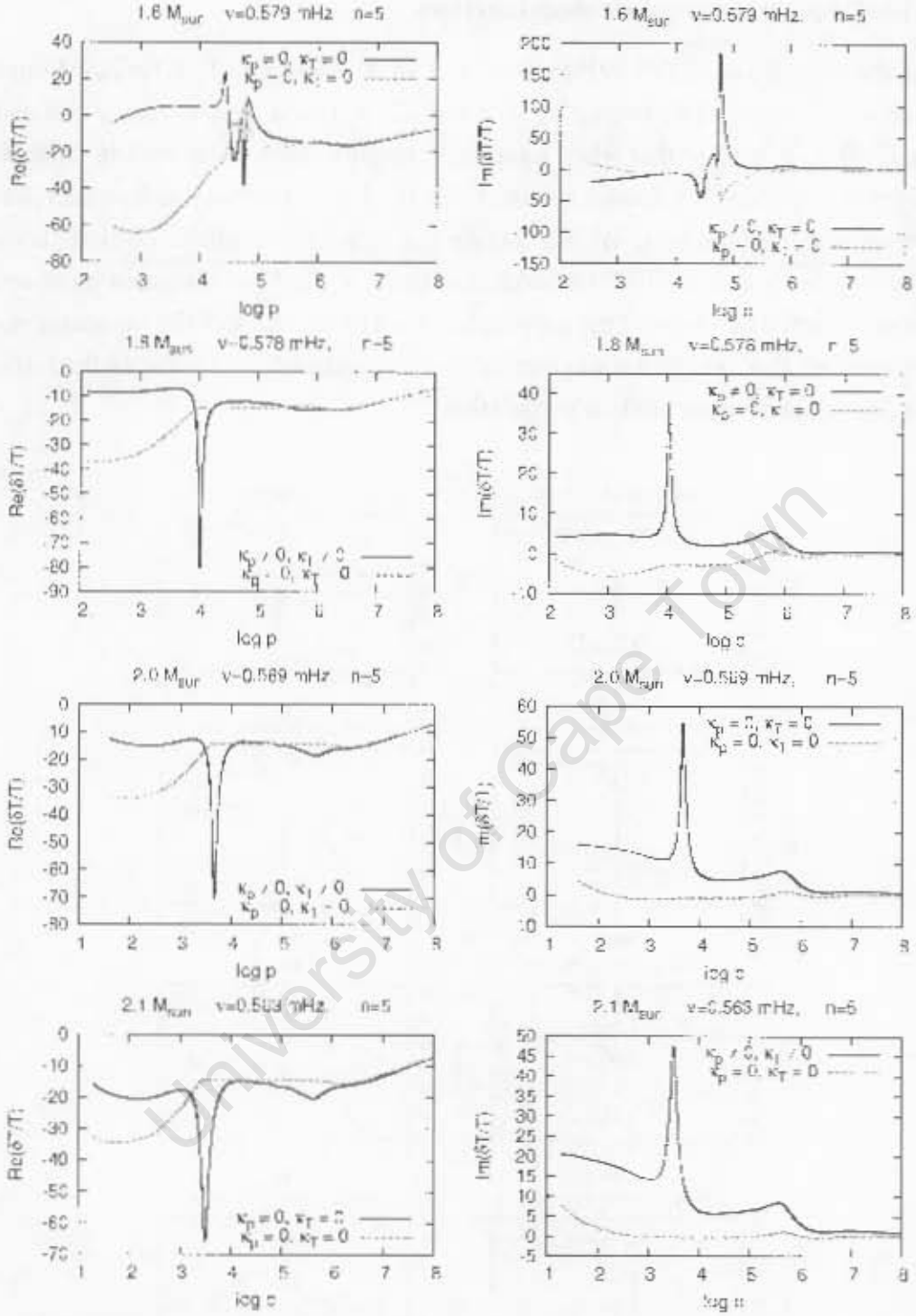

Figure 3.18: The real and imaginary parts of $\delta T/T$ for the ZAMS models listed in Table 3.1 plotted as a function of depth at various frequencies.

3.4.2 Displacement eigenfunctions

The real and imaginary parts of displacement eigenfunctions are shown in Figs. 3.19 to 3.26. We notice that there is slight dip seen in the hydrogen ionization zone which corresponds to the dip seen in $\delta T/T$. It looks like for certain frequencies the displacement respond to the ionization. Clearly the $\delta r/r$ is more responsive to the dip in $\delta T/T$ for $1.5M_{\odot}$ and $1.6M_{\odot}$ models.

3.4.2.1 $1.0M_{\odot}$ model

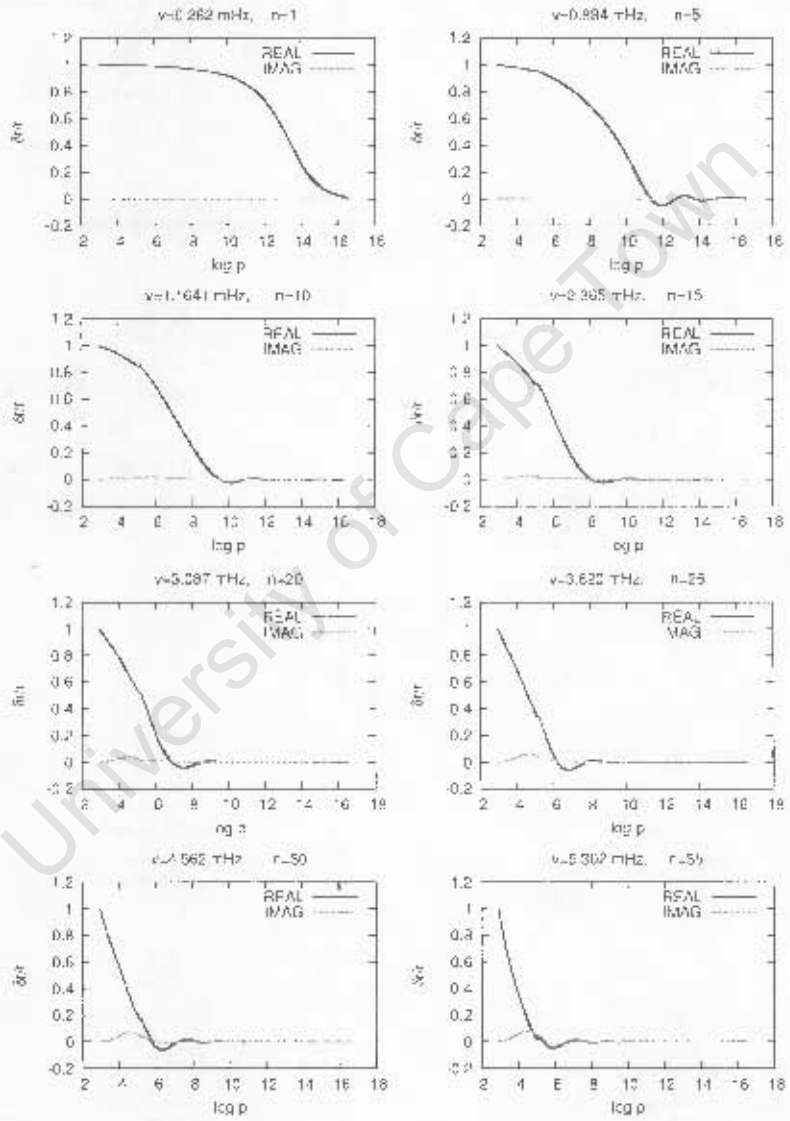

Figure 3.19: The real and imaginary parts of $\delta r/r$ for the $1.0M_{\odot}$ model plotted as a function of depth at various frequencies.

3.4.2.2 $1.2M_{\odot}$ model

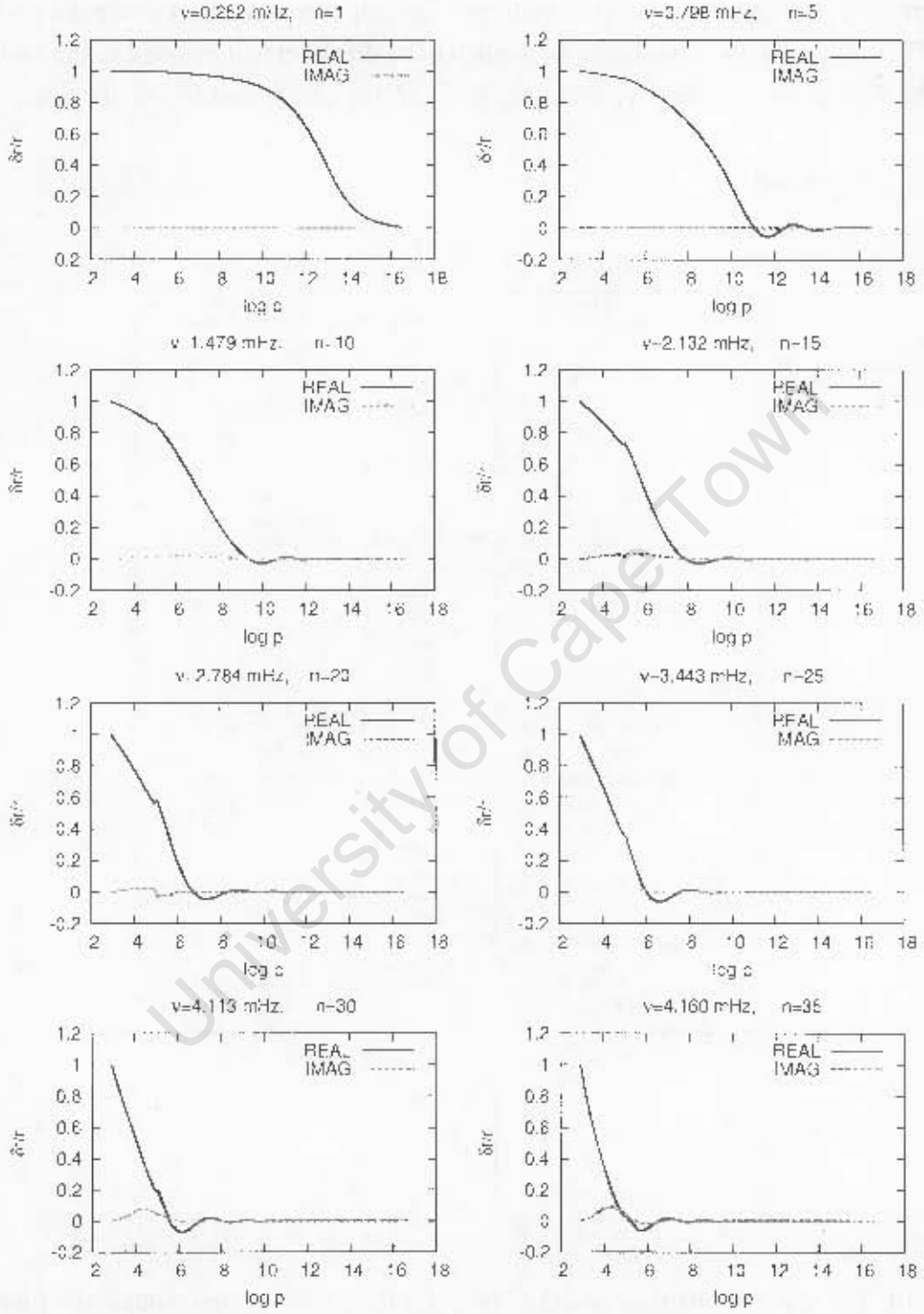

Figure 3.20: The real and imaginary parts of $\delta r/r$ for the $1.2M_{\odot}$ model plotted as a function of depth at various frequencies.

3.4.2.3 $1.3M_{\odot}$ model

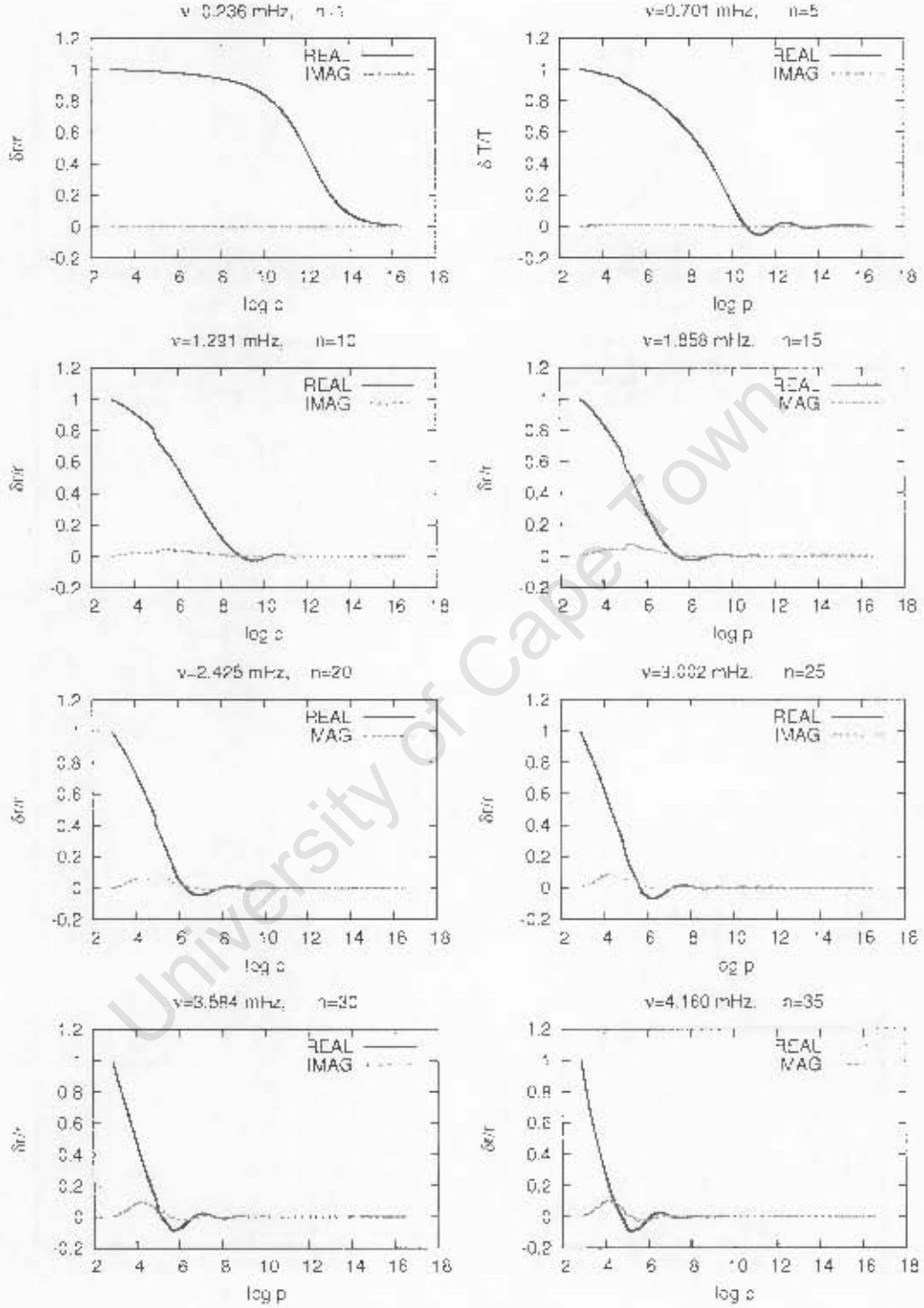

Figure 3.21: The real and imaginary parts of $\delta r/r$ for the $1.3M_{\odot}$ model plotted as a function of depth at various frequencies.

3.4.2.4 $1.5M_{\odot}$ model

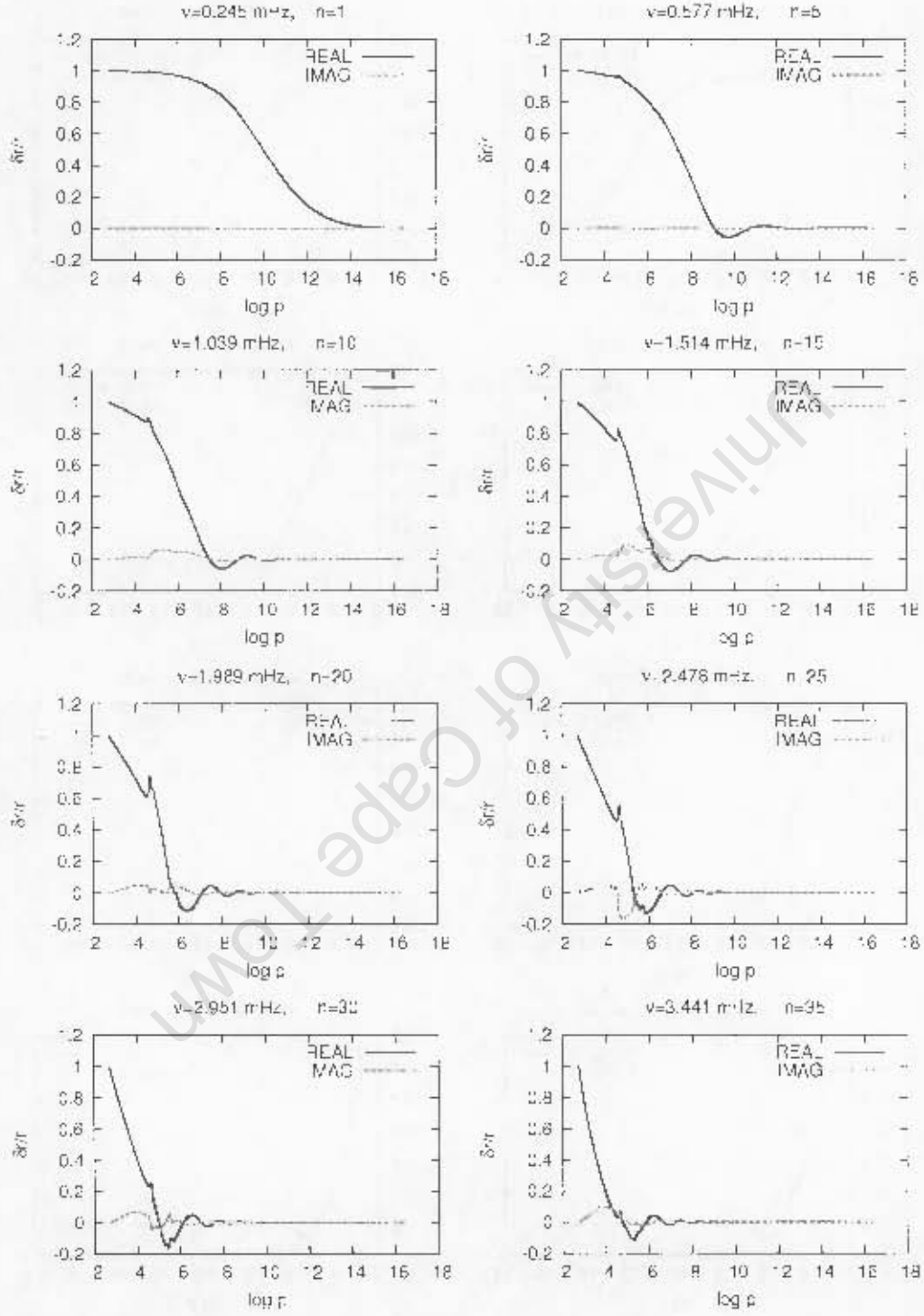

Figure 3.22: The real and imaginary parts of $\delta r/r$ for the $1.5M_{\odot}$ model plotted as a function of depth at various frequencies.

3.4.2.5 $1.6M_{\odot}$ model

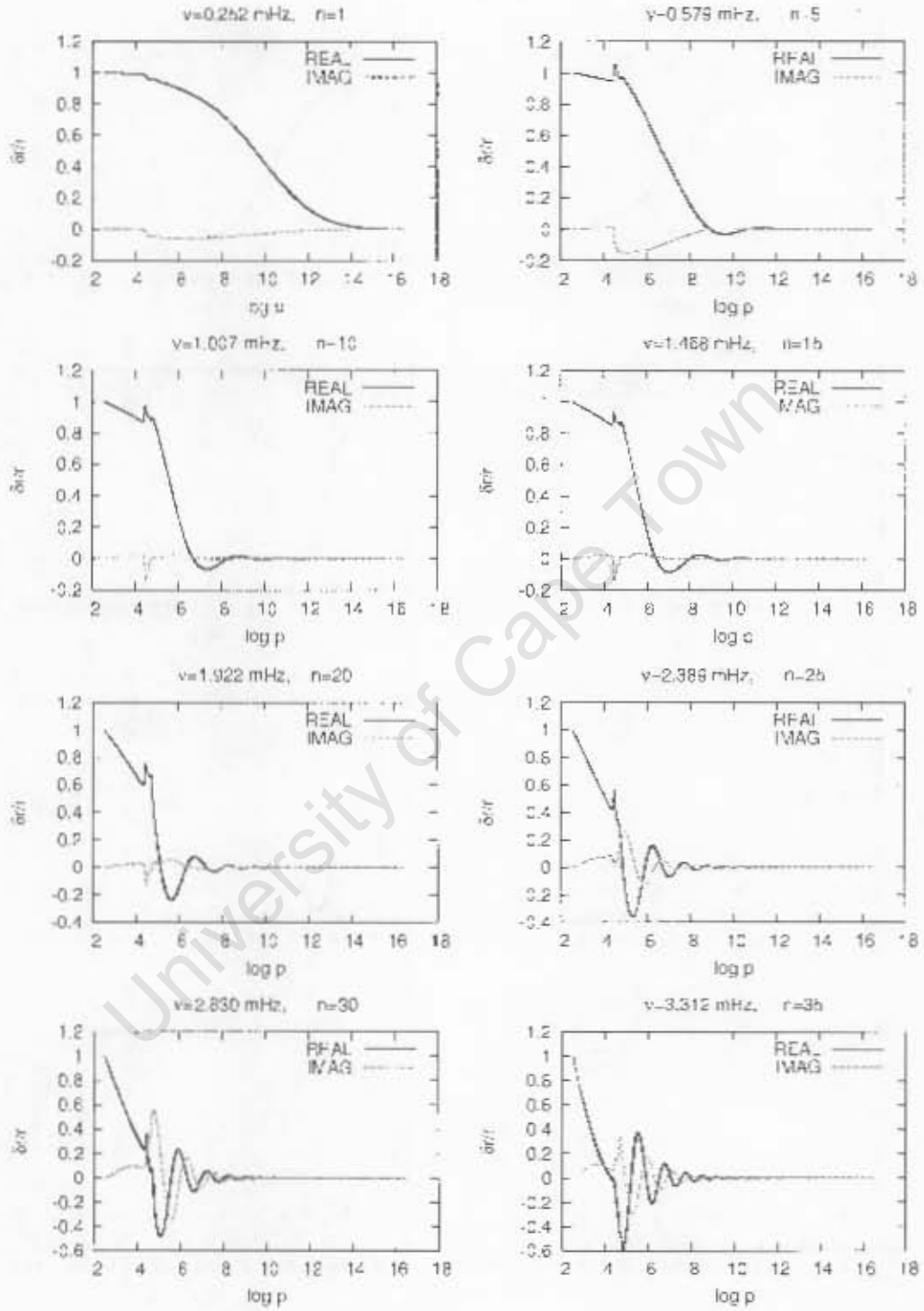

Figure 3.23: The real and imaginary parts of $\delta r/r$ for the $1.6M_{\odot}$ model plotted as a function of depth at various frequencies.

3.4.2.6 $1.8M_{\odot}$ model

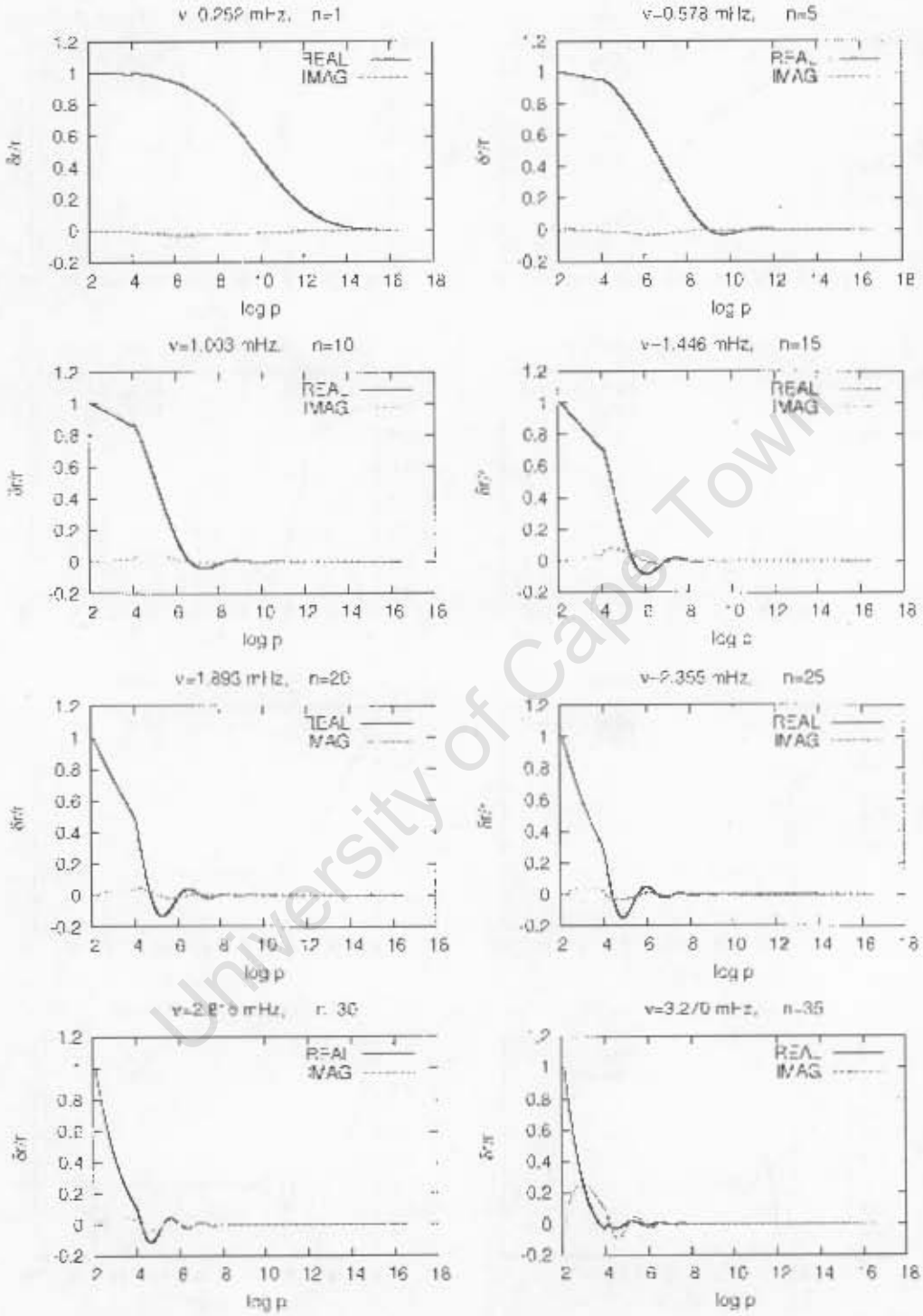

Figure 3.24: The real and imaginary parts of $\delta r/r$ for the $1.8M_{\odot}$ model plotted as a function of depth at various frequencies.

3.4.2.7 $2.0M_{\odot}$ model

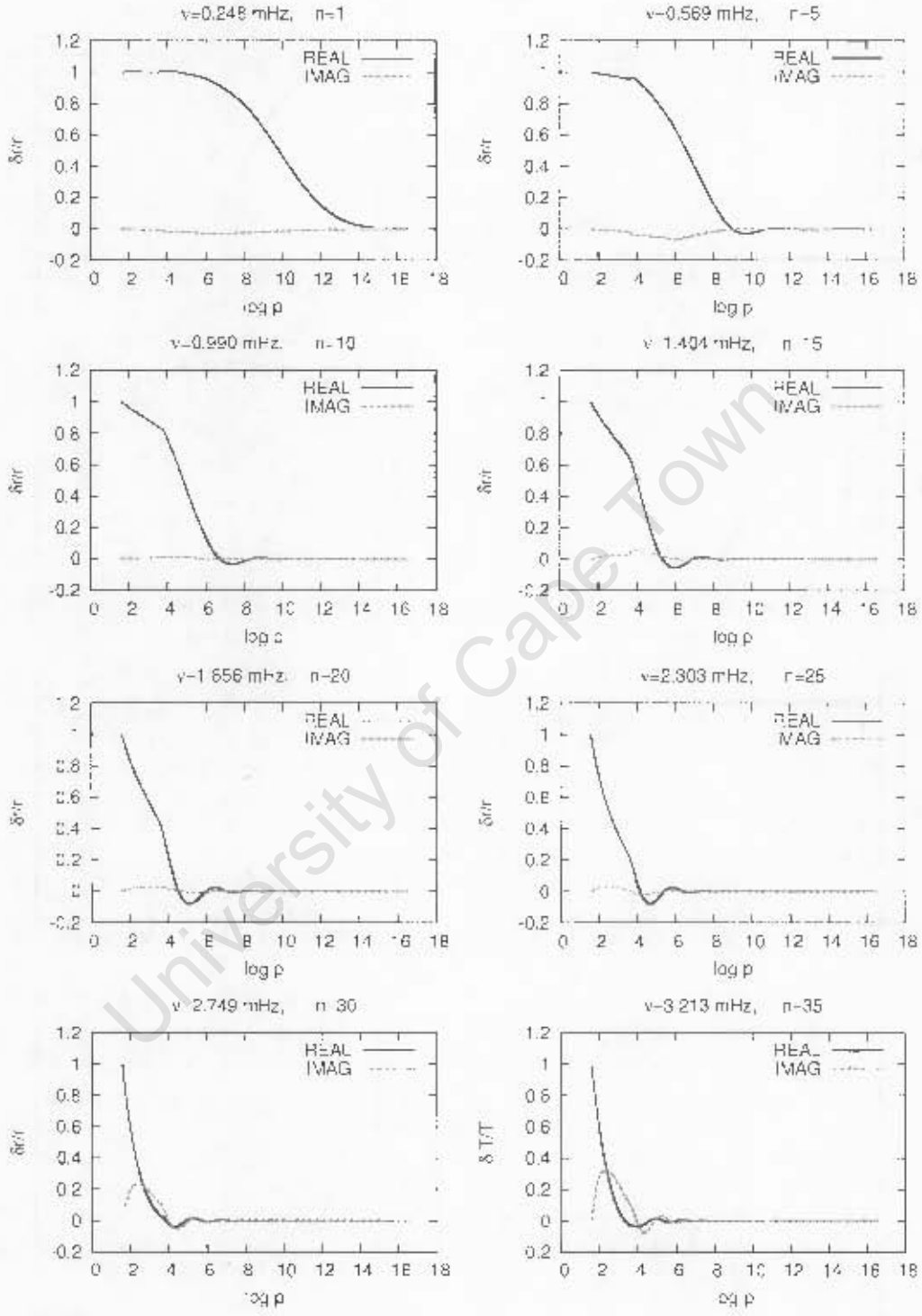

Figure 3.25: The real and imaginary parts of $\delta r/r$ for the $2.0M_{\odot}$ model plotted as a function of depth at various frequencies.

3.4.2.8 $2.1M_{\odot}$ model

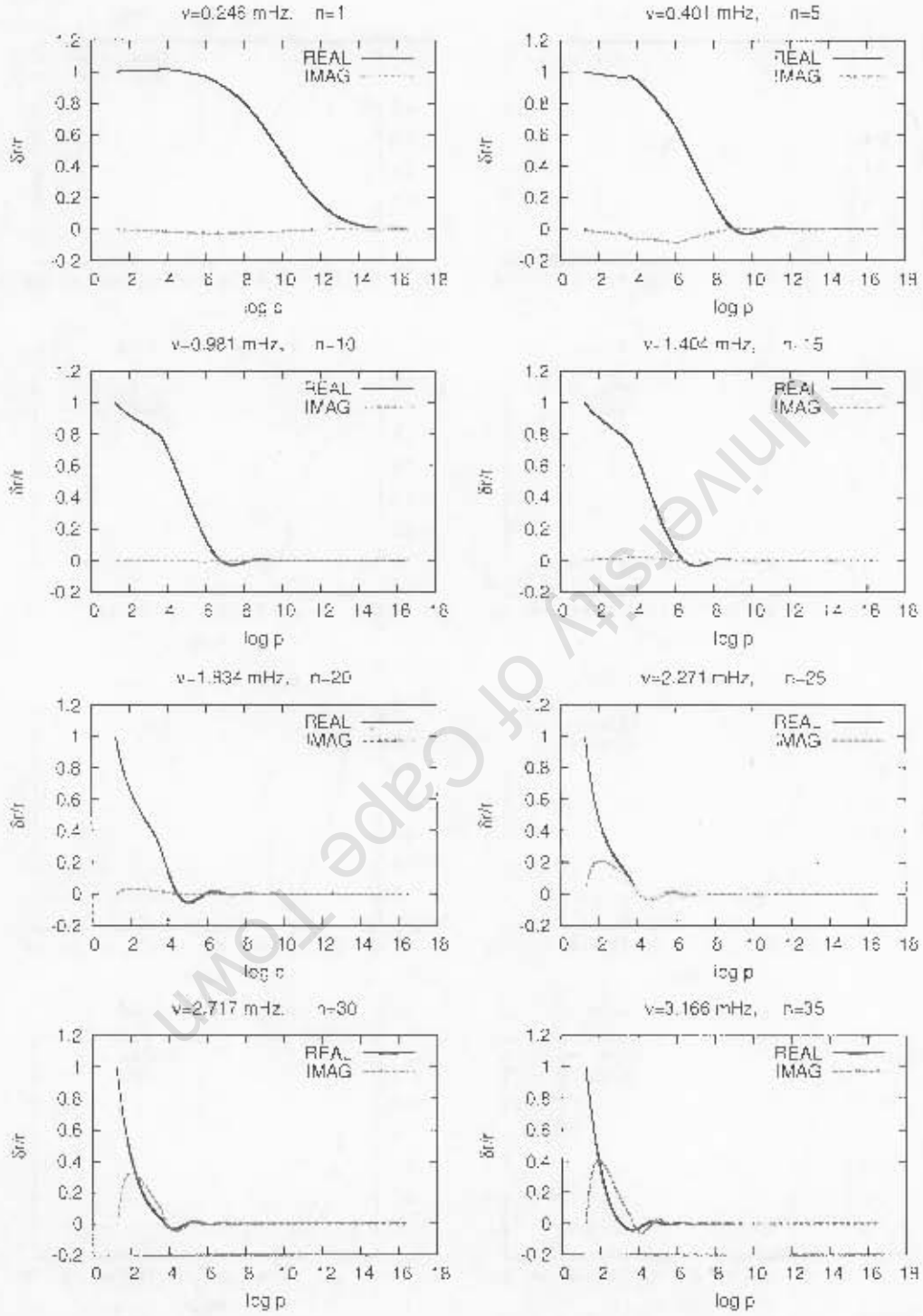

Figure 3.26: The real and imaginary parts of $\delta T/T$ for the $2.1M_{\odot}$ model plotted as a function of depth at various frequencies.

3.5 Growth rates

The growth rates defined $\eta = -\omega_i$ for the equilibrium models listed in Table 3.1 are shown in Fig. 3.27 where ω_i is the imaginary part of the cyclic frequency ω obtained by solving the non-adiabatic pulsation equations presented in Chapter 2. The growth rates are obtained by using the boundary condition that imposes a displacement node at the base of the envelope. Here $\eta > 0$ corresponds to excitation and $\eta < 0$ corresponds to damping.

It is noticeable that there are unstable modes in the roAp frequency region $1.0 < \nu < 3.0$ mHz for the $1.5M_{\odot}$ and $1.6M_{\odot}$ models. The excitation of modes at high frequency in spite of not including the magnetic field in our equilibrium models as was done by Balmforth et al (2001) is an interesting results. For the models with $M \geq 1.5M_{\odot}$ there is a depression in the growth rates just below 2 mHz with 1.5 and $1.8M_{\odot}$ more depressed. It was shown by Balmforth (1992a) that as the non-local mixing length parameters a and b are reduced the depression becomes deeper and shifts to higher frequency. I also notice that there is sharp variations in the growth rates for $1.6M_{\odot}$ model at higher frequencies which according to Balmforth is due to the reduction of non-local parameters a and b. In our case as mentioned in Section 3.1, the mixing length parameters used for our models are $a^2 \quad b^2 \quad 300$ and $\alpha_c = 1.8$. On the other hand if a and b are reduced as shown in Fig. 1.5 the treatment of convection in the equilibrium models reduced to be local. In Fig. 3.28, it is clear that in the roAp frequency region $1.0 < \nu < 3.0$ mHz the growth rates increase as the model parameters ($M/M_{\odot}$, T_{eff}, $L/L_{\odot}$) increase, however the $1.5M_{\odot}$ and $1.6M_{\odot}$ models seem not to follow that trend. In the roAp stars regime the excited modes at the high frequencies are due to the sufficiently strong magnetic fields that suppress envelope convection (see Balmforth et al 2001, Cunha 2002). At the lower frequencies the damping of lower frequencies is due to helium settling (see Cunha & Sousa 2006).

In doing some analysis the imaginary part ω_i can be approximated as follows (see Christensen-Dalsgaard 2003):

$$\omega_i \approx \frac{C_r}{2\omega_r^2 E} \tag{3.4}$$

where

$$C_r = -L_0 \int_M \frac{\delta\rho}{\rho_0}(\Gamma_3 - 1)\frac{d}{dm}\left(\frac{\delta L}{L_0}\right) dm \tag{3.5}$$

and

$$E \quad \int_{r_b}^{r} \rho|\delta r|^2 r^2 dr \tag{3.6}$$

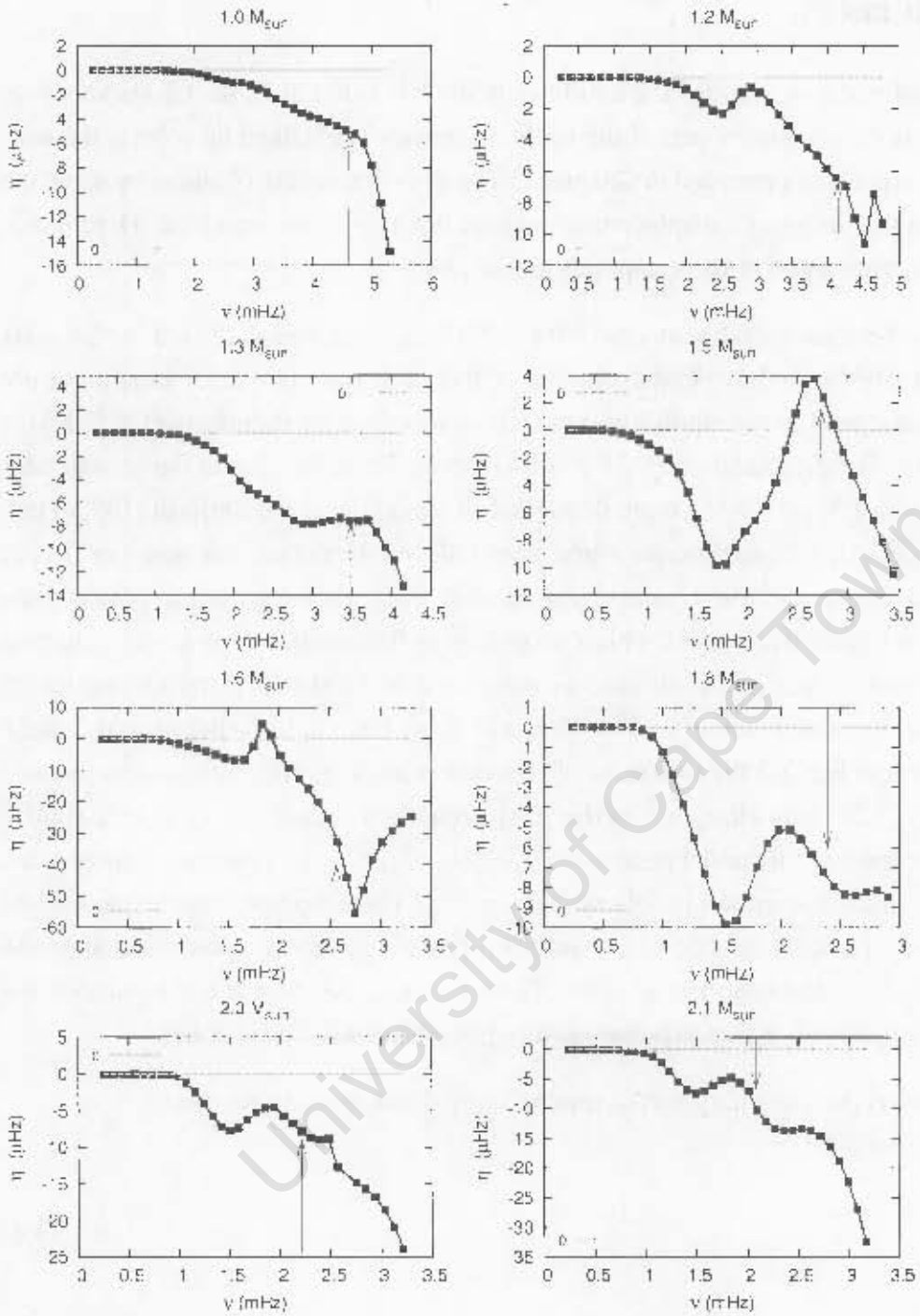

Figure 3.27: The growth rates as function of the cyclic frequency ν for ZAMS models. They are obtained from using the upper boundary condition (2.130) that takes into consideration the fact that modes with $\omega > \omega_{ac}$ are not reflected but propagate through the atmosphere. The arrow indicates the acoustic cut-off frequency.

is the pulsational energy and L_0 is the total luminosity. Therefore we approximate and rearrange energy equation (2.37) as follows:

$$\frac{d}{dm}\left(\frac{\delta L}{L_0}\right) \approx \left(\frac{\delta T}{T_0} - \nabla_{ad}\frac{\delta p}{p_0}\right) - \left(\nu_1\frac{\delta T}{T_0} - \nabla_{ad}\frac{\delta p_t}{p_0}\right) \tag{3.7}$$

where $\nu_1 = p_t/p_0$, and the expression on the first open bracket on the right hand side is the total pressure contribution and the second is the turbulent pressure contribution.

We have shown in Fig. 3.5 that the expression enclosed in the first bracket is zero in the envelope. Also in parts of the envelope where $\nu_1\delta T/T = 0$ and $\nabla_{ad}\delta p_t/p = 0$, there is no turbulence and hence no damping or excitation. But where $\nu_1 \neq 0$ and $\delta p_t \neq 0$ turbulence contributes to damping or excitation.

In the atmosphere $\nu_1 = \delta p_t = 0$ and therefore the damping or excitation comes purely from radiative transfer. If $\nu_1\delta T/T_0 + \nabla_{ad}\delta p_t/p_0 < 0$ there will be excitation, and if $\nu_1\delta T/T_0 + \nabla_{ad}\delta p_t/p_0 > 0$ there will be damping.

3.6 Work Integral

The work integral can be used to locate the damping or excitation zones in the star. In the regions where $W_{tot} > 0$ the pulsation is damped, and where $W_{tot} < 0$ the pulsation is excited. The work integral expressions is given as (see section 2.3):

$$W_{tot}(m) \approx W_g(m) + W_t(m) \tag{3.8}$$

where

$$W_g(m) = \pi\int_{m_b}^{m} \mathrm{Im}(\delta p_g^*\delta\rho)\frac{dm}{\rho_0^2}, \tag{3.9}$$

and

$$W_t(m) = \pi\int_{m_b}^{m} \mathrm{Im}(\delta p_t^*\delta\rho)\frac{dm}{\rho_0^2} \tag{3.10}$$

is the contribution due to gas and turbulent pressures respectively. The growth rate η, in terms of the work integrals (Equations 3.9 and 3.10), can be divided into its contributions from the gas and turbulent pressures as:

$$\eta_g = \frac{\omega_r W_g(M)}{4\pi E_k} \tag{3.11}$$

and

$$\eta_t = \frac{\omega_r W_t(M)}{4\pi E_k}. \tag{3.12}$$

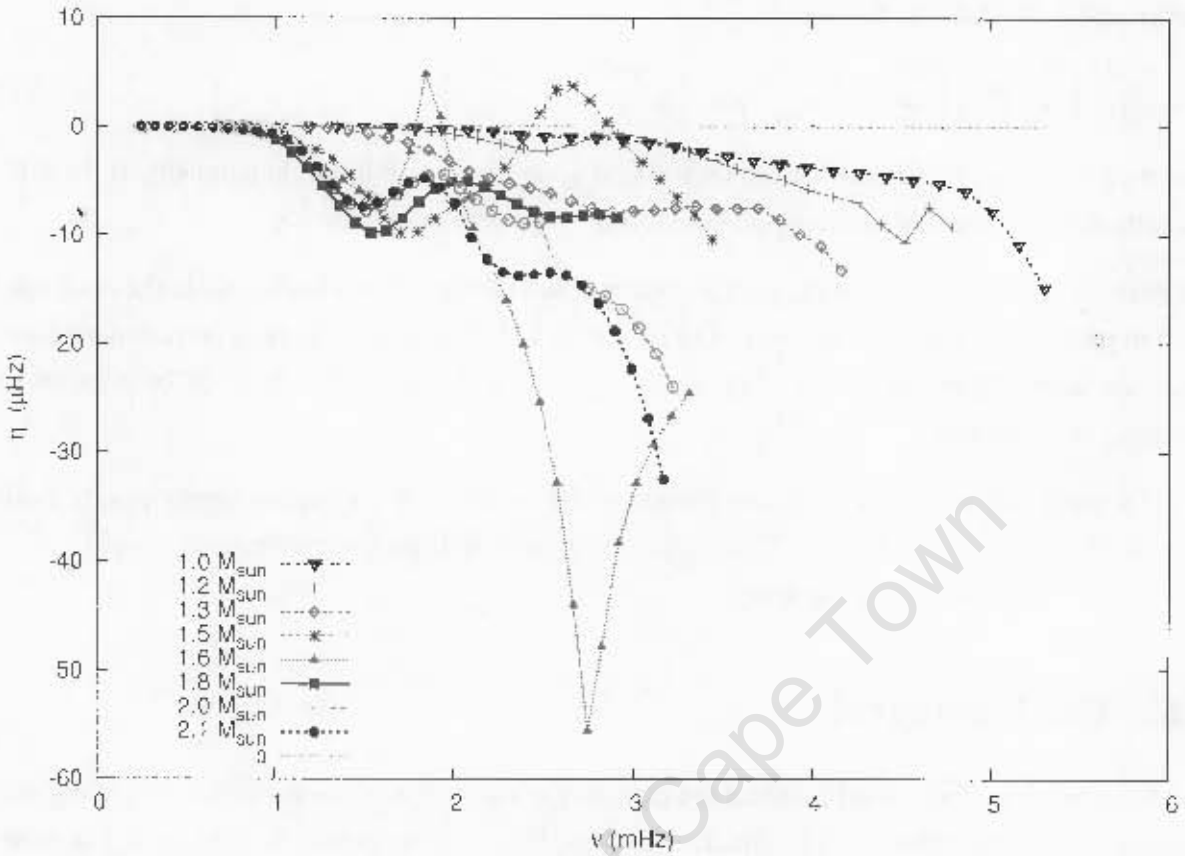

Figure 3.28: Growth rates as a function of frequency for ZAMS models listed in Table 3.1.

where F_k is defined in equation (2.144).

In explaining the unstable modes that appear in the $1.5M_\odot$ and $1.6M_\odot$ models the growth rates η, η_g and η_t are plotted as a function of pulsation frequency in Figures 3.29 and 3.30. We notice that for $1.5M_\odot$ model below 2 mHz both η_g and η_t are negative meaning that the combination of gas and turbulent pressures stabilizes the modes. However the stabilization by gas pressure is much stronger. In the frequency regime $2 < \nu < 3.5$ mHz the modes are unstable due to gas pressure fluctuations. It is clear that for $1.6M_\odot$ model in the frequency regime $1.5 < \nu < 2$ mHz the modes are unstable due to turbulent pressure fluctuations. Below frequency 1.5 mHz and above frequency 2 mHz both the gas and turbulent pressures stabilize the modes. The stabilization by turbulent pressure is much stronger.

In Figures 3.31-3.38 the accumulated work integral for ZAMS equilibrium models listed in Table 3.1 for several frequencies are shown. Here the work integrals are plotted such as to have zero value at the bottom of the model envelope. Therefore in the regions where $W_{tot} > 0$ the

pulsation is damped, and where $W_{tot} < 0$ the pulsation is excited. In those Figures we have also shown the work integral for the same frequencies when the contribution from the turbulent pressure is neglected (i.e W_g in Eq. 3.9). In all the equilibrium models considered here the modes gain most of their energy from the hydrogen ionization zone. Clearly for models with $M < 1.8M_{\odot}$, as was reported by Balmforth et al (2001), turbulent pressure stabilizes all the modes in the hydrogen ionization zone. For models with $M \geq 1.8M_{\odot}$ the contribution from turbulent pressure is negligible.

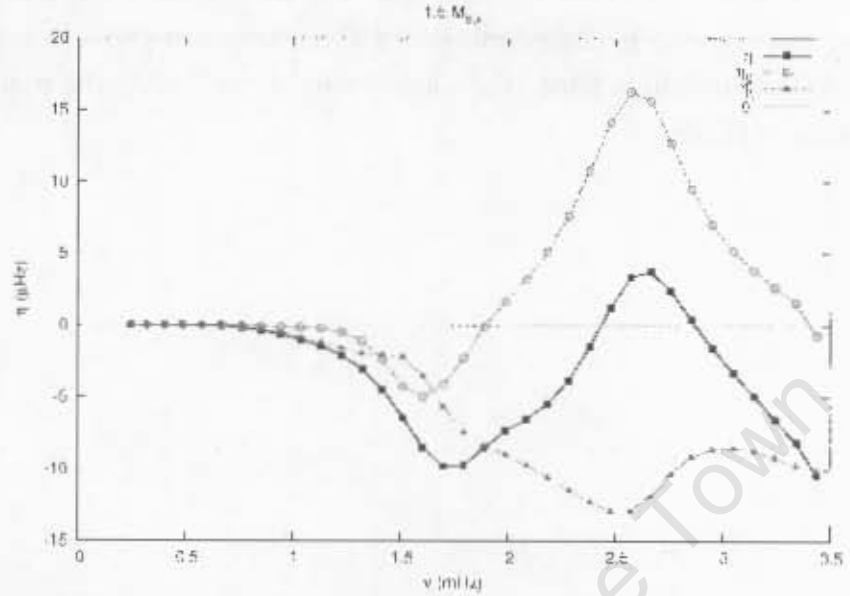

Figure 3.29: The quantities η, η_g and η_l plotted as functions of frequency for $1.5M_\odot$ model.

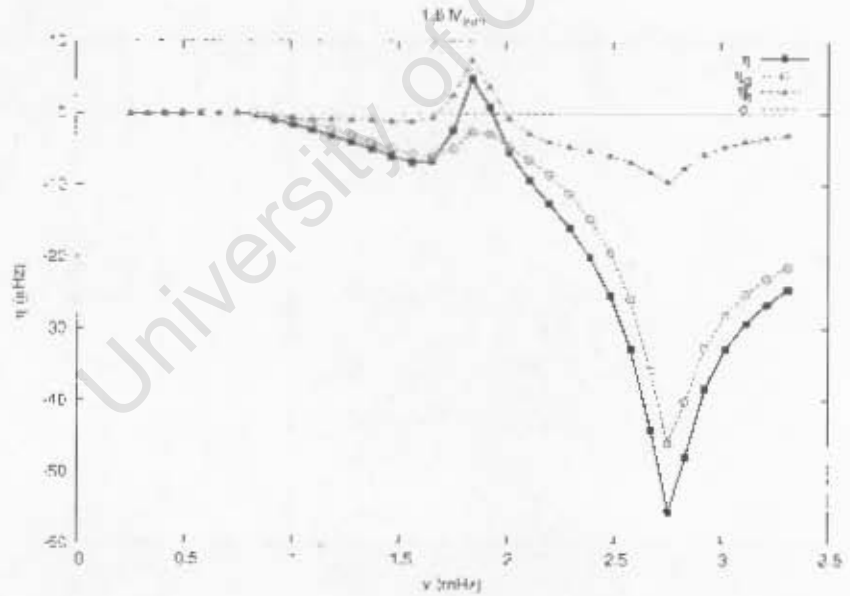

Figure 3.30: The quantities η, η_g and η_l plotted as functions of frequency for $1.6M_\odot$ model.

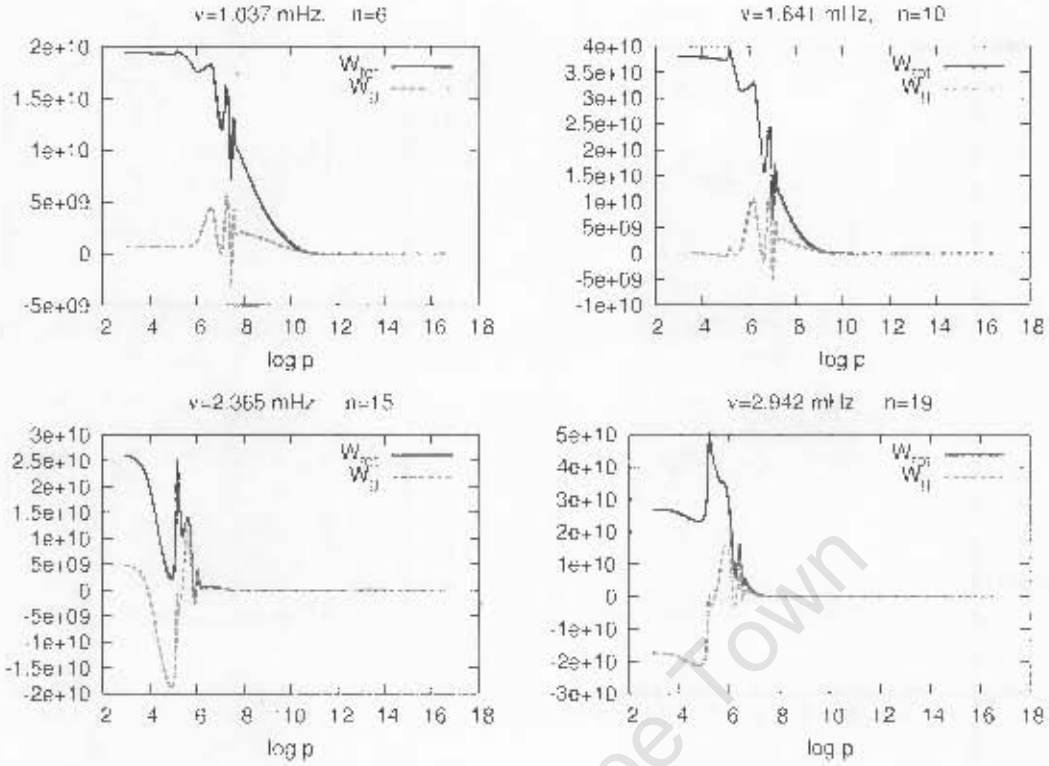

Figure 3.31: The accumulated work integrals (W_{tot}) (in units $10^{30} erg$) for the $1.0 M_{\odot}$ model at various frequencies. The curve labelled W_g shows the work integral for the same mode when the contribution from the turbulent pressure is neglected.

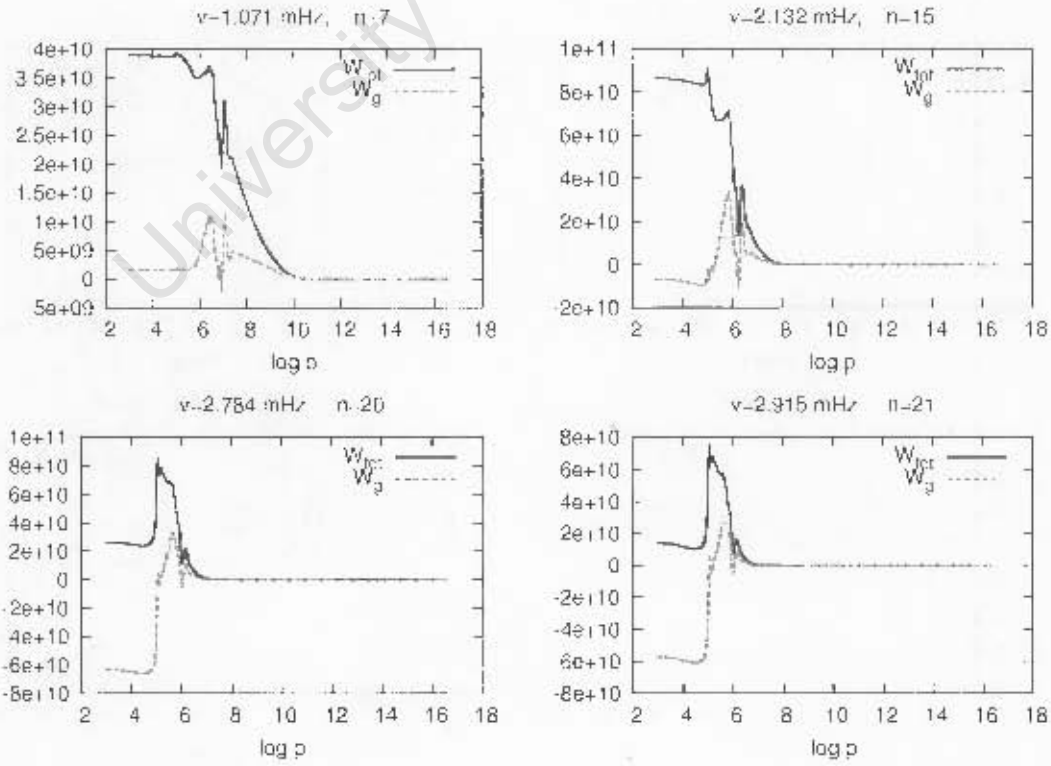

Figure 3.32: The accumulated work integrals (W_{tot}) (in units $10^{30} erg$) for the $1.2 M_{\odot}$ model at various frequencies. The curve labelled W_g shows the work integral for the same mode when the contribution from the turbulent pressure is neglected.

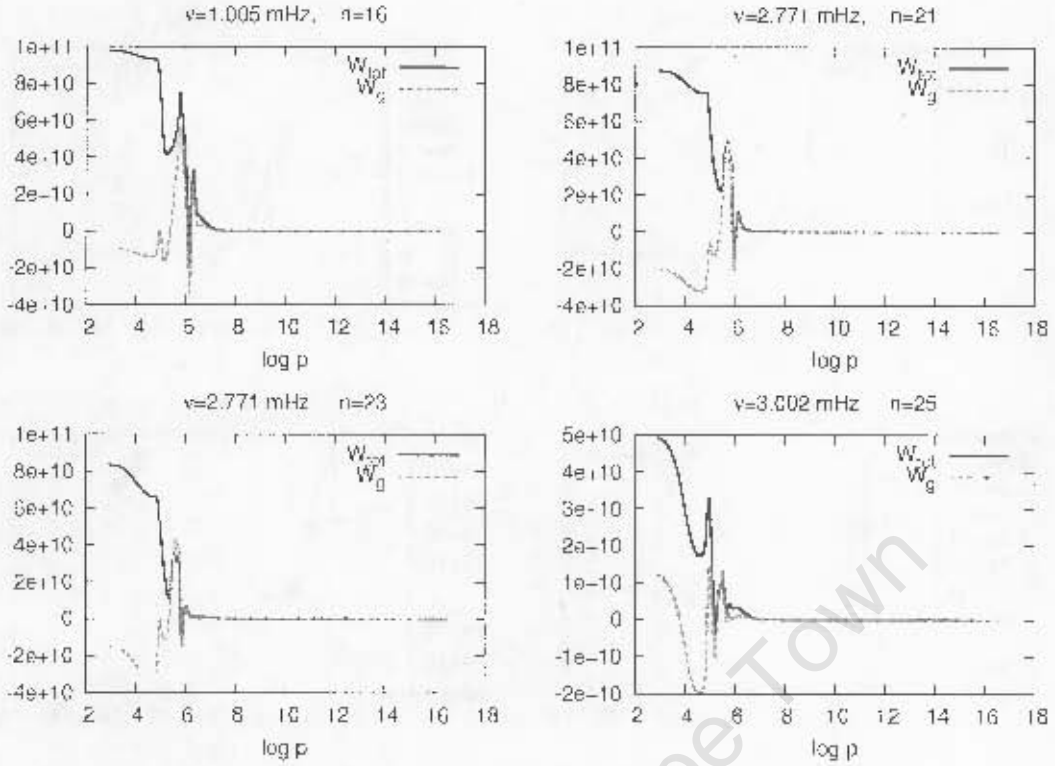

Figure 3.33: The accumulated work integrals (W_{tot}) (in units $10^{30} erg$) for the $1.3M_{\odot}$ model at various frequencies. The curve labelled W_g shows the work integral for the same mode when the contribution from the turbulent pressure is neglected.

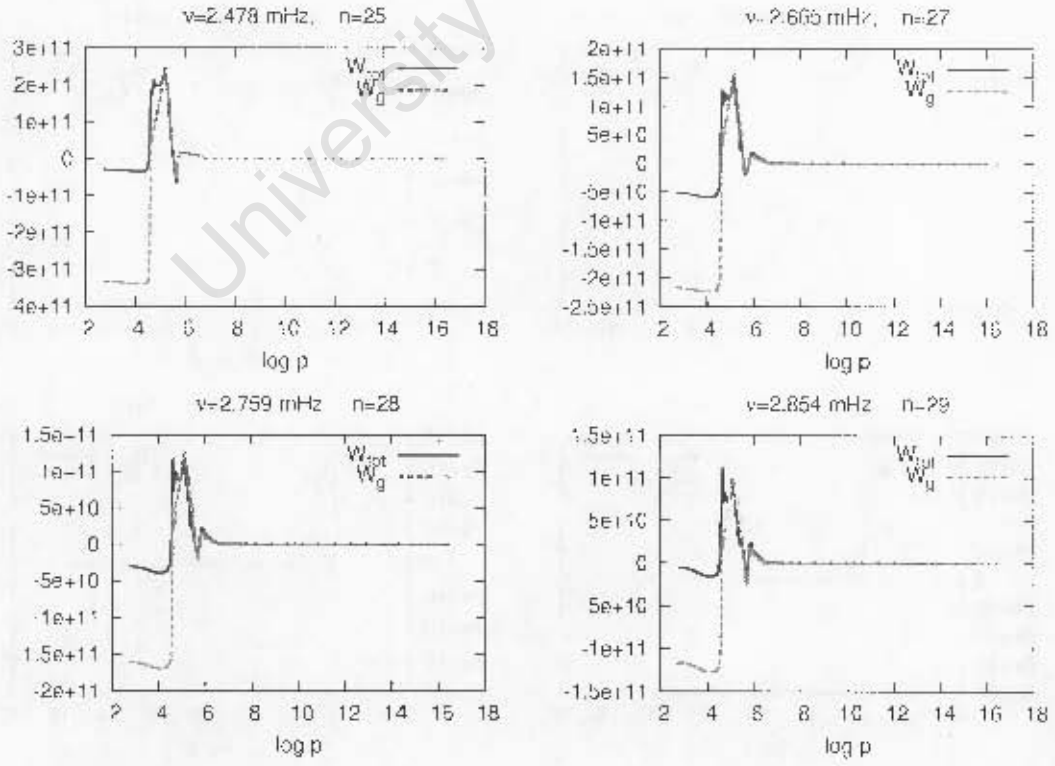

Figure 3.34: The accumulated work integrals (W_{tot}) (in units $10^{30} erg$) for the $1.5M_{\odot}$ model at various frequencies. The curve labelled W_g shows the work integral for the same mode when the contribution from the turbulent pressure is neglected.

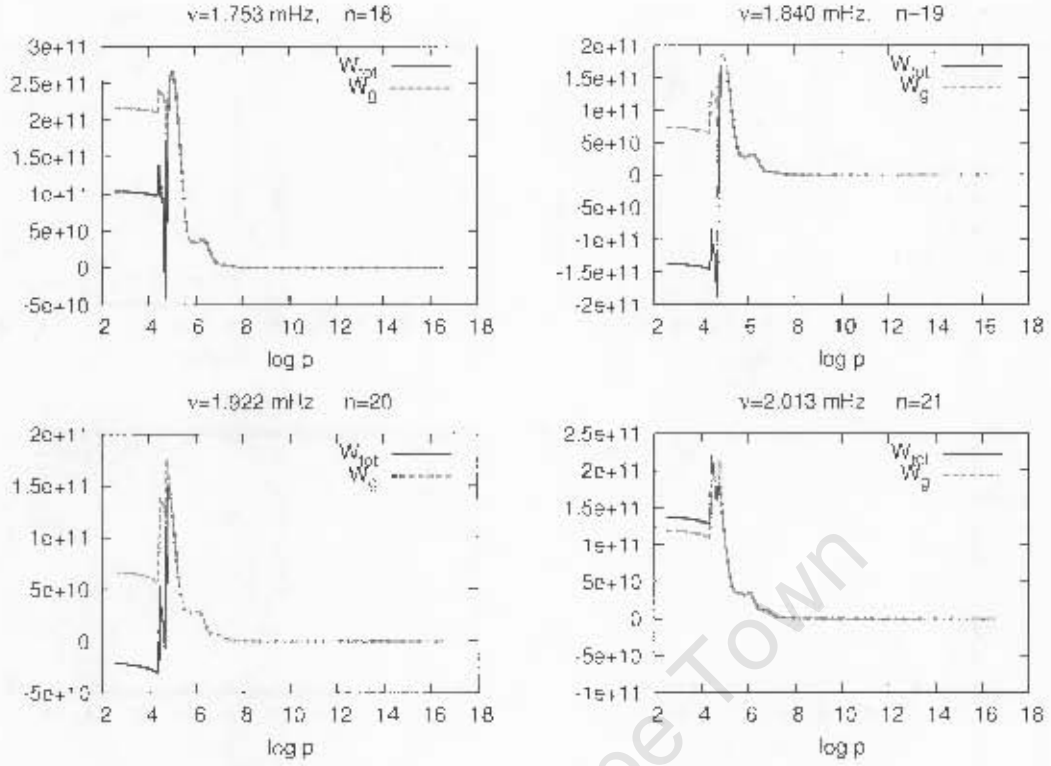

Figure 3.35: The accumulated work integrals (W_{tot}) (in units $10^{30} erg$) for the $1.6 M_{\odot}$ model at various frequencies. The curve labelled W_g shows the work integral for the same mode when the contribution from the turbulent pressure is neglected.

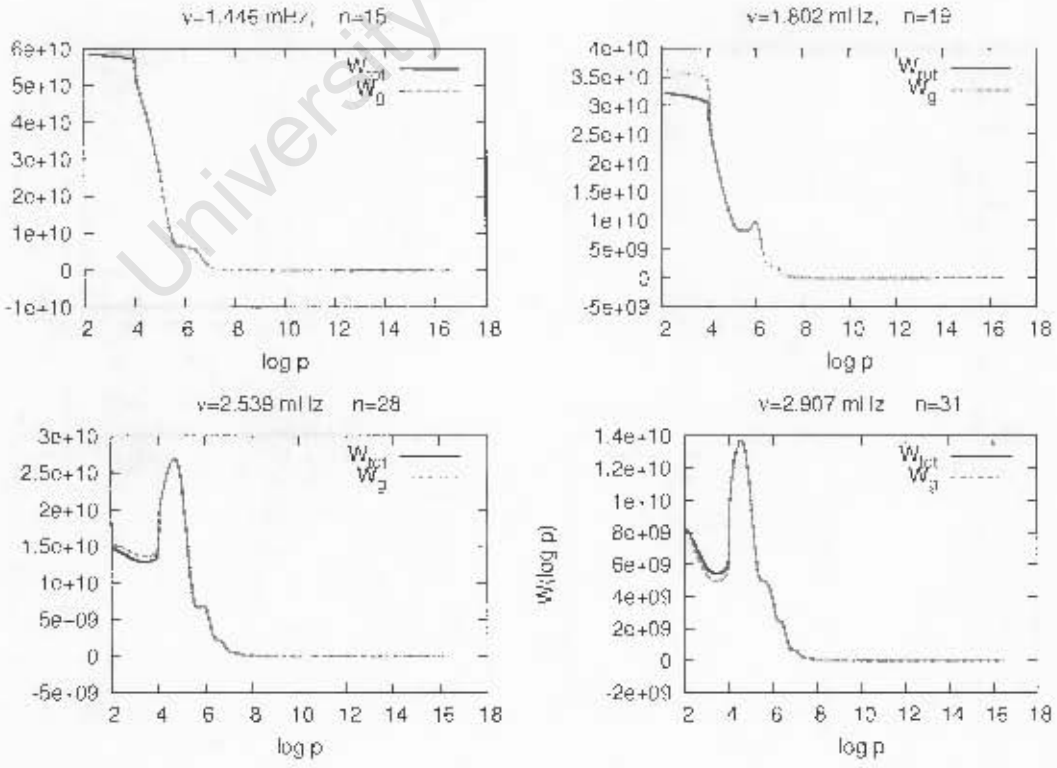

Figure 3.36: The accumulated work integrals (W_{tot}) (in units $10^{30} erg$) for the $1.8 M_{\odot}$ model at various frequencies. The curve labelled W_g shows the work integral for the same mode when the contribution from the turbulent pressure is neglected.

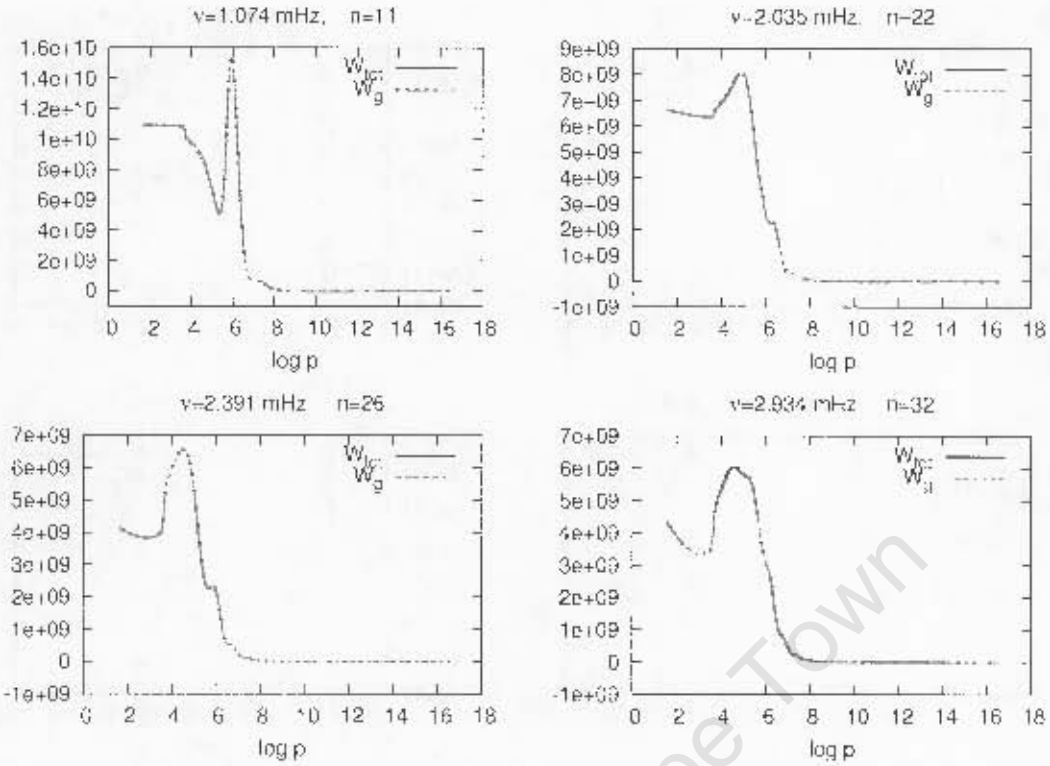

Figure 3.37: The accumulated work integrals (W_{tot}) (in units $10^{30} erg$) for the $2.0 M_{\odot}$ model at various frequencies. The curve labelled W_g shows the work integral for the same mode when the contribution from the turbulent pressure is neglected.

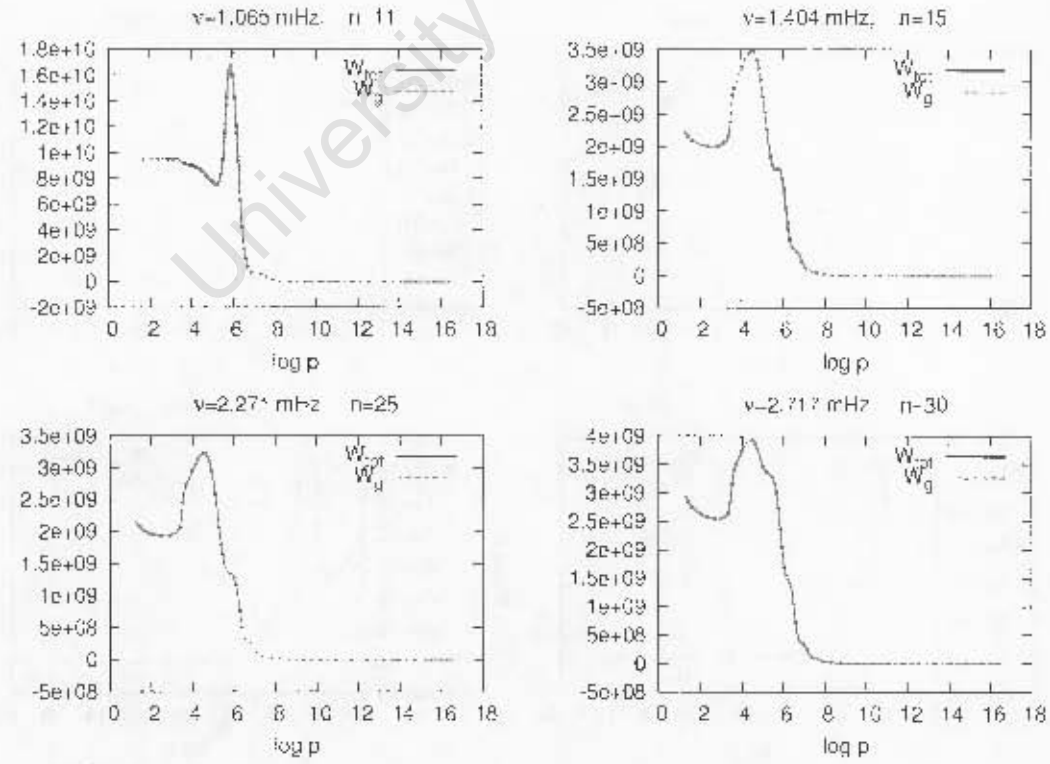

Figure 3.38: The accumulated work integrals (W_{tot}) (in units $10^{30} erg$) for the $2.1 M_{\odot}$ model at various frequencies. The curve labelled W_g shows the work integral when the contribution from the turbulent pressure is neglected.

Chapter 4

Comparison of radiative transfer and Eddington approximation

The solutions obtained using my code (hereafter the new code) and those obtained using Houdek's code are compared. Houdek's code uses the non-local mixing length theory of convection and Eddington approximation to radiative transfer (see Appendix D). We also consider the results obtained using both the equilibrium and pulsation models without convection. Furthermore, I compare the new code with Medupe's code (see Appendix F) which is purely radiative.

4.1 Comparison of Houdek's results with my results

In both cases the results are based on the equilibrium models presented in Table 3.1 and the upper mechanical boundary condition that allows waves with frequencies higher than the acoustic cut-off frequency to propagate through the atmosphere.

4.1.1 The effect on the eigenfrequencies

The eigenfrequencies were computed by requiring that there be a displacement node at the base of the envelope and solving for real and imaginary parts of ω. For comparison purposes I denote the cyclic frequency obtained from Houdek's code as $\nu_{f_{eq}}$ and the one obtained from the new code as $\nu_{f_{osc}}$.

The two approaches are compared in Fig. 4.1. In this figure, the top panel shows $\Delta\nu_r = Re(\nu_{f_{osc}}) - Re(\nu_{f_{eq}})$ and the bottom panel shows $\Delta\nu_i = Im(\nu_{f_{osc}}) - Im(\nu_{f_{eq}})$ where Re and Im denote the real and imaginary parts respectively. This means $\Delta\nu_r = 0$ and $\Delta\nu_i = 0$ implies that the two approaches give the same eigenfrequencies. Clearly from this figure, there is no difference in the calculated frequencies below the frequency 1 mHz irrespective of the equilibrium models. The difference between MP and GH codes are in the atmospheric and sub-atmospheric layers. They both treat the envelope using the same physics. Secondly the low frequencies are sensitive only to deeper parts of the star because that is where the waves spend most of their time.

Hence there is little or no differences in frequencies, below 1 mHz, obtained by the two codes. For frequencies higher than 1 mHz, the difference is somewhat larger but still fairly small on the calculated eigenfrequencies. The largest difference is found in the $1.6M_{\odot}$ model near frequency ν =2 mHz. The difference indicates the error introduced by using Eddington approximation to radiation when calculating eigenfrequencies for A stars. The maximum relative changes in eigenfrequencies for various equilibrium models are listed in Table 4.1.

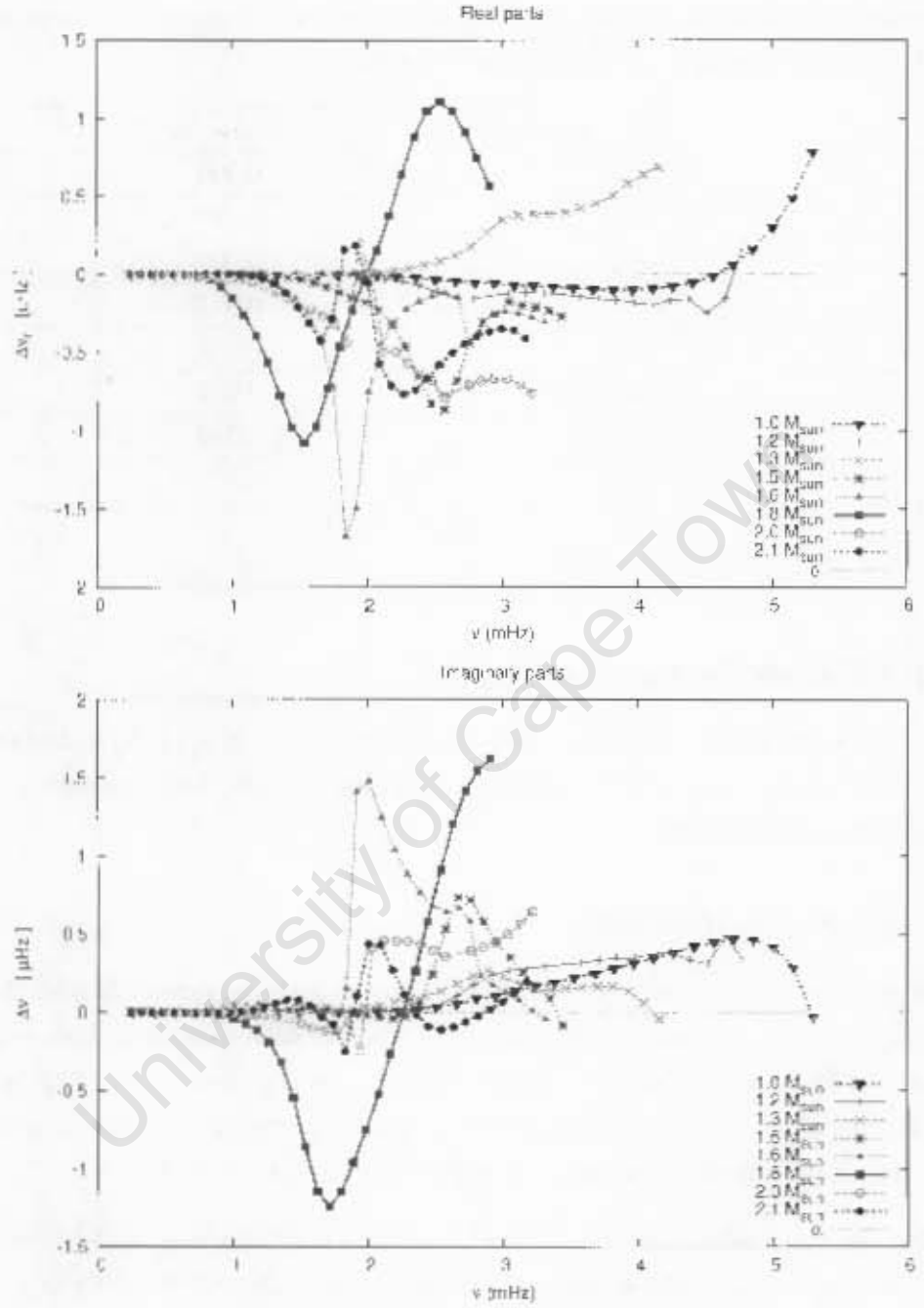

Figure 4.1: The difference between the eigenfrequencies obtained using the new code and the eigenfrequencies computed using Houdek's code for the ZAMS models. The upper panel shows the real part, and the lower shows the imaginary part.

Table 4.1: The maximum differences between the eigenfrequencies obtained using the new code and the eigenfrequencies obtained using Houdek's code. The first column denotes the mass of the equilibrium models, the second column denote the changes $|\Delta\nu_r|$ relative to cyclic frequency ν_r (in mHz), and the third column denotes the changes $|\Delta\nu_i|$ relative to ν_r (in mHz).

$M/M_\odot$	$\lvert\Delta\nu_r/\nu_r\rvert$ (%)	$\lvert\Delta\nu_i/\nu_r\rvert$ (%)
1.0	0.014	0.009
1.2	0.006	0.010
1.3	0.017	0.009
1.5	0.033	0.027
1.6	0.091	0.072
1.8	0.070	0.073
2.0	0.034	0.019
2.1	0.027	0.022

4.1.2 The effect on the eigenfunctions

The new code improves treatment of radiation in the atmosphere only. In the rest of the star the new code uses the same treatment of radiation as in Houdek's code. I only present temperature and displacement eigenfunctions.

4.1.2.1 Temperature eigenfunctions

Here we compare the temperature eigenfunctions obtained from the new code with those using Houdek's code. The plots are shown in Figures 4.2-4.9 where each panel is divided into real and imaginary parts of $\delta T/T$ above the photosphere. There is a large difference in $\delta T/T$ between the two approaches for all the models considered here. The largest relative differences for various equilibrium models are shown in the captions of Figures 4.2-4.9.

It is clear that for the models with $M \geq 1.8M_\odot$ there is a difference in the depth of a dip between the two approaches. The relative difference is up to about 70%, 60% and 11.7% for $1.8M_\odot$, $2.0M_\odot$ and $2.1M_\odot$ models respectively.

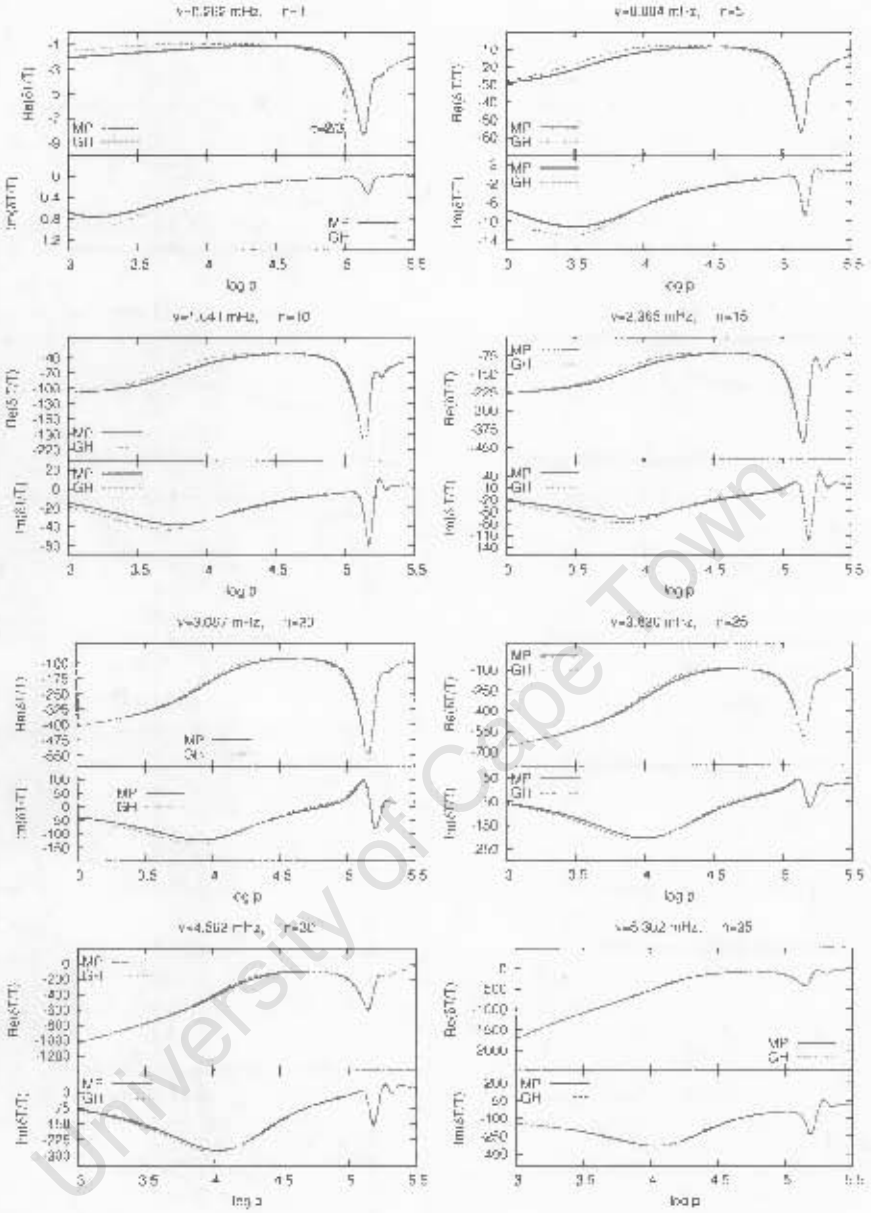

Figure 4.2: A comparison of real and imaginary parts $\delta T/T$ obtained from the the new code (MP) and those using Houdek's code (GH) for the $1.0M_{\odot}$ model at various frequencies. Each panel is divided into real and imaginary parts of temperature eigenfunctions. The position of optical depth $\tau = 2/3$ is indicated on the first panel by an arrow. The largest relative difference between using proper treatment of radiation and Eddington approximation is up to about 25%.

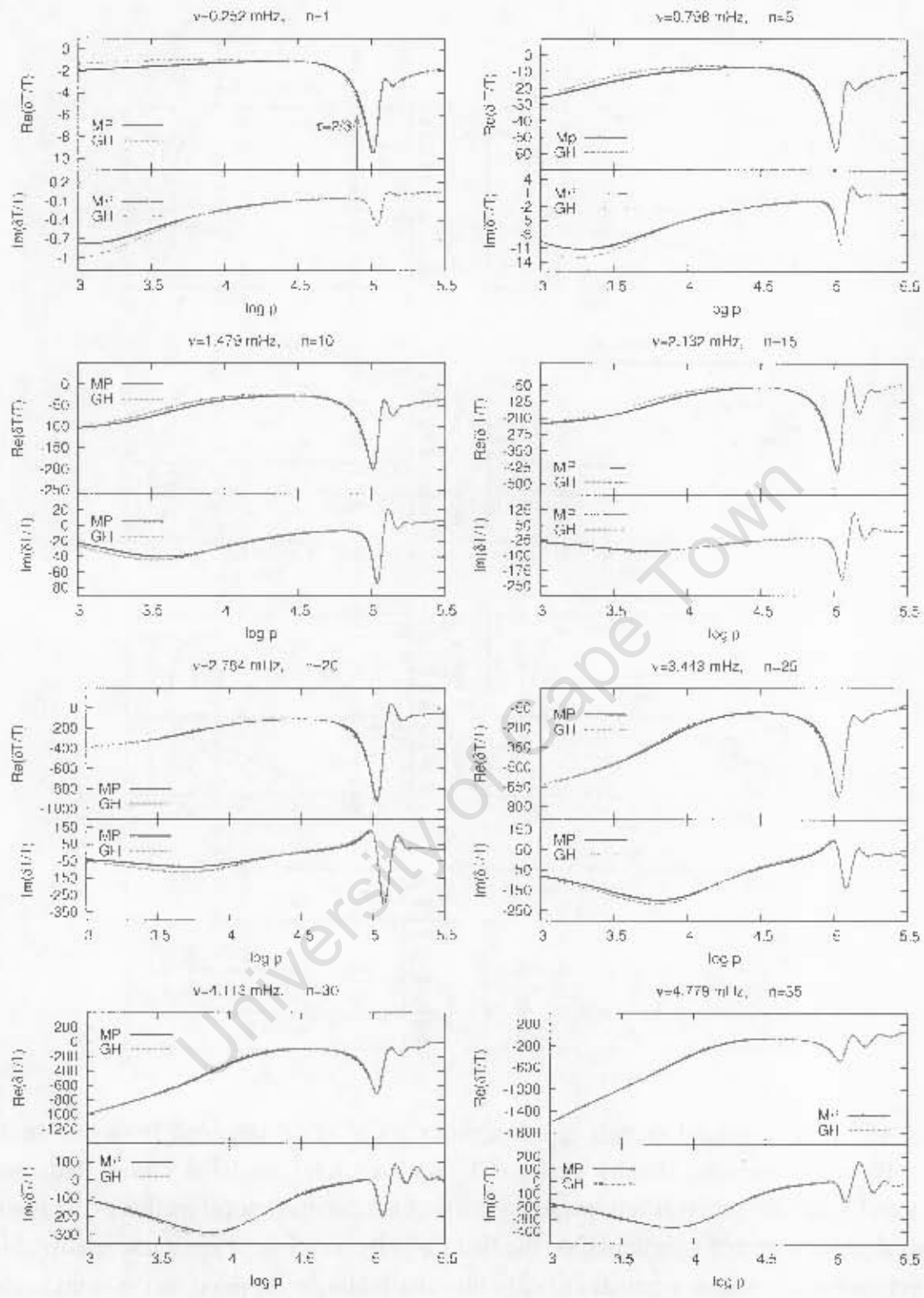

Figure 4.3: A comparison of real and imaginary parts $\delta T/T$ obtained from the new code (MP) and those using Houdek's code (GH) for the $1.2M_{\odot}$ model at various frequencies. Each panel is divided into real and imaginary parts of temperature eigenfunctions. The position of optical depth $\tau = 2/3$ is indicated on the first panel by an arrow. The largest relative difference between using proper treatment of radiation and Eddington approximation is up to about 30%.

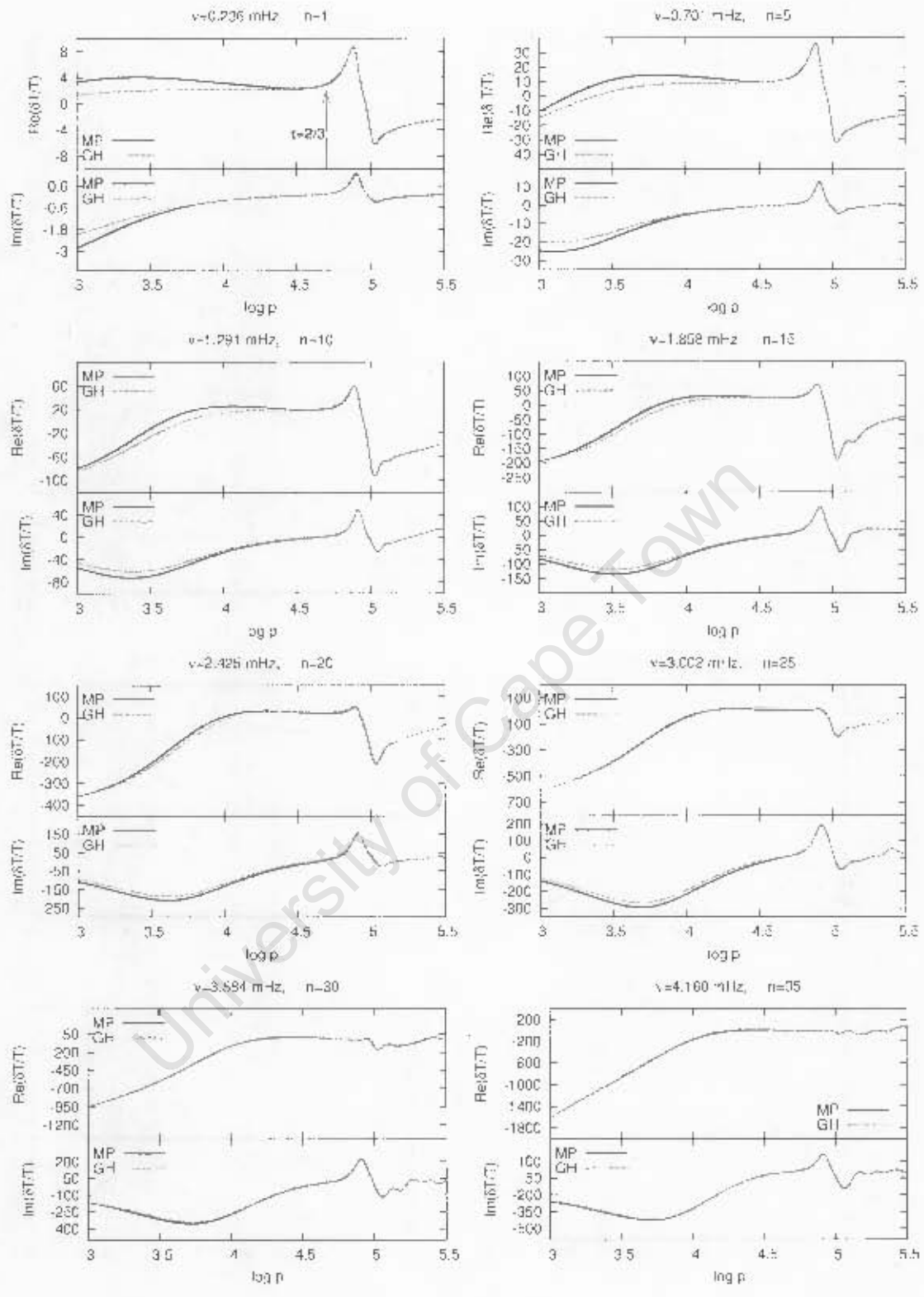

Figure 4.4: A comparison of real and imaginary parts $\delta T/T$ obtained from the new code (MP) and those using Houdek's code (GH) for the $1.3M_{\odot}$ model at various frequencies. Each panel is divided into real and imaginary parts of temperature eigenfunctions. The position of optical depth $\tau = 2/3$ is indicated on the first panel by an arrow. The largest difference between using proper treatment of radiation and Eddington approximation is up to about 72%.

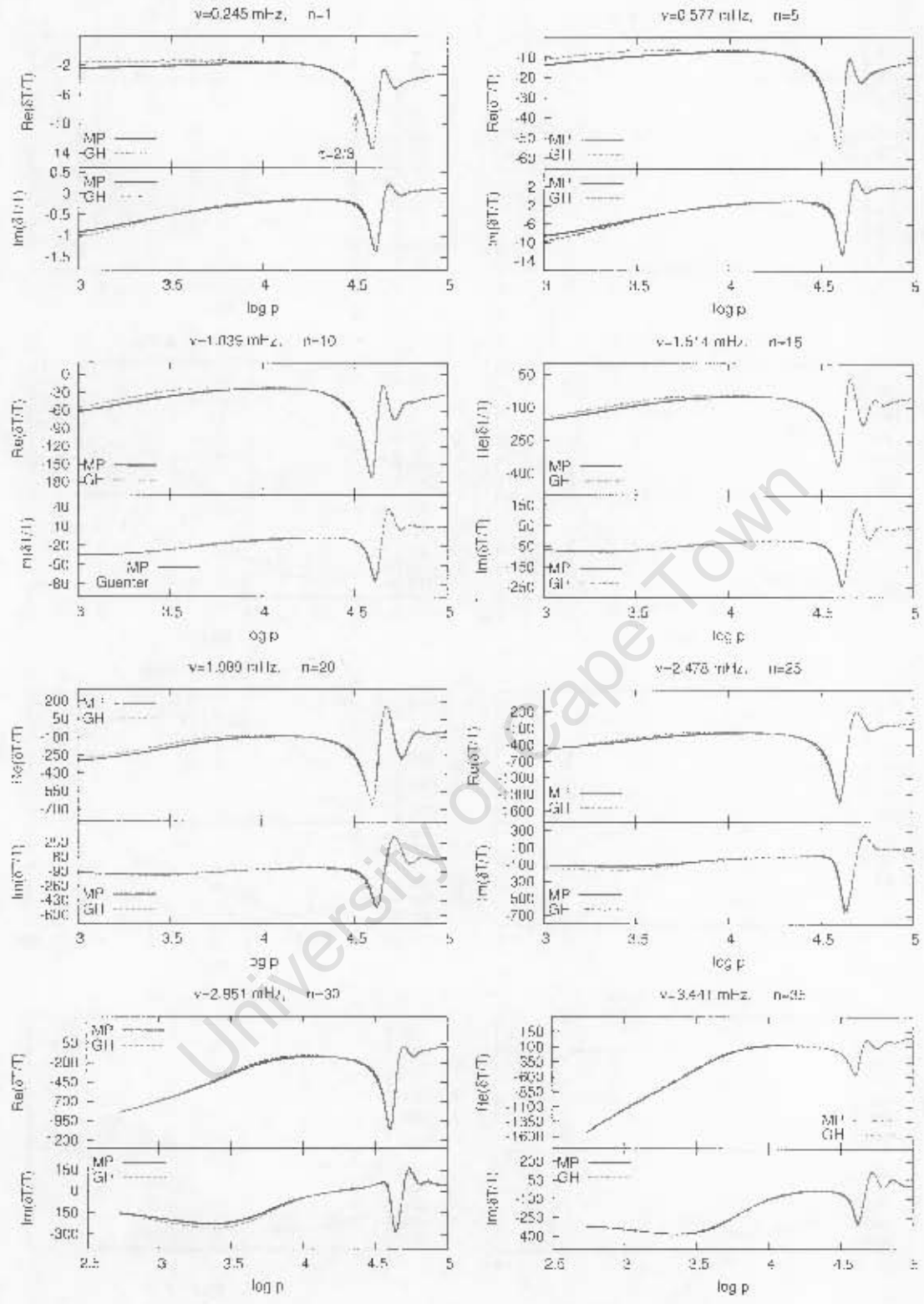

Figure 4.5: A comparison of real and imaginary parts $\delta T/T$ obtained from the new code (MP) and those using Houdek's code (GH) for the $1.5M_\odot$ model at various frequencies. Each panel is divided into real and imaginary parts of temperature eigenfunctions. The position of optical depth $\tau = 2/3$ is indicated on the first panel by an arrow. The largest relative difference between using proper treatment of radiation and Eddington approximation is up to about 33%.

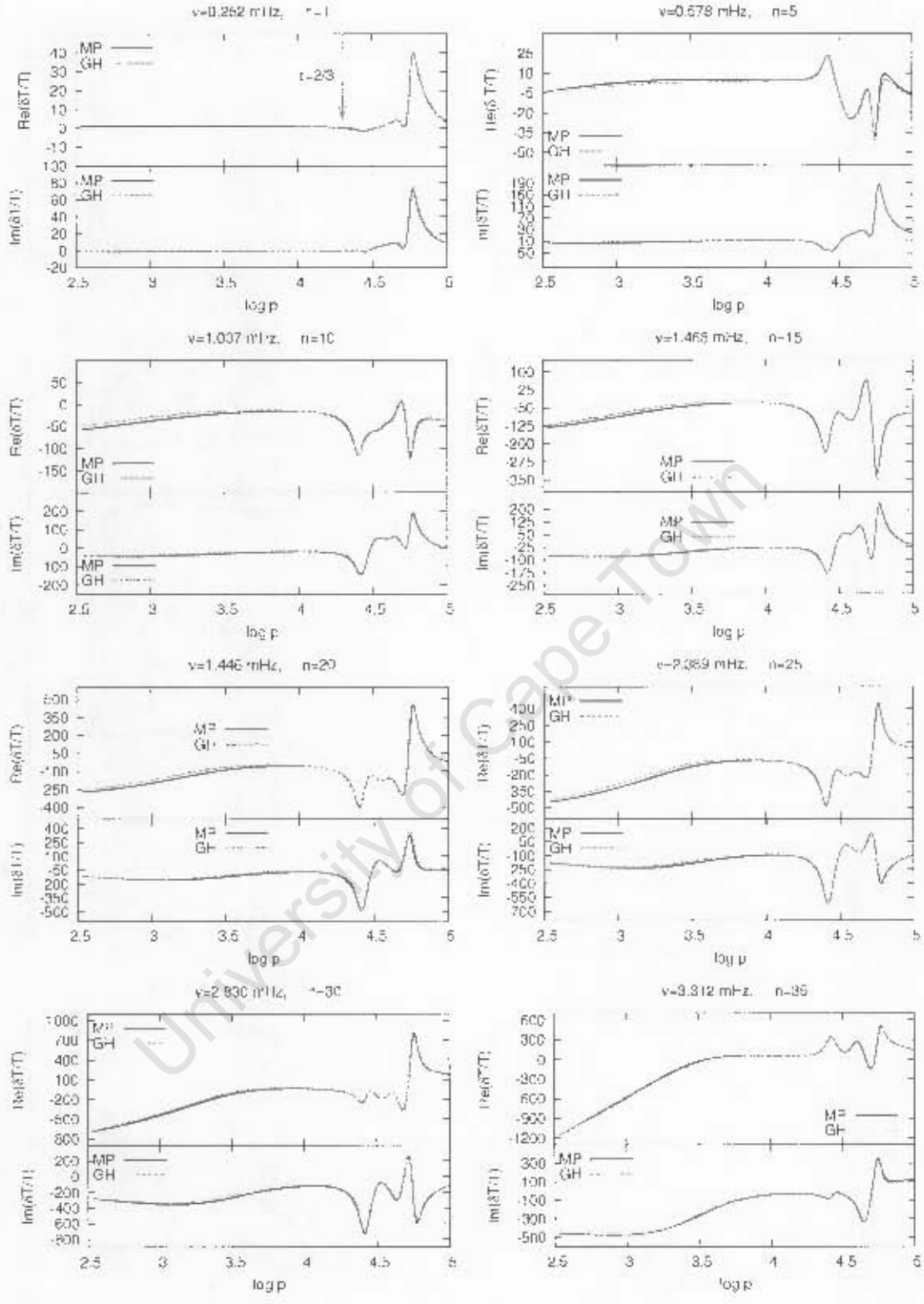

Figure 4.6: A comparison of real and imaginary parts $\delta T/T$ obtained from the new code (MP) and those using Houdek's code (GH) for the $1.6M_{\odot}$ model at various frequencies. Each panel is divided into real and imaginary parts of temperature eigenfunctions. The position of optical depth $\tau = 2/3$ is indicated on the first panel by an arrow. The largest relative difference between using proper treatment of radiation and Eddington approximation is up to about 70%.

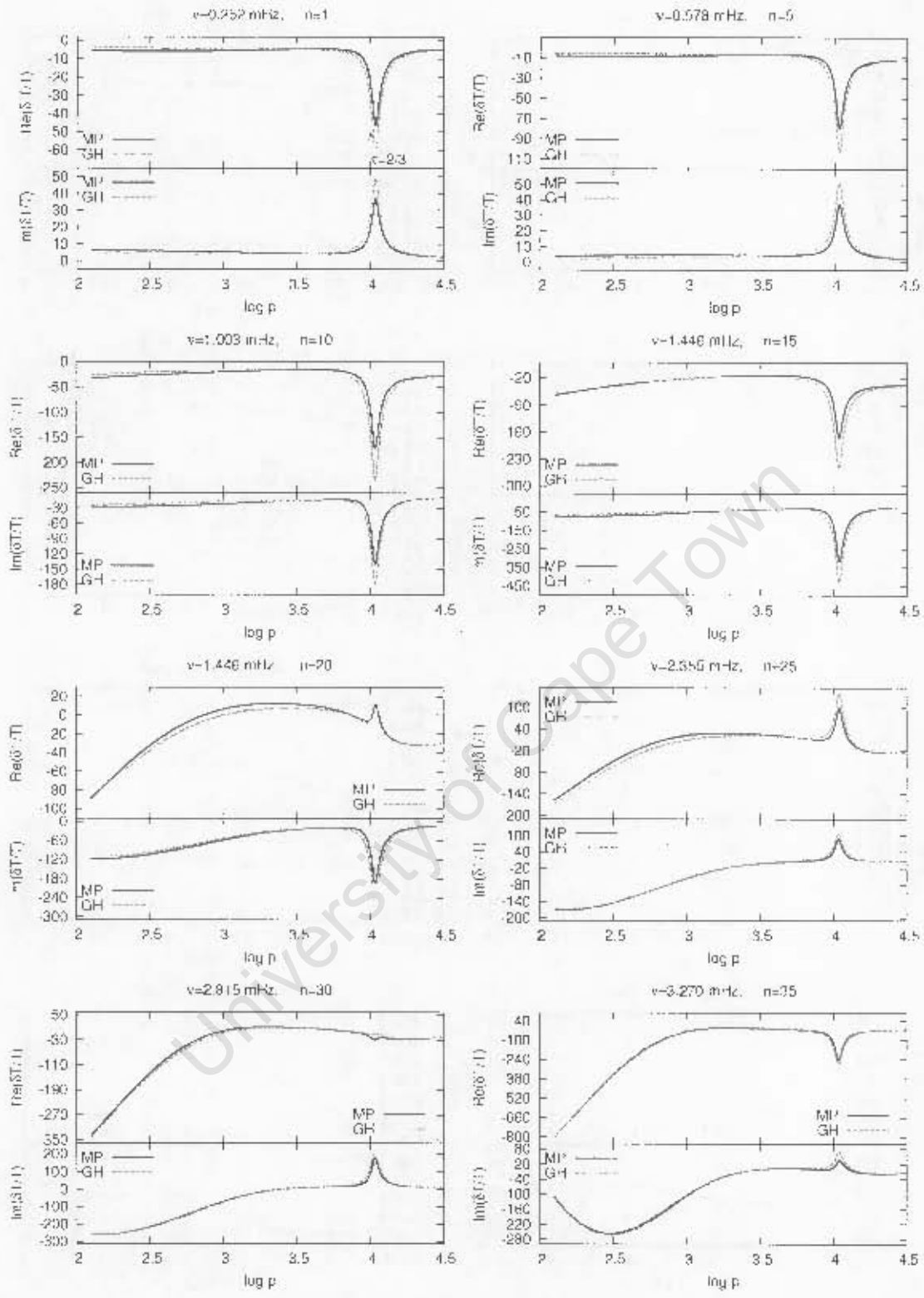

Figure 4.7: A comparison of real and imaginary parts $\delta T/T$ obtained from the new code (MP) and those using Houdek's code (GH) for the $1.8M_{\odot}$ model at various frequencies. Each panel is divided into real and imaginary parts of temperature eigenfunctions. The position of optical depth $\tau = 2/3$ is indicated on the first panel by an arrow. The largest relative difference between using proper treatment of radiation and Eddington approximation is up to about 33%.

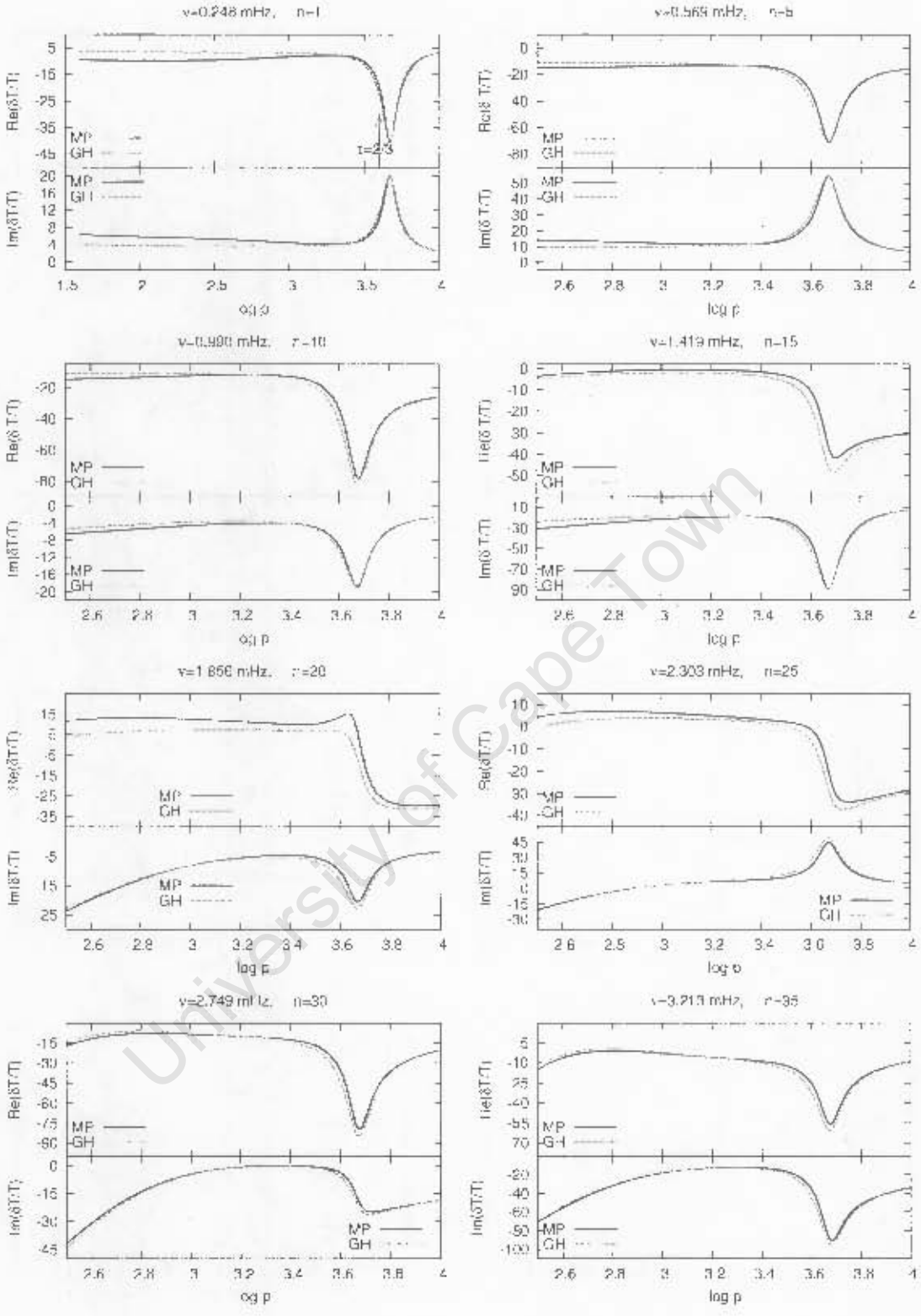

Figure 4.8: A comparison of real and imaginary parts $\delta T/T$ obtained from the new code (MP) and those using Houdek's code (GH) for the $2.0M_{\odot}$ model at various frequencies. Each panel is divided into real and imaginary parts of temperature eigenfunctions. The position of optical depth $\tau = 2/3$ is indicated on the first panel by an arrow. The largest relative difference between using proper treatment of radiation and Eddington approximation is up to about 33%.

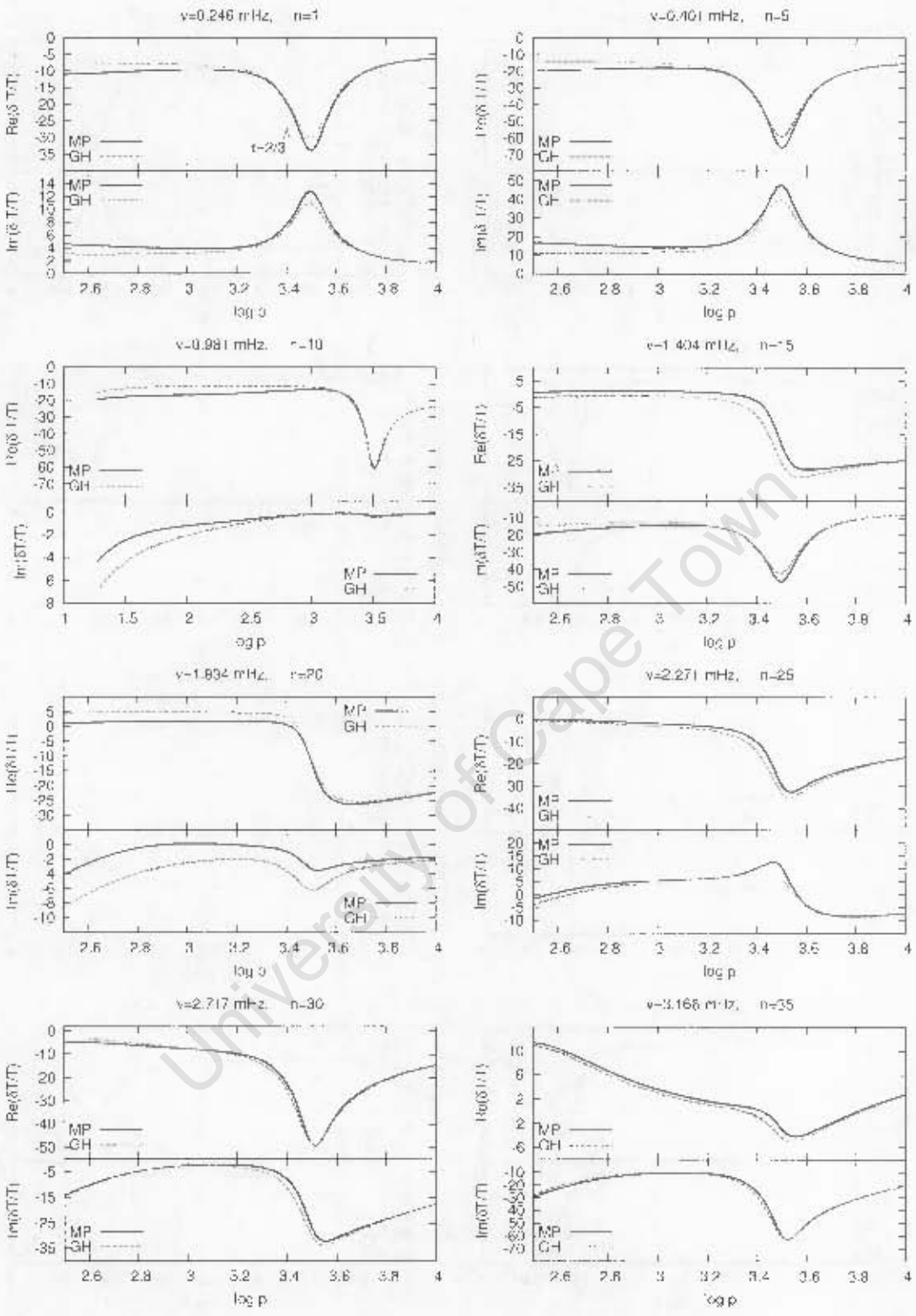

Figure 4.9: A comparison of real and imaginary parts $\delta T/T$ obtained from the new code (MP) and those using Houdek's code (GH) for the $2.1M_{\odot}$ model at various frequencies. Each panel is divided into real and imaginary parts of temperature eigenfunctions. The position of optical depth $\tau = 2/3$ is indicated on the first panel by an arrow. The largest relative difference between using proper treatment of radiation and Eddington approximation is up to about 39%.

4.1.2.2 Displacement eigenfunctions

In Figures 4.10 to 4.17 we compare the displacement eigenfunctions obtained using the new code with those using Houdek's code. The effect of the treatment of radiation on the real part of the displacement is unnoticeable for all the selected modes considered, but noticeable on the imaginary parts. The largest relative differences for various equilibrium models are shown in the captions of Figures 4.10 to 4.17. Here the largest difference is found in the imaginary part of $\delta r/r$ only.

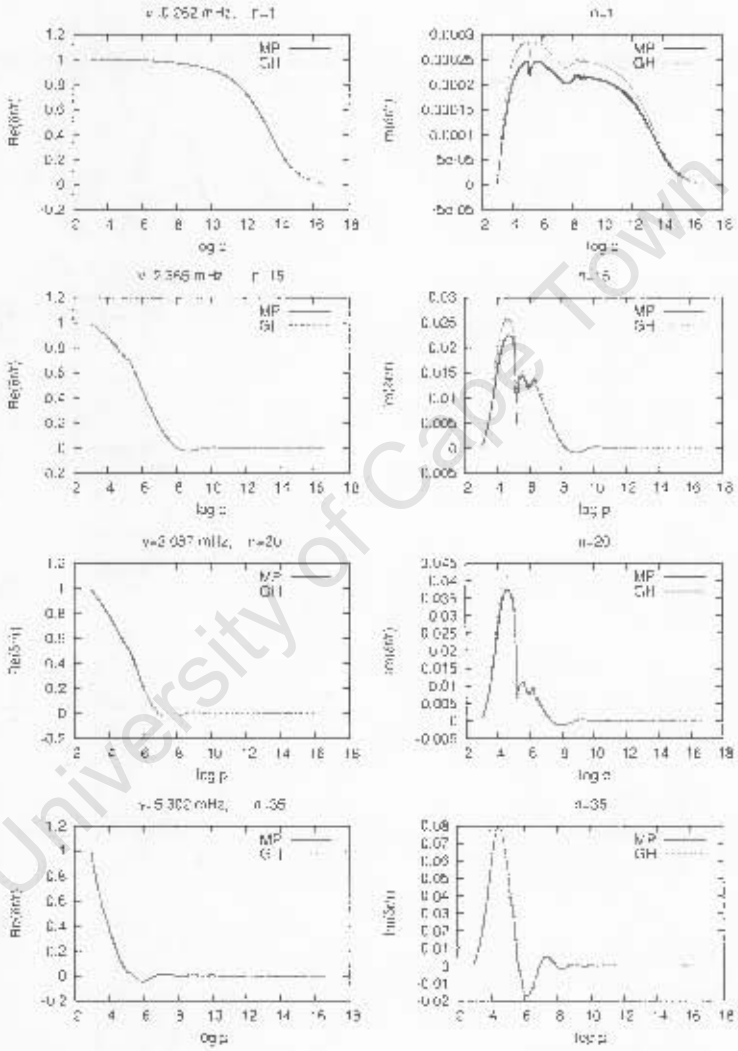

Figure 4.10: A comparison of real and imaginary parts of $\delta r/r$ obtained from the new code (MP) and those using Houdek's code (GH) for the $1.0M_{\odot}$ model at various frequencies. The left and right panels show real and imaginary parts of $\delta r/r$ respectively. The largest relative difference between using proper treatment of radiation and Eddington approximation for the imaginary part of $\delta r/r$ is up to about 21.5%.

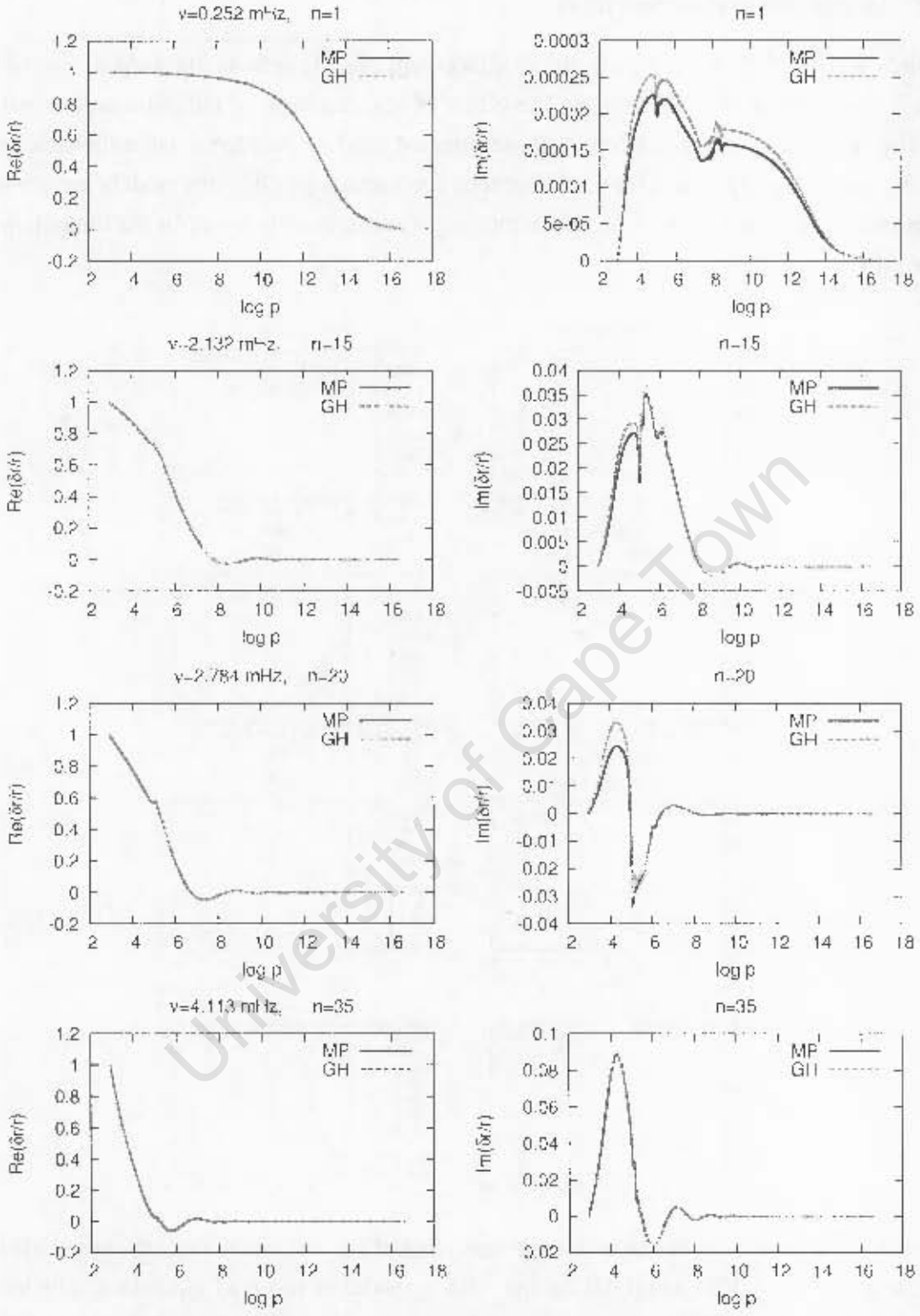

Figure 4.11: A comparison of real and imaginary parts $\delta r/r$ obtained from the new code (MP) and those using Houdek's code (GH) for the $1.2M_{\odot}$ model at various frequencies. The left and right panels show real and imaginary parts of $\delta r/r$ respectively. The largest relative difference between using proper treatment of radiation and Eddington approximation for the imaginary part of $\delta r/r$ is up to about 30%.

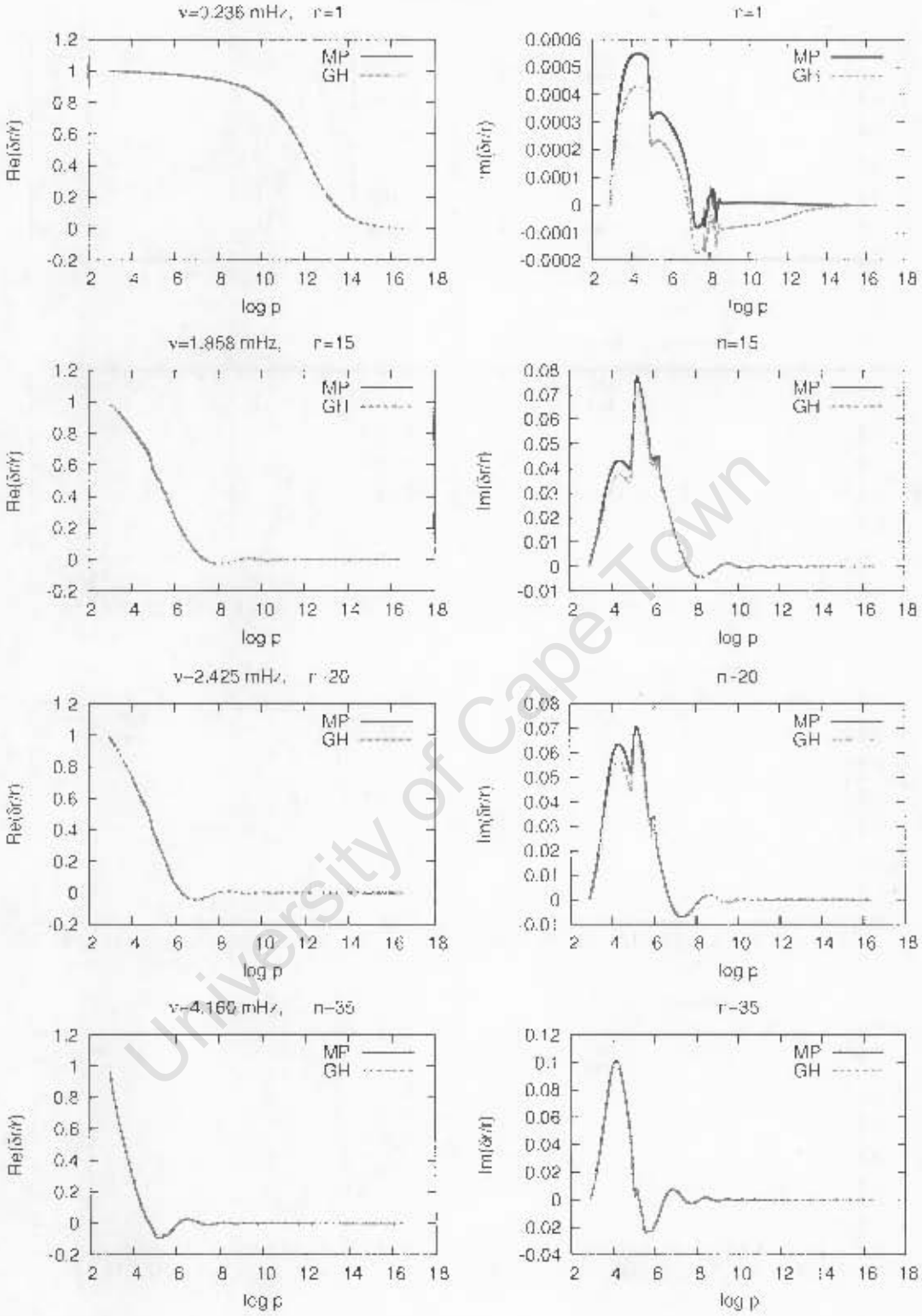

Figure 4.12: A comparison of real and imaginary parts $\delta r/r$ obtained from the new code (MP) and those using Houdek's code (GH) for the $1.3M_{\odot}$ model at various frequencies. The left and right panels show real and imaginary parts of $\delta r/r$ respectively. The largest relative difference between using proper treatment of radiation and Eddington approximation for the imaginary part of $\delta r/r$ is up to about 22.6%.

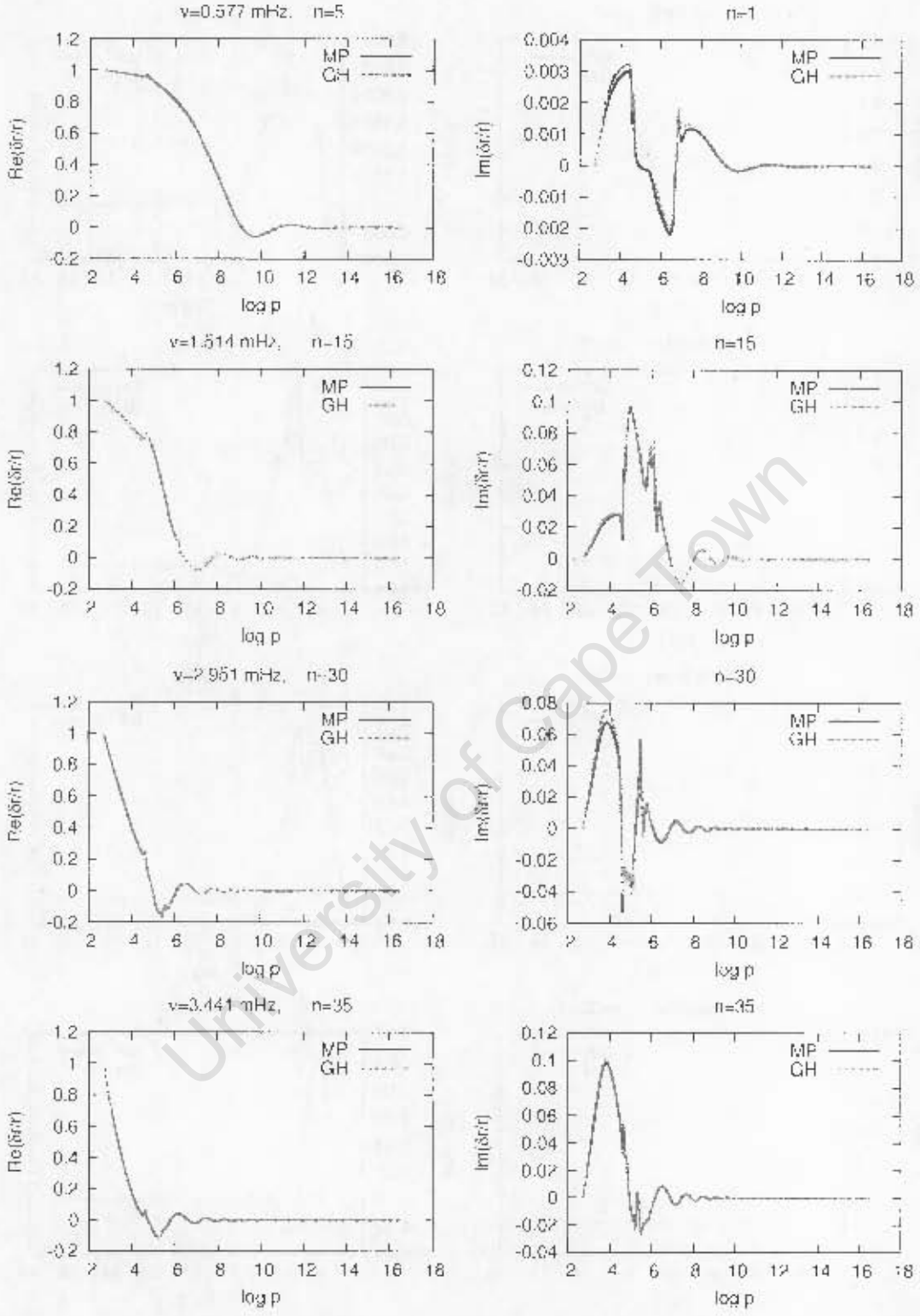

Figure 4.13: A comparison of real and imaginary parts $\delta r/r$ obtained from the new code (MP) and those using Houdek's code (GH) for the $1.5M_{\odot}$ model at various frequencies. The left and right panels show real and imaginary parts of $\delta r/r$ respectively. The largest relative difference between using proper treatment of radiation and Eddington approximation for the imaginary part of $\delta r/r$ is up to about 23.7%.

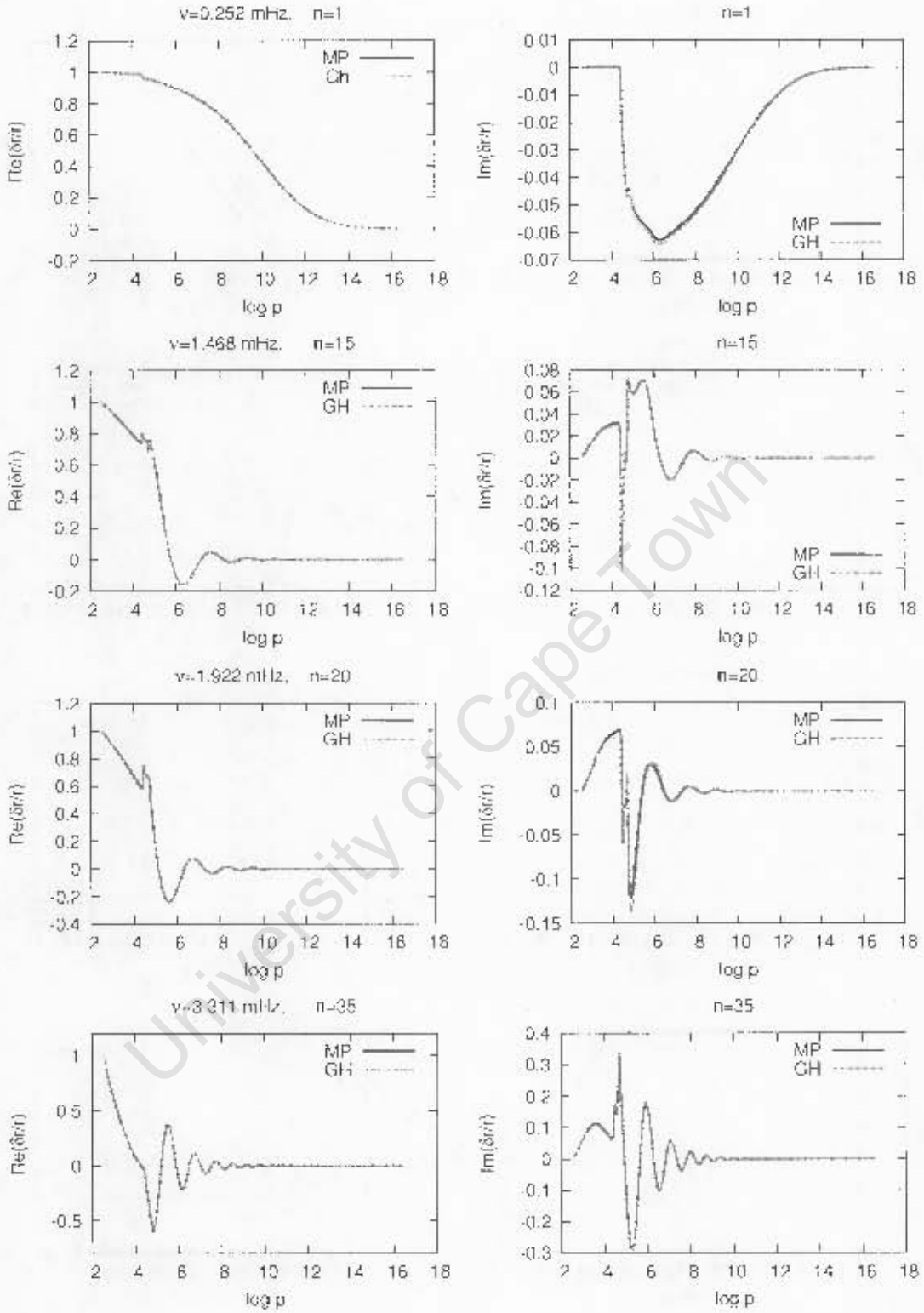

Figure 4.14: A comparison of real and imaginary parts $\delta r/r$ obtained from the new code (MP) and those using Houdek's code (GH) for the $1.6M_{\odot}$ model at various frequencies. The left and right panels show real and imaginary parts of $\delta r/r$ respectively. The largest relative difference between using proper treatment of radiation and Eddington approximation for the imaginary part of $\delta r/r$ is up to about 6.5%.

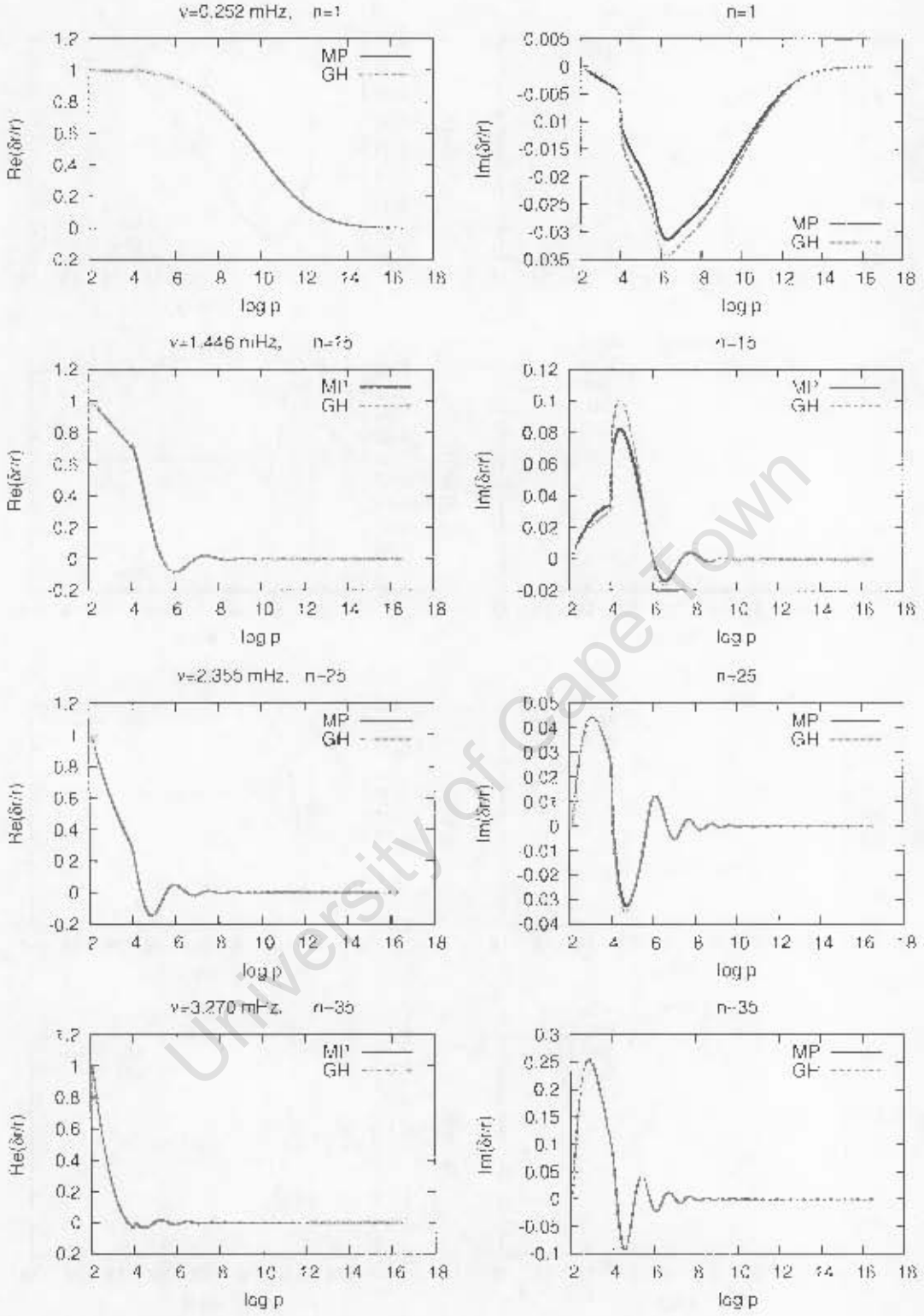

Figure 4.15: A comparison of real and imaginary parts $\delta r/r$ obtained from the new code (MP) and those using Houdek's code (GH) for the $1.8M_{\odot}$ model at various frequencies. The left and right panels show real and imaginary parts of $\delta r/r$ respectively. The largest relative difference between using proper treatment of radiation and Eddington approximation for the imaginary part of $\delta r/r$ is up to about 17%.

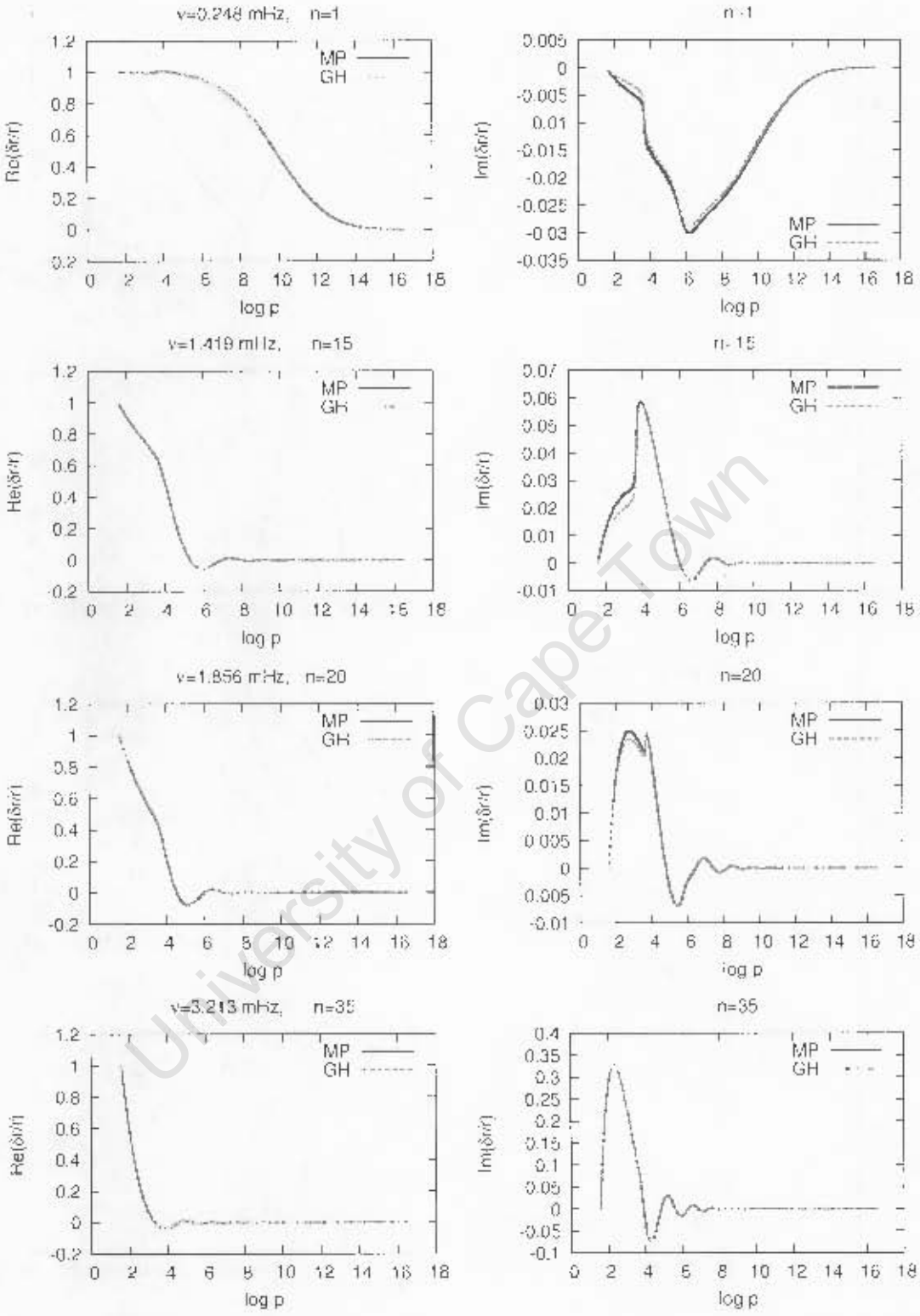

Figure 4.16: A comparison of real and imaginary parts $\delta r/r$ obtained from the new code (MP) and those using Houdek's code (GH) for the $2.0 M_{\odot}$ model at various frequencies. The left and right panels show real and imaginary parts of $\delta r/r$ respectively. The largest relative difference between using proper treatment of radiation and Eddington approximation for the imaginary part of $\delta r/r$ is up to about 33%.

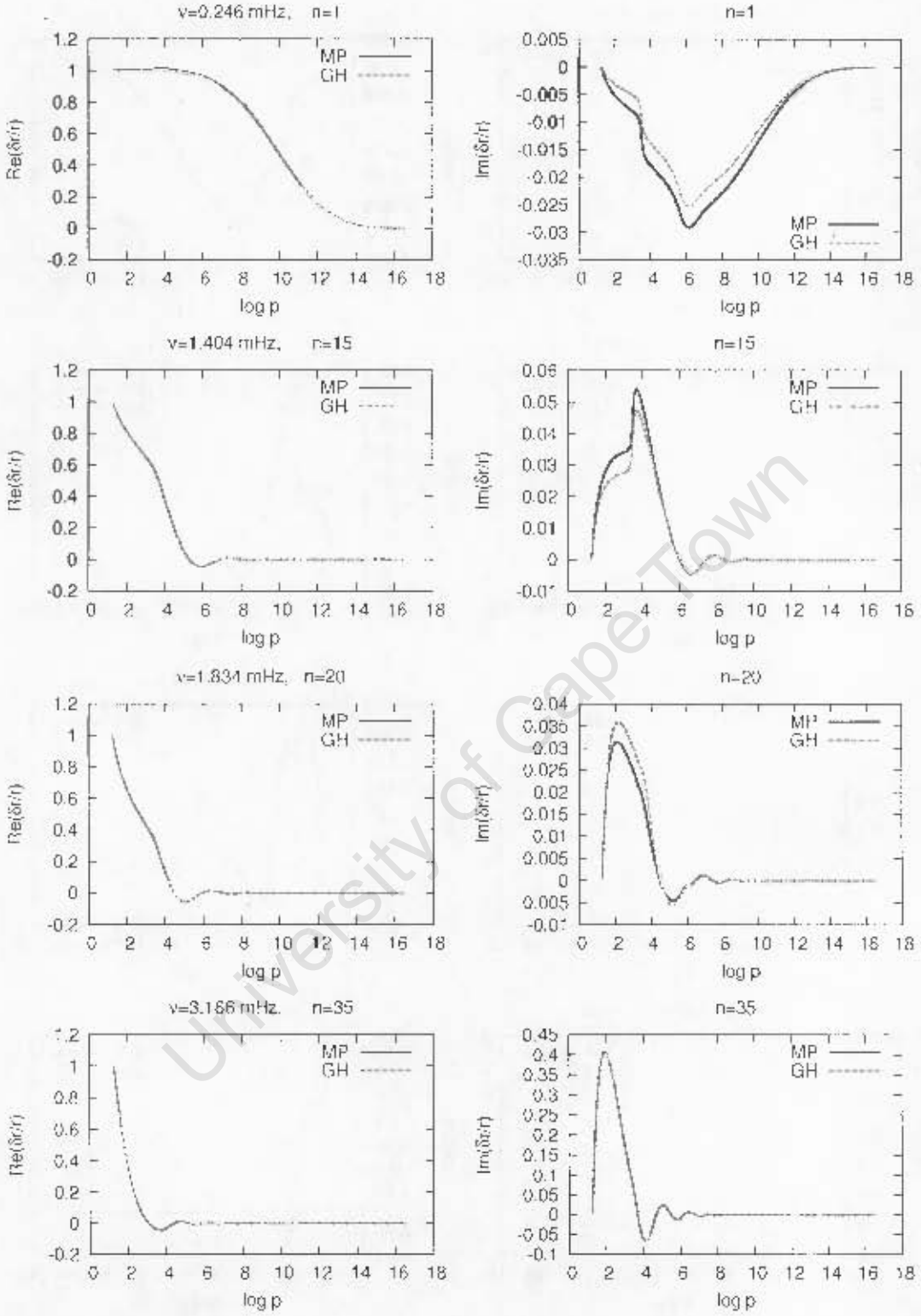

Figure 4.17: A comparison of real and imaginary parts $\delta r/r$ obtained from the new code (MP) and those using Houdek's code (GH) for the $2.1M_{\odot}$ model at various frequencies. The left and right panels show real and imaginary parts of $\delta r/r$ respectively. The largest relative difference between using proper treatment of radiation and Eddington approximation for the imaginary part of $\delta r/r$ is up to about 19%.

4.1.3 The effect on theoretical growth rates

In this section the growth rates computed by imposing a displacement node at the base of the envelope for the consistent treatment of radiative transfer and Eddington approximation are compared. The results are shown in Fig.4.18 for the equilibrium models listed in Tables 3.1. The results are consistent with the eigenfrequencies differences (imaginary parts) shown in the bottom panel of Fig. 4.1. For the $1.8M_{\odot}$ model, below the acoustic cut-off frequency, the consistent treatment of radiative transfer has reduced the growth rates, which increases towards and above acoustic cut-off frequency.

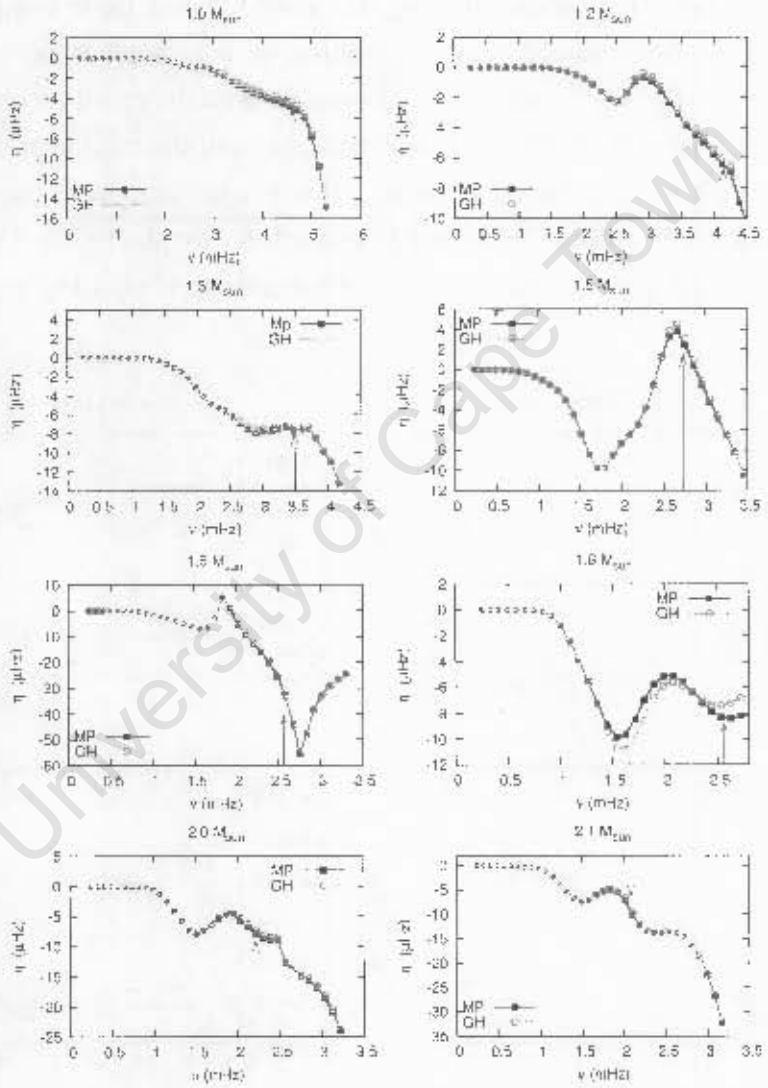

Figure 4.18: The growth rates as function of the cyclic frequency ν for ZAMS models. The curve labelled "MP" was obtained from the new code, whereas for the curve "GH" we used Houdek's code. The arrow indicates the acoustic cut-off frequency.

We notice that for models with $M \leq 1.5M_{\odot}$ proper treatment of radiation slightly increases growth rates within a certain frequency range. For other equilibrium models we notice that at various frequency ranges the consistent treatment of radiation can both decrease and increase the growth rates.

4.1.4 Work Integral

To illustrate the difference in the growth rates obtained using consistent treatment of the radiation field with those obtained using Eddington approximation in section, we compare the cumulative work integrals (W_{tot}) obtained using the new code with those using Houdek's code. In Figures 4.19-4.26 the accumulated work integral for various frequencies for ZAMS equilibrium models are shown. The work integrals are consistent with the result presented in Table 4.1. It is noticeable that for models of the Sun the improvement of the treatment of radiative transfer increases the growth rates in the atmosphere. This is consistent with the earlier works by Christensen-Dalsgaard & Frandsen (1983) and Balmforth & Gough (1988). The largest relative differences for various equilibrium models are shown in the captions of Figures 4.19 to 4.26.

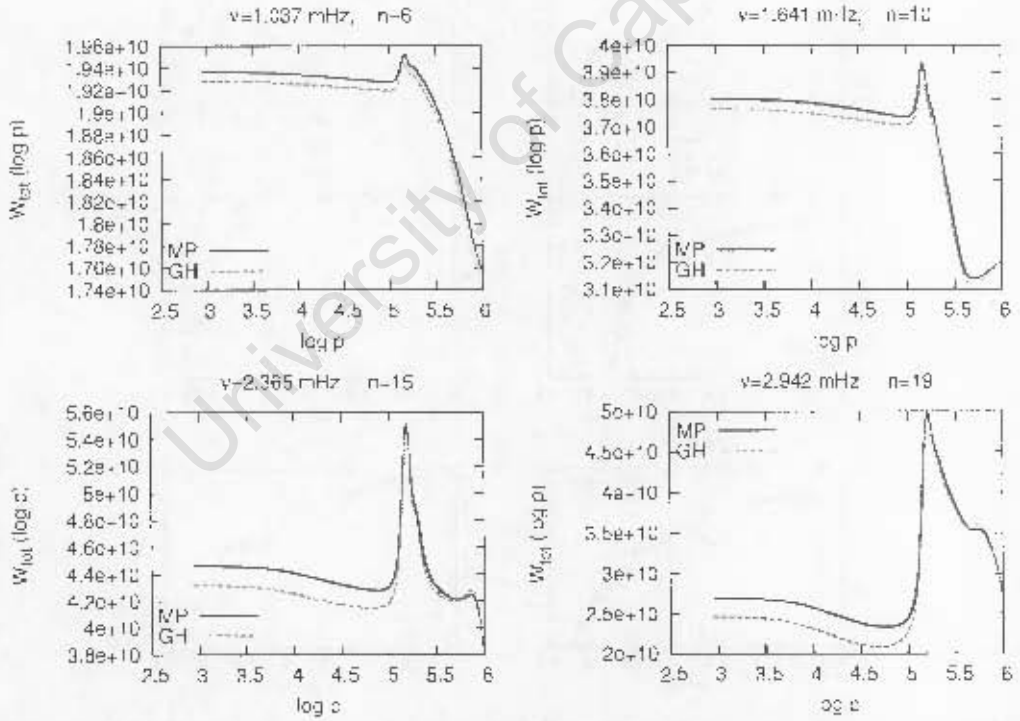

Figure 4.19: A comparison of the accumulated work integrals (in units $10^{30}erg$) computed using the new code (MP) with those using Houdek's code (GH) for the $1.0M_{\odot}$ model at various frequencies. Here the largest relative difference is up to about 9%

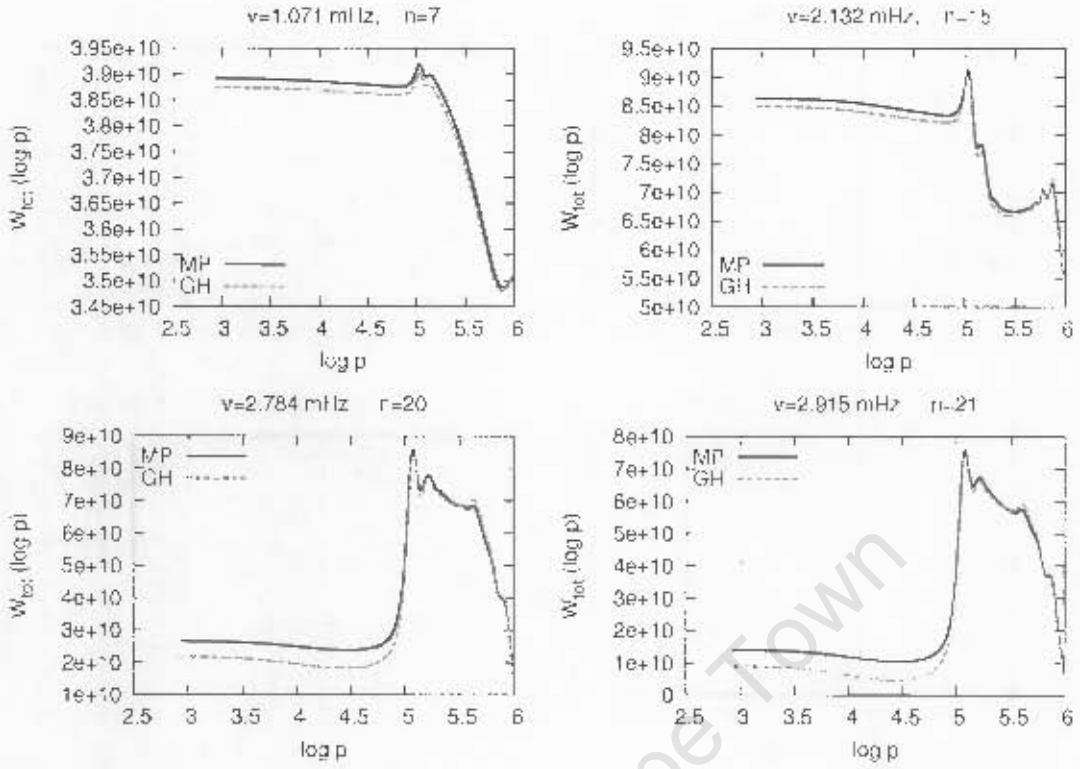

Figure 4.20: A comparison of the accumulated work integrals (in units $10^{30} erg$) computed using the new code (MP) with those using Houdek's code (GH) for the $1.2 M_{\odot}$ model at various frequencies. Here the largest relative difference is up to about 35%

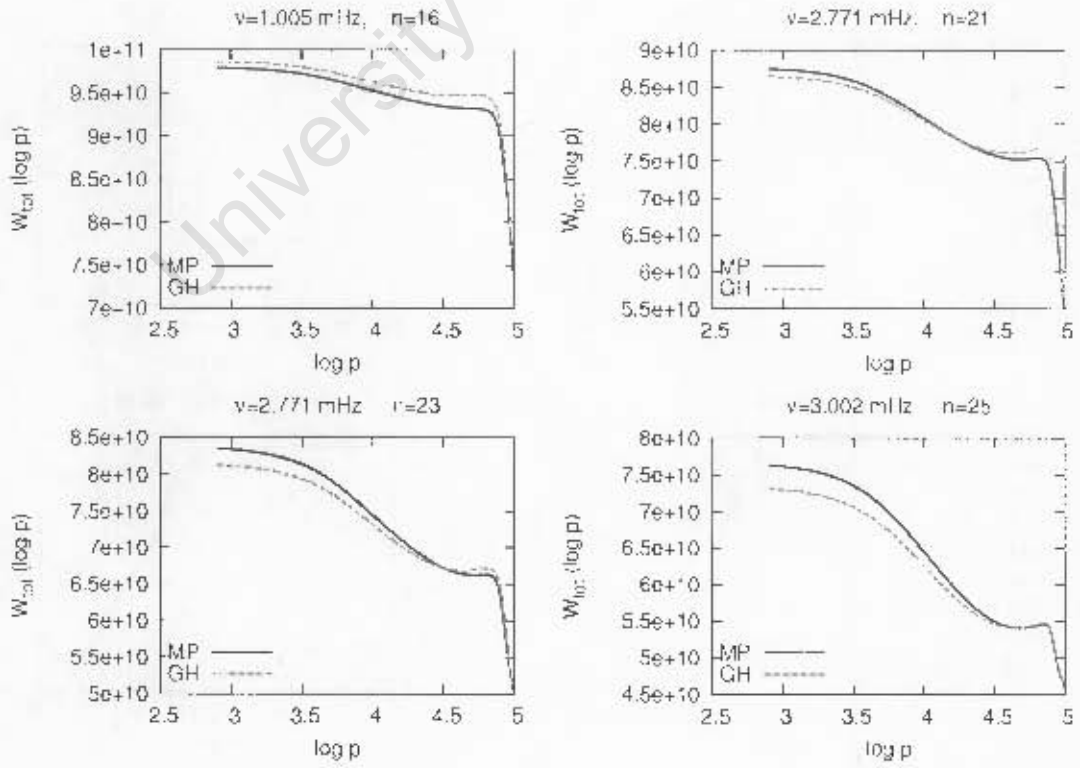

Figure 4.21: A comparison of the accumulated work integrals (in units $10^{30} erg$) computed using the new code (MP) with those using Houdek's code (GH) for the $1.3 M_{\odot}$ model at various frequencies. Here the largest relative difference is up to about 4%

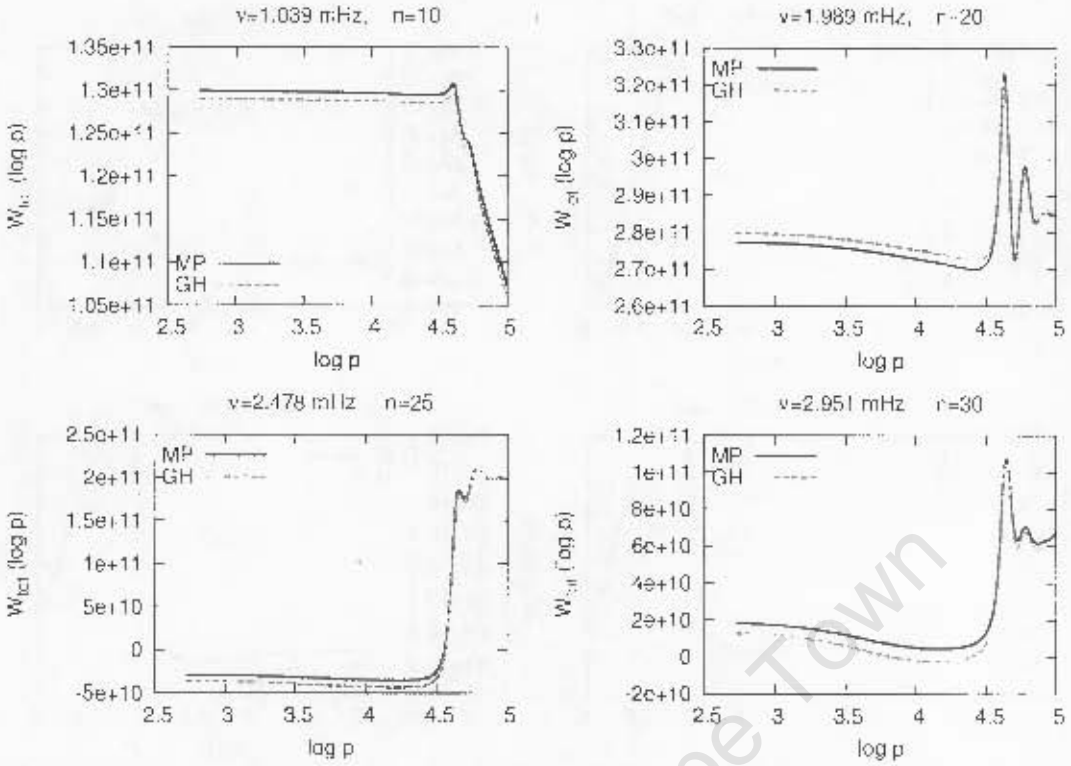

Figure 4.22: A comparison of the accumulated work integrals (in units $10^{30} erg$) computed using the new code (MP) with those using Houdek's code (GH) for the $1.5 M_{\odot}$ model at various frequencies. Here the largest relative difference is up to about 19%

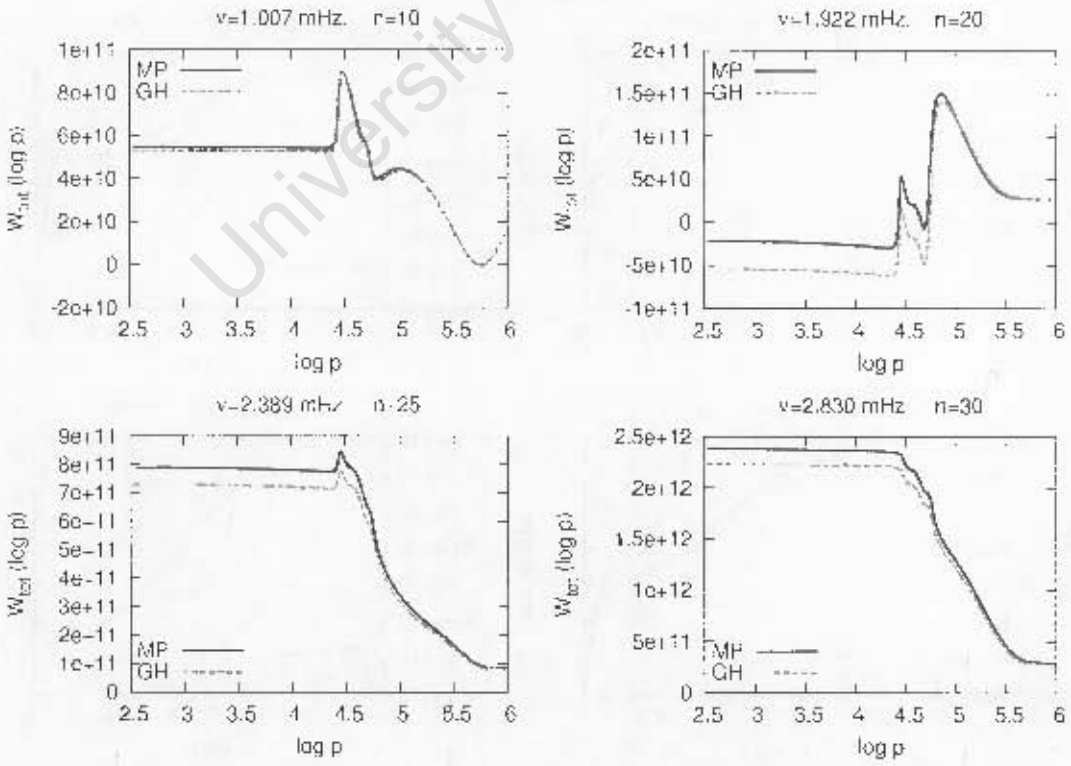

Figure 4.23: A comparison of the accumulated work integrals (in units $10^{30} erg$) computed using the new code (MP) with those using Houdek's code (GH) for the $1.6 M_{\odot}$ model at various frequencies. Here the largest relative difference is up to about 60%.

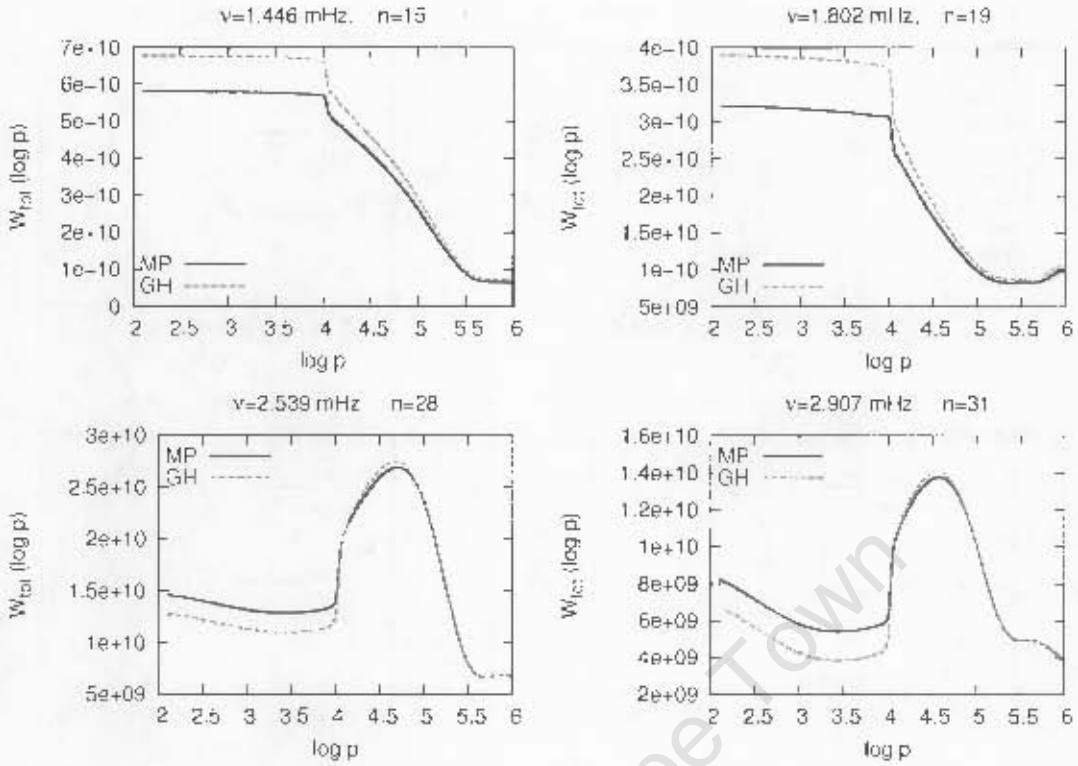

Figure 4.24: A comparison of the accumulated work integrals (in units $10^{30} erg$) computed using the new code (MP) with those using Houdek's code (GH) for the $1.8 M_{\odot}$ model at various frequencies. Here the largest relative difference is up to about 29%

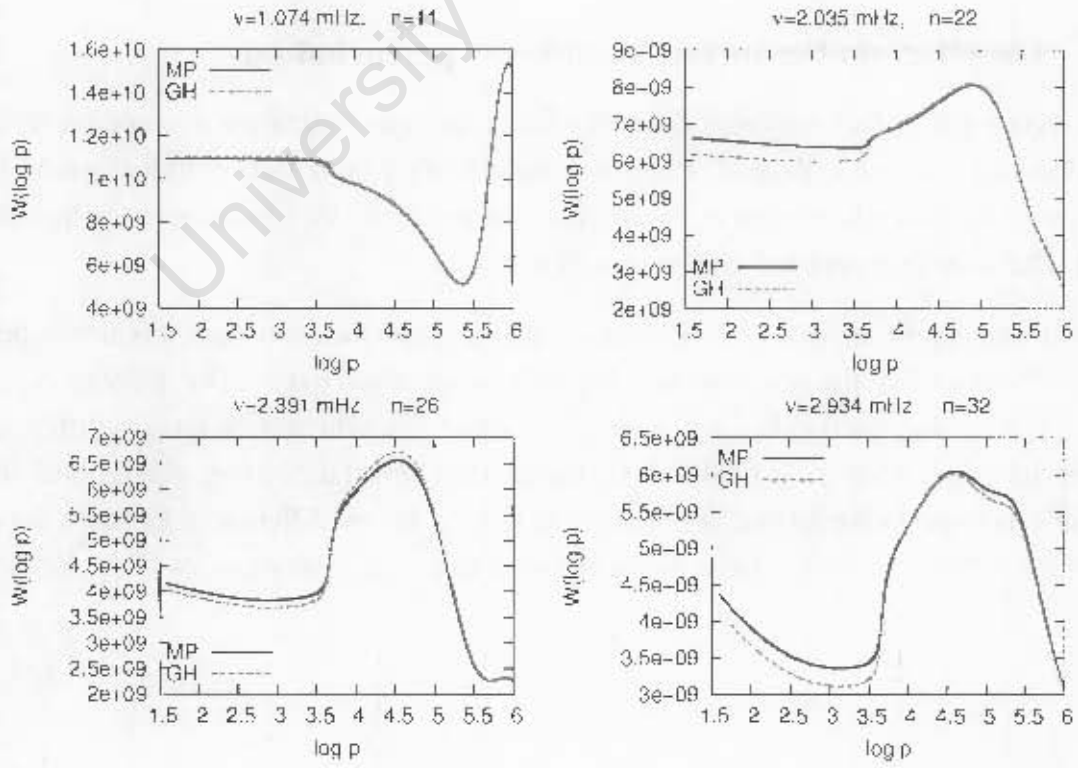

Figure 4.25: A comparison of the accumulated work integrals (in units $10^{30} erg$) computed using the new code (MP) with those using Houdek's code (GH) for the $2.0 M_{\odot}$ model at various frequencies. Here the largest relative difference is up to about 7%

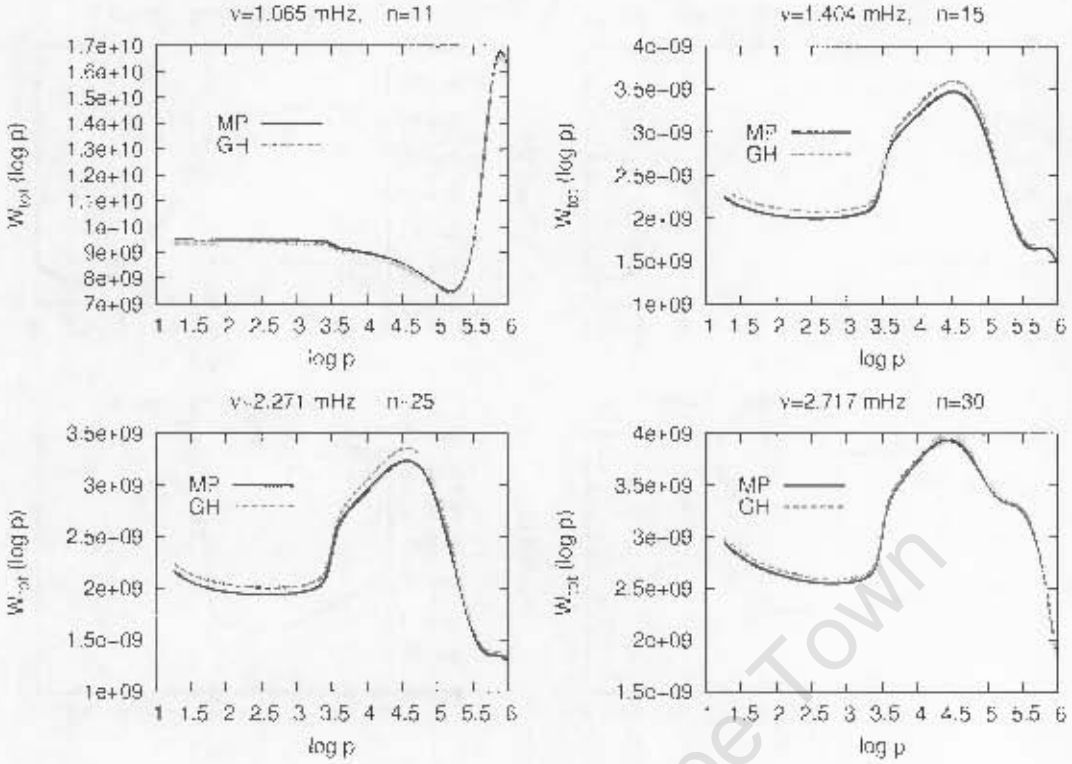

Figure 4.26: A comparison of the accumulated work integrals (in units $10^{30} erg$) computed using the new code (MP) with those using Houdek's code for the $2.1 M_{\odot}$ model at various frequencies. Here the largest relative difference is up to about 3.2%

4.1.5 The effect on the surface luminosity perturbations

In this section the surface luminosity perturbations determined using the new code with those using Houdek's code are compared. The behaviour of surface luminosity perturbations $\delta L/L$ as a function of frequency is relevant to the observations and hence the most interesting quantity to look at. The results are depicted in Figures 4.27 and 4.28.

The results are shown in Table 4.2. Here $L_{f_{osc}}$ and $L_{f_{eq}}$ denote the surface luminosity perturbations obtained using the new code and Houdek's code respectively. The quantity $\Delta L_{s,r} = Re(L_{f_{osc}}) \quad Re(L_{f_{eq}})$ and $\Delta L_{s,i} = Im(L_{f_{osc}}) \quad Im(L_{f_{eq}})$. The largest relative difference is found in the $1.0 M_{\odot}$ near $\nu = 4.5$ mHz. It is clear that the lowest difference, which is almost unnoticeable, is found in the $2.1 M_{\odot}$. It is noticeable that the largest differences are found between 1 mHz and 5 mHz. There is a large difference seen in the imaginary part of $\delta L/L$ for $1.3 M_{\odot}$ model.

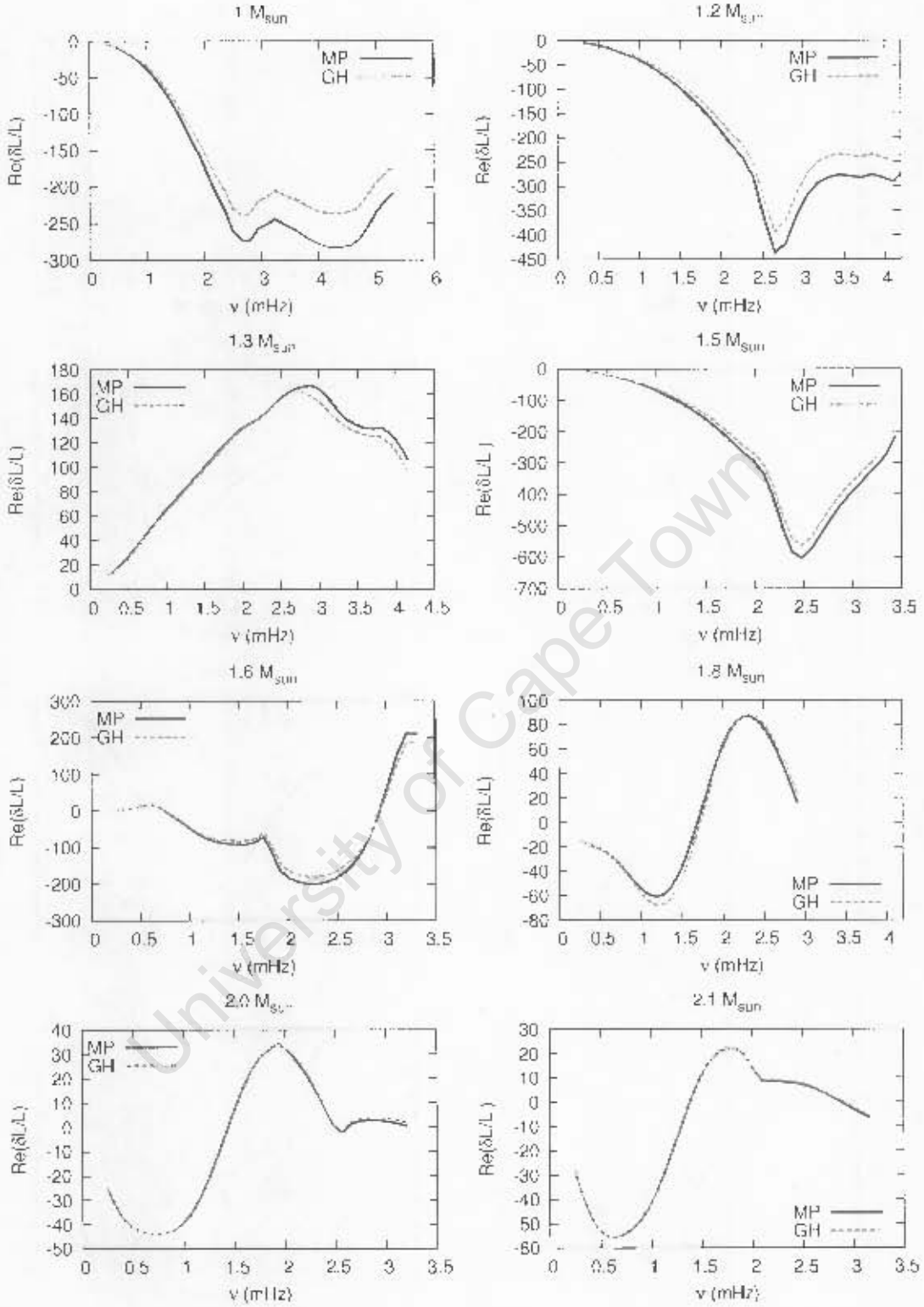

Figure 4.27: The real part of $\delta L/L$ at the surface as a function of frequency for ZAMS equilibrium models listed in table. The curve labelled "MP" was obtained using the new code, whereas for the curve "GH" we used Houdek's code.

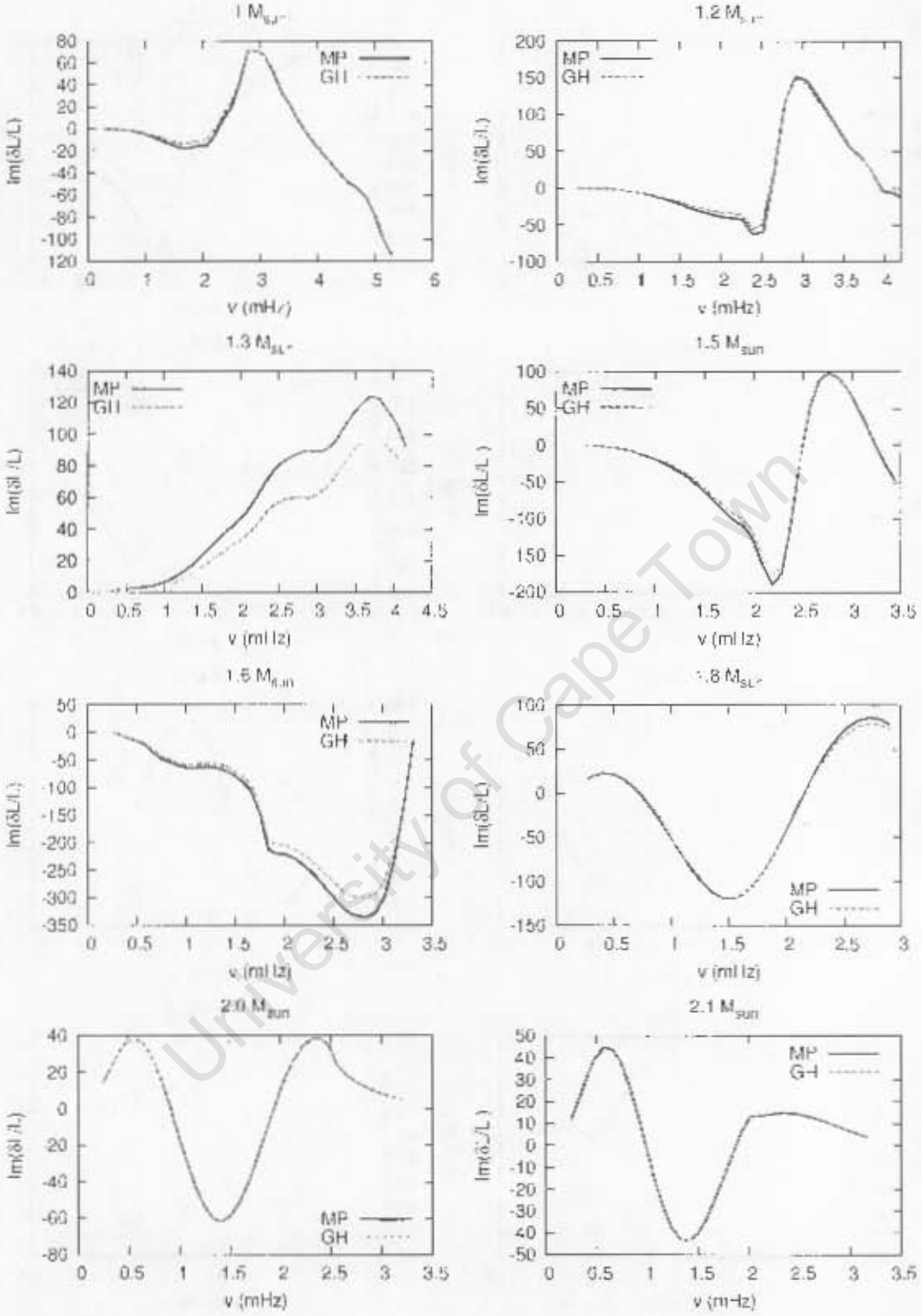

Figure 4.28: The imaginary part of $\delta L/L$ at the surface as a function of frequency for ZAMS equilibrium models listed in table. The curve labelled "MP" was obtained using the new code, whereas for the curve "GH" we used Houdek's code.

Table 4.2: The maximum errors introduced by the Eddington approximation in the surface luminosity perturbations. The first column denotes the mass of the equilibrium models, the second column denotes $|\Delta L_{s,r}|$ relative to $Re(L_{fosc})$, and the third column denotes $|\Delta L_{s,i}|$ relative to $Im(L_{fosc})$.

$M/M_\odot$	$\lvert\Delta L_{s,r}/Re(L_{fosc})\rvert$ (%)	$\lvert\Delta L_{s,i}/Im(L_{fosc})\rvert$ (%)
1.0	19.3	4.5
1.2	10.7	20.0
1.3	7.8	35.0
1.5	7.3	7.3
1.6	10.6	11.6
1.8	16.7	8.9
2.0	3.3	1.0

4.2 Comparison of equilibrium models with convection and those with inefficient convection

In this section, the eigenfrequencies, eigenfunctions, growth rates and surface luminosity obtained by using equilibrium models with convection (hereafter convective models) and those with inefficient convection (hereafter radiative models) are compared. In case of the radiative models we use non-adiabatic pulsation equations without convection. We simulated radiative models by using a mixing length $\alpha_c = 0.035$ which leads to very thin and extremely inefficient convection zones. Parameters $M/M_\odot$, $L/L_\odot$ and T_{eff} for the radiative models $1.8M_\odot$ and $2.1M_\odot$ are the same as listed in Table 3.1. These equilibrium models were kindly provided by Guenter Houdek.

The differences in these equilibrium models are illustrated in Figs. 4.29 and 4.30. There are no differences between the radiative and convective models in T, ρ, κ and ∇_{ad}, as function of $\log p$. These plots, especially $\nabla - \nabla_{ad}$, show that the radiative models are not completely non-convective. There are large differences in p_t/p and F_c/F in both models. All these have to be borne in mind when comparing the results in the next subsections. The comparison of these equilibrium models is illustrated in Figs. 4.29 and 4.30.

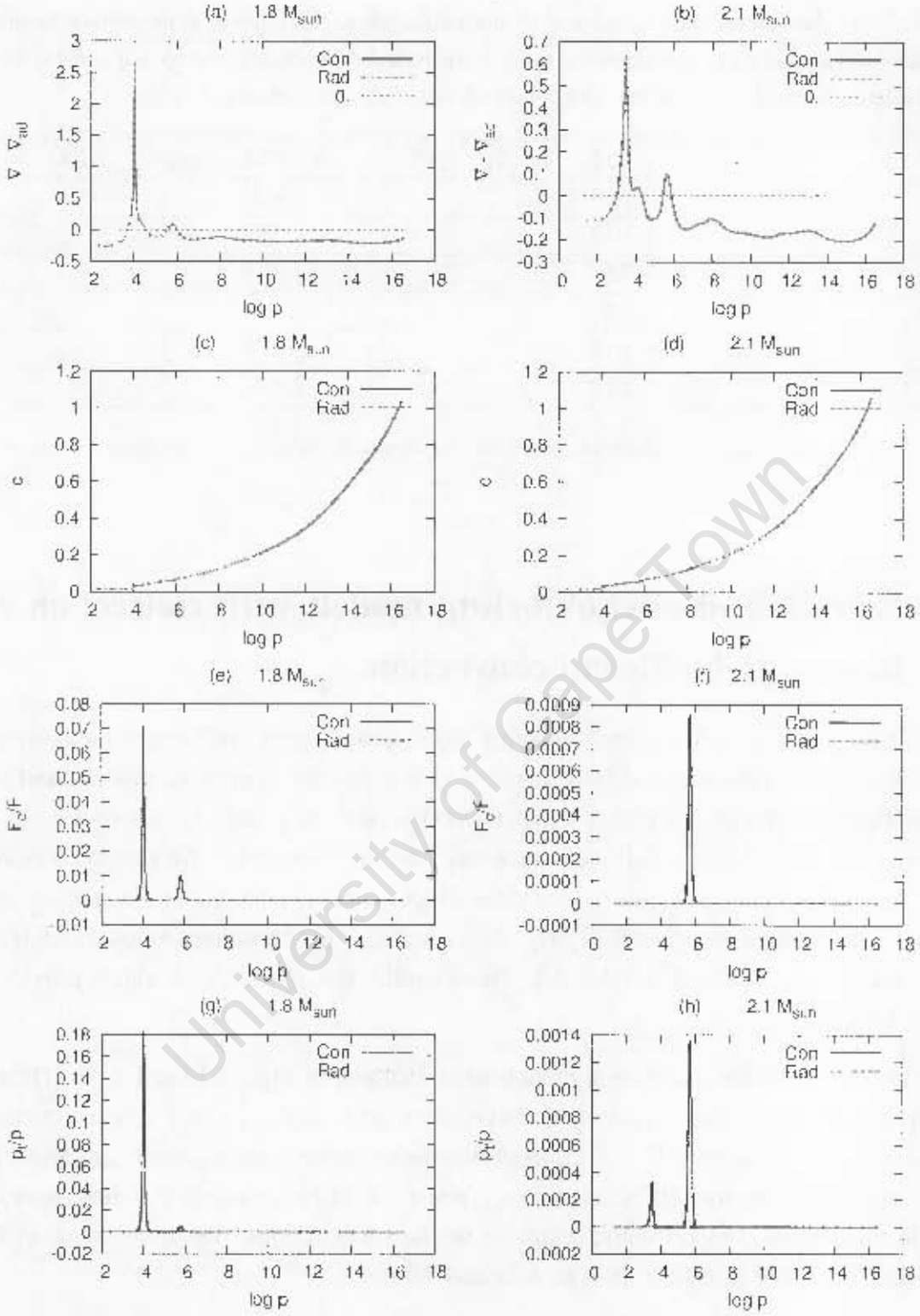

Figure 4.29: The differences between the convective models (Con) and radiative models (Rad) for $1.8M_\odot$ and $2.1M_\odot$ in (a) and (b) superadiabatic gradient $\nabla - \nabla_{ad}$, (c) and (d) dimensionless sound speed, (e) and (f) ratio of convective flux to the total heat flux F_c/F, and (g) and (h) the turbulent pressure fraction p_t/p compared as a function of $\log p$.

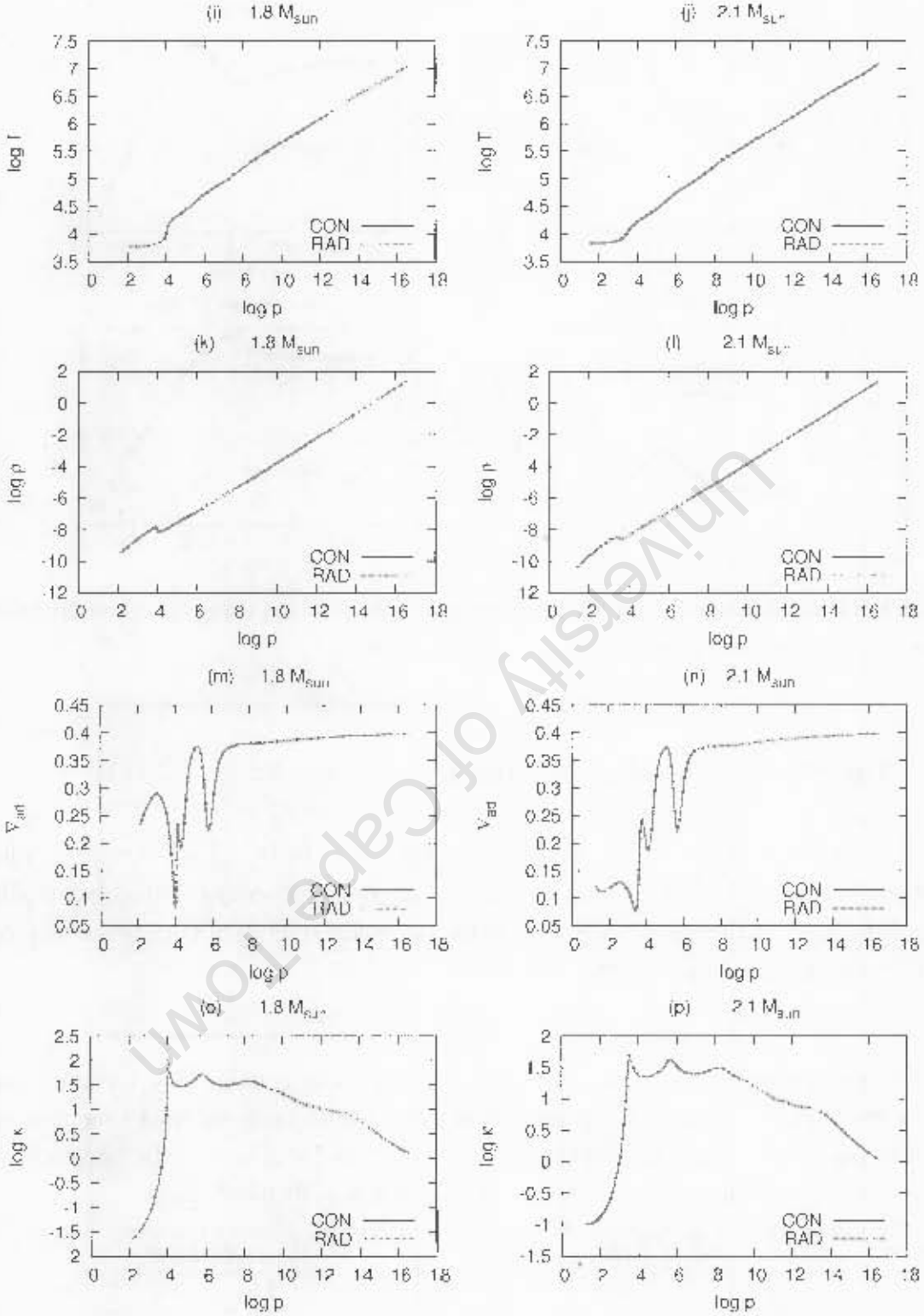

Figure 4.30: The differences between the convective models (Con) and radiative models (Rad) for $1.8M_{\odot}$ and $2.1M_{\odot}$ in (i) and (j) temperature T, (k) and (l) density, (m) and (n) ∇_{ad}, and (o) and (p) compared as a function of $\log p$.

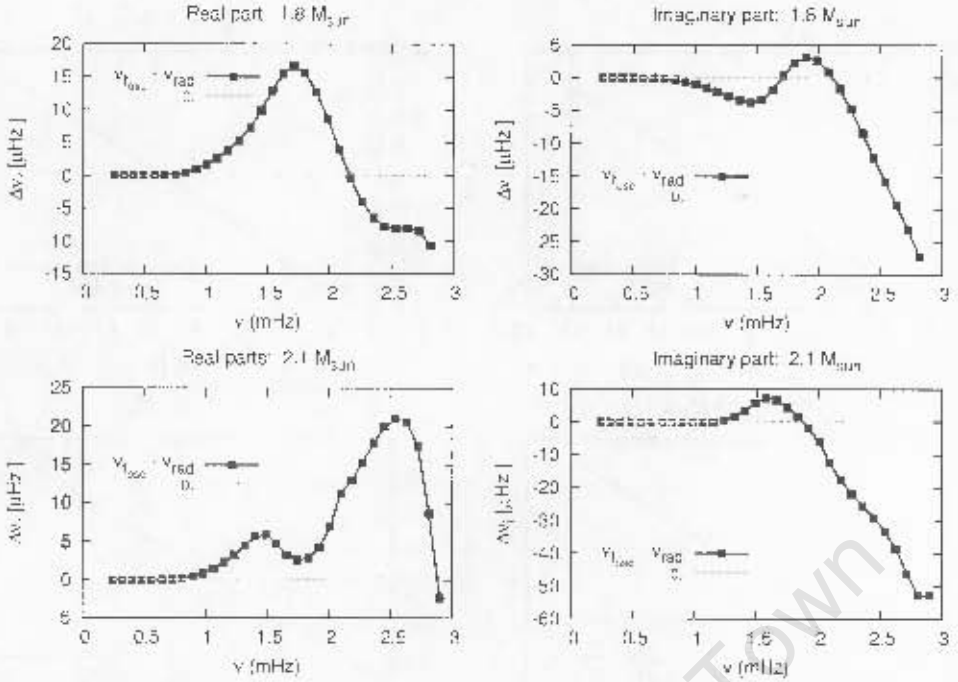

Figure 4.31: The difference between the eigenfrequencies obtained using the convective models and the eigenfrequencies obtained using radiative models.

4.2.1 The effect on the eigenfrequencies

In Fig. 4.31 we show $\Delta\nu_r = Re(\nu_{fasc}) - Re(\nu_{rad})$ and $\Delta\nu_i = Im(\nu_{fasc}) - Im(\nu_{rad})$ for equilibrium models $1.8M_\odot$ and $2.1M_\odot$. Here ν_{rad} denotes the cyclic frequency obtained using radiative models. It is clear that there is no difference in the calculated frequencies below the frequency 1 mHz. The results are shown in Table 4.3.

Table 4.3: The maximum differences between the eigenfrequencies obtained using convective models and the eigenfrequencies obtained using radiative models. The first column denotes the mass of the equilibrium models, the second column denote the changes $|\Delta\nu_r|$ relative to cyclic frequency ν_r (in mHz), and the third column denotes the changes $|\Delta\nu_i|$ relative to ν_i (in mHz).

$M/M_\odot$	$\lvert\Delta\nu_r/\nu_r\rvert$ (%)	$\lvert\Delta\nu_i/\nu_i\rvert$ (%)
1.8	0.97	0.26
2.1	0.83	1.87

4.2.2 The effect on the temperature eigenfunctions

In Figures 4.32 to 4.35 we compare the temperature eigenfunctions obtained using radiative models with those using convective models. First we notice that the suppression of convection on both the equilibrium and pulsation models is sufficiently large in $\delta T/T$. It is also very clear that the inclusion of convection drastically decreases the dip that is seen in the hydrogen ionization zone.

4.2.2.1 $1.8M_{\odot}$ model

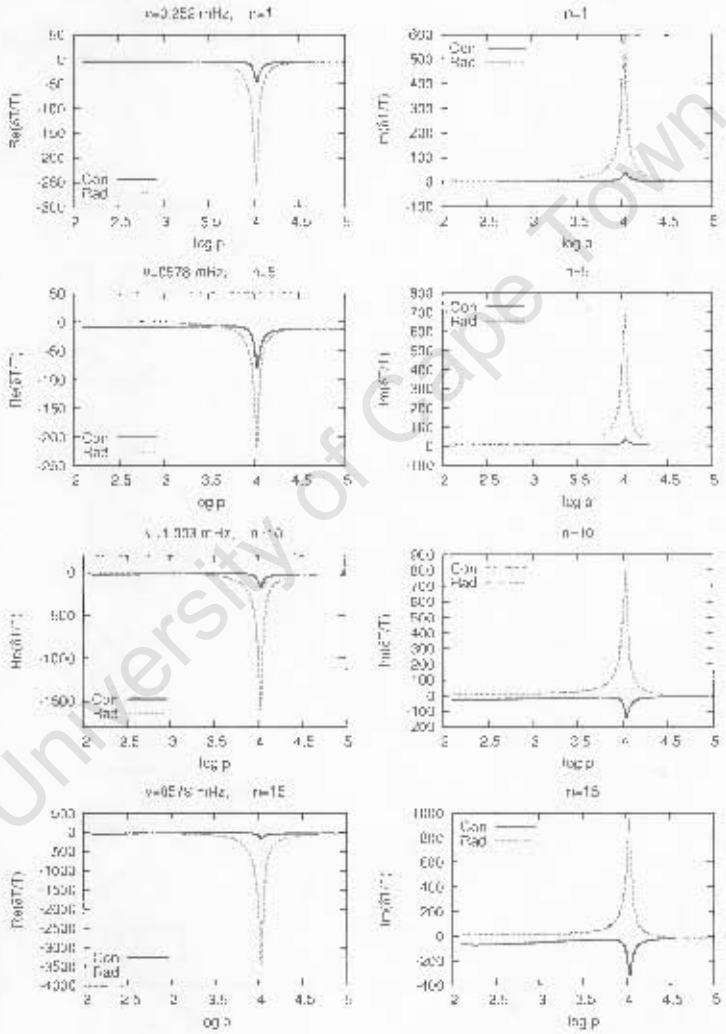

Figure 4.32: A comparison of real and imaginary parts of the temperature eigenfunctions computed using radiative model (Rad) with those using convective model (Con) for the $1.8M_{\odot}$ at various frequencies. The left and right panels show real and imaginary parts of temperature eigenfunctions.

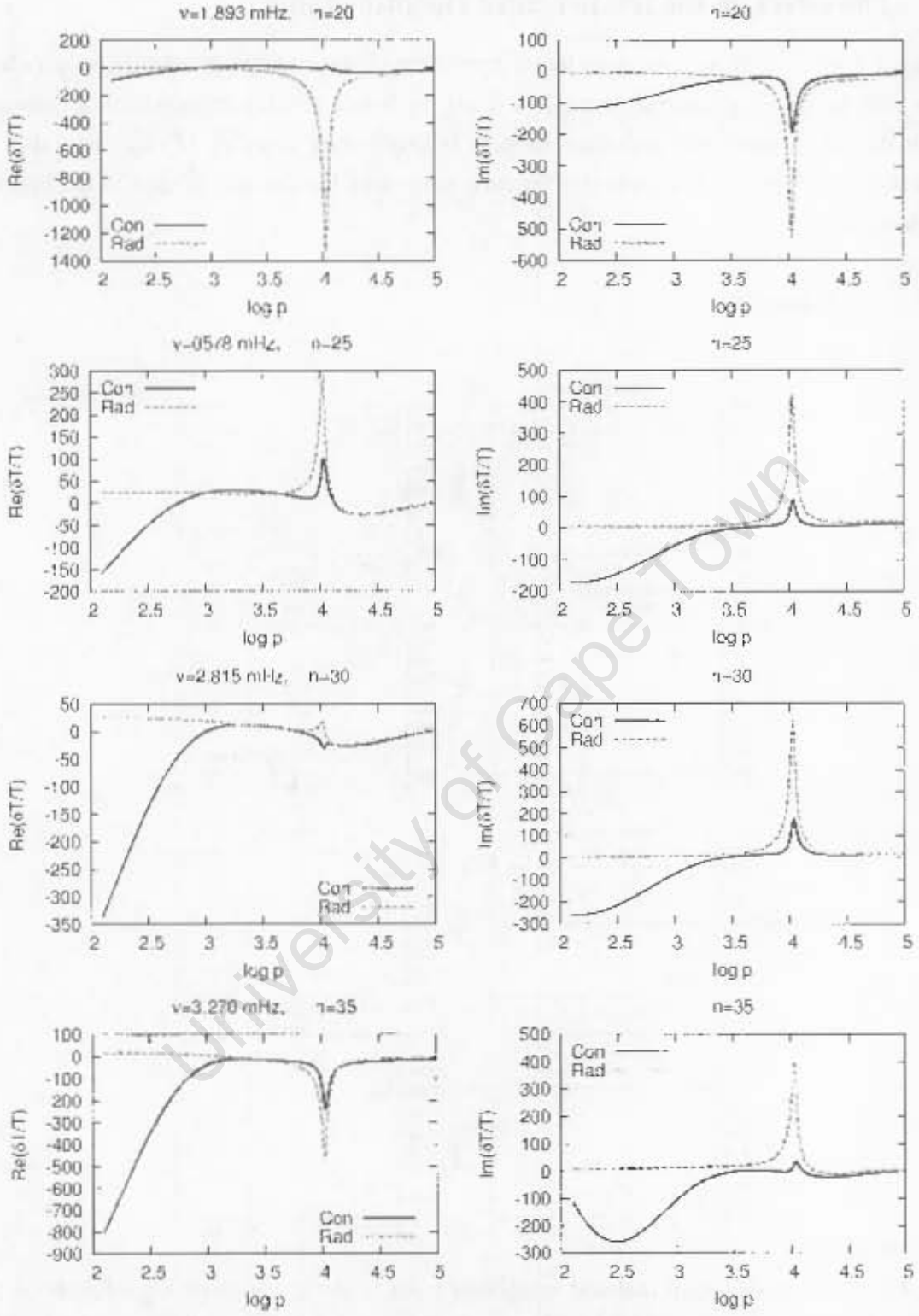

Figure 4.33: A comparison of real and imaginary parts of $\delta T/T$ computed using radiative model (Rad)with those using convective models (Con) for the $1.8M_{\odot}$ model at various frequencies. The left and right panels show real and imaginary parts of temperature eigenfunctions.

4.2.2.2 $2.1M_{\odot}$ model

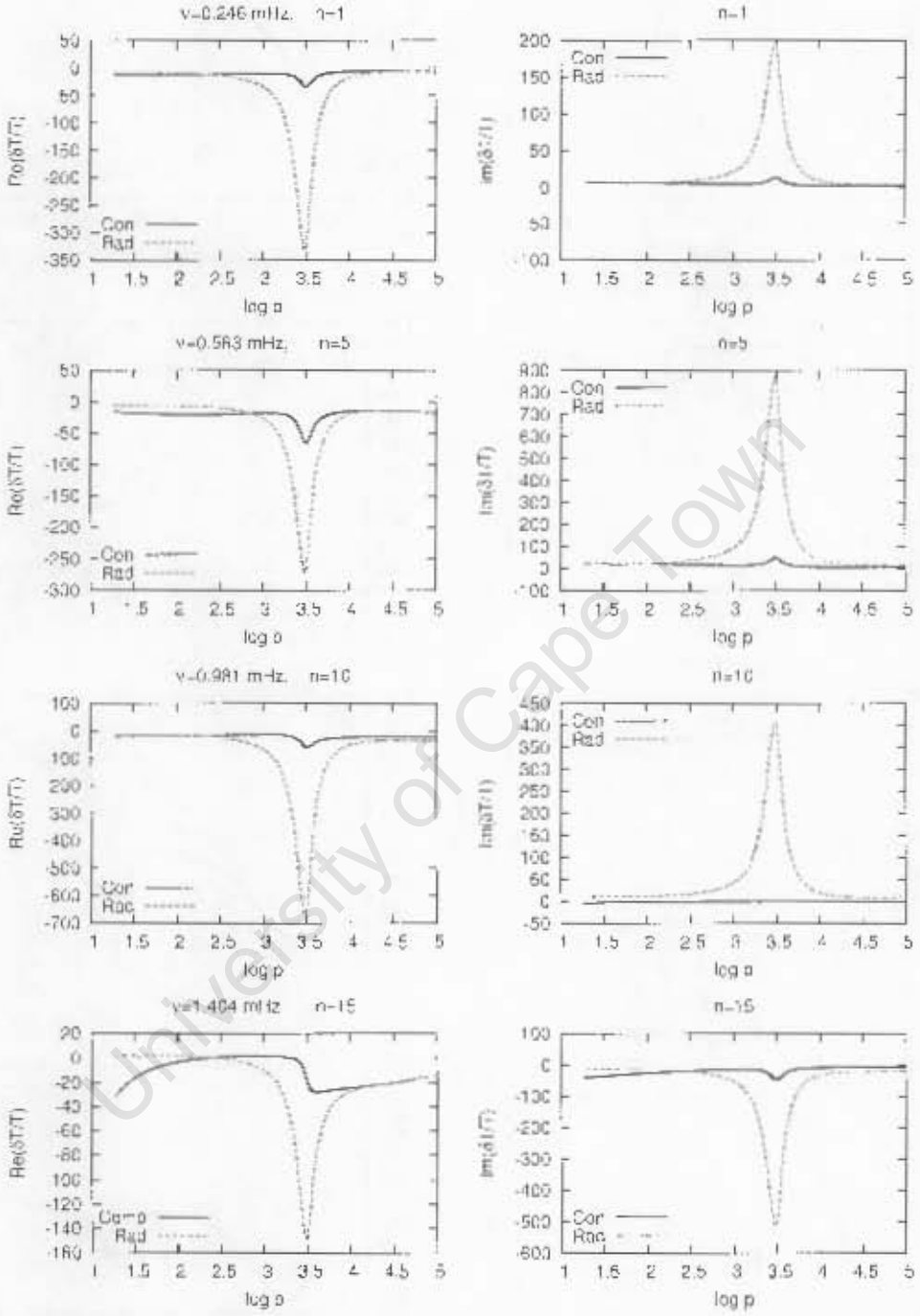

Figure 4.34: A comparison of real and imaginary parts of $\delta T/T$ computed using radiative model (Rad) with those using convective model (Con) at various frequencies. The left and right panels show real and imaginary parts of temperature eigenfunctions for $2.1M_{\odot}$ model.

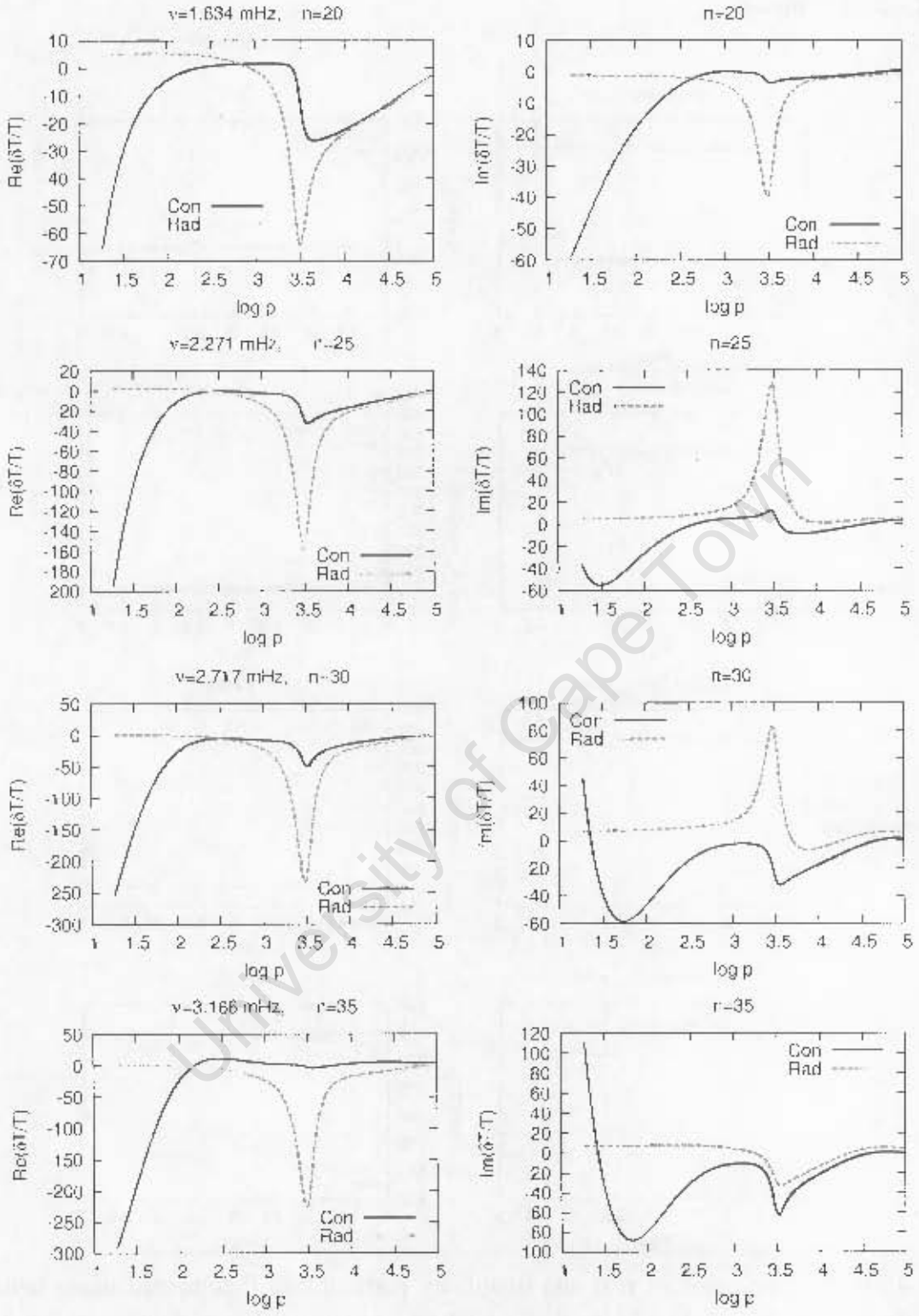

Figure 4.35: A comparison of real and imaginary parts of the temperature eigenfunctions computed using radiative model (Rad) with those using convective model (Con) at various frequencies. The left and right panels show real and imaginary parts of temperature eigenfunctions for $2.1 M_{\odot}$ model.

4.2.3 The displacement eigenfunctions

In Figures 4.36 and 4.37 the displacement eigenfunctions obtained using radiative models with those using convective models are compared. Generally the effect of convection on the displacement eigenfunctions is significantly large.

4.2.3.1 $1.8M_\odot$ model

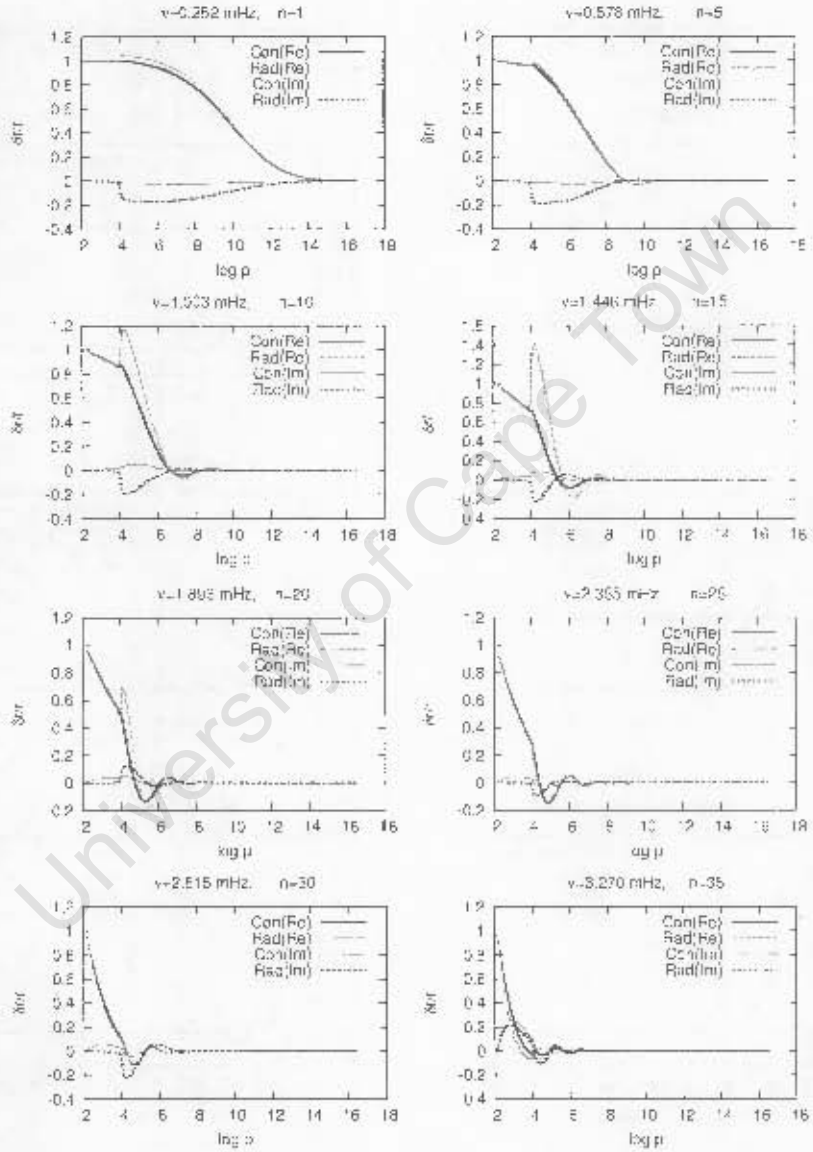

Figure 4.36: A comparison of $\delta r/r$ obtained using radiative model (Rad) with those using convective model (Con) at various frequencies. The real (Re) and imaginary (Im) parts of $\delta r/r$ are shown for $1.8M_\odot$ model.

4.2.3.2 $2.1M_{\odot}$ model

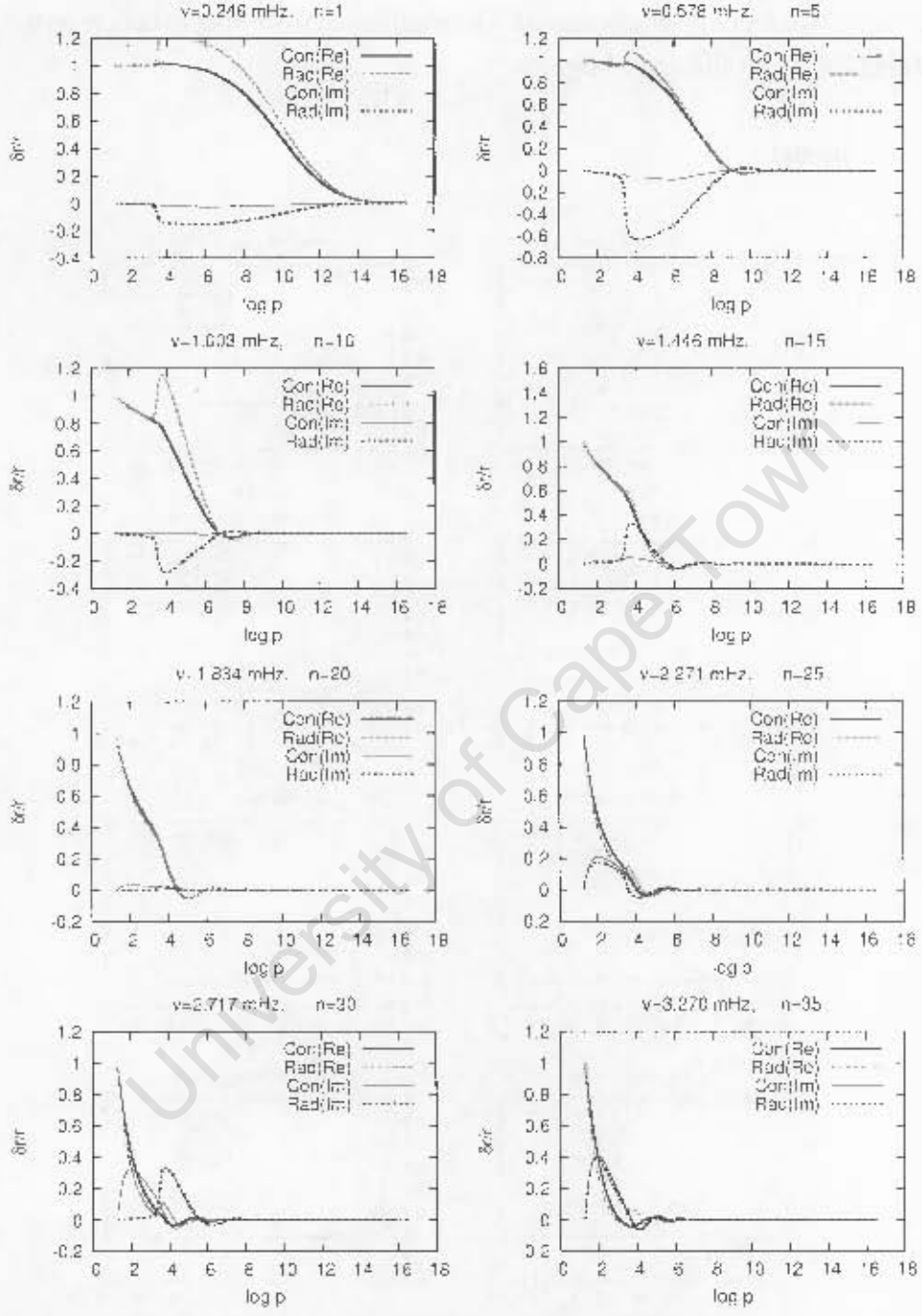

Figure 4.37: A comparison of $\delta r/r$ obtained using radiative model (Rad) with those using convective model (Con) at various frequencies. The real (Re) and imaginary (Im) parts of $\delta r/r$ are shown for $2.1M_{\odot}$ model.

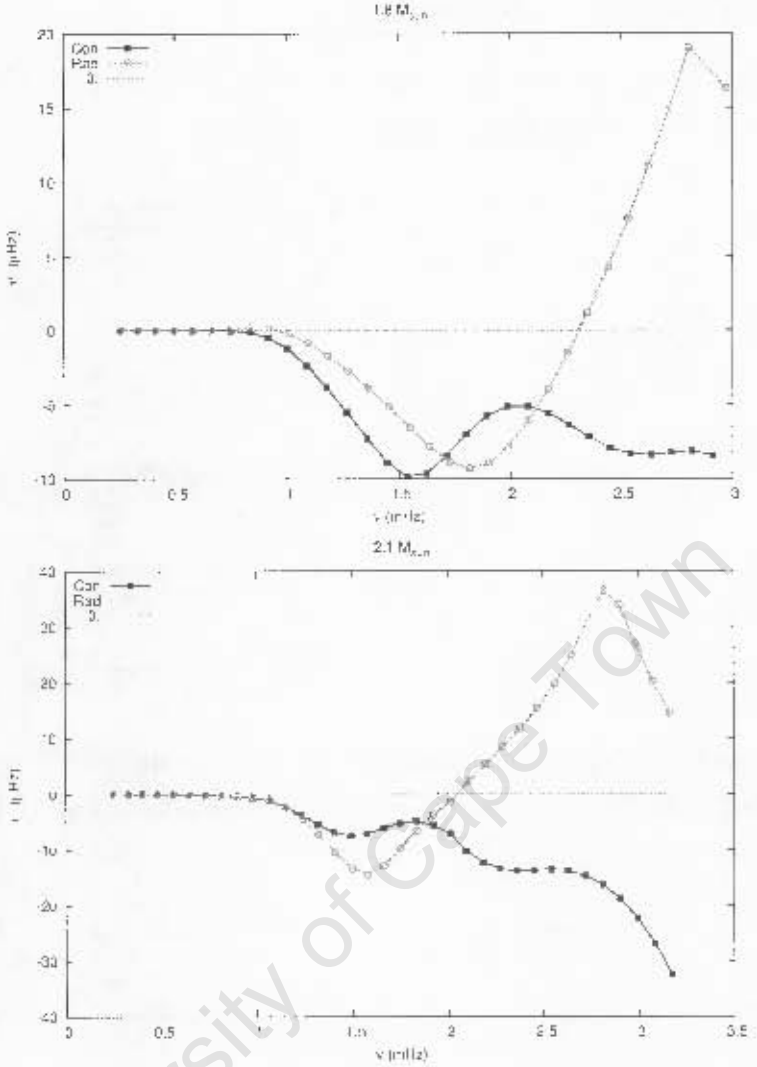

Figure 4.38: The growth rates as function of the cyclic frequency for $1.8M_{\odot}$ and $2.1M_{\odot}$ models. The curve labelled 'Con' was obtained using convective models, whereas for the curve labelled 'Rad' we used radiative models.

4.2.4 The effects on the growth rates

Here the growth rates computed by imposing a displacement node at the base of the envelope using convective models with those using radiative models are compared. The results are shown in Fig. 4.38. It is noticeable that if convection is suppressed in the envelope of A stars then the higher frequency modes larger than 2 mHz can be excited, and for lower frequency modes less than 1 mHz the effect is unnoticeable. In addition, the results show that if convection is excluded in our modelling, this could predict excitation or damping in different frequency regions of the A stars.

4.2.5 The effects on the work integrals

In Figures 4.39 and 4.40 we compare the behaviour of the work integrals obtained using convective models with those obtained using radiative models.

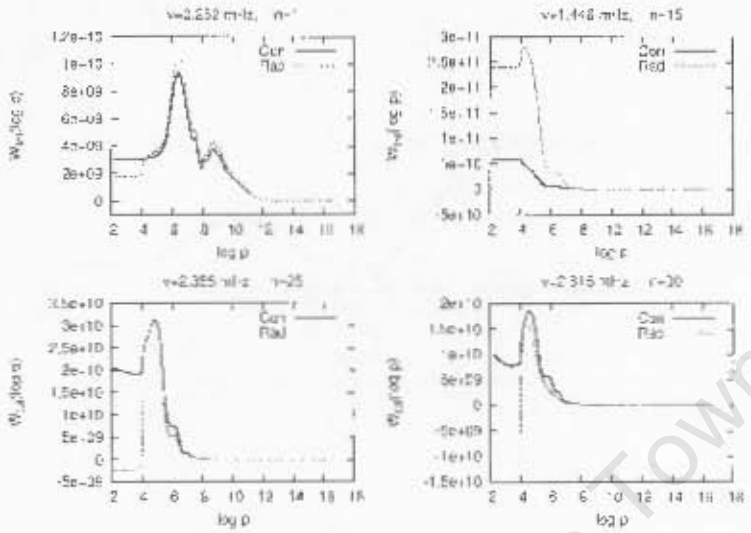

Figure 4.39: A comparison of the accumulated work integrals (in units $10^{30} erg$) computed using radiative model (Rad) with those obtained using convective model (Con) for the $1.8 M_{\odot}$ model at various frequencies.

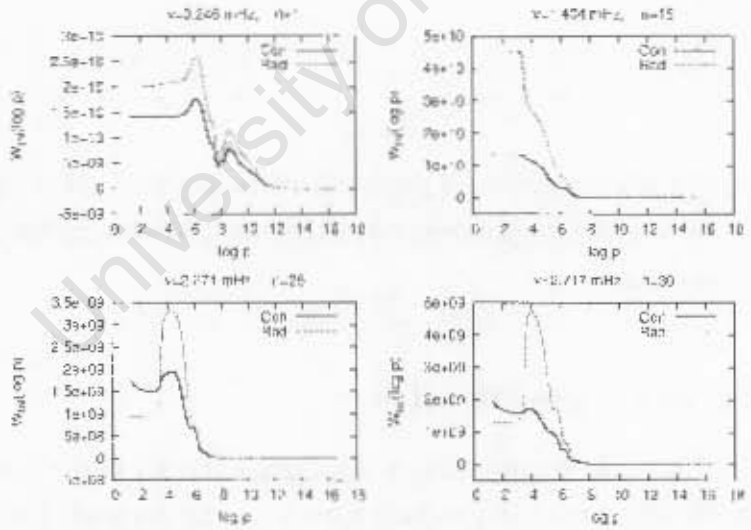

Figure 4.40: A comparison of the accumulated work integrals (in units $10^{30} erg$) computed using radiative model (Rad) with those obtained using convective model (Con) for the $2.1 M_{\odot}$ model at various frequencies.

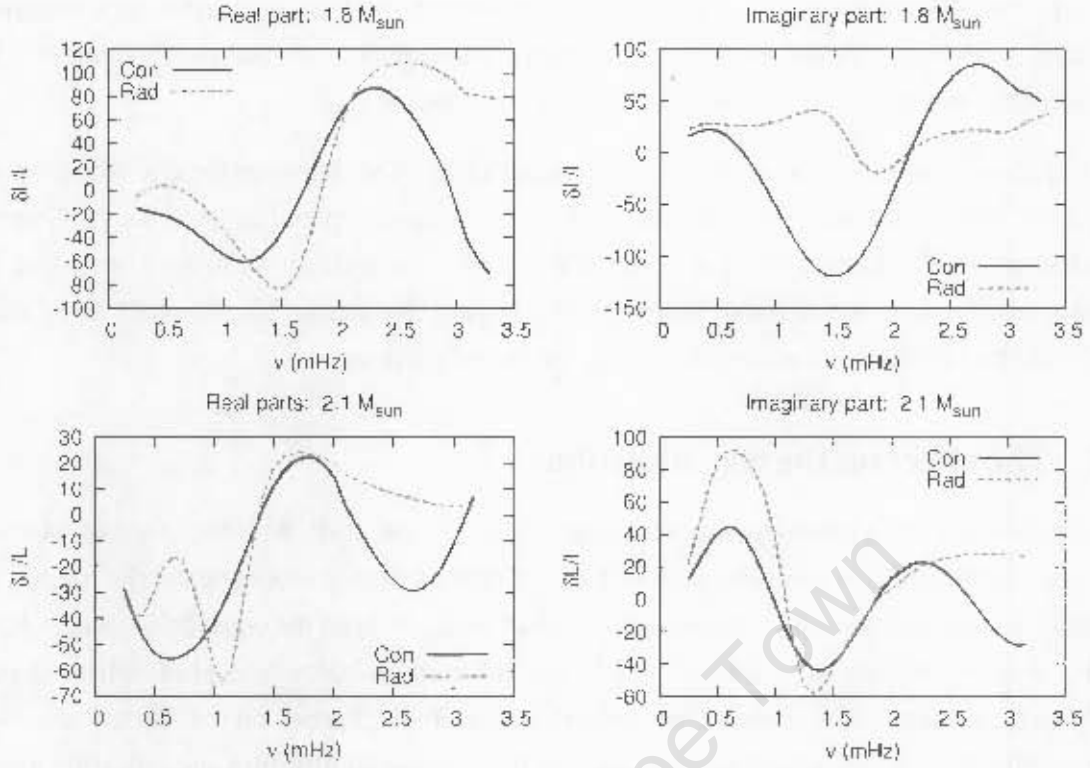

Figure 4.41: The $\delta L/L$ at the surface plotted as function of frequency for $1.8M_{\odot}$ and $2.1M_{\odot}$ equilibrium models. The curve labelled 'Rad' was obtained using radiative model, whereas for the curve labelled 'Con' we used the convective models.

4.2.6 The effect on the surface luminosity perturbations

In Fig. 4.41 we compare the luminosity perturbations at the surface as a function of frequency obtained using convective models with those using radiative models. It is clear that the suppression of convection on both the equilibrium and pulsation model has an effect on the surface $\delta L/L$. There is a maximum relative difference (real parts of surface $\delta L/L$) of up to about 80% near 2.8 mHz for the $1.8M_{\odot}$ model and 100% near 2.7 mHz for $2.1M_{\odot}$ model. For the imaginary parts the maximum relative difference is up to about 100% near 1.5 mHz for $1.8M_{\odot}$ model and 100% near 3 mHz for $2.1M_{\odot}$ model.

4.3 Comparisons of the new code with Medupe's code

In this section we give a brief comparison between the results obtained from the new code and those using Medupe's code. Medupe's code solve the grey non-adiabatic radial pulsation equations with consistent treatment of radiative transfer and does not include convection. The results

obtained from Medupe's code are based on the equilibrium models constructed by Christensen-Dalsgaard. In the equilibrium models by Christensen-Dalsgaard convection is treated in a local approximation and do not include explicit treatment of radiation.

It is quite clear from Figs. 4.42 to 4.45 that there are differences between the equilibrium model by Houdek and Christensen-Dalsgaard in T, ∇_{ad}, κ and ρ compared at fixed $\log p$. Generally the difference in ∇_{ad} is very large as compared to other quantities both in the convective zone and the atmosphere. It is noticeable that there is a large difference in ∇_{ad} for the $1.6M_{\odot}$ model. This should be kept in mind when comparing the eigenfunctions.

4.3.1 The effect on the eigenfunctions

Here we compare the eigenfunctions obtained from the new code with those using Medupe's code. The results are shown in Figs. 4.46 to 4.53. In case of $1.6M_{\odot}$ model below the photosphere the differences in the eigenfunctions we see depend mainly on both the equilibrium and pulsation models. For the models with $M > 1.8M_{\odot}$ the differences below the photosphere depends heavily on the on the calculations of oscillations. In the atmosphere of all the models considered here the differences on the eigenfunctions depend both on the equilibrium and pulsation models. Therefore for $M \geq 1.8M_{\odot}$ models there is a large difference in $\delta T/T$ and $\delta r/r$ between the two approaches. There is a slight difference in the position of a dip below the photosphere which is due to difference in the equilibrium models. It is clear that depth of the dip is very small in $\delta T/T$ obtained from the new code compared to the one obtained from Medupe's code.

4.3.2 The effect on the growth rates

In this subsection the growth rates computed from the new code with those using Medupe's code are compared. The growth rates from Medupe's code are determined by requiring that the part of the star below the base of the stellar envelope does no work on the part above the base. The results are shown in Fig 4.54. In all the equilibrium models considered here we notice that the growth rates obtained using the new code and Medupe's code are in agreement at low frequencies up to about 1 mHz. The growth rates obtained using the new code are small compared to the one obtained from the Medupe's code at high pulsation frequency ($\nu > 1.5$ mHz) for the models with $M \geq 1.8M_{\odot}$. For the $1.6M_{\odot}$ model the growth rates obtained from Medupe's code are small as compared with those obtained using the new code. It can be confirmed that the unstable mode found in $1.6M_{\odot}$ model is due to turbulent pressure because it does not appear in the growth rates from Medupe's code.

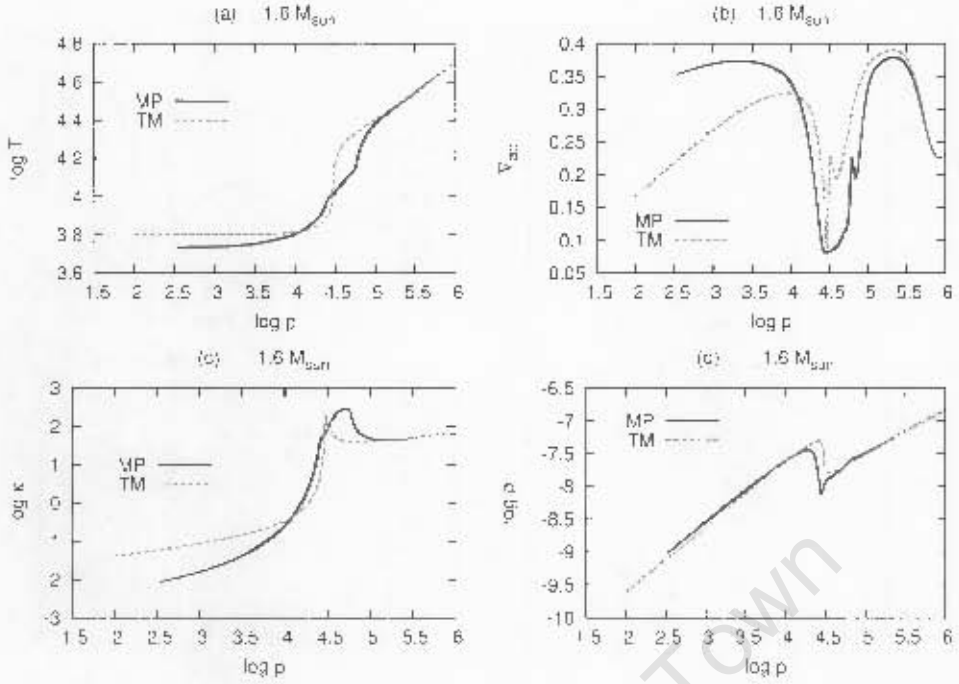

Figure 4.42: A comparison between the equilibrium models used in the new code (MP) with those used in Medupe's code (TM). The quantities ρ, κ, ∇_{ad} and T for $1.6M_{\odot}$ model are compared.

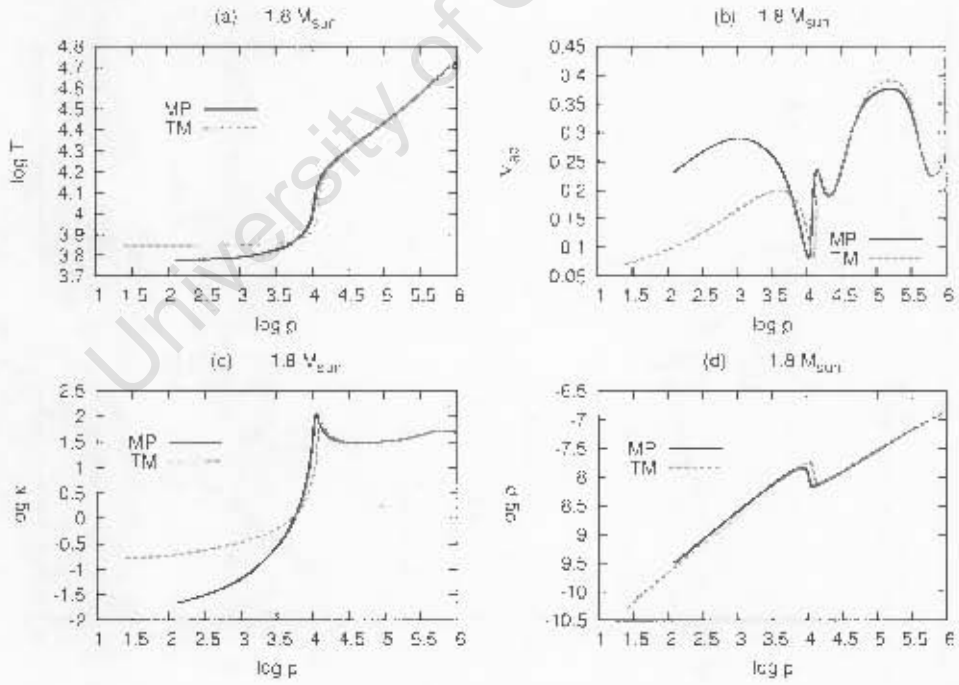

Figure 4.43: A comparison between the equilibrium models used in the new code (MP) with those used in Medupe's code (TM). The quantities ρ, κ, ∇_{ad} and T for $1.8M_{\odot}$ model are compared.

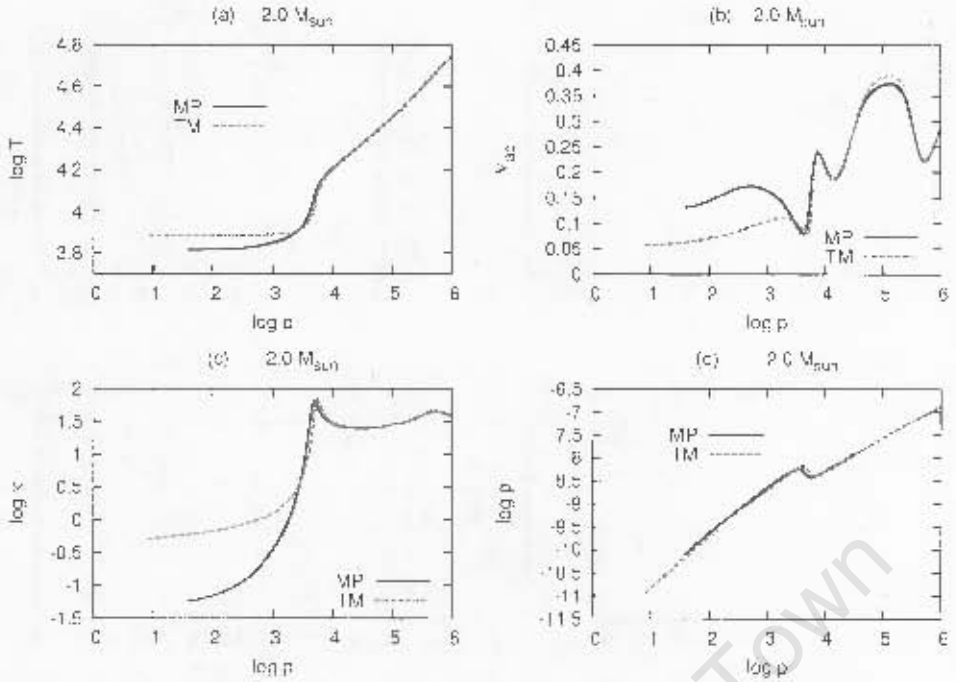

Figure 4.44: The differences between the equilibrium models used in the new code (MP) with those used in Medupe's code (TM). The quantities ρ, κ, ∇_{ad} and T for $2.0M_{\odot}$ model are compared as a function $\log p$.

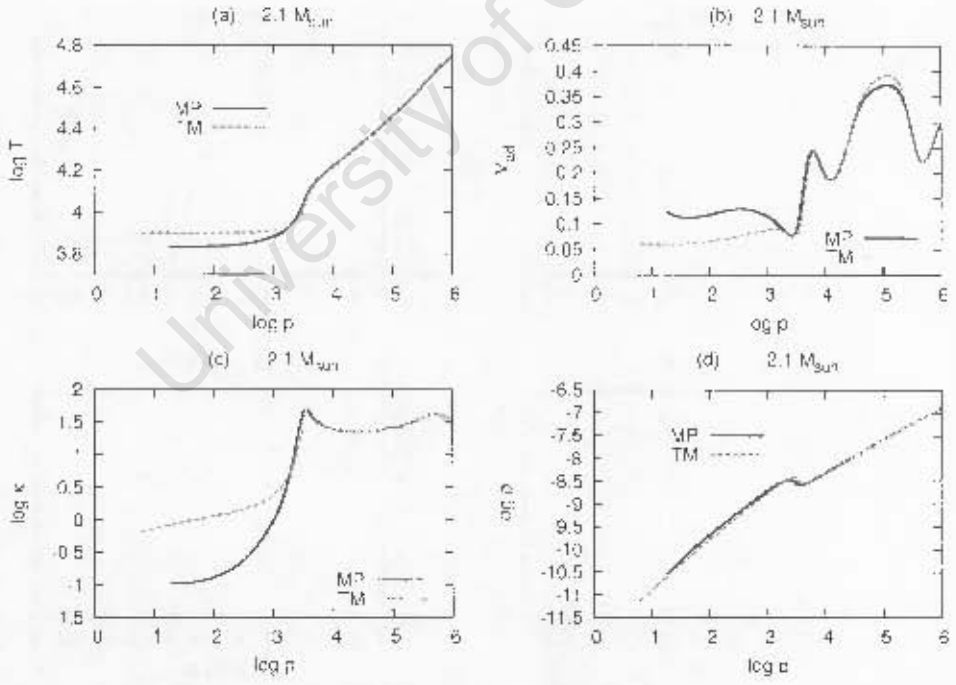

Figure 4.45: The differences between the equilibrium models used in the new code (MP) with those used in Medupe's code (TM). The quantities ρ, κ, ∇_{ad} and T for $2.1M_{\odot}$ model are compared as a function of $\log p$.

4.3.2.1 The temperature eigenfunctions for $1.6\,M_{\odot}$ model

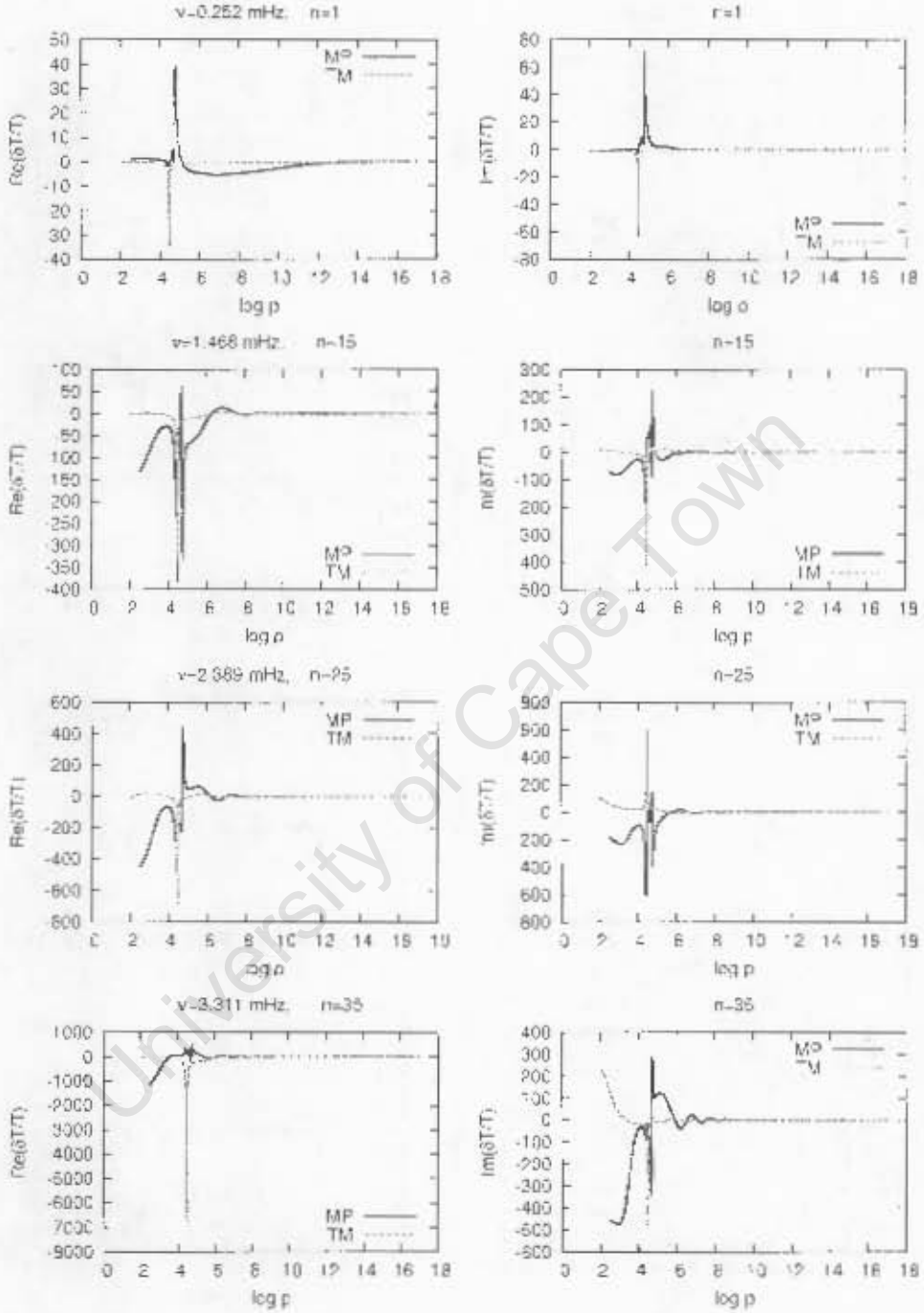

Figure 4.46: A comparison of real and imaginary parts of $\delta T/T$ obtained using the new code (MP) and those using Medupe's code (TM) for the $1.6\,M_{\odot}$ model at various frequencies.

4.3.2.2 The temperature eigenfunctions for $1.8\,M_{\odot}$ model

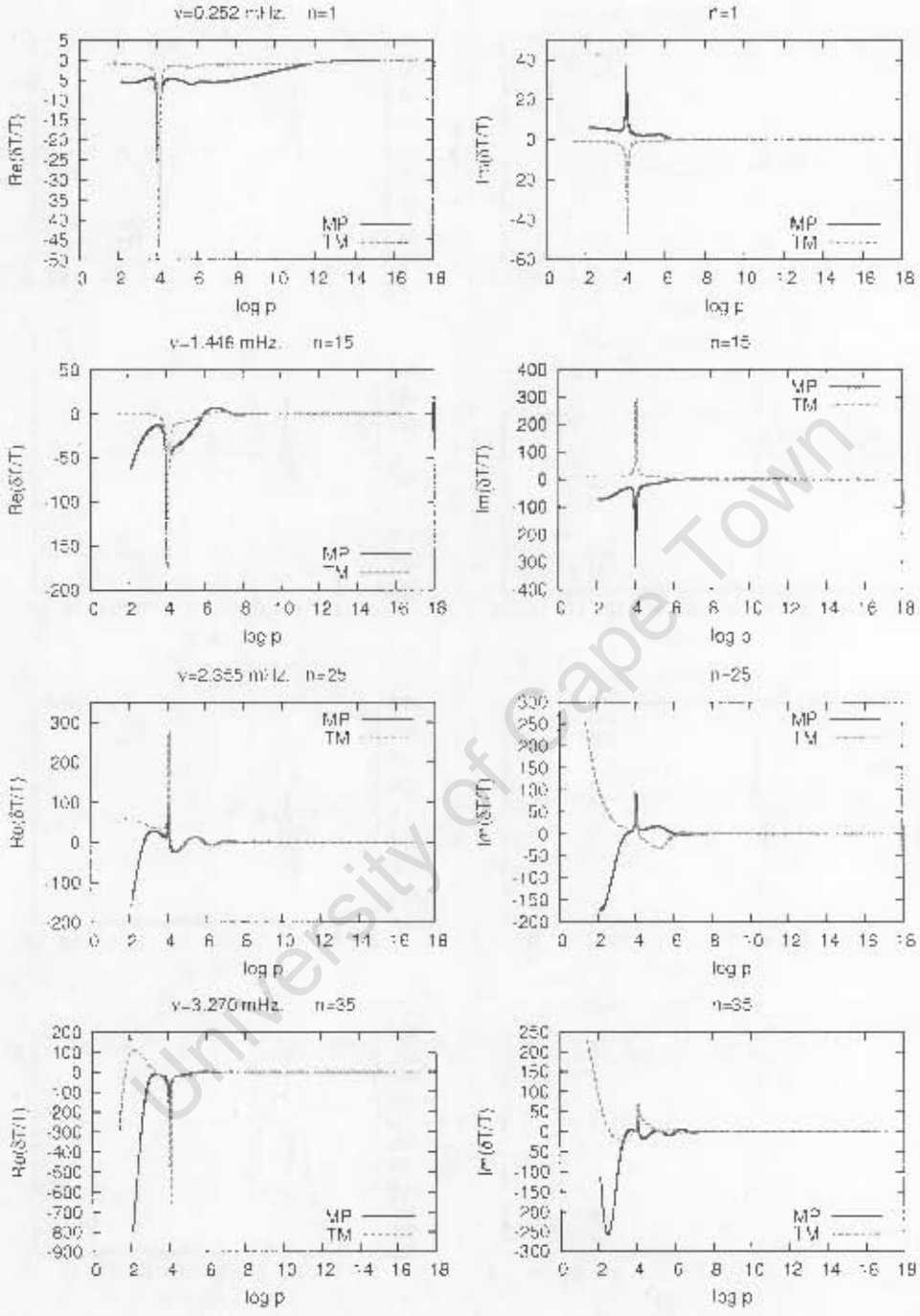

Figure 4.47: A comparison of real and imaginary parts of $\delta T/T$ obtained using the new code (MP) and those using Medupe's code (TM) for the $1.8M_{\odot}$ model at various frequencies.

4.3.2.3 The temperature eigenfunctions for $2.0\,M_{\odot}$ model

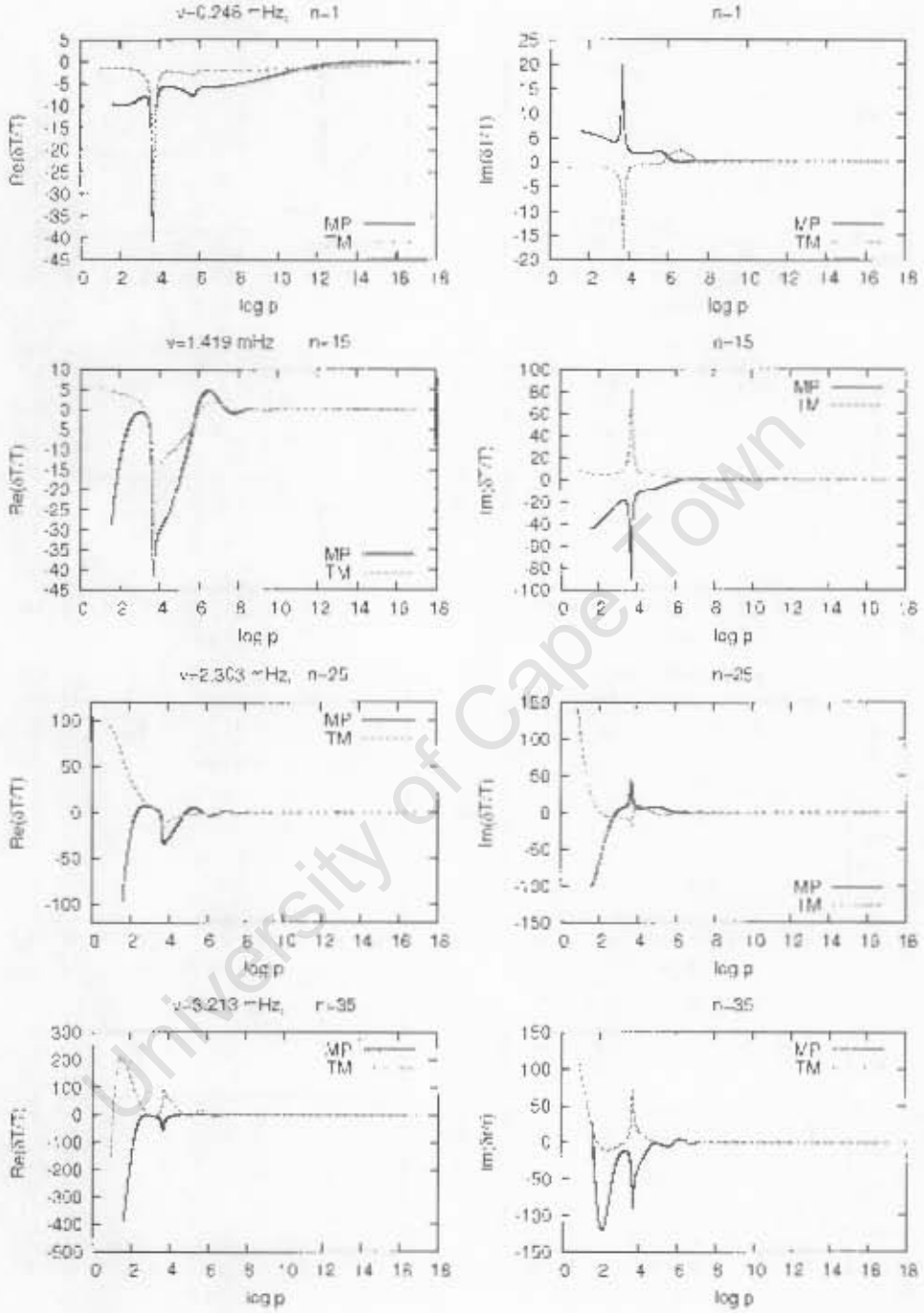

Figure 4.48: A comparison of real and imaginary parts of $\delta T/T$ obtained using the new code (MP) and those using Medupe's code (TM) for the $2.0\,M_{\odot}$ model at various frequencies.

4.3.2.4 The temperature eigenfunctions for $2.1\,M_{\odot}$ model

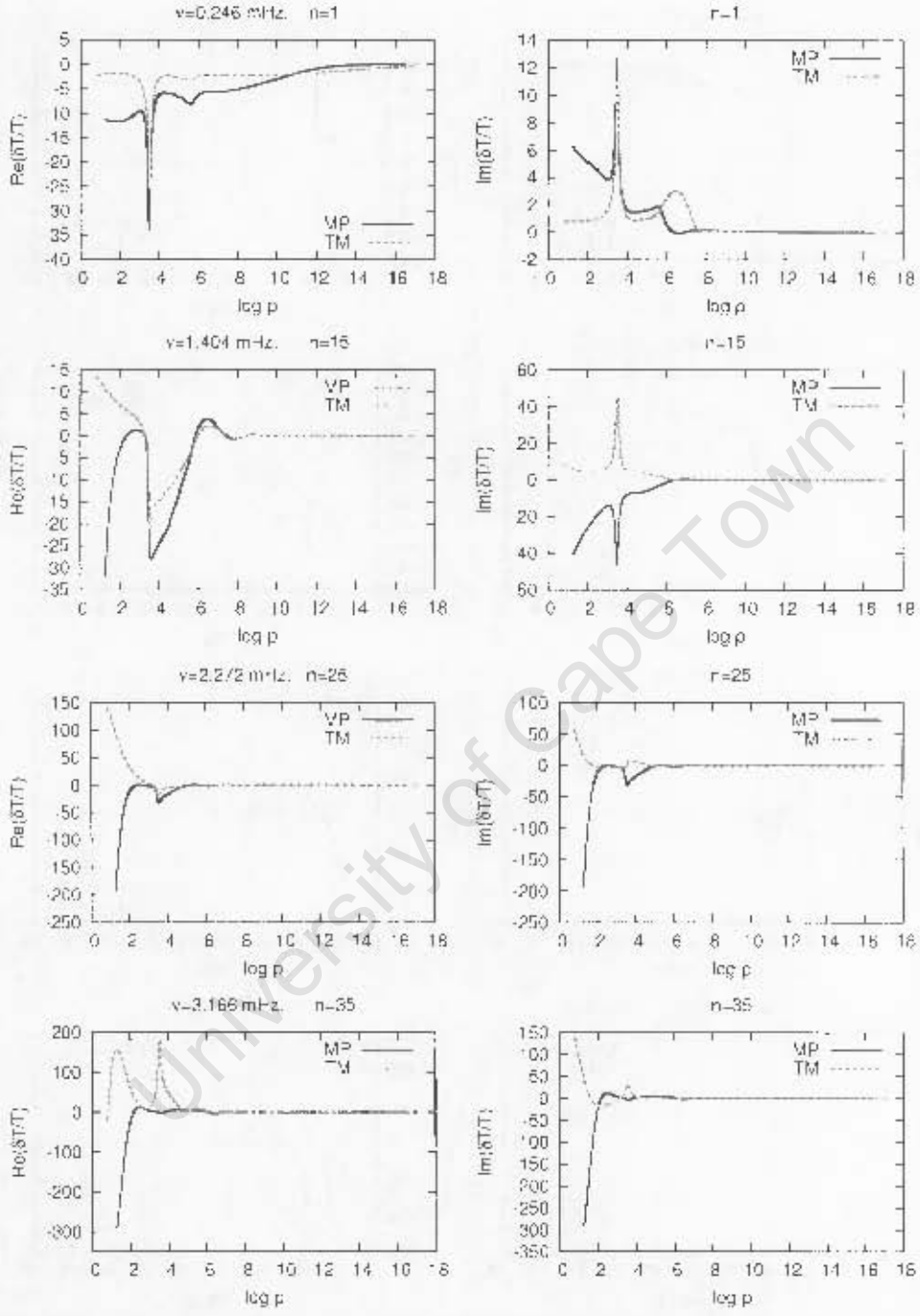

Figure 4.49: A comparison of real and imaginary parts of $\delta T/T$ obtained using the new code (MP) and those using Medupe's code (TM) for the $2.1\,M_{\odot}$ model at various frequencies.

4.3.2.5 The displacement eigenfunctions for $1.6\,M_\odot$ model

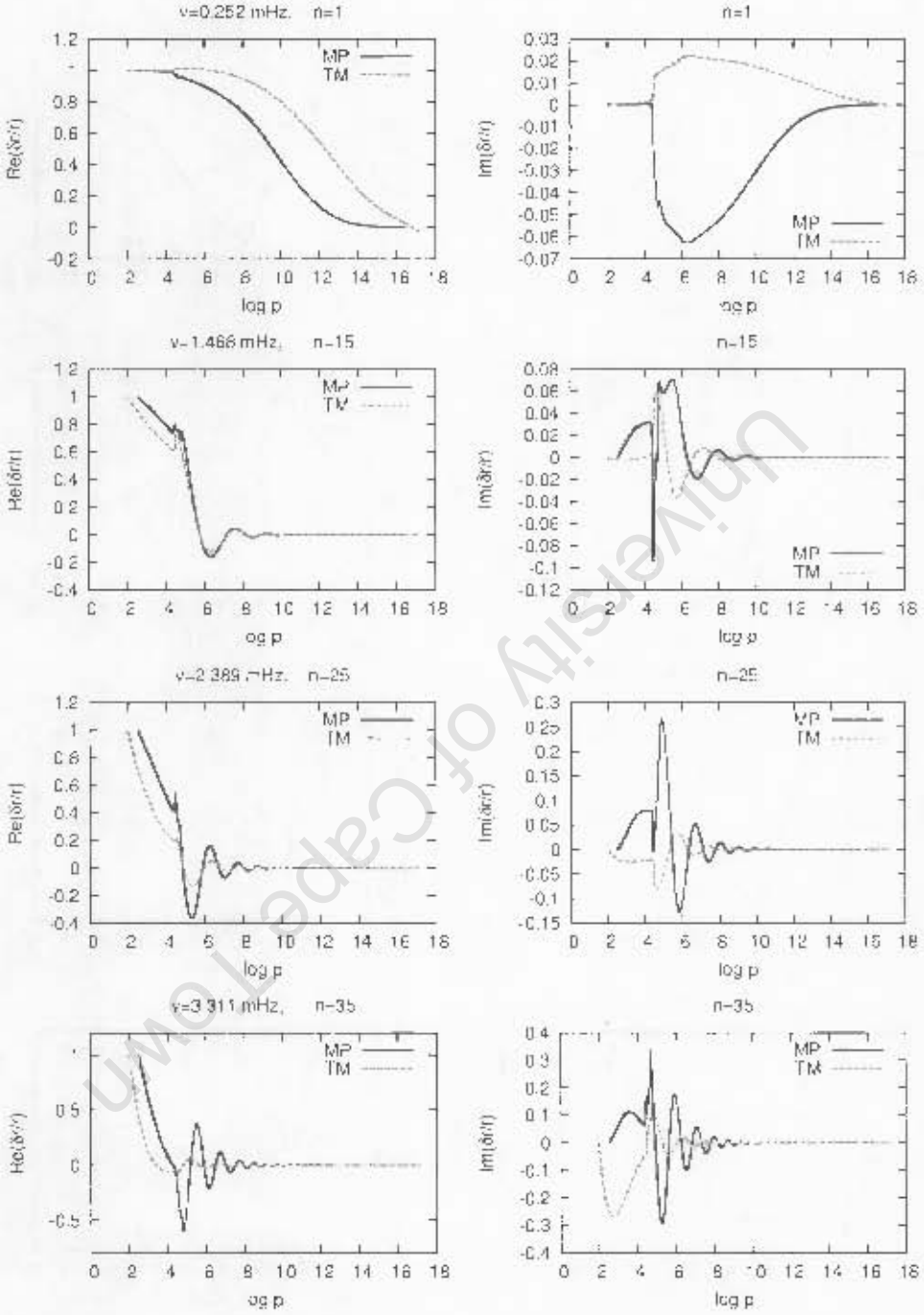

Figure 4.50: A comparison of real and imaginary parts of $\delta r/r$ obtained using the new code (MP) and those using Medupe's code (TM) for the $1.6M_\odot$ model at various frequencies.

4.3.2.6 The displacement eigenfunctions for $1.8\,M_{\odot}$ model

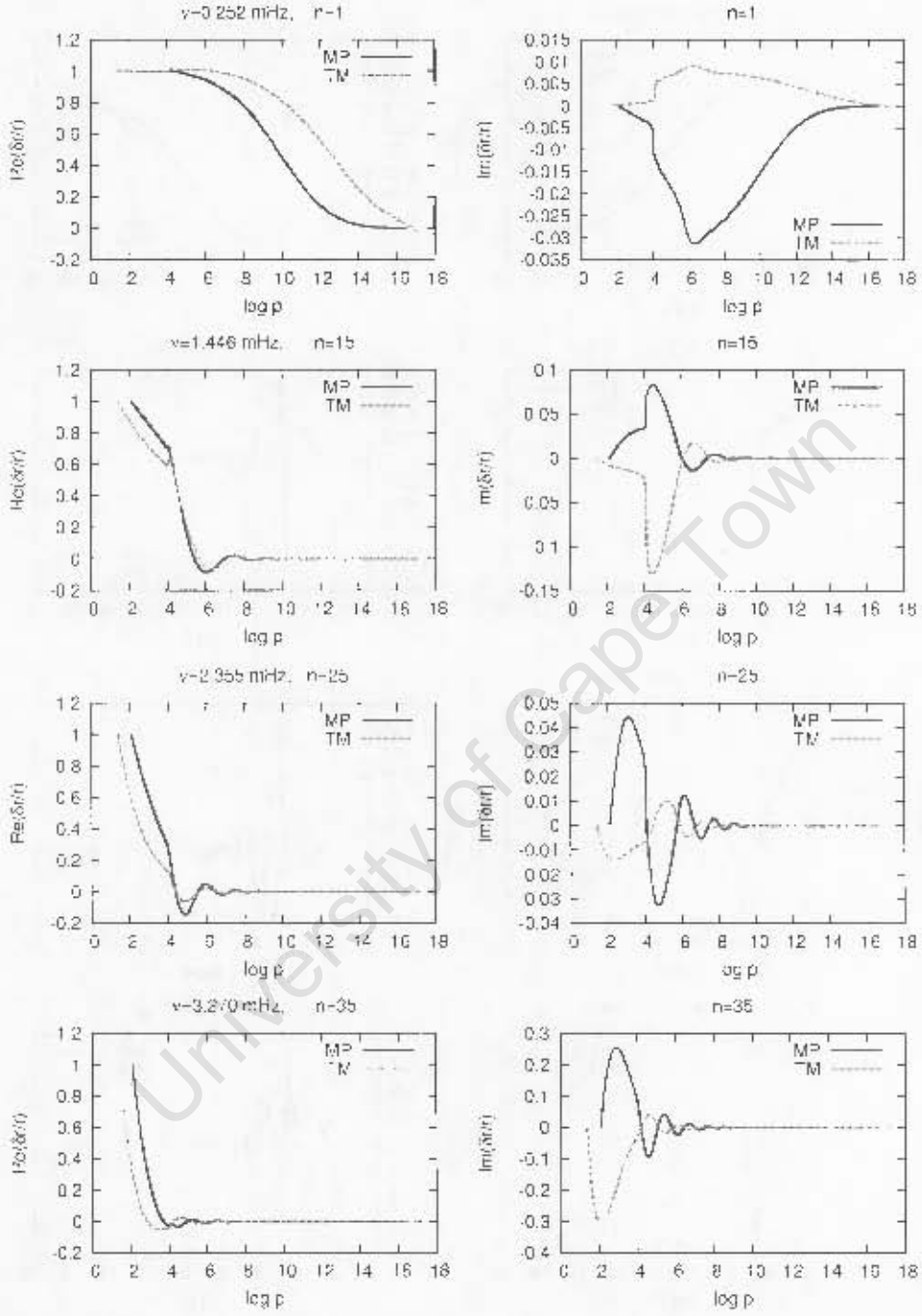

Figure 4.51: A comparison of real and imaginary parts of $\delta r/r$ obtained using the new code (MP) and those using Medupe's code (TM) for the $1.8M_{\odot}$ model at various frequencies.

4.3.2.7 The displacement eigenfunctions for $2.0\,M_{\odot}$ model

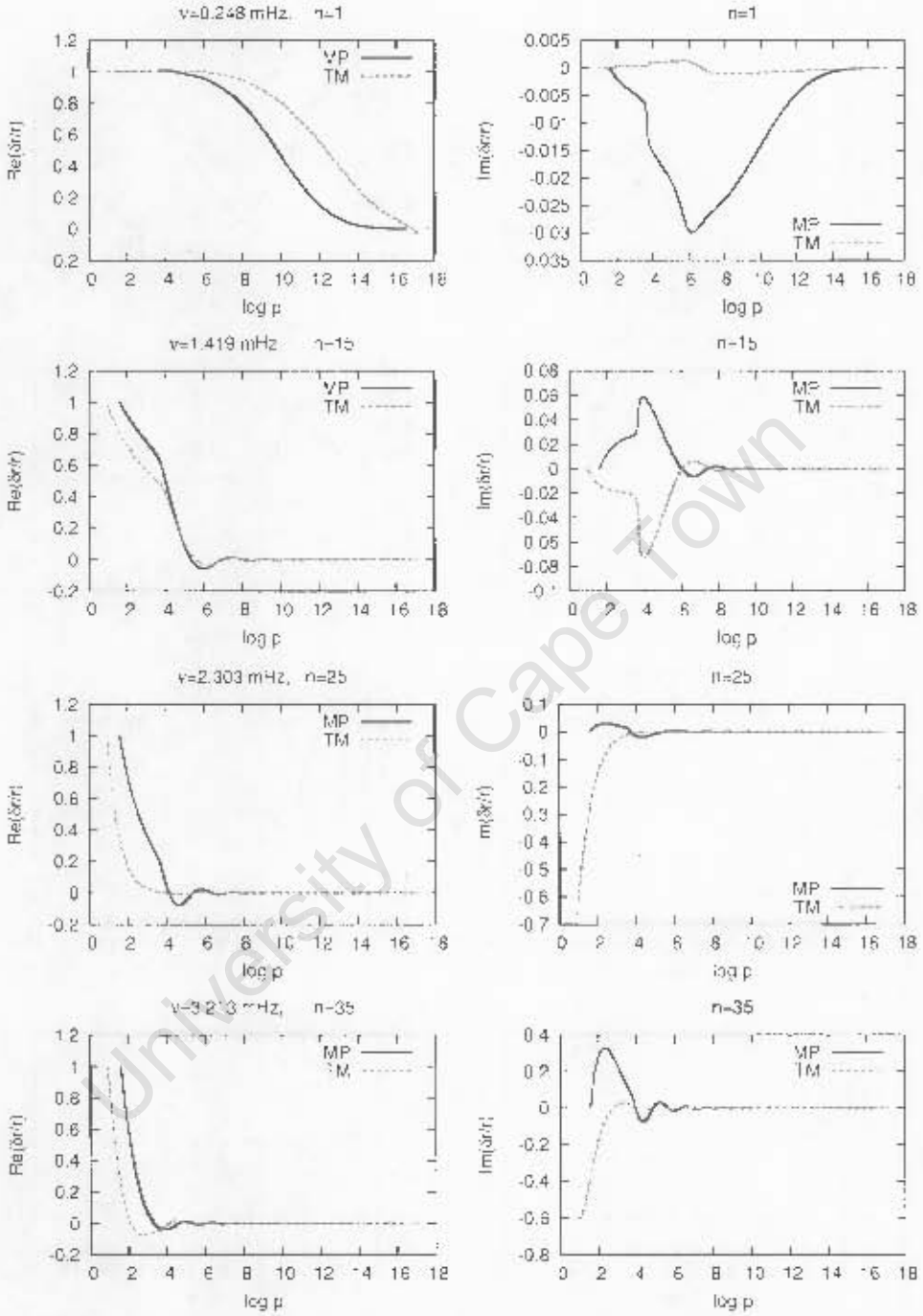

Figure 4.52: A comparison of real and imaginary parts of $\delta r/r$ obtained using the new code (MP) and those using Medupe's code (TM) for the $2.0 M_{\odot}$ model at various frequencies.

4.3.2.8 The displacement eigenfunctions for $2.1\,M_{\odot}$ model

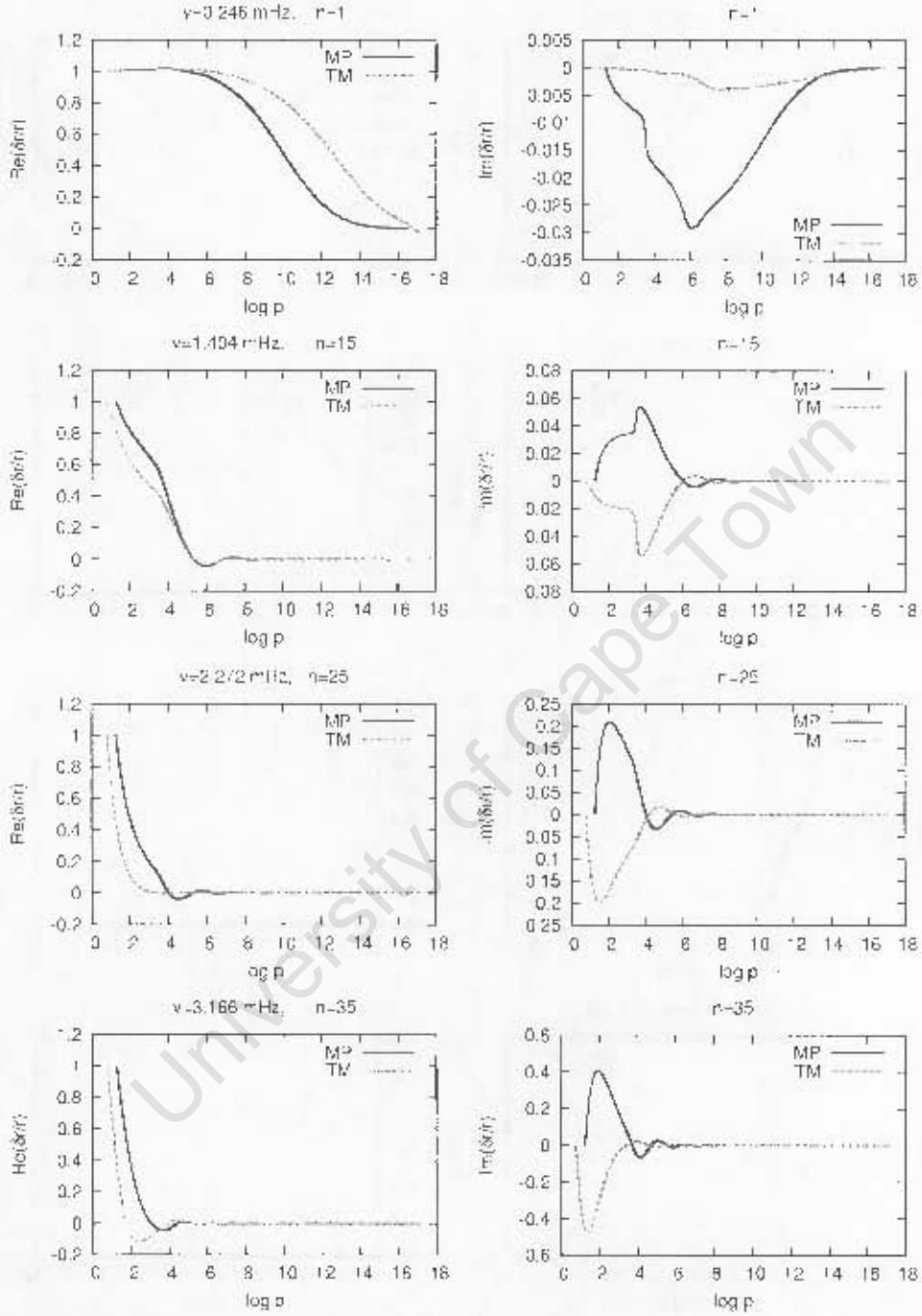

Figure 4.53: A comparison of real and imaginary parts of $\delta r/r$ obtained using the new code (MP) and those using Medupe's code (TM) for the $2.1\,M_{\odot}$ model at various frequencies.

4.3.2.9 Growth rates

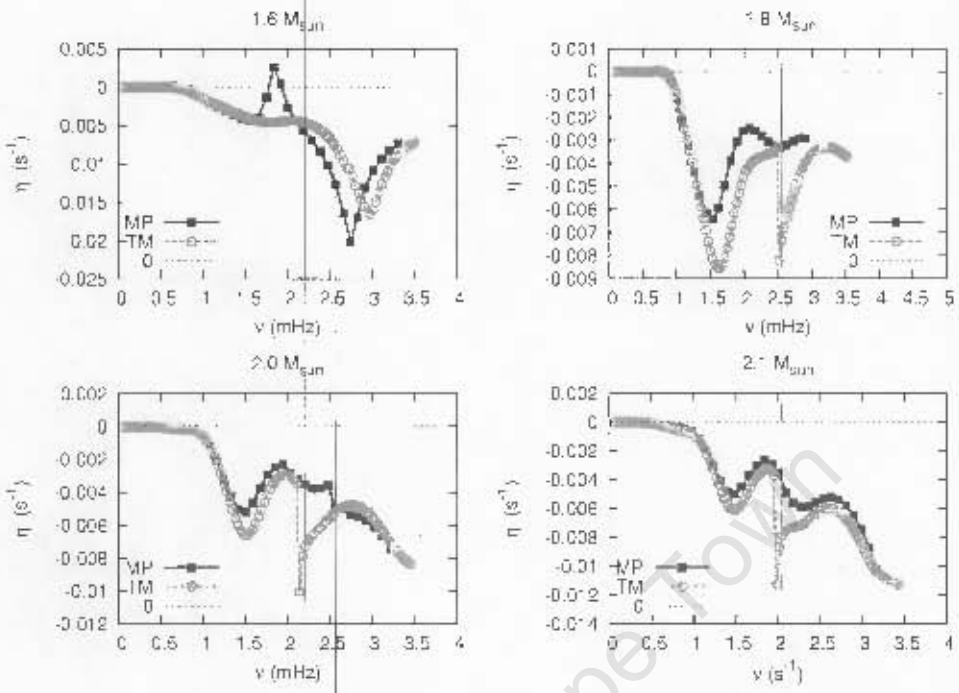

Figure 4.54: The growth rates as function of the cyclic frequency for ZAMS models. The curve labelled "MP" was obtained from the new code, whereas for the curve "TM" we used Medupe's code.

Chapter 5

Conclusions

We have developed a code to solve the non-adiabatic radial pulsation equations with consistent treatment of radiation and non-local mixing length theory of convection. This was achieved by implementing Medupe's radiative transfer routine into Houdek's non-adiabatic, non-local mixing length theory of convection code. The code was applied to the ZAMS models stars with a masses ranging from $1M_{\odot}$ to $2.1M_{\odot}$. Below I will list important findings of our investigation:

- We have shown that the shape of the dip in superadiabatic gradient $\nabla - \nabla_{ad}$ looks the same as the dip found in $\delta T/T$. It was also shown that the main effect that determines whether the dip is there or not is the opacity fluctuation.

- The results also show that for $1.5M_{\odot}$ and $1.6M_{\odot}$ the displacement $\delta r/r$ is more responsive to the dip in $\delta T/T$.

- We have shown from our results that the relative difference of including proper treatment of radiation can be under 1% in the determination of the eigenfrequencies. The significance of this difference can be obtained by comparing this with observational accuracy, as well as with other possible systematic errors in the frequencies. These days, the observed pulsational frequencies can be measured with less than 1% accuracy, thus the effect of including better treatment of radiation is significant if we exclude the effects of uncertainties in other parameters such as the mass and radius. There may still be other effects that would dominate the effect of including better treatment of radiation on the eigenfrequency. Balmforth et al. (2001) and Cunha (2002) found that high frequency oscillations become unstable in models of roAp star if it is assumed that surface convection is suppressed by magnetic field. It has been shown by Bigot et al. (2000) that magnetic field causes a shift of about 1-20 μHz in the real part of the frequency and about 1-15μHz in the imaginary part of the frequencies of roAp stars. In addition Cunha (2006) shows that near the surface of roAp stars the magnetic pressure can become comparable to gas pressure in magnitude. Rotation causes departures from spherical symmetry, and this departure lift the degeneracy, causing a frequency splitting according to the azimuthal order m. In addition, Saio (2005) found that through the dissipation of slow Alfvenic waves, direct

effect of the magnetic field could stabilize the low radial order δ Scuti type pulsations in roAp stars. The relative difference of including proper treatment of radiation can be up to 72% in $\delta T/T$.

- It has become clear that the effect of proper treatment of radiation in the eigenfunctions and eigenfrequencies is very much model dependent. There is a clear distinction in behaviour between the models with $M \leq 1.6M_{\odot}$ and those with $M \geq 1.6M_{\odot}$.

- By comparing the results obtained with my code with those using Houdek's code we have shown that in terms of estimating eigenfrequencies it does not make a big difference whether the Eddington approximation or full radiative transfer is used in the pulsation equations when studying δ Scuti stars. However within the roAp stars frequency region $1 < \nu < 3$ mHz depicted in Fig. 4.1 the differences can be large. Therefore for accurate determination of frequencies it is important to use consistent treatment of radiative transfer when studying the roAp stars. It is also shown that except for radial mode $n = 1$ there is significant difference in the shapes of the temperature eigenfunctions introduced by improved treatment of radiation for models with $M < 1.6M_{\odot}$.

- Except for the $1.5M_{\odot}$ and $1.6M_{\odot}$ models, all the modes are damped. The unstable modes for the $1.5M_{\odot}$ and $1.6M_{\odot}$ models are near 2.5 mHz and 2 mHz respectively.

- Comparison of surface luminosity perturbations obtained using my code with the one using Houdek's code shows the largest difference in the $1.0M_{\odot}$ model and the smallest difference in the $2.1M_{\odot}$.

- Comparison of convective models with radiative models for $1.8M_{\odot}$ and $2.1M_{\odot}$ stars shows that when convection is neglected on both the equilibrium and pulsation model one does not introduce an error at frequencies below 1 mHz, but within the roAp stars frequency region $1 < \nu < 3$ mHz the error is significantly large. This means that when convection is neglected in roAp stars one under-estimates the growth rates. We have also shown that when convection is neglected one over-estimates the dip in the temperature eigenfunctions.

- Comparison of the new code with Medupe's code shows that the growth rates obtained using the new code are lower than those using Medupe's code at higher frequencies. Preliminary results show that the exclusion of convection on stellar oscillations over-estimate the growth rates at high frequencies in A stars. We also notice that there is large difference in $\delta T/T$ and $\delta r/r$ between the two cases. Here the differences in both the equilibrium and pulsation models must be kept in mind when comparing the results of the new code with Medupe's code. Hence preliminary results.

5.1 Limitations of the work

These are some of the limitations that must be borne in mind when critically considering the results presented in chapters 3 and 4:

- Both the equilibrium and pulsation models neglect rotational and magnetic effects. Balmforth et al. (2001) and Cunha (2002) have shown how important magnetic can be in the high frequency oscillations of roAp stars. It has been shown by Saio (2005) that the effect of the magnetic field is to stabilize low order modes in roAp stars. In addition, Cunha & Sousa (2006) have shown that helium settling suppresses lower order modes in roAp stars.
- One of the limitations is that the atmosphere of the equilibrium models constructed by Houdek is based on the semi-empirical $T(\tau)$ relation and hence the atmosphere is not consistent with the radiative transfer.
- Finally, we still lack a proper convection theory that can cope with the interaction of pulsation and convection in a realistic way.

5.2 Suggested Future Research

It is clear that our future work will be to improve the equilibrium models by Houdek because the treatment of radiation in their atmosphere is not adequate. The improved equilibrium models can probably be obtained by basing the $T(\tau)$ relation on the actual Hopf function relevant for a grey atmosphere in radiative equilibrium. We will also need to investigate models for different mixing length parameters. Furthermore, we will also consider a series of models with constant mass $M/M_{\odot}$, luminosity $L/L_{\odot}$ and varying effective temperature T_{eff} parameter to do extensive investigations.

We would also like to apply Medupe's code and my code to exactly the same equilibrium models in order to come up with concrete conclusion.

It would be interesting to see how the results of Balmforth et al (2001) and Cunha & Sousa (2006) change if our new code is used.

I would also like to apply my code to the same equilibrium models, especially models around $1.6\,M_{\odot}$, used by Cunha (2002). This is motivated by the fact that Cunha (2002), when using GH code, found all high radial order modes to be unstable and I found those modes to be overstable.

We will also compare our theoretical results with photometry. This will be done by comparing our grey results with the Watson formula presented in chapter 1. Since we have grey results

and the Watson formula is monochromatic, we will need to convert the formula to bolometric amplitudes by integrating the formula over all the given wavelengths. Medupe (2002) has shown there is no agreement between the bolometric amplitudes computed from the two approaches in the roAp frequency regime $1 < \nu < 3$ mHz. Therefore we will focus our attention on the δ Scuti stars.

We will calculate the amplitude ratio f and phase difference Ψ_T and apply them to Watson formula to see if we can determine n and ℓ values as was done by CDP94.

It is a also clear that we will derive and solve non-adiabatic non-radial pulsation with consistent treatment of radiation and non-local mixing length theory of convection in the near future.

References

Arentoft T., 2001, PhD thesis, Vrije Univesiteit Brussel.

Auer L.H., Mihalas D., 1970, MNRAS, 149, 65.

Baker N. H., 1987, in: Physical Processes in Comets, Stars and Active Galaxies, Hillebrandt W., Meyer-Hofmeister E., Thomas H.-C. (eds.), Springer-Verlag, New York, p. 105.

Baker N. H., Kippenhahn R.., 1962, Zs. f. Ap., 54, 114.

Baker N. H., Kippenhahn R.., 1965, ApJ, 142, 868.

Baker N.H., Moore D.W., Spiegel E.A., 1971, Q. J. Mech. Appl. Math. 24, 391.

Baker N. H., Gough D.O., 1979, ApJ, 234, 232.

Balmforth N. J., Gough D. O., 1990, Sol. Phy.,128,161.

Balmforth N. J., 1992a, MNRAS, 255, 603.

Balmforth N. J., 1992b, MNRAS, 255, 632.

Balmforth N. J., Cunha M. S., Dolez N., Gough D. O., Vauclair S., 2001, MNRAS, 323, 362.

Balmforth N. J., Gough D. O., 1988, in E. Rolfe (ed.), Seismology of the Sun and Sun-Like Stars, ESA, Noordwijk, SP-286, p.47.

Balmforth N. J., Gough D. O., 1990a, Sol. Ph., 128, 161.

Balmforth N. J., Gough D. O., 1990b, ApJ, 362, 256.

Balona L. A., 1986a, MNRAS, 219, 111.

Balona L. A., 1986b, MNRAS, 220, 647.

Balona L. A., Stobie R. S., 1979, MNRAS, 189, 649.

Balona L. A., Evers E. A., 1999, MNRAS, 302, 349.

Balona L. A., James D. J., Motsoasele P., Nombexeza B., Ramnath A., & van Dyk J., 2002, MNRAS, 333, 952.

Bigot L., Dziembowski W. A., 2002, A&A, 391, 235.

Bigot L., Provost J., Berthomieu G., Dziembowski W.A., Goode P.R., 2000, A&A, 356, 218.

Breger M. et al., 1995, A&A, 297, 473.

Breger M., 2000, in Breger M., Montgomery M., eds, ASP Conf. Ser. Vol. 210, Delta Scuti and Related Stars. Astron. Soc. Pac., San Francisco, p. 3.

Carroll B. W., Ostlie D. A., 1996, Introduction to Modern Astrophysics, Addison-Wesley Publishing Company, New York.

Chevalier C., 1971, A&A, 14, 24.

Christensen-Dalsgaard J., 2000, in Delta Scuti and Related Stars, M. Breger and M. Montgomery (eds), ASP Conf. Ser. 210, 187.

Christensen-Dalsgaard J., 2003, Lecturer notes on stellar oscillations,

Christensen-Dalsgaard J., Frandsen S., 1983, Sol. Phy., 82, 165.

Chandrasekhar S., 1961, Hydrodynamic and Hydromagnetic Stability (Oxford: Oxford University Press).

Cox J. P., 1980, Theory of Stellar Pulsation, Princeton University Press.

Cugier H., Dziemboski W.A., Pamyatnykh A.A., 1994, A&A, 291, 143.

Cunha M.S., 2002, MNRAS, 333, 47.

Cunha M. S., Gough D. O., 2000, MNRAS, 319, 1020.

Cunha M. S., Sousa S.A.G., 2006, MmSAI, 77, 354.

Dziembowski W. A, 1977, AcA, 27, 203.

Dziembowski W. A., 1985, Acta. Astr., 27, 203.

Dziembowski W. A., Goode P. R., 1985, ApJ, 296, L27.

Dziembowski W. A., Goode P. R., 1996, ApJ, 458, 338.

Dziembowski W., Pamyatnykh A.A., 1993, MNRAS, 262, 204.

Fontaine G., Brassard P., Bergeron P., Wesmael F., 1996, ApJ, 469, 320.

Garrido R., Garcia-Lobo E., Smeyers P., 1990, A&A, 234, 262.

Gough D. O., 1965, Geophys. Fluid Dyn. II (Woods Hole Oceanographic Institution), p. 49.

Gough D. O., 1969, J. Atmos. Sci., 26, 448.

Gough D. O., 1976, Problems of stellar convection, IAU Colloq. No. 38, p. 15, eds Spiegel E., Zahn J.-P., Springer-Verlag, Berlin.

Gough D. O., 1977, ApJ, 214, 196.

Gough D.O., Tayler R.J., 1966, MNRAS, 133,85.

Gough D.O., Leibacher J.W., Scherrer P.H., Toomre J., 1996, Science, 272, 1281.

Gough D. O., Weiss N.O., 1976, MNRAS, 176, 589.

Hansen C.J., Kawaler S.D., Trimble V., 1994, Stellar Interiors, Physical Priciples, STructure, and Evolution, 2nd Edition, Springer-Verlag, New York, p. 243.

Heynderickx D., Waelkens C., Smeyers P.,1994, A&AS, 105, 447.

Houdek G., 1996, PhD thesis, Universität Wien.

Iglesias C.A., Rogers F.J., 1996, ApJ, 464, 943.

Kambe E., Osaki Y.,1988, PASJ, 40, 313.

Kennelly E. J. et al., 1998, ApJ, 495, 440.

Kippenhahn R., Weigert A., 1990, Stellar structure and evolution, Springer-Verlag, Berlin.

Kochukhov O. & Ryabchikova T., A&A, 374, 615.

Kuhfus R., 1986, A&A, 160,116.

Kurtz D. W., 1982, MNRAS, 200, 807.

Kurtz D. W., 1990, ARA&A, 28, 607.

Ledoux P., 1951, ApJ, 114, 373.

Lee U., Saio H., 1986, MNRAS, 221, 365.

Lee U., Saio H., 1990, ApJ, 349, 570.

Martinez P., Kurtz D.,1995, in: Astrophysical Applications of Stellar Pulsation, ASP Conf. Series, 83, eds.: R. Stobie and P. Whitelock, Astron. Soc. Pacific, San Fransico, p. 58..

Medupe R. T., 2002, PhD thesis, University of Cape Town.

Medupe R., Kurtz D.W., Christensen-Dalsgaard J., 2000, In the impact of Large Scale Surveys on Pulsating Star Research, ASP Conf. Series, 203, eds. L. Szabados & D. Kurtz, p. 451.

Medupe R., Christensen-Dalsgaard J., Kurtz D.W., 2002, in Aerts C., Bedding T.R., Christensen-Dalsgaard J., eds, ASP Conf. Ser. Vol.259, Radial and Nonradial Pulsations as Probes of stellar Physics. Astron. Soc. Pac., San Fransisco, p. 296.

Mihalas D., 1978, Stellar Atmospheres,(2nd Edition, W. H. Freeman, San Fransisco.

North P., Jaschek C., Hauck B., Figueras F., Torra J., Kunzli M., 1997, ESA SP-402, Hipparcos-Venice 97.ESA, Noordwijk, p. 239.

Pesnell W.D., 1989, ApJ, 339, 1038.

Prandtl L., 1925, Zs.f. angew. Math. Mech., 5,136.

Prandtl L., 1932, Beitr.z. Phys. d. freien Atm. 19, 188.

Saio H., 2005, MNRAS, 360, 1022.

Saio H., Cox J.P., 1980, ApJ, 236, 549.

Shibahashi H., Takata M., 1993, PASJ, 45, 617.

Shibahashi H., Kurtz D., Kambe E., & Gough D. O., 2004, ASP Conf. Ser., 310, 287.

Shibahashi H., Gough D. O., Kurtz D., & Kambe E., 2008, PASJ, 60, 63.

Smith M.A., ApJ, 215, 574.

Smith M.A., ApJ, 224, 927.

Spiegel E., 1963, ApJ, 138, 216.

Stamford P. A., Watson R. D., 1981, Ap&SS, 77, 131.

Stellingwerf R.F., 1982, ApJ, 262, 330.

Takata M., Shibahashi H., 1995, PASJ, 47, 219.

Tassoul J., 1978, Theory of Rotating Stars, Princeton University Press, Princeton, New Jersey.

Tassoul M., Tassoul J.L.,1968, ApJ, 153, 127.

Taylor G. I., 1915, Phil. Trans. A 215, 1.

Thompson M.J., 2006, Introduction to Astrophysical Fluid Dynamics, Imperial College Press, London, p. 58.

Tritton D.J., 1977, Physical Fluid Dynamics, Van Nostrand Reinhold, Wokingham, Berkshire, England, p. 14.

Towsend R., 2002, MNRAS, 330, 855.

Vernazza J.E., Avrett E.H., Loeser R., 1981, ApJS, 45,635.

Vogt S.S., Penrod G.D., 1983, ApJ, 275, 661.

Walker G. A. H., Yang S., Fahlman G. G., 1979, ApJ, 140, 255.

Watson R. D., 1988, Ap&SS, 140, 255.

Wolff S. C., 1983, The A-type stars: Problems and Perspective. NASA, SP-463. Washington DC: NASA.

Unno W., 1967, PASJ, 14,416.

Unno W., Spiegel E.A., 1966, PASJ, 14, 416.

Unno W., Osaki Y., Ando H., Saio H., Shibahashi H., 1989, Nonradial Oscillations of Stars (second edition), McGraw-Hill, New York.

Xiong D., 1978, ChA&A, 2, 118.

Appendix A

The Equilibrium model

We summarise differential equations used to construct the equilibrium models as presented by Houdek (1996).

A.1 The differential equations

The equations are:

$$\frac{d\log m}{d\log p} = -4\pi r^2 \frac{p}{mg}\tilde{\mu}, \tag{A.1}$$

$$\frac{dr}{dm} = \frac{1}{4\pi r^2 \rho}\tilde{\mu}, \tag{A.2}$$

$$\frac{d\log J}{d\log p} = \frac{\kappa p L}{16\pi^2 r^2 g(f_{eq}J)}\tilde{\mu}(1-f)\left[1+\frac{d\ln f_{eq}}{d\ln J}\right]^{-1}, \tag{A.3}$$

$$\frac{df}{d\log p} = \frac{z_f}{(\alpha_c \log e)^2}, \tag{A.4}$$

$$\frac{dz_f}{d\log p} = a^2(f-f^L), \tag{A.5}$$

$$\frac{dz_\beta}{d\log p} = b^2(\bar{\beta}-\beta), \tag{A.6}$$

$$\frac{d\nu_1}{d\log p} = \frac{z_t}{(\alpha_c \log e)^2}, \tag{A.7}$$

$$\frac{dz_t}{d\log p} = a^2(\nu_1-\nu_1^L), \tag{A.8}$$

where

$$z_f = (\alpha_c \log e)^2 \frac{df}{d\log p}, \qquad z_\beta = (\alpha_c \log e)^2 \frac{d\bar{\beta}}{d\log p}, \qquad z_t = \frac{1}{p}(\alpha_c \log e)^2 \frac{df}{d\log p}$$

$$f = \frac{L_c}{L}, \qquad \nu_1 = \frac{p_t}{p}, \tag{A.9}$$

f^L and ν_1^L are the source functions from local mixing-length theory.

A.2 Boundary conditions

The mass, radius and effective temperature of the model are specified as the three of the nine boundary conditions. We obtain the remaining six boundary conditions from the fact that away from the overturning layers the source functions f^{loc} and ν_1^{loc} assume to vanish (see section). This provides four boundary conditions:

$$\frac{df}{d\log p} = \pm\frac{af}{\alpha_c \log e}, \tag{A.10}$$

and

$$\frac{d\nu_1}{d\log p} = -\left(1 \pm \frac{a}{\alpha_c}\right)\frac{\nu_1}{\log e}. \tag{A.11}$$

The last two boundary conditions are obtained from the requirement

$$\bar{\beta} = \beta, \tag{A.12}$$

above and below the convective instability region.

Appendix B

The Pulsation model

First the linear adiabatic pulsation equations are solved providing the solution for the linear non-adiabatic pulsation equations. The non-adiabatic pulsation equations are then solved using the local mixing-length theory of convection and diffusion approximation to radiative transfer to provide trial solution non-adiabatic equations using nonlocal mixing-length theory of convection and consistent treatment of radiation.

B.1 Linear adiabatic pulsation equations

The adiabatic pulsation equations are:

$$\frac{d}{d\ln p_0}\left(\frac{\delta r}{r_0}\right) = \frac{p_0 r_0}{Gm\rho_0}\left(3\frac{\delta r}{r_0} + \Gamma_1^{-1}\frac{\delta p}{p_0}\right), \tag{B.1}$$

$$\frac{d}{d\ln p_0}\left(\frac{\delta p}{p_0}\right) = -\frac{\delta p}{p_0} - \left(4 + \frac{\omega^2}{\Omega^2}\right)\frac{\delta r}{r_0}, \tag{B.2}$$

where

$$\Omega^2 = \frac{Gm}{r_0^3}. \tag{B.3}$$

The boundary conditions used the normalization of displacement, vanishing of displacement at the base of the envelope and the mechanical condition by Baker & Kippenhahn (1965). That is:

$$\frac{\delta r}{r_0} = 0, \tag{B.4}$$

$$\frac{\delta r}{r_0} = 1, \tag{B.5}$$

and

$$\frac{\delta p}{p_0} = -\left(4 + \frac{\omega^2}{\Omega^2}\right). \tag{B.6}$$

The problem are solved numerically and provides the trial solution for the non-adiabatic pulsation equations using local mixing length theory of convection.

B.2 Linear non-adiabatic pulsation equations local mixing-length theory of convection

Here the non-adiabatic pulsation equations using the local, time-dependent mixing-length theory for convection and diffusion approximation to radiative transfer are solved. The non-adiabatic radial pulsation equations are:

$$\frac{d}{d\ln p_0}\left(\frac{\delta r}{r_0}\right) = \tilde{\mu}\frac{p_0 r_0}{Gm\rho_0}\left(3\frac{\delta r}{r_0} + \alpha_0\frac{\delta p_g}{p_{g0}} + \delta_0\frac{\delta T}{T_0}\right), \tag{B.7}$$

$$\frac{d}{d\ln p_0}\left(\frac{\delta p}{p_0}\right) = -\left\{\frac{\delta p}{p_0} + \left[3 + \tilde{\mu}\left(1 + \frac{\omega^2}{\Omega^2}\right)\right]\frac{\delta r}{r_0} + \tilde{\mu}\nu_1\frac{p_0 r_0}{Gm\rho_0}\right.$$
$$\left.\times\left[(3-\Phi_0)\left(\alpha_0\frac{\delta p_g}{p_{g0}} - \delta_0\frac{\delta T}{T_0} - \frac{\delta p_t}{p_{t0}}\right) - \delta\Phi\right]\right\}, \tag{B.8}$$

$$\frac{d}{d\ln p_0}\left(\frac{\delta T}{T_0}\right) = \tilde{\mu}\frac{3\kappa L_{r0}p_0}{16\pi a_r cGmT_0^4}\left[\frac{\delta L_r}{L_{r0}} + \kappa_p\frac{\delta p_g}{p_{g0}} + (\kappa_T - 4)\frac{\delta T}{T_0} - 4\frac{\delta r}{r_0}\right], \tag{B.9}$$

$$\frac{d}{d\ln p_0}\left(\frac{\delta L}{L_0}\right) = i\omega\tilde{\mu}\frac{4\pi r_0^4 p_0 c_{p0} T_0}{GmL_0}\left(\frac{\delta T}{T_0} - \nabla_{ad}\frac{\delta p_g}{p_{g0}}\right), \tag{B.10}$$

using

$$\delta L = \delta L_r + \delta L_c, \tag{B.11}$$

and

$$\delta p = \delta p_g + \delta p_t. \tag{B.12}$$

The non-adiabatic pulsation equations (B.7), (B.8), (B.9) and (B.10) require two more boundary conditions as in the adiabatic case. For the thermal outer boundary condition we use

$$\frac{\delta L}{L_0} = 2\left(1 + \frac{\tau_0}{\tau_0 + \frac{2}{3}}\right)\frac{\delta r}{r_0} + \left(4 - \frac{\tau_0}{\tau_0 + \frac{2}{3}}\kappa_T\right)\frac{\delta T}{T_0} - \left(\frac{\tau_0}{\tau_0 + \frac{2}{3}}\right)\kappa_p\frac{\delta p}{p_0}. \tag{B.13}$$

The surface mechanical boundary condition (Eq. B.6) is replaced by

$$\frac{\delta p}{p_0} = -\frac{\Gamma_1 R}{H_p}\lambda_+\frac{\delta r}{r_0}, \tag{B.14}$$

where

$$\lambda_+ = \frac{1}{2} + \frac{1}{2}i\left(\frac{\omega^2}{\omega_{ac}^2} - 1\right)^{1/2}. \tag{B.15}$$

The boundary condition at the bottom of the model envelope is given as:

$$\nabla_{ad}\frac{\delta p_g}{p_{g0}} - \frac{\delta T}{T_0} = 0. \tag{B.16}$$

B.3 Linear non-adiabatic pulsations equations using non-local mixing-length theory of convection

This is the summary of pulsation equations using non-local mixing-length theory of convection and consistent treatment of radiation as presented in chapter 2.

$$\frac{d}{d\ln p_0}\left(\frac{\delta r}{r_0}\right) = \tilde{\mu}\frac{p_0 r_0}{Gm\rho_0}\left[3\frac{\delta r}{r_0} + \frac{\alpha_0}{1-\nu_1}\left(\frac{\delta p}{p_0} - \frac{\delta p_t}{p_0}\right) - \delta_0\frac{\delta T}{T_0}\right]. \tag{B.17}$$

$$\frac{d}{d\ln p_0}\left(\frac{\delta p}{p_0}\right) = -\frac{\delta p}{p_0} - \left[3 + \tilde{\mu}\left(1 + \frac{\omega^2}{\Omega^2}\right)\right]\frac{\delta r}{r_0} + \tilde{\mu}\nu_1\frac{p_0 r_0}{Gm\rho_0} \times \left\{(3-\Phi_0)\left[\delta_0\frac{\delta T}{T_0} - \frac{\alpha_0}{1-\nu_1}\left(\frac{\delta p}{p_0} - \frac{\delta p_t}{p_0}\right) + \frac{1}{\nu_1}\frac{\delta p_t}{p_0}\right] + \delta\Phi\right\}. \tag{B.18}$$

$$\frac{d}{d\ln p_0}\left(\frac{\delta K}{K_0}\right) = \tilde{\mu}\frac{\kappa_0 p_0(1-f)L_0}{16\pi^2 Gm(f_{eq}J_0)}\left[\kappa_T\frac{\delta T}{T_0} + \frac{\kappa_p}{1-\nu_1}\left(\frac{\delta p}{p_0} - \frac{\delta p_t}{p_0}\right) - 4\frac{\delta r}{r_0} - \frac{\delta K}{K_0} + \frac{1}{1-f}\left(\frac{\delta L}{L_0} - \frac{\delta L_c}{L_0}\right)\right] \tag{B.19}$$

$$\frac{d}{d\ln p_0}\left(\frac{\delta L}{L_0}\right) = i\omega\tilde{\mu}\frac{4\pi r_0^4 p_0}{Gm}\frac{p_0\delta_0}{\rho_0 L_0}\left(\frac{1-\nu_1}{\nabla_{ad}}\frac{\delta T}{T_0} - \frac{\delta p}{p_0} + \frac{\delta p_t}{p_0}\right). \tag{B.20}$$

$$\frac{d}{d\ln p_0}\left(\frac{\delta L_c}{L_0}\right) = \frac{\delta z_L}{L_0} + \frac{z_L}{L_0}\frac{d}{d\ln p_0}\left(\frac{\delta p}{p_0}\right). \tag{B.21}$$

$$\frac{d}{d\ln p_0}\left(\frac{\delta z_L}{L_0}\right) = \frac{a^2}{\alpha_c^2}\left[f_L(1-\varphi_L)\frac{d}{d\ln p_0}\left(\frac{\delta p}{p_0}\right) + \frac{\delta L_c}{L_0} - f_L\varphi_L\frac{\delta L_c{}^L}{L_{c0}}\right], \tag{B.22}$$

$$\frac{d}{d\ln p_0}\left(\frac{\delta\bar{\beta}}{\bar{\beta}_0^{osc}}\right) = \frac{z_\beta}{\bar{\beta}_0^{osc}}\frac{d}{d\ln p_0}\left(\frac{\delta p}{p_0}\right) + \frac{\delta z_\beta}{\bar{\beta}_0^{osc}}. \tag{B.23}$$

$$\frac{d}{d\ln p_0}\left(\frac{\delta z_\beta}{\bar{\beta}_0^{osc}}\right) = \frac{b^2}{\alpha_c^2}\left[f_\beta(1-\varphi_\beta)\frac{\partial}{\partial\ln p_0}\left(\frac{\delta p}{p_0}\right) + \frac{\delta\bar{\beta}}{\bar{\beta}_0^{osc}} - f_\beta\varphi_\beta\left(\frac{\delta\beta}{\beta_0}\right)\right], \tag{B.24}$$

$$\frac{d}{d\ln p_0}\left(\frac{\delta p_t}{p_0}\right) = \frac{\delta z_t}{p_0} - \frac{\delta p_t}{p_0} + \frac{z_t}{p_0}\frac{d}{d\ln p_0}\left(\frac{\delta p}{p_0}\right). \tag{B.25}$$

$$\frac{d}{d\ln p_0}\left(\frac{\delta z_t}{p_0}\right) = \frac{a^2}{\alpha_c^2}\left[\nu_1(1-\varphi_t)\frac{d}{d\ln p_0}\left(\frac{\delta p}{p_0}\right) + \frac{\delta p_t}{p_0} - \nu_1\varphi_t\frac{\delta p_t}{p_t 0}^{L}\right] - \frac{\delta z_t}{p_0}. \tag{B.26}$$

In addition to the four boundary conditions given by equations (B.5), (B.13), (B.14) and (B.16), four boundary conditions from non-local mixing-length theory are:

$$\frac{a}{\alpha_c}\frac{\delta L_c}{L_0} = \pm\frac{d}{d\ln p_0}\left(\frac{\delta L_c}{L_0}\right), \tag{B.27}$$

and

$$\frac{a}{\alpha_c}\frac{\delta p_t}{p_0} = \pm\frac{d}{d\ln p_0}\left(\frac{\delta p_t}{p_0}\right). \tag{B.28}$$

The last two boundary conditions are obtained by letting

$$\delta\bar{\beta} = \delta\beta, \tag{B.29}$$

above and below the convective instability region.

Appendix C

The Feautrier method

This method is given in detail by Medupe (2002). Here we summarise the Feautrier method used to solve the radiative transfer equations (1.32) and (2.25) in the atmosphere. At the top boundary the condition of zero incoming radiation is imposed and at the bottom of the atmosphere the diffusion approximation is imposed.

C.1 The unperturbed transfer equation

C.1.1 The atmosphere

We define the mean-intensity like variable:

$$j = \frac{1}{2}\left(I^{+}(+\mu) + I^{-}(-\mu)\right), \tag{C.1}$$

where $I^{+}(+\mu)$ and $I^{-}(-\mu)$ are outgoing and inward-going intensities. The flux-like variable is defined as:

$$h = \frac{1}{2}(I^{+}(+\mu) - I^{-}(-\mu)). \tag{C.2}$$

Both cases are apply for $0 \leq \mu \leq 1$.
Applying $I^{+}(+\mu)$ and $I^{-}(-\mu)$ to the radiative transfer equation:

$$\mu\frac{dI}{d\tau} = I - S \tag{C.3}$$

to obtain the following first differential equations:

$$+\mu\frac{dI^{+}}{d\tau} = I^{+} - S, \tag{C.4}$$

and

$$-\mu\frac{dI^{-}}{d\tau} = I^{-} - S. \tag{C.5}$$

We add equations (C.4) and (C.5) to get:

$$\mu\frac{d(I^{+} - I^{-})}{d\tau} = (I^{+} + I^{-}) - 2S, \tag{C.6}$$

which is

$$\mu \frac{dh}{d\tau} = j - S. \tag{C.7}$$

Subtracting equation (C.5) from equation (C.4) we get:

$$\mu \frac{dj}{d\tau} = h. \tag{C.8}$$

We combine equations (C.7) and (C.8) to get:

$$\mu^2 \frac{d^2 j}{d\tau^2} = j - S. \tag{C.9}$$

It can be noted that:

$$I^+ = h + j. \tag{C.10}$$

C.1.2 The envelope

As presented in section the radiation quantities I, J, H and K in the envelope can be written as (see Mihalas (1978):

$$I(\tau, \mu) = B(\tau) + \mu \frac{dB}{d\tau} + \mu^2 \frac{d^2 B}{d\tau^2} + \cdots, \tag{C.11}$$

$$J(\tau) = B(\tau) + \frac{1}{3} \frac{d^2 B}{d\tau^2} + \cdots, \tag{C.12}$$

$$H(\tau) = \frac{1}{3} \frac{dB}{d\tau} + \cdots, \tag{C.13}$$

$$K(\tau) = \frac{1}{3} B(\tau) + \frac{1}{5} \frac{d^2 B}{d\tau^2} + \cdots, \tag{C.14}$$

where τ is the optical depth. We use equations (C.10) and (C.12) to calculate the Feautrier h at large τ with the following equation:

$$h = B(\tau) + \mu \frac{dB}{d\tau} + \mu^2 \frac{d^2 B}{d\tau^2} - j. \tag{C.15}$$

C.1.3 Moments of the transfer equation

The moments of the transfer equations (1.33), (1.36) and (1.37) are expressed in terms of the Feautrier variables. The mean intensity J is given as

$$J(\tau) = \frac{1}{2} \int_{-1}^{0} I^-(-\mu) d(-\mu) + \frac{1}{2} \int_{0}^{+1} I^+(+\mu) d(+\mu) \tag{C.16}$$

$$= \frac{1}{2} \int_{0}^{+1} I^-(-\mu) d(\mu) + \frac{1}{2} \int_{0}^{+1} I^+(+\mu) d(+\mu) \tag{C.17}$$

Thus equation (C.25) can be expressed in terms of j as:

$$J(\tau) = \int_0^1 j(\mu)d\mu. \tag{C.18}$$

Similarly H and K are:

$$H(\tau) = \int_0^1 h(\mu)\mu d\mu, \tag{C.19}$$

and

$$K(\tau) = \int_0^1 j(\mu)\mu^2 d\mu. \tag{C.20}$$

C.1.4 Boundary conditions

C.1.4.1 At the surface

We expect at the surface of a star to have no radiation from the outside, hence $I^-(-\mu) = 0$. Expressing this in terms of the Feautrier variables (h and j) we obtain $h(\tau = 0) = I^+/2$ and $j(\tau = 0) = I^+/2$. Therefore, using equation (C.8) the upper boundary condition becomes:

$$\mu\frac{dj(0)}{d\tau} = j(0). \tag{C.21}$$

C.1.4.2 At the bottom of the atmosphere

At the bottom of the atmosphere we assume radiation to be modelled by diffusion approximation. The equation (C.12) is given as:

$$I(\tau_{max}) = B(\tau_{max}) + \mu\frac{dB}{d\tau}\Big|_{\tau=\tau_{max}} \quad \text{with} \quad j = B(\tau_{max}). \tag{C.22}$$

Hence the boundary condition:

$$\frac{dj}{d\tau}\Big|_{\tau=\tau_{max}} = \frac{dB}{d\tau}\Big|_{\tau=\tau_{max}}. \tag{C.23}$$

C.2 The perturbed transfer equation

Here we use the Feautrier variables j and h used to solve unperturbed transfer equation.
The equations (C.7) and (C.8), for the case of no-scattering $S_\nu = B_\nu$, are perturbed to obtain:

$$\mu\frac{d\delta h_\nu}{d\tau_\nu} = \frac{\delta\kappa_\nu}{\kappa_\nu}(j_\nu - B_\nu) + (\delta j_\nu - \delta B_\nu), \tag{C.24}$$

and

$$\mu \frac{d\delta j_\nu}{d\tau_\nu} = \delta h_\nu + \frac{\delta \kappa_\nu}{\kappa_\nu} h_\nu. \tag{C.25}$$

Equations (C.24) and (C.25) can be combined to form a second order differential equation:

$$\mu^2 \frac{d^2 \delta j_\nu}{d\tau_\nu^2} = \delta j_\nu - \delta B_\nu + \frac{\delta \kappa_\nu}{\kappa_\nu}(j_\nu - B_\nu) + \mu \frac{d}{d\tau_\nu}\left(\frac{\delta \kappa_\nu}{\kappa_\nu}\right). \tag{C.26}$$

C.2.1 Moments of the perturbed transfer equation

Moments of the perturbed radiative transfer equation can be given as:

$$\delta J_\nu = \int_0^1 \delta j_\nu(\mu) d\mu, \tag{C.27}$$

$$\delta H_\nu = \int_0^1 \delta h_\nu(\mu) \mu d\mu, \tag{C.28}$$

and

$$\delta K_\nu = \int_0^1 \delta j_\nu(\mu) \mu^2 d\mu. \tag{C.29}$$

C.2.2 Boundary conditions for the perturbed transfer equation

C.2.2.1 At the surface

At the surface of a star we expect to have no radiation from the outside, i.e. $I^-(\tau_{s\nu})$ where the subscript s denotes τ_ν at the upper boundary of the atmosphere. The perturbed Feautrier variables become:

$$\delta h_\nu(\tau_{s\nu}) = \delta j_\nu(\tau_{s\nu}) \qquad \text{at} \qquad \tau_\nu = \tau_{s\nu}. \tag{C.30}$$

Therefore, we use equation (C.25) to obtain the boundary condition:

$$\mu \frac{d\delta j_\nu(\tau_{s\nu})}{d\tau_\nu} = \delta j_\nu(\tau_{s\nu}) + \frac{\delta \kappa_\nu(\tau_{s\nu})}{\kappa_{s\nu}} h_\nu(\tau_{s\nu}). \tag{C.31}$$

C.2.2.2 At the bottom of the atmosphere

Here the boundary condition is obtained by applying the diffusion approximation at the base of the atmosphere. The intensity I is expressed as:

$$I_\nu^+(\tau_{max\,\nu}) = B(\tau_{max\,\nu}) + \mu \frac{dB}{d\tau}|_{\tau=\tau_{s\nu}}. \tag{C.32}$$

Using equations (C.10) and (C.8) we get:

$$I_\nu^+ = j_\nu + \mu \frac{dj_\nu}{d\tau_\nu}. \tag{C.33}$$

Perturbing equation (C.33) and (C.32) we obtain:

$$\delta I_\nu^+ = \delta j_\nu + \frac{\delta \kappa_\nu}{\kappa_\nu}(j_\nu - I_\nu^+) + \mu \frac{d\delta j_\nu}{d\tau_\nu}, \tag{C.34}$$

and

$$\delta I_\nu^+ = \delta B_\nu + \frac{\delta \kappa_\nu}{\kappa_\nu}(B_\nu - I_\nu^+) + \mu \frac{d\delta B_\nu}{d\tau_\nu}. \tag{C.35}$$

Equating the right hand sides of equations (C.34) and (C.35) we obtain the boundary condition:

$$\delta j_\nu + \mu \frac{d\delta j_\nu}{d\tau_\nu} - \delta B_\nu + \frac{\delta \kappa_\nu}{\kappa_\nu}(j_\nu - B_\nu) - \mu \frac{d\delta B_\nu}{d\tau_\nu} = 0. \tag{C.36}$$

Appendix D

Houdek's calculations

We summarise the pulsation equations with non-local mixing-length theory of convection and the Eddington approximation to radiative transfer as presented by Houdek (1996). The equations are:

$$\frac{d}{d\ln p_0}\left(\frac{\delta r}{r_0}\right) = \tilde{\mu}\frac{p_0 r_0}{Gm\rho_0}\left[3\frac{\delta r}{r_0} + \frac{\alpha_0}{1-\nu_1}\left(\frac{\delta p}{p_0} - \frac{\delta p_t}{p_0}\right) - \delta_0\frac{\delta T}{T_0}\right]. \tag{D.1}$$

$$\frac{d}{d\ln p_0}\left(\frac{\delta p}{p_0}\right) = -\frac{\delta p}{p_0} - \left[3 + \tilde{\mu}\left(1 + \frac{\omega^2}{\Omega^2}\right)\right]\frac{\delta r}{r_0} + \tilde{\mu}\nu_1\frac{p_0 r_0}{Gm\rho_0} \times \left\{(3-\Phi_0)\left[\delta_0\frac{\delta T}{T_0} - \frac{\alpha_0}{1-\nu_1}\left(\frac{\delta p}{p_0} - \frac{\delta p_t}{p_0}\right) + \frac{1}{\nu_1}\frac{\delta p_t}{p_0}\right] + \delta\Phi\right\}. \tag{D.2}$$

$$\frac{d}{d\ln p_0}\left(\frac{\delta J}{J_0}\right) = \tilde{\mu}\frac{\kappa_0 p_0(1-f)L_0}{16\pi^2 Gm(f_{eq}J_0)}\left[\kappa_T\frac{\delta T}{T_0} + \frac{\kappa_p}{1-\nu_1}\left(\frac{\delta p}{p_0} - \frac{\delta p_t}{p_0}\right) - 4\frac{\delta r}{r_0} - \frac{\delta J}{J_0} + \frac{1}{1-f}\left(\frac{\delta L}{L_0} - \frac{\delta L_c}{L_0}\right)\right] \tag{D.3}$$

$$\frac{d}{d\ln p_0}\left(\frac{\delta L}{L_0}\right) = i\omega\tilde{\mu}\frac{4\pi r_0^4 p_0}{Gm}\frac{p_0\delta_0}{\rho_0 L_0}\left(\frac{1-\nu_1}{\nabla_{ad}}\frac{\delta T}{T_0} - \frac{\delta p}{p_0} + \frac{\delta p_t}{p_0}\right). \tag{D.4}$$

$$\frac{d}{d\ln p_0}\left(\frac{\delta L_c}{L_0}\right) = \frac{\delta z_L}{L_0} + \frac{z_L}{L_0}\frac{d}{d\ln p_0}\left(\frac{\delta p}{p_0}\right). \tag{D.5}$$

$$\frac{d}{d\ln p_0}\left(\frac{\delta z_L}{L_0}\right) = \frac{a^2}{\alpha_c^2}\left[f_L(1-\varphi_L)\frac{d}{d\ln p_0}\left(\frac{\delta p}{p_0}\right) + \frac{\delta L_c}{L_0} - f_L\varphi_L\frac{\delta {L_c}^L}{L_{c0}}\right], \tag{D.6}$$

$$\frac{d}{d\ln p_0}\left(\frac{\delta\bar{\beta}}{\bar{\beta}_0^{osc}}\right) = \frac{z_\beta}{\bar{\beta}_0^{osc}}\frac{d}{d\ln p_0}\left(\frac{\delta p}{p_0}\right) + \frac{\delta z_\beta}{\bar{\beta}_0^{osc}}. \tag{D.7}$$

$$\frac{d}{d\ln p_0}\left(\frac{\delta z_\beta}{\bar{\beta}_0^{osc}}\right) = \frac{b^2}{\alpha_c^2}\left[f_\beta(1-\varphi_\beta)\frac{\partial}{\partial\ln p_0}\left(\frac{\delta p}{p_0}\right) + \frac{\delta\bar{\beta}}{\bar{\beta}_0^{osc}} - f_\beta\varphi_\beta\left(\frac{\delta\beta}{\beta_0}\right)\right], \tag{D.8}$$

$$\frac{d}{d\ln p_0}\left(\frac{\delta p_t}{p_0}\right) = \frac{\delta z_t}{p_0} - \frac{\delta p_t}{p_0} + \frac{z_t}{p_0}\frac{d}{d\ln p_0}\left(\frac{\delta p}{p_0}\right). \tag{D.9}$$

$$\frac{d}{d\ln p_0}\left(\frac{\delta z_t}{p_0}\right) = \frac{a^2}{\alpha_c^2}\left[\nu_1(1-\varphi_t)\frac{d}{d\ln p_0}\left(\frac{\delta p}{p_0}\right) + \frac{\delta p_t}{p_0} - \nu_1\varphi_t\frac{\delta p_t{}^L}{p_t 0}\right] - \frac{\delta z_t}{p_0}. \tag{D.10}$$

The boundary conditions are exactly the same as in section B.3.

Appendix E

Medupe's calculations

Here we summarise the non-adiabatic pulsation equations with consistent treatment of radiative transfer as presented by Medupe (2002). Convection, rotation magnetic fields are neglected in a well defined way in these equations. The pulsation equations are divided into the atmosphere and the envelope. The solutions are then matched.

E.1 The atmosphere

The atmosphere is treated as plane parallel.

$$\frac{d\delta\tilde{r}}{d\tau} = \frac{1}{H_p\kappa_R\rho}\left(\kappa_T\frac{\delta T}{T} + \kappa_p\frac{\delta p}{p}\right), \tag{E.1}$$

$$\frac{d}{d\tau}\left(\frac{\delta p}{p}\right) = \frac{1}{\kappa_R p}\left[g\frac{\delta p}{p} + \left(\omega^2 - \frac{dg}{dr} - 4\pi G\rho\right)H_p\delta\tilde{r}\right], \tag{E.2}$$

$$\begin{aligned}\frac{d\delta\tilde{H}}{d\tau} = -\frac{B}{H_0}\Bigg[&\frac{4i\omega\nabla_{ad} - \omega_R\Delta_c(\kappa_p + \rho_p)}{i\omega - \omega_R(4 - \Delta_c(\kappa_T + \rho_T))}\frac{\delta p}{p} \\ &- \frac{i\omega + \omega_R\Delta_c(\kappa_T + \rho_T)}{i\omega - \omega_R(4 - \Delta_c(\kappa_T + \rho_T))}\frac{\delta J}{B} - \Delta_c\frac{\delta\kappa}{\kappa}\Bigg],\end{aligned} \tag{E.3}$$

$$\frac{d\delta\tilde{K}}{d\tau} = \left[\kappa_T\frac{H}{K_0}\frac{\delta T}{T} + \kappa_p\frac{H}{K_0}\frac{\delta p}{p} + \delta\tilde{H}\frac{H_0}{K_0}\right], \tag{E.4}$$

where

$$\delta r = H_p\delta\tilde{r}, \qquad \delta H = H_0\delta\tilde{H}, \qquad \text{and} \qquad \delta K = K_0\delta\tilde{K}. \tag{E.5}$$

The quantity $\delta T/T$ is obtained from

$$\{i\omega - \omega_R[4 - \Delta_c(\kappa_T + \rho_T)]\}\frac{\delta T}{T} = \{i\omega\nabla_{ad} - \omega_R\Delta_c(\kappa_p + \rho_p)\}\frac{\delta p}{p} - \omega_R\frac{\delta J}{B}. \tag{E.6}$$

E.2 The envelope

In the envelope the transport of radiative energy assumes the diffusion approximation and the pulsations equations become:

$$\frac{d\delta\tilde{r}}{d\tau} = \frac{1}{H_p\kappa\rho}\left(\rho_T\frac{\delta T}{T} + \rho_p\frac{\delta p}{p} + 2H_p\frac{\delta\tilde{r}}{r}\right), \tag{E.7}$$

$$\frac{d}{d\tau}\left(\frac{\delta p}{p}\right) = -\frac{g}{\kappa p}\frac{\delta p}{p} - \frac{H_p}{\kappa p}\left(\omega^2 + \frac{2}{r}g(1+\lambda) - \frac{dg}{dr} - 4\pi G\rho\right)\delta\tilde{r}, \tag{E.8}$$

$$\frac{d}{d\tau}\left(\frac{\delta T}{T}\right) = \frac{d\ln T}{d\tau}\{(\kappa_T - 4)\frac{\delta T}{T} + \kappa_p\frac{\delta p}{p} + \left(\frac{H_0}{H}\delta\tilde{H} - 2H_p\frac{\delta\tilde{r}}{r}\right)\}, \tag{E.9}$$

$$\frac{d\delta\tilde{H}}{d\tau} = 2\frac{\delta\tilde{H}}{\kappa\rho r} - \frac{i\omega C_p T}{4\pi H_0\kappa}\left(\frac{\delta T}{T} - \nabla_{ad}\frac{\delta p}{p}\right), \tag{E.10}$$

where λ is the ratio of effective gravity to actual gravity. Since turbulent pressure is neglected we let $\lambda = 1$.

E.3 Boundary condition

Three of the four boundary conditions are the same as given in equations (B.5), (B.14) and (B.16). The fourth boundary condition is:

$$\delta H = g_{osc}\frac{\delta K}{f_{osc}}, \tag{E.11}$$

where g_{osc} is determined from the iteration for f_{osc}.

Appendix F

Coefficients of Gough's time-dependent mixing-length equations

In this appendix we summarise the coefficients of the linearised perturbed equations (1.126), (1.127) and (1.128) according to Gough (1977) and Baker & Gough (1979) as:

$$W_{10} = \frac{\delta g}{g_0} + \frac{\delta(\delta)}{\delta_0} + \frac{\delta(\Delta)}{\Delta_0} - \epsilon^2 k_{10} - (1-\epsilon^2)\mu_{10} + \frac{2i}{\hat{\sigma}} \frac{(1+\epsilon)\mu_{11} - \epsilon(1-i\hat{\sigma})k_{11}}{2 - i\hat{\sigma}(1-\epsilon)} + 2(\Phi_0 - 1)\frac{\delta\kappa}{\kappa_0}, \tag{F.1}$$

$$W_{11} = -\frac{2i}{\hat{\sigma}} \frac{(1+\epsilon)\mu_{11} - \epsilon k_{11}}{2 + i\hat{\sigma}(1-\epsilon)}, \tag{F.2}$$

$$W_{12} = (1+\epsilon)\mu_{10} - \epsilon k_{10}, \tag{F.3}$$

$$W_{21} = -2\left[\left(W_{11} - \frac{\delta\ell}{\ell_0}\right)\left(1 + i\frac{\omega}{\hat{\sigma}}\right)^{-1} - \frac{\delta r}{r_0}\right], \tag{F.4}$$

$$\Theta_{10} = W_{10} + W_{12} + \Phi_{10}, \tag{F.5}$$

$$\Theta_{12} = W_{12}, \tag{F.6}$$

$$\Phi_{10} = -2(1 - \Phi_0^{-1})\left(3\frac{\delta r}{r_0} + \frac{\delta\rho}{\rho_0} + \Phi_0\frac{\delta\kappa}{\kappa_0}\right), \tag{F.7}$$

$$\Phi_{11} = 2(1 - \Phi_0^{-1})\left(3\frac{\delta r}{r_0} + \frac{\delta\rho}{\rho_0}\right), \tag{F.8}$$

where

$$\frac{\delta g}{g_0} = -\left(2 + \frac{\omega^2 r^3}{Gm}\right)\frac{\delta r}{r_0}, \tag{F.9}$$

$$2\mu_{10} = -\Phi_{10}, \tag{F.10}$$

$$2\mu_{11} = \delta_p \frac{\delta p}{p_0} + (\delta_T - 1)\frac{\delta T}{T_0} - \Phi_0^{-1}\hat{\sigma}(1+\epsilon)^{-1}[\hat{\sigma}(1-\epsilon) - 2i\epsilon]\left(\frac{\delta\rho}{\rho_0} + 2\frac{\delta r}{r_0}\right) - 2(1-\Phi_0^{-1})\left(\frac{\delta\rho}{\rho_0} + 3\frac{\delta r}{r_0}\right) + \frac{\delta\beta}{\beta_0} + \frac{\delta g}{g_0}, \tag{F.11}$$

$$2\mu_{12} = \frac{\delta g}{g_0} + \frac{\delta(\delta)}{\delta_0} + \frac{\delta\beta}{\beta_0} - \frac{\delta T}{T_0} + 2(\Phi_0 - 1)\frac{\delta\chi}{\chi_0}, \tag{F.12}$$

$$k_{10} = -2\phi_0\left[(2 - 3\Phi_0^{-1})\frac{\delta r}{r_0} + (1 - \Phi_0^{-1})\frac{\delta\rho}{\rho_0} + \frac{\delta H_p}{H_{p0}} - \frac{\delta\kappa}{\kappa_0}\right], \tag{F.13}$$

$$k_{11} = 2\phi_0\left[(2 - 3\Phi_0^{-1})\frac{\delta r}{r_0} + (1 - \Phi_0^{-1})\frac{\delta\rho}{\rho_0}\right] + 3\frac{\delta T}{T_0} + (1 - 2\phi)\frac{\delta\kappa}{\kappa_0} - \frac{\delta c_p}{c_{p0}} + \frac{1}{2}i\tilde{\sigma}(\epsilon^{-1} - 1)\left[(1 - \delta + c_{pT})\frac{\delta T}{T_0} - \delta_T\frac{\nabla_{ad}}{1-\nu_1}\frac{\delta p}{p_0} - \frac{\delta g}{g_0} - \frac{\delta(\delta)}{\delta_0} + 2(3 - 4\Phi_0^{-1})\frac{\delta r}{r_0} + (2 - 3\Phi_0^{-1})\frac{\delta\rho}{\rho_0}\right], \tag{F.14}$$

$$k_{12} = 3\frac{\delta T}{T_0} - 2\phi\left(\frac{\delta\ell}{\ell_0} + \frac{\delta\rho}{\rho_0} - \frac{\delta\kappa}{\kappa_0}\right) + (1 - 2\phi)\frac{\delta\kappa}{\kappa_0} - \frac{\delta c_p}{c_{p0}}, \tag{F.15}$$

$$\frac{\delta(\Delta)}{\Delta_0} = \frac{\delta\ell}{\ell_0} + \frac{\delta\beta}{\beta_0} - \frac{\delta T}{T_0} + \epsilon(1-\epsilon)(\mu_{12} - k_{12}), \tag{F.16}$$

$$\frac{\delta\kappa}{\kappa_0} = \frac{1}{8}\left[\frac{\delta(\delta)}{\delta_0} - \left(2 + \frac{\omega^2}{\Omega^2}\right)\frac{\delta r}{r_0} + 2\left(\frac{\delta c_p}{c_{p0}} - \frac{\delta\kappa}{\kappa_0}\right) + 4\left(\alpha_0\frac{\delta p_g}{p_{g0}} - \delta_0\frac{\delta T}{T_0}\right) + 4\frac{\delta\ell}{\ell_0} - 7\frac{\delta T}{T_0}\right], \tag{F.17}$$

$$\frac{\delta\beta}{\beta_0} = \left(1 + \frac{\delta_0 g_0}{\tilde{\mu}\beta_0 c_{p0}}\right)\left(2\frac{\delta r}{r_0} + \alpha_0\frac{\delta p_g}{p_{g0}} - \delta_0\frac{\delta T}{T_0}\right) + \frac{\delta_0 g_0}{\tilde{\mu}\beta_0 c_{p0}}\left\{\left(\frac{\rho_0 c_{p0} T_0}{\delta_0 p_0}\nabla + \nu_2\delta_0\right)\frac{\delta T}{T} + \frac{\rho_0 c_{p0} T_0}{\delta_0 p_0}\frac{\partial}{\partial \ln p_0}\left(\frac{\delta T}{T_0}\right) + (1 - \nu_2)\left(\frac{\delta c_p}{c_{p0}} - \frac{\delta(\delta)}{\delta_0}\right) + \tilde{\mu}\left(2 + \frac{\omega^2}{\Omega^2}\right)\frac{\delta r}{r_0} + \nu_1\frac{\partial}{\partial \ln p_0}\left(\frac{\delta p_t}{p_{t0}}\right) + \nu_2\left(\frac{\delta p_t}{p_{t0}} - \alpha_0\frac{\delta p_g}{p_{g0}}\right)\right\} - \frac{\nu_1\delta_0 p_0}{\beta_0\rho_0 c_{p0} r_0}\left[(3 - \Phi_0)\left(\frac{\delta p_t}{p_{t0}} - \alpha_0\frac{\delta p_g}{p_{g0}} + \delta_0\frac{\delta T}{T_0} - \frac{\delta r}{r_0}\right) - \delta\Phi\right] \tag{F.18}$$

$$\frac{\delta H_p}{H_{p0}} = \frac{\delta p}{p_0} - \tilde{m}u\left\{\alpha_0\frac{\delta p_g}{p_{g0}} - \delta_0\frac{\delta T}{T_0} - \left(2+\frac{\omega^2}{\Omega^2}\right)\frac{\delta r}{r_0}\right.$$
$$\left.\nu_1\frac{p_0 r_0}{Gm\rho_0}\left[(3-\Phi_0)\left(\frac{\delta p_t}{p_{t0}} - \frac{\delta r}{r_0}\right) - \delta\Phi\right]\right\}, \tag{F.19}$$

$$\epsilon = (1+\hat{\eta}_0^2 S)^{-1/2}, \quad \hat{\sigma} = \frac{\omega}{\hat{\sigma}}, \quad \nu_1 = \frac{p_{t0}}{p_0}, \quad \nu_2 = \frac{dp_{t0}}{dp_0} \quad \text{and} \quad \delta\ell = \alpha_c \delta H_p. \tag{F.20}$$

The functional expressions $\mathcal{F}$, $\mathcal{G}$ and $\mathcal{H}$ in equations (1.126), (1.127) and (1.128) are given as

$$\mathcal{F} = \mathcal{J}_1\Gamma(2-i\hat{\sigma}), \tag{F.21}$$

$$\mathcal{G} = \mathcal{J}_1/\mathcal{J}_2 + \Psi(2-i\hat{\sigma}), \tag{F.22}$$

$$\mathcal{H} = \left[2\frac{\delta r}{r_0} + (1+\epsilon)\mu_{12} - \epsilon k_{12}\right]\mathcal{F}$$
$$-(2-i\hat{\sigma})(W_{10}-W_{12})\mathcal{F} - W_{12}\mathcal{F}[1+(2-i\hat{\sigma})\mathcal{G}] \tag{F.23}$$

where

$$\mathcal{J}_2 = 107\{E_1[2.88(1+i\hat{\sigma})] - 320E_1[2.88(3+i\hat{\sigma})]\} \tag{F.24}$$

$$\mathcal{J}_1 = i\frac{d\mathcal{J}_1}{d\hat{\sigma}} = \frac{12}{(1+i\hat{\sigma})(3+i\hat{\sigma})}\left(\frac{5^{1/2}s}{2}\right)^{i\hat{\sigma}}, \tag{F.25}$$

where Γ, Ψ and E_1 are the gamma function, digamma function and exponential integral of order unity, s=0.05.